Modelling and analysis of paste flow in high performance Søderberg electrodes





Alissa A. Kamilova
St Anne's College
University of Oxford

Trinity 2021

A thesis submitted for the degree of
Doctor of Philosophy

I dedicate this work to Dr. Mel Beckerleg, the kindest human being I have ever met.

Acknowledgements

I would like to express my deepest thanks to the following people:

To my academic supervisors, **Ian Hewitt** and **Peter Howell**, for their patience, time, and efforts that have consistently inspired me to become a better mathematician. Your expertise and intuition pushed this work forward, and I will never forget the valuable lessons you have taught me.

To **Robert Van Gorder**, for his mentorship, support, and encouragement week after week during this PhD, both personal and academic. Thank you for all the early morning conversations that have kept the mathematical spark alive.

To **Colin Please** and **Chris Breward** (C^2) for their dedication to the InFoMM CDT and their commitment to driving mathematics in industry.

To my industrial supervisors at Elkem ASA, without whom this project would never have seen the light of day: **Aasgeir Valderhaug**, **Ben Sloman**, and **Bjørnar Larsen**. To **Solveig Steinsland**, **Aslak Skjeldestad**, and **Bente Faaness** for their helpful advice and vast knowledge on the subject matter.

To cohort 3 of the InFoMM CDT, who were always there when I needed them, and with whom I will forever share a special bond. I would especially like to thank **Atta** (Dr. Kovács) for telling me to calm down when I needed it, and for always stepping up to the plate when things seemed impossible. I am also incredibly grateful to **Fede** (Dr. Danieli), for his help in my many numerical problems and for his willingness to have helpful discussions with me. Above all, a huge thank you to **Mel** (Dr. Beckerleg), for every second we spent together. I miss you, friend.

To my parents, **Lili** and **Alicher**, for never complaining that I chose mathematics over music. Thank you for all the sacrifices and hard work that it took to get me here. You are my inspiration in life.

To my friends: **Antonia Krasteva**, for never giving up on me and supporting every step of this lifelong dream. **Alanna Thomas**, for enduring mathematical conversations for (at least) five years, and for making me laugh throughout it all. **Sergio Cavazos**, for always having my back and for his willingness to listen to my mathematical complaints.

And finally, I would like to thank my incredible partner, **Frederik Hartmann**. Your kind words, unwavering support, positivity, and honest belief in me is a huge reason this document is possible. You are the light at the end of the tunnel.

Abstract

The Søderberg electrode is a continuously consumed electrode invented about 100 years ago by the company now known as Elkem ASA. It remains the most commonly used electrode system, which provides the energy necessary for the production of ferroalloys and calcium carbide. The electrode paste is the raw material that makes the electrodes: a mixture of pitch tar binder and calcined anthracite. It can be added in the form of solid cylinders at the inlet of the steel casing that encloses the electrode column. As the temperature increases inside the electrode column, the paste softens and spreads until it reaches the electrode casing, and then is baked as the temperature reaches 450 °C. In normal operation, hot paste from lower down the casing may be recirculated up to the top, forming a viscous *pool* of paste which in turn contributes to the softening of new incoming cylinders.

In this thesis we derive mathematical models focusing on the top part of the electrode where the paste softening process occurs. An incorrect softening profile of the paste may lead to a baked electrode with non-uniform material properties, leading to costly and dangerous breakages. For the models presented in this work, we have incorporated an exponential dependence of viscosity on temperature to account for how sensitive the paste is to temperature variations. Temperature variations result from the heating supplied by hot air outside the casing, as well as electrical induction effects caused by the proximity of the copper tubes that supply the electrical current to the casing.

In Chapter 2, we begin by formulating a two-dimensional flow and temperature model in steady state, which is then asymptotically reduced to a one-dimensional extensional flow model. We obtain numerical solutions to understand which physical effects control the position where the paste touches the casing for the first time, $x = \lambda$. In Chapter 3, we investigate this model further by looking at time dependent solutions. We use boundary layer theory and the theory of multiple scales to understand how the addition of cylinders affects the time evolution of $\lambda(t)$. In Chapter 4, we construct and solve a finite element model to gain some intuition on the role of the recirculating paste near the top of the electrode, and we discuss how we can make some conclusions on cylinder addition from this model. In Chapter 5, we use the structure of the solutions found in Chapter 4 to motivate a hybrid extensional flow model with lubrication flow near the walls where the temperature is higher and the viscosity is lower. We find asymptotic solutions for both the flow profile and the temperature distribution in the various boundary layers found in the problem, which we then interpret in the context of the industrial problem. We conclude this thesis with a summary and a discussion in Chapter 6.

Statement of Originality

All the work presented in this thesis has been done by the author, unless otherwise indicated.

Contents

1 Introduction **1**

1.1 Overview . . . 1

1.1.1 Electrode breakages and segregation . . . 2

1.2 Literature review . . . 4

1.3 Industrial data available . . . 6

1.3.1 Viscosity data . . . 6

1.3.2 Temperature and heat flux data . . . 8

1.4 Scope of the thesis . . . 10

2 A coupled flow and temperature model for paste softening **13**

2.1 Formulating an axisymmetric model . . . 13

2.1.1 Boundary conditions and coordinate system . . . 15

2.2 Derivation of one-dimensional model . . . 17

2.2.1 Non-dimensionalisation . . . 17

2.2.2 Asymptotic expansions . . . 19

2.2.3 Fluid problem . . . 19

2.2.4 Temperature problem . . . 21

2.3 Simplification of the one-dimensional model . . . 22

2.4 Steady state . . . 23

2.4.1 Constant viscosity case . . . 24

2.4.2 Numerical solutions . . . 25

2.4.3 Dependence on non-dimensional parameters . . . 27

2.4.4 The casing wall effect on the temperature . . . 29

2.4.5 Large Pe limit . . . 32

2.5 Concluding remarks . . . 34

3 Time dependent solutions for coupled flow and temperature model for paste softening **36**

3.1 Non-steady solutions . . . 37

3.1.1 Mathematical formulation . . . 37

3.1.2 Validating the numerical scheme . . . 40
3.2 Exploring P_{in} variation numerically . . . 42
3.3 Control strategies with $P_{\text{in}}(t)$ . . . 45
3.3.1 Control strategy 1 . . . 45
3.3.2 Control strategies 2a and 2b . . . 48
3.3.3 Varying slipping velocity . . . 52
3.4 Exploring P_{in} variation analytically . . . 53
3.4.1 Analysing fast oscillations . . . 54
3.4.2 Thermal boundary layer . . . 59
3.5 Multiple scales structure for isothermal problem . . . 64
3.6 Concluding remarks . . . 72

4 Two-dimensional axisymmetric CFD model with FEniCS 75
4.1 Governing equations and boundary conditions . . . 77
4.1.1 Non-dimensionalisation and variational problem formulation . . . 79
4.2 Isothermal problem . . . 80
4.2.1 Convergence test for a manufactured solution . . . 80
4.2.2 Electrode isothermal problem . . . 83
4.2.3 Normal stress calculation and corner singularities . . . 85
4.2.4 Alternative mesh constructions . . . 87
4.3 Coupled problem . . . 90
4.3.1 Varying coordinate systems . . . 90
4.4 Investigating parameters . . . 94
4.4.1 Dependence on heating parameters . . . 94
4.5 Relationship to weight of added cylinders . . . 96
4.5.1 Unsteady solutions with $u_{\text{in}} \neq 1/D$ . . . 96
4.5.2 Steady solutions with a displaced free surface . . . 98
4.6 Concluding remarks . . . 100

5 A coupled temperature and flow problem with extreme transverse viscosity variation 102
5.1 Flow problem with known temperature . . . 104
5.1.1 Governing equations and boundary conditions . . . 104
5.1.2 Non-dimensionalisation and scaling . . . 105
5.1.3 Asymptotic expansions . . . 107
5.1.4 Laplace's method for integrals . . . 110
5.1.5 Fully developed flow . . . 112
5.1.6 Solutions dependent on x . . . 112
5.1.7 Example with known temperature quadratic in y . . . 114

5.1.8 Examples with known temperature dependent on x . . . 118
5.2 Temperature problem with known flow . . . 120
5.2.1 Problem statement . . . 120
5.2.2 Boundary layer asymptotics for the temperature problem . . . 121
5.3 Solutions for constant u . . . 123
5.3.1 Equations and boundary conditions . . . 123
5.3.2 Numerical method and validation . . . 124
5.3.3 Comparing with an exact solution . . . 127
5.3.4 Regularising with diffusion in x . . . 128
5.3.5 Local solutions near the corner $(0, 1)$ . . . 130
5.4 Asymptotics for $u \approx q$ . . . 132
5.4.1 The outer problem . . . 133
5.4.2 Zooming into the $(1, 1)$ corner . . . 133
5.4.3 Zooming into the $(0, 1)$ corner . . . 134
5.5 Fully coupled flow and temperature problem . . . 137
5.5.1 Numerical method . . . 137
5.6 Dependence of solutions on parameters . . . 142
5.7 Concluding remarks . . . 144

6 Conclusions **146**
6.1 Summary of results and industrial recommendations . . . 146
6.2 Future work . . . 149
6.3 Closing remarks . . . 151

References **153**

A Finite volume scheme for time dependent problem in Chapter 3 **159**

Chapter 1

Introduction

1.1 Overview

The Søderberg electrode is a continuously consumed electrode invented about 100 years ago by the company now known as Elkem ASA (Söderberg, 1923). It remains the most commonly used electrode system, which provides the energy necessary for the production of ferroalloys and calcium carbide (Innvaer and Olsen, 1979). This type of electrode conducts currents of up to 150 kA to the centre of a smelting furnace, and operates at temperatures of more than 2000 °C. Traditionally, smelting furnaces are circular AC furnaces with 3 electrodes arranged in a triangular configuration (McDougall, 2013). A detailed schematic is shown in Figure 1.1.1 where the different layers forming a single electrode are illustrated. We refer the reader to this figure for the following description of the Søderberg electrode.

The electrode outer casing is made out of steel, and it is lowered at an average rate of about 0.5-1 m day^{-1}, which is called the *slipping rate* (Bergstrøm et al., 1989; Meyjes et al., 2010; Skjeldestad, 2019). The slipping process typically consists of intermittent short slips, typically of the order of 20 mm, every hour, rather than a continuous rate (McDougall, 2013). The paste is the raw material that makes the electrodes. It is a mixture of pitch tar binder and calcined anthracite (Mason, 1970). Unbaked paste is also called green paste in the literature (McDougall, 2013). It can be added in the form of solid cylinders, as shown in Figure 1.1.1, briquettes or blocks (Larsen et al., 1998). The temperature increases in the top of the electrode column due to the heat supplied by the fans blowing hot air along the walls and the heat induced by the current supplied to the current clamps by the copper tubes. The heating air flows between the suspension mantle and the casing, entering below the slipping equipment and exiting just above the current bars (Skjeldestad, 2019). Throughout this temperature increase, the paste cylinder softens until it reaches the electrode casing, and then is baked as the temperature reaches 450 °C (Fitt and Aitchison, 1993). The electrode paste is compressed by the weight of cylinders added from the top, which are added once a day, typically one to three at a time, causing the paste to fill the casing due to increased pressure (Skjeldestad,

2019). The casing fins are steel plates, that surround the inside of the casing. The softened paste fills the space between the fins and then becomes attached to them as it is baked. The fins support the weight of the baked electrode and are oxidised inside the furnace, together with the steel casing. As part of this continuous process, new casing segments are welded at the top to replace the consumed casing (McDougall, 2013).

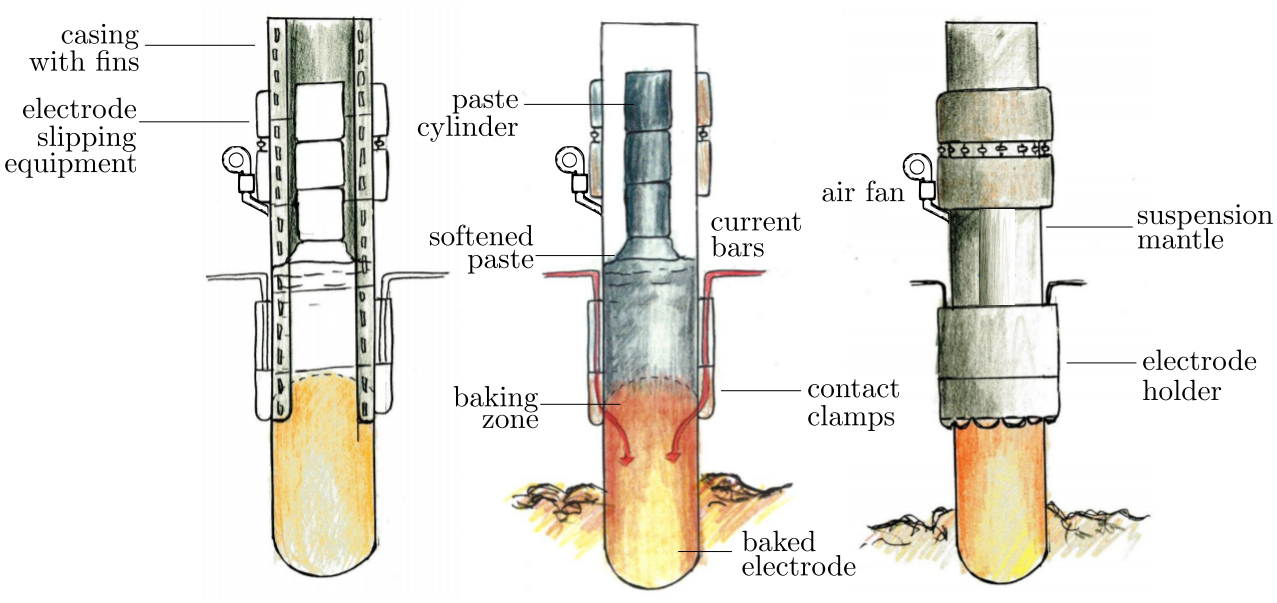

Figure 1.1.1 – Detailed schematic of a Søderberg electrode adapted from Hannesson (2016) to include labels and hot air fan.

A vertical cross-section schematic of the paste evolution as it is heated up is shown in Figure 1.1.2, with a top view of the casing fins on the left. As it is baked, it becomes highly conductive and enables the electrode to conduct current to the tip where the arcs are formed. The arcs are the primary source of heat that powers the smelting process and causes the electrode to be consumed at the bottom as new cylinders are added at the top. The correct softening and baking of paste is essential to produce electrodes with the desired mechanical, thermal, and electrical properties on which the entire production process depends (Innvaer, 1989; Larsen et al., 1998; Ray et al., 2007; Wilkinson et al., 2001). Particularly, it is crucial that the paste cylinders soften in such a way that they form the softening profile indicated in the softened paste region in Figure 1.1.2, where the paste gradually deforms until it reaches the casing (Nelson and Prins, 2004). Note that there is no phase change occurring when the paste begins to flow, as this solely depends on the drastic decrease in viscosity caused by an increase in temperature. However, in the literature, often 'softening' and 'melting' are used interchangeably (e.g. in Larsen et al. (1998)).

1.1.1 Electrode breakages and segregation

In normal operation, hot paste from lower down the casing may be recirculated up to the top, forming a viscous *pool* of paste which in turn contributes to the softening of new incoming cylinders. However,

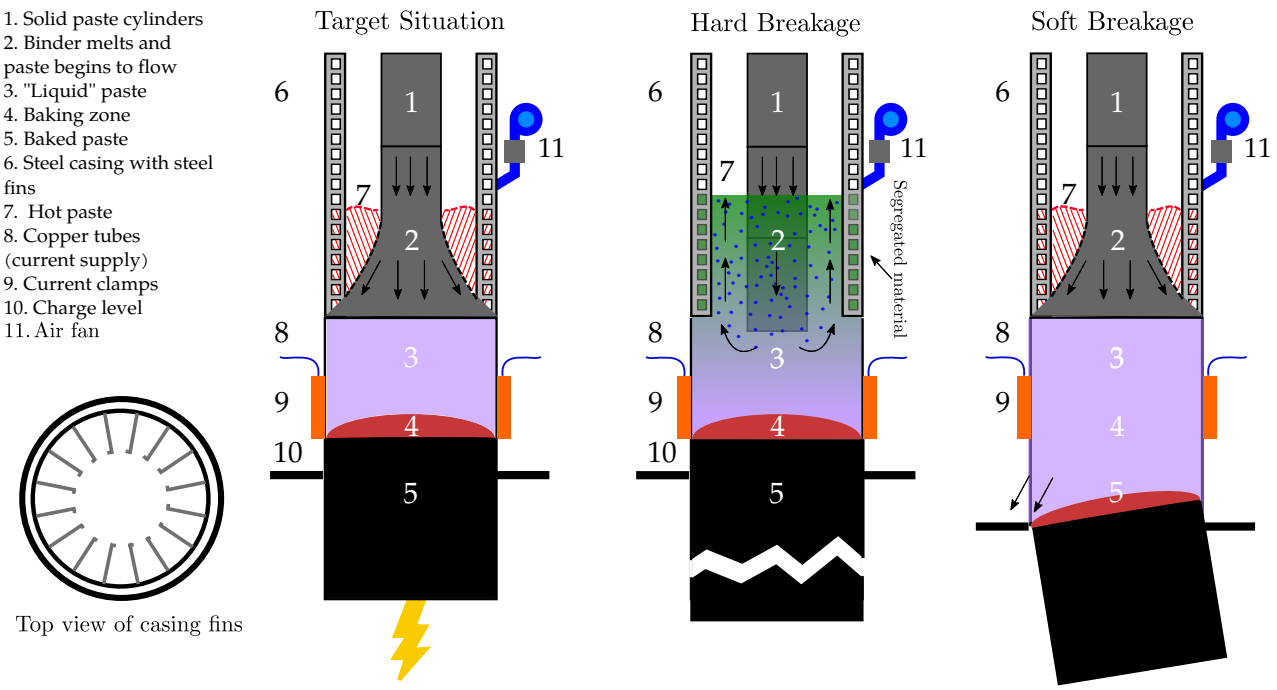

Figure 1.1.2 – Schematic of a Søderberg electrode, showing the changes the paste undergoes as the temperature is increased. An example of a baked electrode with desirable properties is shown on the left.

when the paste softening is out of balance, separation between the binder and the anthracite particles can occur, depicted in the middle panel in Figure 1.1.2. This is called segregation, and the causes of this phenomenon are not well understood, but it is known that the problem began to occur more frequently when changes in design led to a decrease in the space between the copper tubes that supply the current to the clamps and the electrode casing (items 8 and 6 in Figure 1.1.2), resulting in unwanted electrical induction within the cylinder (Larsen, 2012; Skjeldestad et al., 2015). The added heat due to induction causes an increase in temperature near the pre-heating zone (just above the current clamps), leading to a separation between the binder and the anthracite particles in the paste. The binder, with a much lower viscosity than that of the paste, forms gas bubbles and moves up towards the region where the cylinders melt (Nelson and Prins, 2004). Furthermore, the binder itself is formed of several liquid components, so the separation of lighter and heavier binder components can also occur. Consequently, a low viscosity *swamp* is formed in the area where the cylinders are added, corresponding to the green region in the middle panel in Figure 1.1.2.

This eventually leads cylinders to sink down into the liquid paste, causing the resulting electrode to have sections with different material properties. Segregation decreases the efficiency of the Søderberg electrode significantly, and can cause the resulting electrode to break after baking. This is called a *hard breakage*. Aside from segregation, McDougall (2013) reports other causes of hard breakages as thermal stresses or thermal shock, investigated numerically in Larsen et al. (2013), underbaking or overbaking of the electrode, and unbalanced lateral forces, investigated experimentally in Nelson and Prins (2004). In all these cases, the baking zone drops below the contact clamps, leading to

the hard breakage.

A *soft breakage* occurs in the unbaked region, when the electrode loses its anchoring to the casing fins, causing the entire baked portion to fall off, so the liquid paste flows freely into the furnace causing fires and often explosions (McDougall, 2013; Ray et al., 2007). This is depicted in the rightmost figure in Figure 1.1.2. These types of breakages occur less frequently than hard breakages but they can be very costly to repair. They are typically caused by damage to the casing (McDougall, 2013), using a slipping rate that is too high (Innvaer et al., 1995), and a low furnace load (Skjeldestad, 2019). There are also significant health and safety concerns related to these incidents (Ray et al., 2007; Shoko et al., 2013). It has been reported that inadequate and variable heating conditions in the paste softening zone are a common cause in both types of breakages (Ord et al., 1995).

A mathematical model is required to understand the behaviour of the paste in Søderberg electrodes, particularly the position of the paste pool, the softening profile, the formation of a low viscosity swamp, and the baking zone, as well as to determine the robustness of the process and the circumstances under which it loses stability. In this work, we focus on the top part of the electrode above the contact clamps, namely, the paste softening zone and how it is affected by induction heating from the clamps, cylinder addition, paste viscosity, and heating from the air fan on the casing.

1.2 Literature review

Different parts of the Søderberg electrode operation have been studied, both numerically and mathematically, over the years. In this section, we give an overview of such studies, and we will provide a more detailed review of the relevant literature at the beginning of each chapter. The temperature distribution within Søderberg electrodes has been studied numerically by Olsen et al. (1972) and Innvaer and Olsen (1979) who found that the electrode load current and slipping rate are of major importance for the position of the baking zone. Skjeldestad et al. (2015) used a Comsol model to determine that the steel fins fitted in the casing, indicated by item 6 in Figure 1.1.2, are indispensable for the heating profile in the casing, as the heat conduction by the steel fins counteracts the induction heating and subsequent current clamp cooling mechanism. The fins also keep the baked electrode from falling into the furnace, as the softened paste fills the space between the current fins and becomes attached to them during the baking process.

Some segregation mechanisms considered over the years include the settling of coarse anthracite particles, accumulation of volatiles and fines due to thermally buoyant transport from the viscous swamp or even fluid flow induced by rising volatile bubbles (Olsen and Sandberg, 1967). Nelson and Prins (2004) performed industrial electrode paste trials and noted that a low level of the paste pool, indicated by the red dotted line in Figure 1.1.2, as well as paste volatisation were present in breakages. Additionally, they found that the dropping instead of lowering of paste cylinders down

the electrode column, as well as the repeated oveloading of the cylinders and resulting high paste levels, can lead to segregation. Segregation only occurs when paste cylinders are used, so a common way to prevent it in practice is to alternate the use of briquettes and cylinders (Ray et al., 2007). The most relevant mathematical models are the Bergstrøm et al. (1989) segregation model, the Fitt and Howell (1998) briquette model, the Lacey (1995) thermo-electrical stability model, and the Van Gorder et al. (2021) baking model. These are briefly described below.

Bergstrøm et al. (1989) modelled billets of paste as a very viscous two-phase particulate medium. The particle size distribution is assumed to consist of coarse (~ 10 mm) particulates corresponding to the anthracite, in a distribution of finer particles (100 μm) which correspond to the binder sludge and milled anthracite. Consequently, equations for slow two-phase flow are presented to describe the flow in the unsegregated paste. The mechanism of segregation is taken to be the separation between the coarse and the fine parts of the paste, and it is assumed to occur near the walls of the electrode casing, creating a segregated region. It is found that the applied load, i.e. the cylinders or briquettes added at the top of the electrode, can reduce the length of this region. The more the applied load increases, the more easily the coarse matrix can be deformed by the weight, preventing the separation of the coarse and fine particulates in the paste. The relative difference between the velocities of the coarse and the fine particulates is found to be very small, so an approximation is made taking these to be asymptotically equal, and the problem is reduced to the one-phase slow flow equations, which are further reduced to an extensional flow model by assuming that the cylinder is long and thin. It is found that segregation occurs when the paste at the top of the electrode is so viscous, it does not deform from the incoming billets.

Fitt and Howell (1998) derived a briquette model taking a two phase slow flow approach with the same geometry as for the Bergstrøm et al. (1989) model. The possibility of segregation is not considered. Instead, the analysis considers how paste briquettes melt while interacting with the air surrounding them. The paste is thought of as a network of pores which slowly fill with paste as the temperature increases. When the paste begins to bake, it is compressed and so the pores decrease in size. The remaining smaller voids will remain as part of the electrode, as there is no more liquid to fill them. In this model, as opposed to the one in Bergstrøm et al. (1989), the temperature distribution is modelled for both phases. The problem is separated into two parts, one where the network of pores are being filled with paste, and another for when the paste is baked and begins to compress. The results are compared to an experiment conducted in Elkem ASA, and it is found that variations in viscosity are indispensable to have accurate predictions.

Lacey (1995) considers the operation of a Søderberg electrode under transient conditions, and explores instabilities of the steady states. The flow of the paste is not taken into account and the focus is solely on the heat flow and electric-current going through the paste, and the possibility of thermal runaway. The electrical conductivity is assumed to be a function of the temperature, whereas the density, specific heat and thermal conductivity of the paste are considered constant

when compared to the electrical conductivity temperature variations. A linear stability analysis is carried out for a one-dimensional model, where either the voltage or the (direct) current is fixed. A stabilising term is found, which depends on the temperature and the effective heat transfer coefficient. This term allows one to anticipate if the problem will have unstable, symmetric or stationary solutions.

Most recently, Van Gorder et al. (2021) investigated the position baking isotherm, i.e. the location within the electrode where the paste bakes, and how it is affected by electrode slipping rate, the aspect ratio of the cylindrical electrode, and the applied current at the current clamps. A mathematical model for heat, mass, and current transfer of a Søderberg electrode is described to investigate the softening and solidification of paste, under the assumption of cylindrical geometry with a fixed radius. The temperature distribution is modelled as a thermistor problem with temperature dependent electrical and thermal conductivity functions, taken from previous electrode thermistor numerical studies in Bermúdez et al. (1998) and Larsen (2006). It is found that, for given operational parameters, there is some critical effective velocity before the process fails and that wider electrodes are viable only if they are lowered more slowly into the furnace. Finally, it was determined that the applied current increases the position of the baking isotherm, however for realistic applications, there is a practical limit to the current which may be applied to the clamps, and hence an excessively high slip velocity cannot always be mitigated by this factor.

1.3 Industrial data available

The main industrial data available is shown in Table 1.3.1, and we will refer to it in each chapter as necessary. Note that in practice the thermal conductivity k and heat transfer coefficient h depend on the temperature of the paste and position along the casing, respectively. However, we expect variations in k and h to be small in the top part of the electrode, where our models are focused on, so we take the constant values in Table 1.3.1 for all calculations in this work. Furthermore, note that each furnace will have different load, current, and production requirements, which lead to different model parameters. We use the values in Table 1.3.1 as reference only, with the caveat that each mathematical model derived in this work can be easily evaluated on the required parameter space for each particular situation.

1.3.1 Viscosity data

The viscosity of the paste is perhaps the most important material property that has an impact on the mathematical models derived. In reality, since the paste is formed by pitch tar binder and calcined anthracite, it behaves as a shear thinning fluid, i.e. the viscosity decreases under shear strain, as noted by Larsen et al. (1998). Formally, we define for temperature T and shear rate $\frac{\partial u}{\partial x}$,

$$\mu\left(T, \frac{\partial u}{\partial x}\right) = \mu_0 e^{\bar{\Gamma}(T_{\text{in}} - T)} \left|\frac{\partial u}{\partial x}\right|^{\alpha - 1}, \tag{1.1}$$

Notation	Parameter	Estimated value
T_{in}	Temperature at the inlet[d]	343 K
T_{top}	Temperature at the top of air column[d]	353 K
T_{bot}	Temperature at the bottom of air column[d]	393 K
ρ	paste density[b]	1.8×10^3 kg m^{-3}
k	thermal conductivity [c]	3 W m^{-1}K^{-1}
c	heat capacity	900 J kg^{-1}K^{-1}
g	acceleration due to gravity	10 m s^{-2}
u_{c}	slipping rate[b]	10^{-5}m s^{-1}
$\bar{L}$	length of top part of the electrode[a]	5 m
R_0	radius of paste cylinder[a]	0.5 m
R_1	radius of electrode casing[b]	1 m
μ_0	viscosity of the paste at reference temperature[d]	10^{10} kg s^{-1}m^{-1}
$\hat{P}_{\text{in}}$	compressive applied load[d]	10000 N
$\hat{h}_c$	height of one paste cylinder[d]	1 m
h	heat transfer coefficient between the casing and the paste[e]	7 W m^{-2}K^{-1}
Q_I	Induction heating at the clamps area[d]	2800 W m^{-3}
$[x_1, x_2]$	position of contact tubes (where we expect induction)[a]	$[3.5, 4.5]$ m
$\bar{\Gamma}$	parameter for T dependence of μ[d]	11.1 K^{-1}

Table 1.3.1 – Estimated values for parameters in the model, taken from Skjeldestad et al. (2015)[a], Bergstrøm et al. (1989)[b], Fitt and Howell (1998)[c], Skjeldestad (2019)[d], and Van Gorder et al. (2021)[e]. Note that Q_I is computed from typical ΔT values shown in Skjeldestad (2019) for our domain of interest.

where T_{in} is a reference temperature, $\bar{\Gamma}$ is a parameter with units K^{-1} that determines how much the viscosity changes with temperature, and $\alpha \leq 1$ is a fitting parameter which captures the shear thinning behaviour of the paste. This is a standard approach for modelling temperature dependent viscosity, as detailed in e.g. Pearson and Shah (1972) when investigating glass fibre drawing and polymer-fibre production processes. For a paste cylinder with diameter 1 m and height 0.5 m, the shear rate is roughly $2 \times 10^{-4} - 5 \times 10^{-5}$s^{-1} (Larsen et al., 1998). For simplicity, we will not include the effects of shear thinning but consider an exponential temperature dependent model for the viscosity, as applied to electrode paste by, for example Fitt (1991). We suppose that the viscosity μ at a temperature T is given by

$$\mu(T) = \mu_0 e^{\bar{\Gamma}(T_{\text{in}} - T)}, \tag{1.2}$$

where T_{in} is a reference temperature, at which the viscosity is μ_0, and $\bar{\Gamma}$ is a material parameter. This fit is shown in Figure 1.3.1 with $T_{\text{in}} = 293$ K (20 °C), $\mu_0 = 4.5 \times 10^{10}$ kg s^{-1}m^{-1}, and $\bar{\Gamma} = 11.1$ K^{-1} and is compared against the viscosity data presented in Skjeldestad (2019). This data corresponds to the apparent viscosity as obtained from experiments done on paste with 23.9% pitch content and a combination of large coarse particles (10 mm) and fines (100 μm), detailed in Skjeldestad (2019). The electrode paste was preheated for 2 hours and 30 minutes at 30 °C before the measurements

started, and then the temperature was set to increase linearly up to 80 °C. The electrode paste was then compressed for 24-48 hours, similar to the times and shear rates experienced by the cylinders in industrial electrodes. Note that the data in Figure 1.3.1 do not take into account the pressure applied on the paste. Additionally, the measurements on the same electrode paste present variations due to particle interactions. Therefore, these results are taken only as an approximation and the viscosity fit presented was used for the purposes of numerical experiments.

It is important to note that for the full range of temperatures in the Søderberg electrode consumption process, the paste has a non-monotone viscosity function, as the paste is first softened, and then baked. However, for the temperature ranges that we are interested in $(20-160°\text{C})$ for the softening of the paste, a function of the form (1.2) captures the necessary changes.

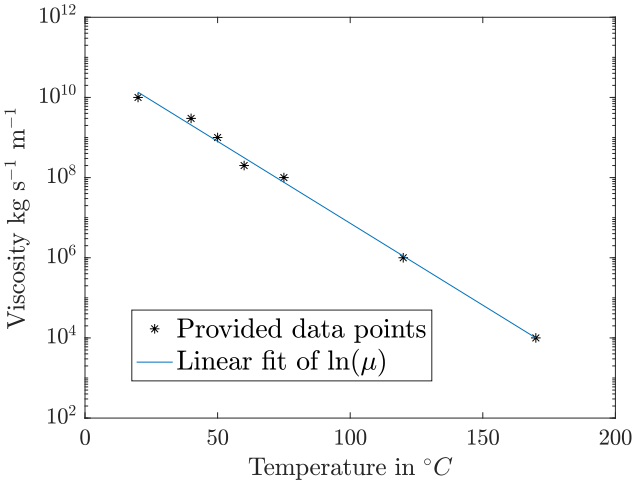

Figure 1.3.1 – Viscosity data taken from experiments reported in Skjeldestad (2019) compared with a linear fit of the logarithmic viscosity with $\mu_0 = 4.5 \times 10^{10}$ kg s^{-1}m^{-1}, $\bar{\Gamma} = 11.1$ K^{-1}, and $T_{\text{in}} = 293$ K (20 °C).

1.3.2 Temperature and heat flux data

Temperature experiments were performed by Elkem ASA, where thermocouples were placed at different points on the casing, as well on the paste cylinders, as described in detail in Skjeldestad (2019), and we note the relevant results here. Often complications arise when measuring the temperature in the lower zones where the thermocouples melt as the temperature exceeds 1000 °C, resulting in incorrect data. However, in our area of interest, the experimental data should give a good indication of the actual temperature inside the electrode casing. The temperature measurements, which were performed on the same type of electrode paste as the one used for viscosity measurements in §1.3.1, show that the softened paste reaches about 80 °C, and that temperatures of up to 280 °C are reached above the contact clamp. This high temperature above the contact clamp is caused by the induced current coming from the current tubes approaching the electrode casing before entering the contact clamps (region 8 in Figure 1.1.2). It is important to note that we are given viscosity measurements for temperatures up to 160 °C,

while temperature profiles suggest a maximum temperature closer to 280 °C. We use the exponential viscosity-temperature relationship (1.2) for the required higher temperature range, with the caveat that this is a first approximation and further experiments should be conducted in order to obtain a better viscosity fit for higher temperatures. For the paste used in Elkem ASA, the baking has been known to occur near 350 °C. However, when the paste reaches temperatures of 270 °C, the volatilization of light coal-tar pitch components may begin to occur (Skjeldestad et al., 2015), setting an upper limit on our extrapolation for the viscosity.

In our models, we incorporate the hot air heating from the air fan (item 11 in Figure 1.1.2) by prescribing a known air temperature $T_{\mathrm{a}}(x)$, where x is the vertical axis, in direction of the paste flow (i.e. with $x = 0$ at the top of the electrode column). In Chapters 2 and 3 we take T_{a} to be a constant corresponding to T_{top} in Table 1.3.1. In Chapters 4 and 5 we consider the linear function

$$T_{\mathrm{a}}(x) = \frac{T_{\mathrm{bot}} - T_{\mathrm{top}}}{\bar{L}} x + T_{\mathrm{top}}, \tag{1.3}$$

where $\bar{L}$ is the length of the electrode up to the position where paste baking begins, as seen in Table 1.3.1. Normally the clamps are cooled with water to counteract the additional heating caused by the induction from the copper tubes, as the heating air does not cool the area most affected by this induction (Skjeldestad, 2019). For simplicity, this effect is not included in the models described in this work, but in principle it could be added by modifying T_a appropriately.

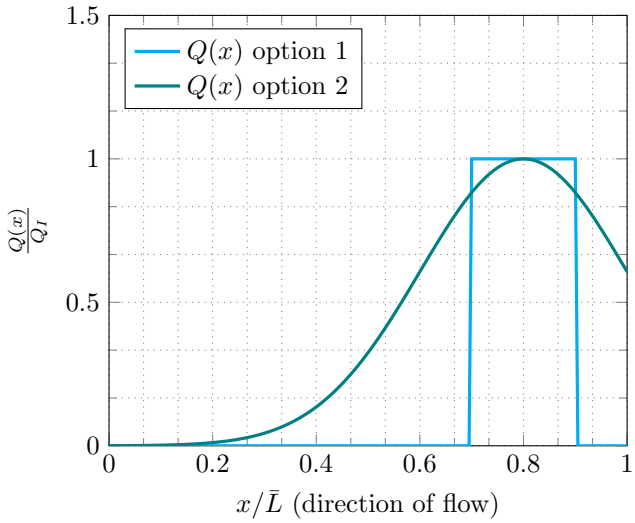

Figure 1.3.2 – Options for induction heating used throughout this thesis.

Rather than solving the electromagnetic problem for the induction heating, we impose an effective volumetric heating term which is denoted by $Q(x)$, with x again denoting vertical distance from

the top of the electrode. A simple choice for $Q(x)$ is the piecewise constant function

$$Q\left(x\right) = \begin{cases} Q_I & \text{for } x_1 < x < x_2, \\ 0 & \text{otherwise.} \end{cases} \tag{1.4}$$

Here $[x_1, x_2]$ corresponds to an approximate position on the casing where the copper tubes, shown in Figure 1.1.2 (item 8), provide additional induction heating. We use this approach for Chapter 2 and most of Chapter 3. An alternative approach is to use the smooth continuous function

$$Q(x) = Q_I \exp\left(-\frac{\left(x - \frac{x_1+x_2}{2}\right)^2}{2(x_2 - x_1)^2}\right), \tag{1.5}$$

which we use predominantly to improve the convergence of numerical methods, in particular for the cylinder addition examples at the end of Chapter 3 and the FEniCS simulations in Chapter 4.

We show both approaches for $Q(x)$ in Figure 1.3.2. In both cases, we determine Q_I by imposing that the integrated total heating $\int_0^{\bar{L}} Q(x)\mathrm{d}x$ is sufficient to raise the temperature of the bottom of the domain to its observed value of around 260°C (Skjeldestad et al., 2015). Note that each electrode configuration and type of paste used will have a different temperature distribution, and this value is used as reference only.

1.4 Scope of the thesis

The focus of this thesis is to formulate mathematical models that will help understand the paste softening process shown in Figure 1.1.2, in the top region of the casing, above the contact clamps. We focus on a single electrode, so proximity effects to the other electrodes in the furnace are not considered. Although the segregation of paste is not modelled, we investigate the mechanisms that are reported to lead to segregation, such as the viscous pool at the top of the electrode, failure of the softening process, and induction heating from the copper tubes. Since segregation only occurs when paste cylinders are used, we do not consider paste briquettes or blocks in this work. We show the various simplifications and assumptions made in each chapter schematically in Figure 1.4.1.

In Chapter 2, we begin by using some of the same assumptions as in Bergstrøm et al. (1989), namely we take a one-phase approach for the paste in steady state and we calculate the point at which the paste touches the casing for the first time, $x = \lambda$, without explicitly considering the paste pool on the sides. This is shown in the top right schematic in Figure 1.4.1. The viscosity is highly dependent on the temperature, and so the flow equations are coupled with the heat equation in a two dimensional model. This is investigated analytically with asymptotic expansions, leading to the derivation of a one dimensional model corresponding to the behaviour of the paste averaged over the cross-sectional area, where the temperature is treated as being uniform across the cross-section. The focus in Chapter 2 is on steady state solutions, which are computed analytically and

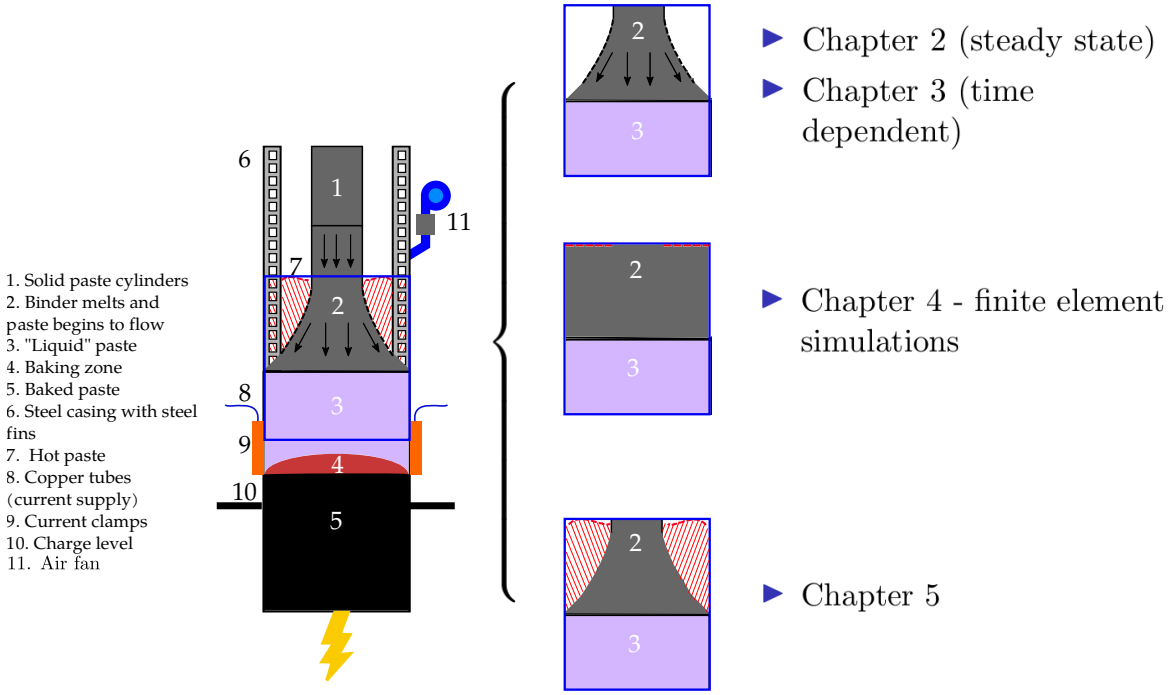

Figure 1.4.1 – Schematic description of the scope of the thesis.

numerically. The qualitative dependence of λ on the non-dimensional parameters is explored.

Then, the time dependent version of this one dimensional model is explored in Chapter 3, where we are interested in calculating the free boundary $\lambda(t)$ and its time evolution. We describe a finite volume numerical scheme and focus on numerical experiments where we vary the applied compressive load, $P_{\text{in}}(t)$, through time. P_{in} corresponds to the weight of the cylinders above the domain (i.e. region 1 in Figure 1.4.1). We design two control strategies that replicate the cylinder addition patterns used during normal operations and make observations on how the flow and temperature profile react to such variations. We explore the fluctuations in $P_{\text{in}}(t)$ further by using asymptotic analysis in the limit where P_{in} varies rapidly compared to the natural advective time-scale of the electrode.

In Chapter 4 we move onto finite element simulations with FEniCS (Langtangen and Logg, 2017) of the two-dimensional axisymmetric coupled temperature and flow problem. In order to make the problem tractable, we 'flatten' the free boundary as illustrated in Figure 1.4.1. A physical interpretation of this approach might be that gravitational effects are sufficiently strong to keep the surface of the paste pool effectively flat. In this model, we allow the temperature to vary across the cross-section, which enables us to capture the presence of the paste pool, which emerges as a recirculating region near the casing wall. It is unclear what are the correct boundary conditions to impose on the free surface for this simplified problem, so we show results from imposing zero normal stress or zero normal flow. Although we do not model cylinder addition, we relate the imposed inlet velocity to the corresponding weight of cylinders for different example cases.

We use the numerical results from Chapter 4 as a guide for our two dimensional model in Chapter 5, where we exploit the small aspect ratio of the geometry and seek to understand the recirculation of hot paste near the top of the domain, allowing temperature variations across the cross-section. Since there are extreme viscosity variations across the fluid layer, this leads to a hybrid model, with extensional flow in the centre and lubrication flow towards the edge of the domain. We simplify the calculations by considering a two-dimensional geometry, with the fluid occupying a rectangular domain, but in principle an analogous approach will work for the axisymmetric geometry relevant to a Søderberg electrode. We solve this problem in stages, namely, we begin by considering the flow problem with known temperature. This model is then reduced asymptotically by approximating integrals of the temperature profile using Laplace's method, resulting in a system dependent solely on the values of the temperature and temperature gradients at the wall and the centre-line. We use these approximations for the velocity to asymptotically reduce the temperature problem, and finally we couple both problems together and show numerical solutions under various parameter regimes relevant to the industrial problem.

Finally, in Chapter 6 we draw conclusions from the various simplifications presented for paste softening, we provide some industrial recommendations based on the results, and we discuss future work.

Chapter 2

A coupled flow and temperature model for paste softening

In this chapter we aim to understand how the paste cylinders added at the top of the electrode soften and spread to fill the whole radius of the casing, depicted as region 2 in Figure 1.1.2. The widening profile of the paste as the cylinders are added at the top has been observed empirically to have a strong effect on the resulting baked electrodes (Nelson and Prins, 2004). Following Bergstrøm et al. (1989), we assume that the anthracite particles move at approximately the same speed as the pitch tar binder, and so the paste is modelled as a one phase flow. We treat the viscous pool and the softened paste as the same material. The resulting flow model is equivalent to the extensional flow equations, described by Howell (1994). A comprehensive review of the vast literature on extensional flow models is given by Petrie (1995).

In §2.1 we consider an axisymmetric coupled flow and temperature model, neglecting inertia. The viscosity is highly dependent on the temperature, and so the flow equations are coupled with the heat equation, where the temperature is assumed to be uniform across the cross-section. In §2.2 this problem is investigated analytically with asymptotic expansions in the long and thin (small aspect ratio) limit, which leads to the derivation of a one dimensional model corresponding to the behaviour of the paste averaged over the cross-sectional area, explored in §2.3. Steady state solutions are computed in §2.4, where the qualitative dependence on the non-dimensional parameters is explored.

2.1 Formulating an axisymmetric model

We model the paste in the electrode casing as an incompressible Newtonian fluid of strongly temperature-dependent viscosity. A schematic of the problem is shown in Figure 2.1.1. Based on typical parameter values for the process (see Table 1.3.1), we find that the Reynolds number for the flow, based on the radius of the casing and the viscosity of the binder, is of order 10^{-11}. We

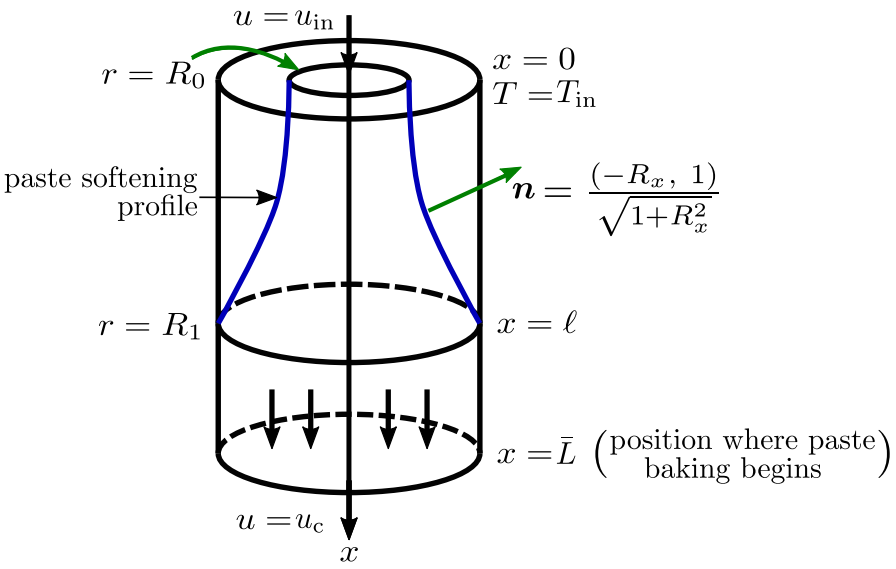

Figure 2.1.1 – Schematic of the model proposed for Chapter 2.

therefore neglect inertia effects throughout, so the fluid flow is governed by the Stokes equations (Dewynne et al., 1989)

$$\nabla \cdot \boldsymbol{u} = 0, \tag{2.1}$$

$$\nabla p = \nabla \cdot \left[\mu \left(\nabla \boldsymbol{u} + (\nabla \boldsymbol{u})^T\right)\right] + \rho g \boldsymbol{i}, \tag{2.2}$$

for velocity $\boldsymbol{u}$, pressure p, viscosity μ, and constant density ρ, where g is the acceleration due to gravity. We have taken the x axis, together with the unit vector $\boldsymbol{i}$, pointing vertically downwards. The viscosity μ is related to the temperature T by equation (1.2). To close the problem we need to solve the heat equation, that is

$$(\rho c T)_t + \nabla \cdot (\rho c \boldsymbol{u} T) = \nabla \cdot (k \nabla T) + Q, \tag{2.3}$$

for temperature T, specific heat capacity c, thermal conductivity k and, heat source Q, corresponding to the induction heating resulting from the proximity of the copper tubes to the steel casing. We neglect viscous dissipation, as the relevant Brinkman number is small: of order $\mathcal{O}(10^{-6})$. The heat source Q is taken to be a prescribed function of x. As mentioned in Chapter 1, there is no consistent form found in the literature for this expression, so for this model we choose the piecewise constant function (1.4), where it is a constant value Q_I within a certain range $[x_1, x_2]$ (representing the location of the copper tubes), and zero elsewhere. We note that the industrial problem can be symmetry breaking as proximity effects from the other two electrodes in the furnace provide additional heating in the softening and baking regions, as described in Palsson and Jonsson (2000). However, we do not include these effects into our simplified model, which allows us to work with an axisymmetric geometry.

2.1.1 Boundary conditions and coordinate system

We assume the flow is axisymmetric and use cylindrical coordinates, with x in the downward direction and r in the radial direction, so that equations (2.1),(2.2), and (2.3) are, in component form,

$$u_x + \frac{1}{r}\left(rv\right)_r = 0, \tag{2.4a}$$

$$p_r = \frac{1}{r}\left(2\mu r v_r\right)_r + \left(\mu\left(v_x + u_r\right)\right)_x - \frac{2\mu v}{r^2}, \tag{2.4b}$$

$$p_x = \frac{1}{r}\left(\mu r\left(v_x + u_r\right)\right)_r + \left(2\mu u_x\right)_x + \rho g, \tag{2.4c}$$

$$\rho c\left(T_t + uT_x + vT_r\right) = k\left(T_{xx} + \frac{1}{r}\left(rT_r\right)_r\right) + Q, \tag{2.4d}$$

where (u, v) are the longitudinal and radial velocity components of $\boldsymbol{u}$. We define the free boundary of the paste by $r = R(x,t)$, where the kinematic condition holds for the velocity of the paste,

$$v = R_t + uR_x \qquad \text{at } r = R(x,t), \quad 0 < x < \ell(t). \tag{2.5}$$

At the inlet, paste cylinders of radius R_0 are added and begin to soften until the paste reaches the electrode casing, of radius R_1, at $x = \ell(t)$, where $\ell(t)$ is to be determined, leading to conditions

$$R = R_0 \quad \text{at} \quad x = 0, \tag{2.6a}$$

$$R = R_1 \quad \text{at} \quad x = \ell(t), \tag{2.6b}$$

where the latter condition effectively defines $\ell(t)$. Once non-dimensional (see below), we will denote ℓ by λ, as introduced in Chapter 1.

For $x > \ell(t)$, a no slip condition applies at the casing, and since the casing moves downward with velocity u_c, this gives

$$u = u_c, \quad v = 0 \quad \text{at} \quad r = R_1, \quad \ell(t) < x < \bar{L}. \tag{2.7}$$

At the centre-line of the electrode casing, symmetry provides the conditions

$$v = u_r = 0, \quad \text{at} \quad r = 0, \quad 0 < x < \bar{L}. \tag{2.8}$$

We also require the stress to be continuous across the free boundary. We normalise to take the atmospheric pressure to be zero and so we have the dynamic condition $\boldsymbol{\sigma} \cdot \boldsymbol{n} = \boldsymbol{0}$ on $r = R(x,t)$; that is

$$-p + 2\mu v_r = R_x(\mu(u_r + v_x)) \qquad \text{at} \quad r = R(x,t), \quad 0 < x < \ell(t), \tag{2.9a}$$

$$\mu(u_r + v_x) = R_x(-p + 2\mu u_x) \qquad \text{at} \quad r = R(x,t), \quad 0 < x < \ell(t), \tag{2.9b}$$

where we neglect any effects due to surface tension since these are certainly very small (Bergstrøm et al., 1989). The fluid problem is closed by specifying the velocity at $x = 0$ and $x = \bar{L}$, where our domain terminates,

$$u = u_{\text{in}}, \quad v = 0, \qquad \text{at} \quad x = 0, \quad r \leq R_0, \tag{2.10a}$$

$$u = u_{\text{c}}, \quad v = 0, \qquad \text{at} \quad x = \bar{L}, \quad r \leq R_1. \tag{2.10b}$$

When the system is in steady state, the input velocity u_{in} and the casing velocity u_{c} are related through net mass conservation by

$$u_{\text{in}} R_0^2 = u_{\text{c}} R_1^2. \tag{2.11}$$

The position $x = \bar{L}$ is assumed to be known, and is where the paste begins to bake and subsequently moves with constant velocity $\boldsymbol{u} = (u_{\text{c}}, 0)$.

For the temperature problem, we assume the paste has an inlet temperature T_{in}, i.e.

$$T = T_{\text{in}} \quad \text{at} \quad x = 0. \tag{2.12}$$

At $r = R(x,t)$ there is transfer of heat to the surrounding atmosphere, which is assumed to be at a known temperature $T_a(x)$. This is modelled using Newton's law of cooling, namely

$$-k\nabla T \cdot \boldsymbol{n} = h\,(T - T_a(x)) \quad \text{at} \quad r = R(x,t), \quad 0 < x < \ell(t), \tag{2.13}$$

where $\boldsymbol{n}$ is the unit outward normal to the free boundary, shown in Figure 2.1.1, and h is a heat transfer coefficient, which depends on the properties of the surrounding atmosphere. This is also imposed on the fixed boundary $R = R_1$, i.e.

$$-k\nabla T \cdot \boldsymbol{n} = h\,(T - T_a(x)) \quad \text{at} \quad r = R_1, \quad \ell(t) < x < \bar{L}. \tag{2.14}$$

We have chosen h to be constant for simplicity, although in principle it could depend on position, as the paste interacts with the hot air and the casing fins. In our coordinate system, (2.13) and (2.14) are explicitly written as

$$-k\left(\frac{-R_x T_x + T_r}{\sqrt{1+R_x^2}}\right) = h\,(T - T_a(x)) \quad \text{for} \quad r = \begin{cases} R(x,t) & 0 < x < \ell(t), \\ R_1 & \ell(t) < x < \bar{L}. \end{cases} \tag{2.15}$$

Note that in (2.15) we assume $h = h_{\text{ap}} = h_{\text{pc}}$, where h_{ap} denotes the heat transfer coefficient between air and paste, and h_{pc} denotes the one between paste and the casing. In reality we expect these two values to be different, although the precise values for these coefficients depend on the paste composition, which is information protected by industrial confidentiality. Therefore, we take both of these values to be h as a modelling simplification, which can be easily changed to e.g. a

function $h(x)$ that depends on the position along the casing, as was done in Van Gorder et al. (2021). Assuming that the heat conduction through the bottom of the domain is negligible, we impose the boundary condition

$$T_x = 0 \quad \text{at} \quad x = \bar{L}. \tag{2.16}$$

This is a simplification of the problem, as in reality there will undoubtedly be conductive heat flux from the furnace below the tip of the electrode, as well as from the baking process itself. Alternatively, we could have imposed some non-zero heat flux at $x = \bar{L}$, which could potentially be taken from measurement data, or the temperature profile itself. However, in the parameter regime of most industrial interest, we find that the thermal condition imposed at $x = \bar{L}$ has little effect on the solution in the rest of the domain, and the passive condition (2.16) is convenient and avoids introducing artificial boundary layers at the downstream end. The viscosity-temperature relationship is described by (1.2).

2.2 Derivation of one-dimensional model

2.2.1 Non-dimensionalisation

To proceed analytically, we assume that the casing is long and thin. We suppose that the typical lengths and velocities for the flow are $\bar{L}$ and u_{c}, in the x-direction, and $\epsilon\bar{L}$ and ϵu_{c} in the r-direction, where ϵ is the dimensionless aspect ratio assumed to be small, namely

$$\epsilon = \frac{R_1}{\bar{L}} \ll 1. \tag{2.17}$$

We consider a time-scale over which the paste is moved a distance of order $\bar{L}$ in the x direction, i.e. $\bar{L}/u_{\mathrm{c}}$. Typical values of the dimensional parameters in the problem are given in Table 1.3.1, and the corresponding dimensionless parameters are given in Table 2.2.1.

Thus we non-dimensionalise as follows.

$$\begin{aligned}
&x = \bar{L}x', && r = \epsilon\bar{L}r',\\
&u = u_{\mathrm{c}}u', && v = \epsilon u_{\mathrm{c}}v',\\
&R = R_1R', && p = \frac{u_{\mathrm{c}}\mu_0}{\bar{L}}p',\\
&\mu = \mu_0\mu', && t = \frac{\bar{L}}{u_{\mathrm{c}}}t',\\
&T = T_{\mathrm{in}} + \Delta T\theta, && T_a = T_{\mathrm{in}} + \Delta T\theta_a,\\
&Q = \frac{Q_I\,(x_2 - x_1)}{\bar{L}}Q',
\end{aligned} \tag{2.18}$$

where μ_0 is a reference value for the viscosity. Given that we have access to temperature measurements for our region of interest, we fix our expected final temperature to 553 K (280 °C),

giving $\Delta T = 553 - T_{\text{in}} = 260$ K. The source term Q_I models the induction heating and cooling of the clamps. The net heat provided by these two effects is not well known, so we infer a suitable value from the known temperature, namely

$$Q_I = \frac{\rho c u_{\text{c}} \Delta T}{(x_2 - x_1)} \approx 2800 \text{Wm}^{-3}. \tag{2.19}$$

This yields the following non-dimensional, scaled equations for the flow and temperature (dropping primes)

$$\frac{1}{r}(rv)_r + u_x = 0, \tag{2.20a}$$

$$p_r = \frac{1}{r}(2\mu r v_r)_r + \left(\mu\left(\epsilon^2 v_x + u_r\right)\right)_x - \frac{2\mu v}{r^2}, \tag{2.20b}$$

$$\epsilon^2 p_x = \frac{1}{r}\left(\mu r\left(\epsilon^2 v_x + u_r\right)\right)_r + \left(2\mu\epsilon^2 u_x\right)_x + \epsilon^2 \text{St}, \tag{2.20c}$$

$$\epsilon^2 \text{Pe}\left(\theta_t + u\theta_x + v\theta_r\right) = \epsilon^2\theta_{xx} + \frac{1}{r}(r\theta_r)_r + \epsilon^2 \text{Pe} Q, \tag{2.20d}$$

where the non-dimensional induction heating is given by

$$Q(x) = \begin{cases} \frac{1}{x_2 - x_1} & \text{for } x_1 < x < x_2, \\ 0 & \text{otherwise.} \end{cases} \tag{2.21}$$

We have also defined the Stokes number

$$\text{St} = \frac{\rho g \bar{L}^2}{u_{\text{c}} \mu_0}, \tag{2.22}$$

which measures the balance between gravity and viscous stress, and the Péclet number,

$$\text{Pe} = \frac{\rho c u_{\text{c}} \bar{L}}{k}, \tag{2.23}$$

which measures the rate of heat advection relative to the rate of heat conduction. The dimensionless boundary conditions are

$$v = R_t + uR_x, \tag{2.24a}$$

$$-p + 2\mu v_r = R_x(\mu(u_r + \epsilon^2 v_x)), \tag{2.24b}$$

$$\mu(u_r + \epsilon^2 v_x) = \epsilon^2 R_x(-p + 2\mu u_x), \tag{2.24c}$$

$$\left(\epsilon^2 R_x^2 + 1\right)^{-\frac{1}{2}}\left(\theta_r - \epsilon^2\theta_x R_x\right) = -\epsilon^2 \text{Bi}\left(\theta - \theta_a\right), \tag{2.24d}$$

on $r = R(x,t)$ for $x < \lambda(t) = \ell(t)/\bar{L}$ where $\lambda(t)$ is the dimensionless position at which the paste reaches the casing, which will be computed as part of the solution. Here

$$\text{Bi} = \frac{\bar{L}^2 h}{R_1 k} \tag{2.25}$$

is the reduced Biot number and represents the importance of heat transfer relative to conduction (Taroni et al., 2013). Additionally, we have the no slip condition for the paste at the casing, namely

$$u = 1, \quad v = 0, \quad \text{at} \quad r = 1, \quad \lambda(t) < x < 1. \tag{2.26}$$

We have boundary conditions on the temperature and velocity at the inlet and as it reaches the casing, namely

$$u = \frac{1}{D}, \quad v = 0, \quad R = \sqrt{D}, \quad \theta = 0, \qquad \text{at} \quad x = 0, \tag{2.27a}$$

$$R = 1, \qquad \text{at} \quad x = \lambda(t), \tag{2.27b}$$

$$u = 1, \quad v = 0, \quad \theta_x = 0, \qquad \text{at} \quad x = 1. \tag{2.27c}$$

Here $D = u_c/u_{in} = R_0^2/R_1^2$ is the area ratio of our problem, or equivalently the ratio of the axial speed of the casing to input speed.

Notation	Parameter Group	Definition	Value
Γ	Dimensionless fitting parameter for $\mu(\theta)$	$\bar{\Gamma}\Delta T$	23
ϵ	Aspect ratio	$\frac{R_1}{\bar{L}}$	0.2
St	Stokes number	$\frac{\rho g \bar{L}^2}{\mu_0 u_c}$	1
Pe	Péclet number	$\frac{\rho c u_c \bar{L}}{k}$	27
Bi	Reduced Biot number	$\frac{\bar{L}^2 h}{R_1 k}$	58
D	Area ratio	$\frac{u_c}{u_{in}}$	0.25
P_{in}	Dimensionless applied load	$\frac{\hat{P}_{in}\bar{L}}{R_1^2 u_c \mu_0}$	0.7
ζ	Transition region between 0 and 1 for $\mathcal{H}$ in (2.60)	-	0.01

Table 2.2.1 – Nondimensional parameters calculated with the data in Table 1.3.1.

2.2.2 Asymptotic expansions

We seek solutions in the form of asymptotic expansions in powers of the small parameter ϵ^2, i.e.

$$u \sim u^{(0)} + \epsilon^2 u^{(1)} + \epsilon^4 u^{(2)} + \cdots, \quad v \sim v^{(0)} + \epsilon^2 v^{(1)} + \epsilon^4 v^{(2)} + \cdots, \text{etc.} \tag{2.28}$$

All other parameters will be treated as $\mathcal{O}(1)$ constants so that viscous forces, gravity, convection, and diffusion are all comparable. In this way we include as many effects as possible in the model while retaining a tractable problem. We substitute into (2.20) and (2.24) and equate like powers of ϵ^2.

2.2.3 Fluid problem

The only $\mathcal{O}(1)$ term in (2.20c) gives

$$\left(r\mu^{(0)}u_r^{(0)}\right)_r = 0 \tag{2.29}$$

with the boundary condition (2.24c)

$$\mu^{(0)}u_r^{(0)} = 0 \quad \text{at} \quad r = R(x,t), \quad 0 < x < \lambda(t), \tag{2.30}$$

where we assume $\mu^{(0)} \neq 0$. This is a homogeneous problem for $u^{(0)}$ and admits the non-unique eigensolution,

$$u^{(0)} = u^{(0)}(x,t). \tag{2.31}$$

Hence to leading order we have an extensional flow, i.e. the axial velocity is uniform across the domain, whatever the variation of the viscosity across the electrode. From (2.20a)

$$v^{(0)} = -r\frac{u_x^{(0)}}{2}. \tag{2.32}$$

We integrate (2.20a) with respect to r and use the kinematic condition (2.24a) to find

$$\left(R_t + u^{(0)}R_x\right) + \int_0^R \left(ru_x^{(0)}\right)_r \mathrm{d}r = 0, \tag{2.33}$$

which can be rewritten as the net mass conservation equation

$$(R^2)_t + \left(R^2u^{(0)}\right)_x = 0, \tag{2.34}$$

for $0 < x < \lambda(t)$. For $\lambda(t) < x < 1$ we apply the boundary condition (2.27c) to equation (2.29) and get directly that

$$u^{(0)} = 1, \quad v^{(0)} = 0 \quad \text{at} \quad \lambda(t) < x < 1. \tag{2.35}$$

From equation (2.20b) to leading order together with (2.32) we have

$$p^{(0)} = -\mu^{(0)}u_x^{(0)}. \tag{2.36}$$

Note that the leading order dimensionless axial stress $(\sigma_{xx})^{(0)} = -p^{(0)} + 2\mu^{(0)}u_x^{(0)}$ is given by $3\mu^{(0)}u_x^{(0)}$.

To close the model, we must examine the field equations and boundary conditions at the next order in the expansion. Boundary condition (2.24c) with (2.32) and (2.36) gives

$$\mu^{(0)}u_r^{(1)} = R_x\left(3\mu^{(0)}u_x^{(0)}\right) + \frac{\mu^{(0)}u_{xx}^{(0)}}{2}, \tag{2.37}$$

at $r = R(x,t)$. Then, we substitute (2.37) into (2.20c) and integrate with respect to r, as before, to find

$$3\mu|_R RR_x u_x^{(0)} + 3\int_0^R r\mu^{(0)}u_{xx}^{(0)}\,\mathrm{d}r + 3\int_0^R r\mu_x^{(0)}u_x^{(0)}\,\mathrm{d}r + \frac{R^2}{2}\mathrm{St} = 0. \tag{2.38}$$

We define the radially averaged viscosity,

$$\bar{\mu}^{(0)}(x,t) = \frac{2}{R^2}\int_0^R \mu^{(0)} r \, \mathrm{d}r \,, \tag{2.39}$$

and substitute into (2.38) which simplifies to the net stress balance

$$\left(3\bar{\mu}^{(0)} R^2 u_x^{(0)}\right)_x + R^2 \mathrm{St} = 0. \tag{2.40}$$

The system (2.34), (2.40) is known as the Trouton model (Howell, 1994; Trouton, 1906), where the Trouton ratio 3 is the expected ratio for an axisymmetric geometry (Dewynne et al., 1992). These equations are well known and have formed the basis of many studies of glass draw-down (Dewynne et al., 1989; Howell, 1994) and redraw processes (O'Kiely et al., 2015), as well as polymer-fibre production and its stability (e.g. Matovich and Pearson, 1969).

2.2.4 Temperature problem

At leading order in (2.20d) we get

$$\frac{1}{r}\left(r\theta_r^{(0)}\right)_r = 0, \tag{2.41}$$

subject to

$$\theta_r^{(0)} = 0 \quad \text{at} \quad r = R(x,t). \tag{2.42}$$

It follows that $\theta^{(0)}$ is a function of only x and t, i.e. the temperature is approximately uniform in each cross-section of the electrode. At order ϵ^2 we find that $\theta^{(1)}$ satisfies the problem

$$\frac{1}{r}\left(r\theta_r^{(1)}\right)_r = \mathrm{Pe}\left(\theta_t^{(0)} + u^{(0)}\theta_x^{(0)} - Q\right) - \theta_{xx}^{(0)} \qquad \text{for} \quad r < R(x,t), \tag{2.43a}$$

$$\theta_r^{(1)} = \theta_x^{(0)} R_x - \mathrm{Bi}\left(\theta^{(0)} - \theta_{\mathrm{a}}^{(0)}\right) \qquad \text{at} \quad r = R(x,t), \tag{2.43b}$$

$$\theta_r^{(0)} = 0 \qquad \text{at} \quad r = 0. \tag{2.43c}$$

This is an inhomogeneous version of problem (2.41)-(2.42) satisfied by $\theta^{(0)}$. Therefore the Fredholm alternative implies that (2.43) will have no solutions for $\theta^{(1)}$ unless a solvability condition is satisfied, namely

$$\int_0^{R(x,t)} \left(\mathrm{Pe}\left(\theta_t^{(0)} + u^{(0)}\theta_x^{(0)} - Q\right) - \theta_{xx}^{(0)}\right) r \, \mathrm{d}r = \left(r\theta_r^{(1)}\right)\Big|_{r=0}^{r=R(x,t)}, \tag{2.44}$$

which is solved and rearranged into the net energy conservation equation

$$\left(R^2\theta^{(0)}\right)_t + \left(R^2\theta^{(0)}u^{(0)}\right)_x = \frac{1}{\mathrm{Pe}}\left(R^2\theta_x^{(0)}\right)_x - 2R\frac{\mathrm{Bi}}{\mathrm{Pe}}\left(\theta^{(0)} - \theta_a^{(0)}\right) + \overline{Q}R^2, \tag{2.45}$$

where $\overline{Q}$ is the cross-sectionally averaged volumetric heat source (identical to Q, given that we take Q to be only a function of x). Equation (2.45) is the leading-order governing equation for heat flow in a thin rod. Taroni et al. (2013) derived a simplified model with heat transport in the fibre due to conduction, convection, and radiative heating. They address various asymptotic limits for the

temperature profile in different heat-transfer regimes. The temperature profile we will look at in this chapter corresponds to their small Péclet number limit of interest.

2.3 Simplification of the one-dimensional model

The leading order equations for flow (2.34), (2.40) and temperature (2.45) derived in §2.2 form a simplified one-dimensional axisymmetric model for flow in the spreading cylinder of paste above the electrode, since all the dependent variables only vary with x. These are now rewritten in terms of the cross-sectional area A and net compressive stress P, together with the corresponding boundary conditions.

We drop the superindices and the overbar notation and let $A = R^2$ denote the cross-sectional area of the paste column (divided by π) and to rewrite the system using the following equations for the conservation of mass, momentum, and energy,

$$A_t + (Au)_x = 0, \tag{2.46a}$$

$$P = -3\mu(\theta)Au_x, \tag{2.46b}$$

$$P_x = \mathrm{St}A, \tag{2.46c}$$

$$(A\theta)_t + (A\theta u)_x = \frac{1}{\mathrm{Pe}}(A\theta_x)_x - 2\frac{\mathrm{Bi}}{\mathrm{Pe}}\sqrt{A}\,(\theta - \theta_{\mathrm{a}}(x)) + Q(x)A, \tag{2.46d}$$

with the boundary conditions

$$P = P_{\mathrm{in}}, \quad A = D, \quad \theta = 0 \qquad \text{at } x = 0, \tag{2.47a}$$

$$A = u = 1 \qquad \text{at } x = \lambda(t), \tag{2.47b}$$

$$\theta_x = 0 \qquad \text{at } x = 1. \tag{2.47c}$$

Here, $x = 0$ denotes the point where the cylinders start to soften and P_{in} is the non-dimensional compressive force representing the weight of the cylinders added above $x = 0$, defined as

$$P_{\mathrm{in}} = \frac{\hat{P}_{\mathrm{in}}\bar{L}}{R_1^2 u_c \mu_0} \tag{2.48}$$

where $\hat{P}_{\mathrm{in}}$ is the dimensional compressive load applied at the top.

Note that (2.46c) is valid for $0 < x < \lambda(t)$. We apply boundary condition (2.47b) to (2.35) and find that

$$A = u = 1 \quad \text{for} \quad \lambda(t) < x < 1, \tag{2.49}$$

and on that region it only remains to solve the energy equation

$$\theta_t + \theta_x = \frac{1}{\mathrm{Pe}}\theta_{xx} - 2\frac{\mathrm{Bi}}{\mathrm{Pe}}(\theta - \theta_{\mathrm{a}}(x)) + Q(x) \quad \text{for} \quad \lambda(t) < x < 1. \tag{2.50}$$

We assume $\lambda(t) < 1$. It may be that for certain values of D and P_{in} this will not be the case, which in our model represents that the cylinders have not softened enough to reach the casing before the clamp area, leading to the issues described in §1.1, i.e. paste segregation, breakages, and non-uniform electrode properties. We use the condition $\lambda(t) \not< 1$ as an indicator of a failure in the process for the simulations in §2.4.2.

The dimensionless viscosity is given by

$$\mu(\theta) = \exp\left(-\Gamma\theta\right), \tag{2.51}$$

where $\Gamma = \bar{\Gamma}\Delta T$. We expect Γ to be large to reflect the extreme variation of the viscosity with the temperature. Furthermore, we use (2.21) for induction heating $Q(x)$ and we require an expression for $\theta_a(x)$ in dimensionless form. For the moment we assume that the ambient air is maintained at a constant temperature close to T_{in} and therefore set θ_a constant. Specifically, we take $\theta_a \lesssim 0.23$, representing a dimensional air temperature that is around 80 °C based on the temperatures used by Elkem ASA for the hot air (see §1.3).

2.4 Steady state

For the problem described in §2.3, we have the following dimensionless steady state equations for $A = R^2$, temperature θ and extensional velocity u:

$$\frac{\mathrm{d}}{\mathrm{d}x}\left(Au\right) = 0, \tag{2.52a}$$

$$\frac{\mathrm{d}}{\mathrm{d}x}\left(3\mu(\theta)A\frac{\mathrm{d}u}{\mathrm{d}x}\right) + \mathrm{St}A = 0, \tag{2.52b}$$

$$\frac{\mathrm{d}}{\mathrm{d}x}\left(A\theta u\right) = \frac{1}{\mathrm{Pe}}\frac{\mathrm{d}}{\mathrm{d}x}\left(A\frac{\mathrm{d}\theta}{\mathrm{d}x}\right) - 2\frac{\mathrm{Bi}}{\mathrm{Pe}}\sqrt{A}(\theta - \theta_a) + QA. \tag{2.52c}$$

Equation (2.52a) shows that the volume flux Au is constant, and equal to 1 from the boundary condition (2.47b). Thus $u = 1/A$ and u can be eliminated from the problem. We express the problem as a system of first-order ODEs by defining the diffusive heat flux

$$J = A\frac{\mathrm{d}\theta}{\mathrm{d}x}, \tag{2.53}$$

and therefore obtain the system:

$$\frac{\mathrm{d}P}{\mathrm{d}x} = \mathrm{St}A, \tag{2.54a}$$
$$\frac{\mathrm{d}A}{\mathrm{d}x} = \frac{PA}{3\mu(\theta)}\mathcal{H}\left(1-A\right) \tag{2.54b}$$
$$\frac{1}{\mathrm{Pe}}\frac{\mathrm{d}J}{\mathrm{d}x} = \frac{J}{A} + 2\frac{\mathrm{Bi}}{\mathrm{Pe}}\sqrt{A}(\theta-\theta_a) - QA, \tag{2.54c}$$
$$\frac{\mathrm{d}\theta}{\mathrm{d}x} = \frac{J}{A}. \tag{2.54d}$$

In (2.54b), $\mathcal{H}$ denotes the Heaviside function, where $\mathcal{H}(0) = 0$ (so the argument is never negative). This term allows A to increase until it reaches the casing, and then stop. Thus, rather than solving a free boundary problem for the position $x = \lambda$, we solve (2.54) for $x \in [0, 1]$ and then read off the value of λ from the solution.

The boundary conditions are:

$$P(0) = P_{\mathrm{in}}, \tag{2.55a}$$
$$A(0) = D, \tag{2.55b}$$
$$\theta(0) = 0, \tag{2.55c}$$
$$J(1) = 0. \tag{2.55d}$$

The temperature at the bottom of the electrode $\theta(1)$ and the position of the free boundary λ will be obtained as part of the solution.

2.4.1 Constant viscosity case

It is useful to have analytical solutions, even for simplified versions of the problem, to use as a comparison for numerical results. A simplified version of (2.54) is the constant viscosity case, where we decouple the flow and temperature problems. Setting $\mu = 1$ we have the simplified flow problem

$$\frac{\mathrm{d}P}{\mathrm{d}x} = \mathrm{St}A, \tag{2.56a}$$
$$\frac{\mathrm{d}A}{\mathrm{d}x} = \frac{PA}{3}. \tag{2.56b}$$

The solution is found explicitly as

$$P = \sqrt{6D\mathrm{St} - P_{\mathrm{in}}^2}\tan\left(\frac{\sqrt{\left(6D\mathrm{St} - P_{\mathrm{in}}^2\right)}\left(x + x^*\right)}{6}\right), \tag{2.57a}$$
$$A = \frac{6D\mathrm{St} - P_{\mathrm{in}}^2}{6\mathrm{St}}\tan^2\left(\frac{\sqrt{\left(6D\mathrm{St} - P_{\mathrm{in}}^2\right)}\left(x + x^*\right)}{6}\right) - \frac{P_{\mathrm{in}}^2}{6\mathrm{St}} + D, \tag{2.57b}$$

where we define

$$x^* = \frac{6\arctan\left(\frac{P_{\text{in}}}{\sqrt{6D\text{St}-P_{\text{in}}^2}}\right)}{\sqrt{(6D\text{St}-P_{\text{in}}^2)}}. \tag{2.57c}$$

We find λ by setting $A = 1$, which gives us the formula

$$\lambda = \frac{6}{\sqrt{6D\text{St}-P_{\text{in}}^2}}\arctan\left(\sqrt{\frac{P_{\text{in}}^2+6\text{St}-6D\text{St}}{6D\text{St}-P_{\text{in}}^2}}\right) - x^*. \tag{2.58}$$

With $A(x)$ now known, the temperature problem is given by

$$A\frac{\mathrm{d}^2\theta}{\mathrm{d}x^2} + \left(\frac{\mathrm{d}A}{\mathrm{d}x} - \text{Pe}\right)\frac{\mathrm{d}\theta}{\mathrm{d}x} - 2\text{Bi}\sqrt{A}\theta = -2\text{Bi}\sqrt{A}\theta_a - Q(x)A\text{Pe}, \tag{2.59}$$

with $\theta(0) = 0$ and $\frac{\mathrm{d}\theta}{\mathrm{d}x} = 0$ at $x = 1$. Equation (2.59) can be solved analytically in the region $x > \lambda$ where $A \equiv 1$, using a standard variation of parameters approach. In principle, it then only remains to solve (2.59) numerically in $0 < x < \lambda$, with an effective boundary condition on θ imposed at $x = \lambda$.

2.4.2 Numerical solutions

In this section, we present numerical solutions of the steady boundary-value problem (2.54)-(2.55) and explore the dependence on governing parameters to gain a qualitative understanding of the solution. Finally, some further simplifications are done on the model and compared to asymptotic results.

Using the parameter estimates shown in Table 1.3.1, i.e. $P_{\text{in}} = 0.1$, $\text{Bi} = 58$, $\text{St} = 1$, and $\text{Pe} = 27$, as well as $\theta_a = 0.23$ we obtain the solutions shown in Figure 2.4.1, where we see good agreement with the analytical solutions obtained in §2.4.1, plotted as black dashed lines. The system of equations (2.54) with boundary conditions (2.55) was solved in MATLAB using the inbuilt boundary value problem solver `bvp4c`, which uses Simpson's method (Kierzenka and Shampine, 2001). A value of $\Gamma = 10$ was used for these simulations (the data available suggests $\Gamma \approx 23$, but such a large value makes the problem prohibitively stiff for this numerical implementation as it appears in the exponent of the viscosity temperature dependence in (2.51); an alternative is discussed in Chapter 3). A regularised Heaviside function was used in (2.54b), of the form

$$\mathcal{H} = \max\left\{1 - \exp\left(\frac{-(1-A(x))}{\zeta}\right), 0\right\}, \tag{2.60}$$

where ζ is a regularising parameter that smoothens the function between 0 and 1. For the simulations presented in this section we have used $\zeta = 10^{-2}$.

The profile of the electrode is determined by the shape of $A(x)$, and the dimensionless cylinder radius is given by $\sqrt{A(x)}$. The area of the paste increases until it reaches the casing with $A = 1$

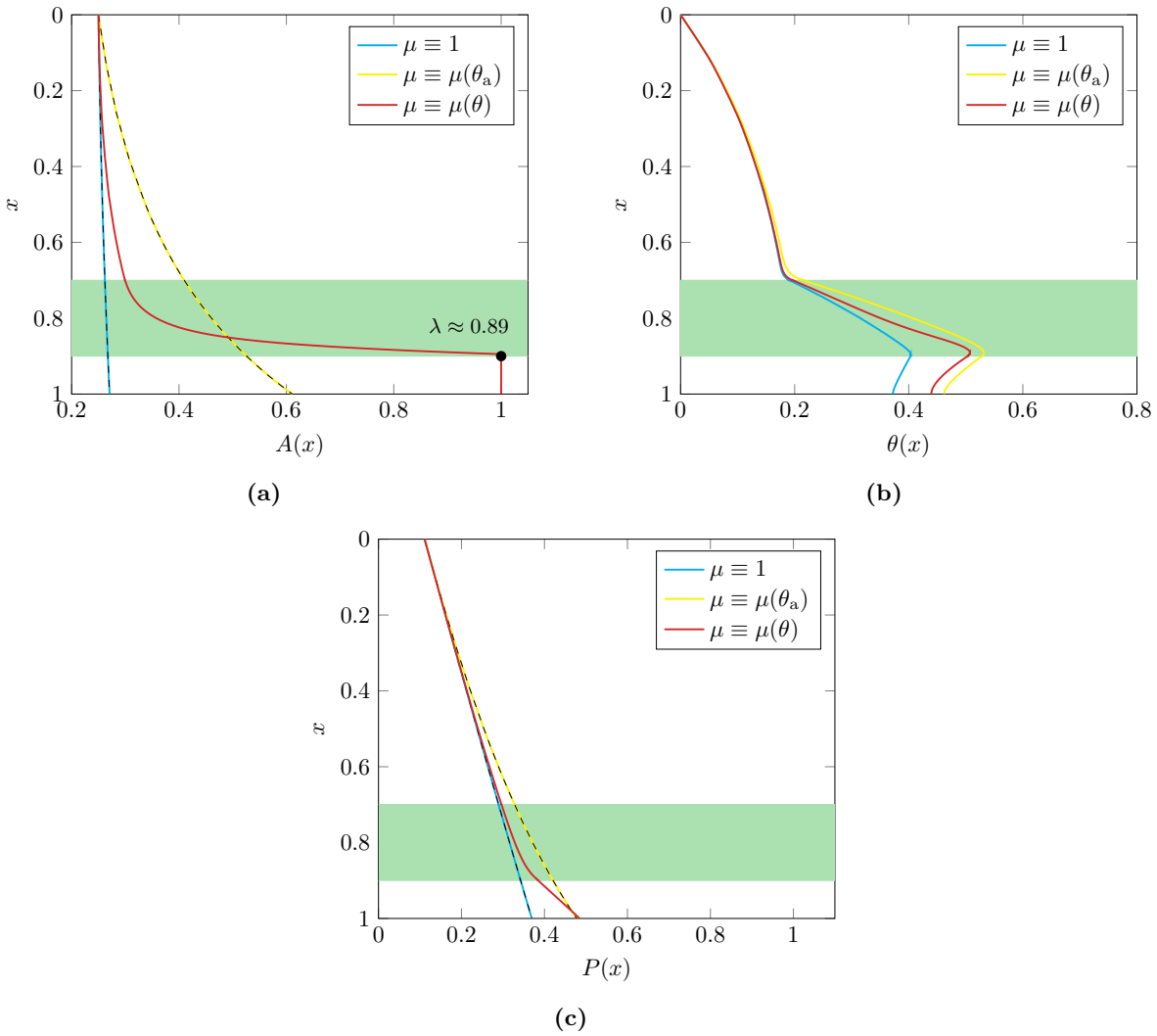

Figure 2.4.1 – Numerical solutions (red) to (2.54), defined in §2.2.1 using $P_{\text{in}} = 0.1$, Bi $= 58$, St $= 1$, $\theta_a = 0.23$, and Pe $= 27$, showing changes in area A, temperature θ, and applied load P, as compared to the constant paste viscosity problem for $\mu = 1$ (blue) and $\mu = \mu(\theta_a)$ (yellow). The green shaded region refers the area $[x_1, x_2] = [0.7, 0.9]$ of the induction heating. The dashed curves correspond to the available analytical solutions presented in §2.4.1.

at some $x = \lambda$, and then continues constant as required. With these parameter values, we find $\lambda \approx 0.89$, which is right before the end of the induction region Q, marked in the green shaded region in Figure 2.4.1. Therefore, despite the large induction heating applied at $x \in [x_1, x_2]$, the cross-sectional area over which it applies does not fill the casing, so the temperature profile does not reach temperatures higher than $\theta \approx 0.55$. As we will see in Chapter 3, for a larger Γ, the free position of λ moves upwards, leading to higher temperatures in the induction region.

The viscosity is a strong function of the temperature, by construction. It starts as 1 (non-dimensional) where the paste is effectively solid, and then decreases as it is heated up in the induction zone. Note that the area changes dramatically in the region where the heating Q is applied, depicted by the green shading in Figure 2.4.1(a), where it is compared to the constant

viscosity case, shown for both the reference viscosity $\mu \equiv 1$ and the viscosity at temperature θ_a. As the cylinders are added at temperatures lower than the softening point of the paste, the change in viscosity is essential to allow the paste to reach the casing (the value of λ predicted for the constant viscosity solution (2.58) is larger than 1 for these parameters).

The compressive load $P(x)$ is determined by the weight of the paste cylinders applied at the top and is shown in Figure 2.4.1(c). It starts at $P_{\text{in}} = 0.1$, corresponding to the weight of paste cylinders applied at the top, and increases as we move further down the electrode due to the increasing hydrostatic pressure.

The dimensionless temperature $\theta(x)$ increases with the heat transfer from the casing wall. The effects from the inductive heat source Q are reflected in the steep temperature increase after $x = x_1$, where the induction is applied in our model. The apparently small diffusion of heat above the induction region reflects the large value of the Péclet number Pe. The constant air heating imposed at the wall creates a cooling effect, seen in Figure 2.4.1(b) after exiting the induction region where the temperature is larger than θ_{a} and there is no other heating term.

2.4.3 Dependence on non-dimensional parameters

The Stokes number St tells us how important the hydrostatic loading is with respect to the stiffness of the paste. The larger the value of St, the more readily the paste deforms and the sooner it makes contact with the casing. The position of the free boundary $x = \lambda$ thus depends sensitively on St, as seen in Figure 2.4.2(a), where we show λ varying as we change St. In Figure 2.4.2(b), we see that λ depends even more sensitively on P_{in}, the applied load. In order to prevent a catastrophic failure of the process, which in our system can be interpreted as $\lambda > 1$, we need both the extra forcing from P_{in} at the top, as well as a larger St. As was concluded in Bergstrøm et al. (1989), the higher the weight of the cylinders added at the top of the electrode, the sooner the free boundary $x = \lambda$ is reached. In the time dependent problem in Chapter 3 we provide a detailed study on the effects of varying P_{in} over time, showing both numerical and analytical results.

It also is helpful to consider limiting values of St. If we take the limit $\text{St} \to 0$ in (2.54a) we find $P = P_{\text{in}}$ and

$$A(x) = D \exp\left(\frac{P_{\text{in}}}{3}\int_0^x e^{\Gamma\theta(x)}\mathrm{d}x\right), \tag{2.61}$$

although we must still solve a coupled problem for θ in order to evaluate this expression. When $\Gamma = 0$, however, this gives a simple relationship that estimates λ for a given choice of parameters, namely

$$\lambda = 3\ln\left(\frac{1}{D}\right)\frac{1}{P_{\text{in}}}. \tag{2.62}$$

This shows that while increasing D and P_{in} will reduce the value of λ, the free boundary is less sensitive to changes in D due to the logarithmic relationship in (2.62). Although (2.62) is only valid

for $\mathrm{St} = 0$ and $\Gamma = 0$, we explore it further in Figure 2.4.2(c), where we note that even for larger values of St, (2.62) is a good approximation for λ, in particular for larger values of P_{in}, or conversely, larger values of D. However, even a small increase in Γ has a great effect in the the estimation of λ, as seen in Figure 2.4.2(d), where the resulting slope for $\Gamma \gtrapprox 1$ does not follow (2.62).

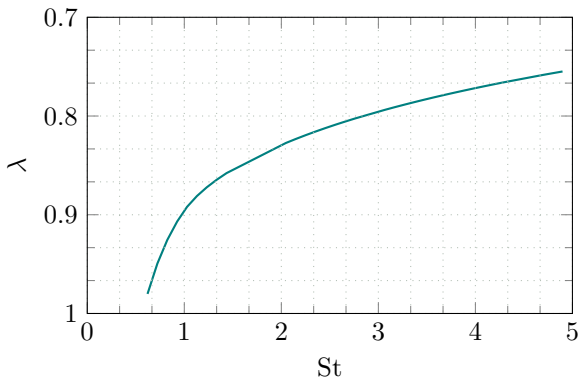

(a) $\Gamma = 10$, $P_{\text{in}} = 0.1$

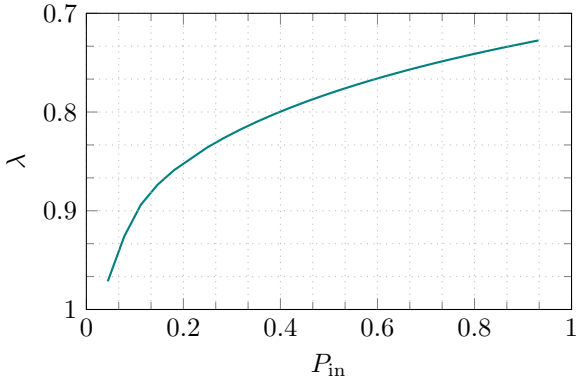

(b) $\Gamma = 10$, $\mathrm{St} = 1$

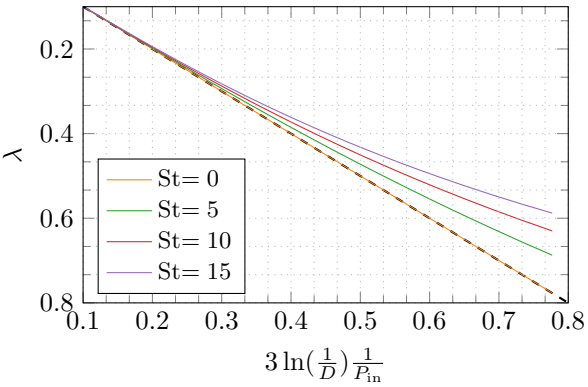

(c) $\mathrm{St} \to 0$ limit, with $\Gamma = 0$

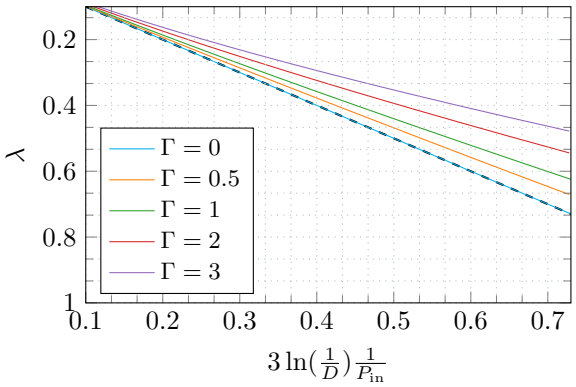

(d) $\mathrm{St} \to 0$ limit, increasing Γ

Figure 2.4.2 – Steady profiles for free boundary λ, showing the (a) Stokes number and (b) applied load parameter space with $\mathrm{Pe} = 27$, $\mathrm{Bi} = 58$, $\Gamma = 10$, $D = 0.25$, and $\theta_a = 0.23$. (c) Comparison of relationship (2.62) with numerical results, when varying the Stokes number keeping $\Gamma = 0$, (d) when varying the viscosity dependence parameter Γ keeping $\mathrm{St} = 0$.

We also write the limiting behaviour of the $\Gamma = 0$ solution of (2.54) as $\mathrm{St} \to \infty$. Taylor expanding (2.58) leads to

$$\lambda \sim \sqrt{\frac{6}{D}} \cos^{-1}\left(\sqrt{D}\right) \frac{1}{\sqrt{\mathrm{St}}}. \tag{2.63}$$

Note that since $\Gamma = 0$, we obtain $\lambda > 1$ for $\mathrm{St} = 1$ in (2.63).

Elkem ASA are interested in the scalability of their electrodes, in particular looking at a larger electrode casing radius and how this would affect the softening profile of the paste. In our model, this corresponds to modifying D, the area ratio, which we can interpret as the amount of space available at the top of the casing for the softened paste to fill. With the dimensions considered here, $D \approx 0.25$, as noted in Table 2.2.1. In Figure 2.4.3(a) we examine how λ depends on D. We note that as we increase D the paste reaches the casing sooner, as this corresponds to a smaller

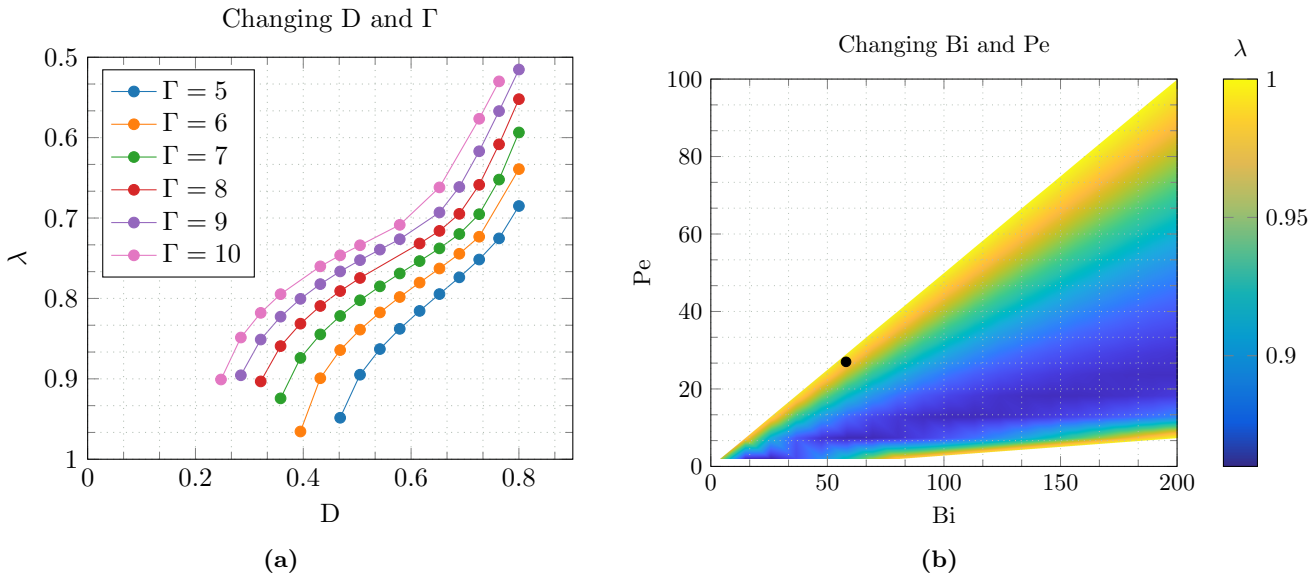

Figure 2.4.3 – Free boundary λ (a) as we vary D and Γ with Bi $= 58$, Pe $= 27$ and (b) as we vary Bi and Pe, with $D = 0.25$, $\Gamma = 10$. In both cases we have used $P_{\text{in}} = 0.1$, St $= 1$, and $\theta_a = 0.23$. A black dot in (b) indicates the estimated λ with the parameters from Table 5.2.1, while keeping $\Gamma = 10$.

electrode radius so the paste cylinder fills up a larger portion of it initially. Conversely, a smaller value of D results in a position of λ further down the domain, until we reach the situation where the paste does not reach the casing at all for $0 < x < 1$. Additionally, we note that the change in λ with respect to D is similar for each value of Γ, so it is reasonable to assume that for realistic values of Γ, (e.g. $\Gamma \approx 23$) we will observe the same behaviour. This means that for scaling the Søderberg electrode, a change in the radius alone is not sufficient to ensure a good softening profile of paste, and it should always be done in combination with other control parameters which affect the softening of the paste, described above.

The parameters that determine the heating profile of the paste are the Biot number, relating the heat transfer from the casing wall to the conduction of the paste, and the Péclet number, measuring the ratio of advection to conduction. We explore the Bi-Pe parameter space in Figure 2.4.3(b), where the colour scheme indicates the size of λ. The heat transfer from the casing walls facilitates the softening, but if Pe is too large, the effects from the induction heat Q will not affect the softening at all, preventing the paste from reaching the casing entirely. A black dot in Figure 2.4.3(b) indicates the estimated λ with the parameters from Table 5.2.1, while keeping $\Gamma = 10$. Keeping all other parameters constant, we see that in order to allow for the paste to reach the casing sooner, we can choose a smaller Pe, or increase the effects of the wall heating by taking a larger Bi. We will explore this further in the next subsection.

2.4.4 The casing wall effect on the temperature

We next examine the effect of varying the constant hot air temperature θ_a. As we increase θ_a, the paste temperature increases, leading to significant increase of temperature at the end of the domain,

as seen in Figure 2.4.4(a). Consequently, it has an effect on the area profile, as a higher θ_a will lead to the paste reaching the casing sooner, as seen in Figure 2.4.4(b). The effects of the conduction only become apparent near the induction region, where the temperature begins to increase slightly above the green region in Figure 2.4.4(a).

The maximum temperature in the examples we have seen so far is always reached inside the region where the induction heating is activated. We explore the effects of varying θ_a in Figure 2.4.4(a), where after the end of the induction heating, delimited by the green region, the temperature decreases. This shows that the transfer from the wall acts as a heating mechanism until the temperature reaches θ_a, at which point it becomes a cooling mechanism for the paste. Thus, the hot air column modelled by θ_a is an important control mechanism that regulates not only the paste softening at the top, but the maximum temperature reached in this region.

Note that we have simplified this heating by considering it to be a constant, but in the industrial problem, it is only when the paste comes into contact with the casing that we see large effects coming from the external heating. As the heat transfer coefficient of air is much smaller than the one of steel, we expect Bi to be smaller before reaching $x = \lambda$, with an increase as the paste touches the casing. To illustrate this effect, we consider the extreme case where $\mathrm{Bi} = 0$ for $x < \lambda$ and $\mathrm{Bi} = 58$ for $x \geq \lambda$, and we show the results of this experiment in Figure 2.4.5, where we have used $\mathrm{St} = 5$ to allow the paste to reach the casing. We can distinguish the $\mathrm{Bi} = 0$ and the two region Bi cases from each other by looking at the behaviour after the end of the induction heating region, where the temperature would remain constant in the absence of wall heating, but would decrease for non-zero θ_a. This is also reflected in Figure 2.4.5(b), where the paste reaches the casing at a much lower position if we consider the two region Bi. We expect a more realistic model for the wall temperature to give a temperature profile between the two region $\mathrm{Bi} = 0$ and $\mathrm{Bi} = 58$ cases. Varying the temperature of the air column as a function of position is explored in Chapter 4 and Chapter 5.

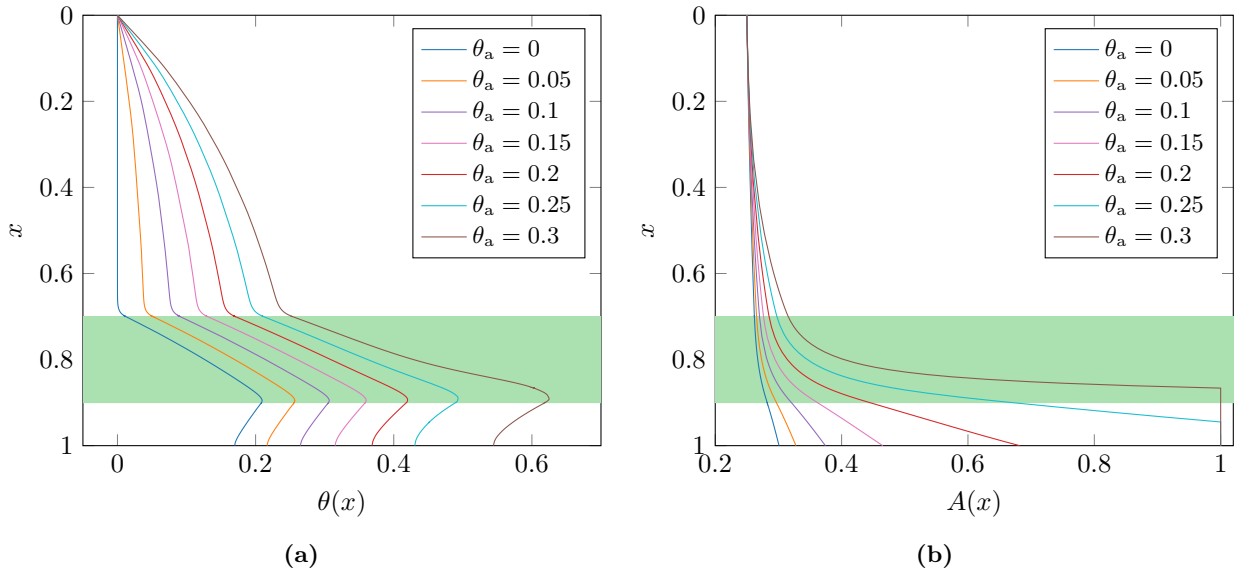

(a) **(b)**

Figure 2.4.4 – Steady (a) temperature and (b) area profiles with $\Gamma = 10$, $P_{\text{in}} = 0.1$, $\text{Bi} = 58$, $\text{St} = 1$, $\theta_a = 0.23$, and $\text{Pe} = 27$, for different θ_a. The green shaded region represents the area of the induction heating.

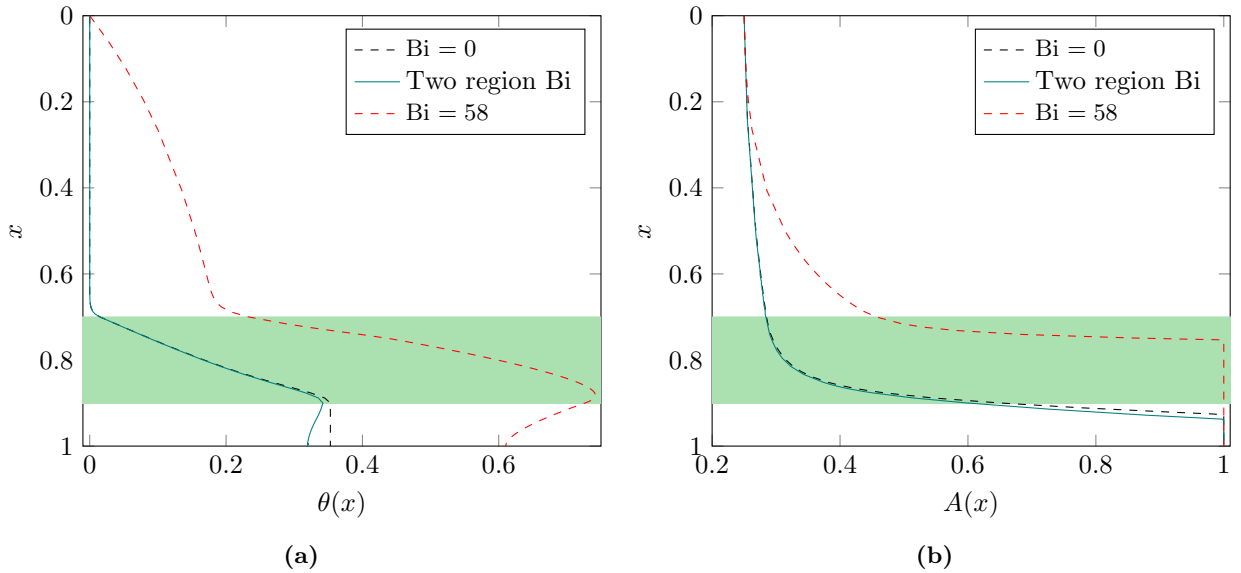

(a) **(b)**

Figure 2.4.5 – (a) Temperature and (b) area profile, where we look at the extreme Bi variation over the domain, compared with the $\text{Bi} = 0$ and $\text{Bi} = 58$ cases. We have used $\Gamma = 10$, $P_{\text{in}} = 0.1$, $\theta_a = 0.23$, and $\text{St} = 5$.

2.4.5 Large Pe limit

The Péclet number for our problem is large, which implies that the conduction of heat to the upper part of the electrode is weak. Looking at higher Pe corresponds to having a larger slipping rate, which allows us to effectively neglect conduction.

In the limit $\mathrm{Pe} \to \infty$, equations (2.54) become

$$\frac{\mathrm{d}P}{\mathrm{d}x} = \mathrm{St}A, \tag{2.64a}$$

$$\frac{\mathrm{d}A}{\mathrm{d}x} = \frac{PAe^{\Gamma\theta}}{3}, \tag{2.64b}$$

$$\frac{\mathrm{d}\theta}{\mathrm{d}x} = QA. \tag{2.64c}$$

We solve (2.64) analytically subject to the initial conditions (2.55a), (2.55b), and (2.55c): in this singular perturbation, the downstream condition (2.55d) cannot be satisfied. We split the domain into three regions: $0 < x < x_1$, $x_1 < x < x_2$, and $x_2 < x < 1$. The first and third regions are equivalent to the isothermal problem solved in §2.4.1, with $\theta = 0$ in the first region, and $\theta = \theta(x_2)$ in the third region, and with boundary conditions that ensure continuity with the solution of the second region. In the remaining second region, we have the system (2.64) with constant Q, boundary conditions $A(x_1)$ and $P(x_1)$ taken from (2.57), and $\theta(x_1) = 0$. We make some analytical progress and find that

$$A(x) = \frac{1 - P(x_1)\widehat{Q} + \left(P\widehat{Q} - 1\right) e^{(P - P(x_1))\widehat{Q}}}{3\widehat{Q}^2\mathrm{St}} + A(x_1), \tag{2.65}$$

$$\theta(x) = \frac{Q}{\mathrm{St}} \left(P - P(x_1)\right), \tag{2.66}$$

for the grouped parameter $\widehat{Q} = \frac{Q\Gamma}{\mathrm{St}}$, where P is given by substituting (2.65) in (2.64a) and solving numerically.

We show the resulting temperature and area profile as a dashed line in Figure 2.4.6 and compare with numerical solutions of the full model (2.54)-(2.55) with large but finite Pe. Note that with these parameter values, the limiting solution for A does not reach $A = 1$, as suggested previously by the results in Figure 2.4.3(b) .

Since the Biot number is also large, it is physically relevant to consider an alternative limit in which we set $\xi = 2\frac{\mathrm{Bi}}{\mathrm{Pe}}$ to be $\mathcal{O}(1)$. The parameter ξ is sometimes called the Stanton number, relating the heat transfer with the heat capacity or bulk energy advection (Scheid et al., 2009). We take

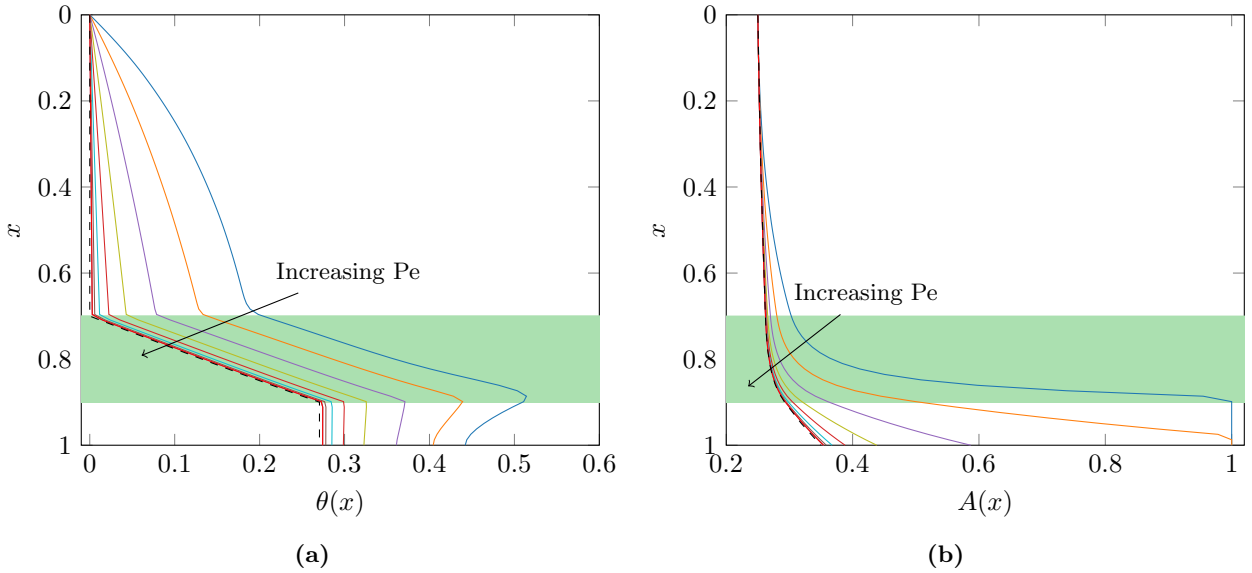

Figure 2.4.6 – (a) Temperature and (b) area profile for $\mathrm{Pe} = \{50, 100, \ldots, 12800\}$, with $\Gamma = 10$, $\mathrm{Bi} = 58$, $P_{\mathrm{in}} = 0.1$, $\theta_a = 0.23$, and $\mathrm{St} = 1$. The dashed line shows the solution for the no conduction case, given by (2.64).

$\mathrm{Pe} \to \infty$, which gives the equations

$$\frac{\mathrm{d}P}{\mathrm{d}x} = \mathrm{St}A, \tag{2.67a}$$

$$\frac{\mathrm{d}A}{\mathrm{d}x} = \frac{PAe^{\Gamma\theta}}{3}, \tag{2.67b}$$

$$\frac{\mathrm{d}\theta}{\mathrm{d}x} = QA - \xi\sqrt{A}\,(\theta - \theta_a)\,, \tag{2.67c}$$

which we solve numerically and show the resulting temperature and area profile in Figure 2.4.7 along with the corresponding solutions of (2.54)-(2.55) with large but finite Pe. As before, the temperature and the area approach the $\mathrm{Pe} \to \infty$ approximation as we increase Pe. Compared to the solution in Figure 2.4.6, more softening of paste is present before the induction area as the hot air increases the temperature, and this results in smaller values of λ than for the case in Figure 2.4.6.

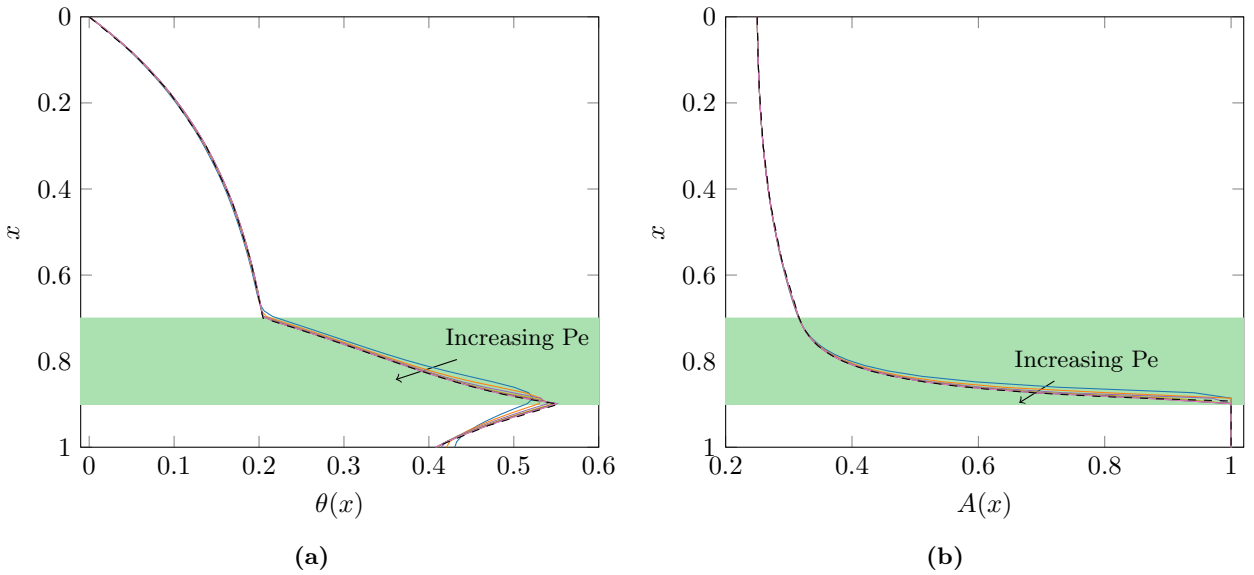

Figure 2.4.7 – (a) Temperature and (b) area profile for $\mathrm{Pe} = \{50, 100, \ldots, 12800\}$, $\mathrm{Bi} = \xi\mathrm{Pe}/2$, with $\xi = 6$, $\Gamma = 10$, $P_{\mathrm{in}} = 0.1$, $\theta_a = 0.23$, and $\mathrm{St} = 1$. The dashed line shows the numeric solution for the no conduction case, given by (2.67).

2.5 Concluding remarks

In §2.1 we have described an axisymmetric Stokes flow model, coupled with the heat equation and a temperature-dependent viscosity. We have written down the appropriate free boundary problem for the softening and spreading of the paste, and in §2.2 we have assumed a long and thin domain, such that the aspect ratio $\epsilon \ll 1$. We have then proceeded with asymptotic expansions in powers of ϵ^2, analogous to Dewynne et al. (1992).

For the flow problem, we have derived the so-called Trouton model which governs the flow of a viscous rod with variable viscosity. These are valid for $0 < x < \lambda$ in our domain, as the paste softens and reaches the casing. Once the paste reaches the casing, i.e. for $x > \lambda$, we found that it moves at a constant velocity at leading order which matches the velocity of the casing.

The temperature problem reduces to a one-dimensional heat flow equation in a thin rod, as expected from the long and thin assumption, and is valid for all x. It is coupled with the flow problem through a temperature dependent viscosity (2.51), which is assumed to be exponential in θ. The Trouton model for $0 < x < \lambda$, the plug flow for $x > \lambda$, the thin rod heat flow equation, and the viscosity-temperature relation, together with boundary conditions (2.27) form a one-dimensional model described in §2.3. Steady state solutions have been computed numerically in §2.4 and have been compared to known analytical solutions.

We have explored the qualitative dependence on non-dimensional parameters in §2.4.3 and have made the following observations:

- The position of the free boundary $x = \lambda$ depends sensitively on the Stokes number St and

the applied compressive load P_{in}. Decreasing these parameters sufficiently leads to $\lambda > 1$, a failure of the industrial process as the paste does not reach the casing in the appropriate region. Elkem ASA have observed that they expect $x = \lambda$ to be reached at the top part of the casing during good operating conditions, which corresponds to a larger number of cylinders added on top of $x = 0$. This also matches observations made by Bergstrøm et al. (1989) regarding the weight of cylinders stacked at the top part of the electrode.

- Increasing the radius of the casing while keeping the radius of the cylinders fixed (decreasing D) also lowers the position of λ so if it is required to produce Søderberg electrodes with a larger radius, it is necessary to modify other model parameters as well, such as the weight or radius of the cylinders at the top, the hot air along the casing wall, and the slipping rate (included in St).
- The heating from the air along the casing, contributes significantly to the softening of paste. In our model the paste softens along the casing due to θ_a and its temperature then dramatically increases as it reaches the induction area. Since the conduction of heat to the upper part of the electrode is weak, it is important to include θ_a to capture the effect of paste softening above the induction heating area.
- The role of the air column alternates between a heating mechanism and a cooling mechanism, with the switch occurring when θ becomes larger than θ_a.

In the next chapter, we shall investigate the time dependent version of this problem both numerically and analytically, showing examples for $\lambda(t)$ varying under specific parameter choices as well as the effect of the addition of cylinders.

Chapter 3

Time dependent solutions for coupled flow and temperature model for paste softening

The steady model solved in Chapter 2 assumes that material is fed in at a constant rate. In normal electrode operation, solid paste cylinders are added to the top of the domain in an unsteady and often irregular way (Nelson and Prins, 2004). To shed light on this process, we extend the model presented in Chapter 2 to the unsteady case, for which we present numerical solutions and some analytical approximations.

In §3.1, we describe a finite volume numerical scheme which calculates the time evolution of the area $A(x,t)$, the velocity $u(x,t)$, the temperature $\theta(x,t)$, and the position of the free boundary, $\lambda(t)$, where the paste touches the casing for the first time. The motion of the free boundary is tackled by splitting the domain into two regions, the one above $x = \lambda$ and the one below, mapping each region onto a fixed domain, and joining the solutions with the appropriate continuity conditions.

After validating the numerical scheme, in §3.2 we focus on numerical experiments where we vary the applied compressive load, P_{in}, as a function of time. We design two control strategies that replicate the cylinder addition patterns used during normal operations and make observations on how the flow and temperature profile react to such variations. Additionally, we briefly explore the effects of varying the casing velocity in such a system.

In §3.4, we explore the industrially relevant limit where the variations in the applied compressive load occur on a time-scale much shorter than the natural convective time-scale in the problem. The resulting asymptotic approximations to the expected fluctuations in A, u, and θ are then compared to the numerical results produced with the scheme developed in §3.1. This comparison reveals a boundary layer for θ near $x = 0$, as well as a multiple scales structure to A, which we investigate in

§3.5 for the isothermal problem, before summarising our conclusions in §3.6.

The work in this chapter is related to previous work on modelling unsteady extensional flows, which we briefly mention. The time-dependent one-dimensional equations for extensional flow and temperature (uniform across the cross-section) without conduction were developed by Kase and Matsuo (1965) for viscous fibres polymer spinning applications. The flow is assumed to be Newtonian with a temperature dependent viscosity and steady solutions were calculated, which showed good agreement with available polymer data. Since then, many analytical and numeric studies have been performed on the linear stability such problems, most notably by Shah and Pearson (1972) for fibre drawing applications including the effects of inertia, surface tension, and gravity forces. In particular, it has been of high interest to study the linear stability of such problems and the potential for draw resonance, a phenomenon in which oscillating perturbations propagate along the viscous fibre (or sheet) and grow in amplitude, resulting in a product with non-uniform thickness (Fisher and Denn, 1975).

3.1 Non-steady solutions

3.1.1 Mathematical formulation

Consider again the time-dependent problem (2.46) illustrated in Figure 2.1.1. We split the domain into two regions: the *top* region, when $0 < x < \lambda(t)$, and the *bottom* region, when $\lambda(t) < x < 1$. Then, the governing equations for the top region are

$$A_t + (Au)_x = 0, \tag{3.1a}$$

$$(3\mu(\theta)Au_x)_x + \mathrm{St}A = 0, \tag{3.1b}$$

$$A\left(\theta_t + u\theta_x\right) = \frac{1}{\mathrm{Pe}}\left(A\theta_x\right)_x - 2\frac{\mathrm{Bi}}{\mathrm{Pe}}\sqrt{A}\left(\theta - \theta_{\mathrm{a}}(x)\right) + Q(x)A, \tag{3.1c}$$

with boundary conditions

$$A = D, \quad u_x = \frac{-P_{\mathrm{in}}(t)}{3D}, \quad \theta = 0 \qquad \text{at} \quad x = 0, \tag{3.1d}$$

$$A = 1, \quad u = 1 \qquad \text{at} \quad x = \lambda(t). \tag{3.1e}$$

Here, $x = 0$ is a particular reference height above the furnace that we choose as our origin, and P_{in} is the non-dimensional compressive force representing the weight of the cylinders added above $x = 0$. We use the same heating terms as in Chapter 2, namely wall heating $\theta_{\mathrm{a}} = 0.23$ and piecewise linear induction heating $Q(x)$ given by (2.21).

In the bottom region, we have $A = u = 1$. The temperature in this region is denoted Φ and is given by

$$\Phi_t + \Phi_x = \frac{1}{\mathrm{Pe}}\Phi_{xx} - 2\frac{\mathrm{Bi}}{\mathrm{Pe}}\left(\Phi - \theta_{\mathrm{a}}(x)\right) + Q(x) \tag{3.2a}$$

with

$$\Phi_x = 0 \quad \text{at} \quad x = 1. \tag{3.2b}$$

We ensure a smooth transition between the top and bottom temperature solution by imposing the continuity conditions

$$\theta = \Phi, \quad \theta_x = \Phi_x \quad \text{at} \quad x = \lambda(t). \tag{3.3}$$

We obtain an equation for the evolution of $\lambda(t)$ by differentiating (3.1e) and using (3.1a), resulting in

$$\dot{\lambda} = u + \frac{Au_x}{A_x} \quad \text{at} \quad x = \lambda(t), \tag{3.4}$$

where $\dot{\lambda}$ denotes differentiation with respect to t. Finally, we choose initial conditions consistent with the steady state, namely

$$A = A_0(x), \quad u = u_0(x), \quad \theta = \theta_0(x) \quad \text{at} \quad t = 0, \tag{3.5}$$

where the subindex 0 refers to the solution of the steady state problem. Note that (3.5) implicitly also determines $\lambda(0) = \lambda_0$.

To tackle the free boundary problem numerically, we rescale the top and bottom regions with respect to $\lambda(t)$ and solve each problem separately, imposing the continuity conditions (3.3).

We first focus on the flow problem for the top region, applying the rescaling

$$X = \frac{x}{\lambda(t)}, \tag{3.6}$$

and temporarily writing $t = \hat{t}$ (to clarify that X and $\hat{t}$ are now the independent variables). Then the partial derivatives become

$$\frac{\partial}{\partial x} = \frac{1}{\lambda}\frac{\partial}{\partial X}, \quad \frac{\partial}{\partial t} = -\frac{X\dot{\lambda}}{\lambda}\frac{\partial}{\partial X} + \frac{\partial}{\partial \hat{t}}. \tag{3.7}$$

The rescaled equations are, upon dropping the hat notation for t,

$$(\lambda A)_t + \left[\left(u - \dot{\lambda}X\right)A\right]_X = 0, \tag{3.8a}$$

$$(3\mu A u_X)_X + \lambda^2 \mathrm{St} A = 0, \tag{3.8b}$$

with boundary conditions

$$A = D, \quad u_X = \frac{-P_{\text{in}}}{3D}\lambda \qquad \text{at} \quad X = 0, \tag{3.9a}$$

$$u = 1, \quad \dot{\lambda} = 1 + \frac{u_X}{A_X} \qquad \text{at} \quad X = 1, \tag{3.9b}$$

and initial conditions (3.5). Note that the additional term in the velocity of (3.8a) reflects how the area in the stretched coordinate reacts to the movement of the free boundary.

Similarly, for the temperature problem in the top region, we apply the rescaling (3.6) to (3.1c) and obtain

$$(A\theta)_t + \frac{1}{\lambda}\left[\left(u - \dot{\lambda}X\right)A\theta\right]_X = -\frac{\dot{\lambda}A\theta}{\lambda} + \frac{1}{\lambda^2 \mathrm{Pe}}\left(A\theta_X\right)_X - \frac{2\ \mathrm{Bi}}{\mathrm{Pe}}\sqrt{A}\left(\theta - \theta_{\mathrm{a}}(\lambda X)\right) + Q(\lambda X)A, \quad (3.10)$$

with boundary condition

$$\theta = 0 \quad \text{at} \quad X = 0. \quad (3.11)$$

In the bottom region, we introduce the rescaling

$$\bar{X} = \frac{x - \lambda(t)}{L - \lambda(t)}, \quad (3.12)$$

and $t = \bar{t}$, leading to the partial derivatives

$$\frac{\partial}{\partial x} = \frac{1}{L - \lambda(\bar{t})}\frac{\partial}{\partial \bar{X}}, \quad \frac{\partial}{\partial t} = \frac{\dot{\lambda}(\bar{t})\left(\bar{X} - 1\right)}{L - \lambda(\bar{t})}\frac{\partial}{\partial \bar{X}} + \frac{\partial}{\partial \bar{t}}. \quad (3.13)$$

Then, the rescaled equation (3.2) for Φ is, (after dropping the bar notation for t),

$$\Phi_t + \frac{1}{L - \lambda}\left[\left(\left(\bar{X} - 1\right)\dot{\lambda} + 1\right)\Phi\right]_{\bar{X}} = \frac{\dot{\lambda}}{L - \lambda}\Phi + \frac{1}{(L - \lambda)^2\,\mathrm{Pe}}\Phi_{\bar{X}\bar{X}} - \frac{2\ \mathrm{Bi}}{\mathrm{Pe}}\left[\Phi - \theta_{\mathrm{a}}\left(L - \bar{X}\,(L - \lambda)\right)\right] + Q\left(L - \bar{X}\,(L - \lambda)\right), \quad (3.14)$$

with boundary condition

$$\Phi_{\bar{X}} = 0 \quad \text{at} \quad \bar{X} = 1. \quad (3.15)$$

The continuity conditions (3.3) at $x = \lambda(t)$ are transformed to

$$\theta\big|_{X=1} = \Phi\big|_{\bar{X}=0}, \quad (3.16)$$

$$\frac{1}{\lambda}\theta_X\Big|_{X=1} = \frac{1}{L - \lambda}\Phi_{\bar{X}}\Big|_{\bar{X}=0}. \quad (3.17)$$

We discretise each equation in space and turn it into a system of ODEs in time that are solved using MATLAB with `ode15s.m`. This is a standard method of lines approach, as described in Schiesser and Griffiths (2009). The numerical scheme used is an implementation of Godunov's method (Godunov, 1959), which is first-order accurate, using the definition of Roe flux (Roe, 1981), as described in LeVeque (1992). We explain our numerical method in detail in Appendix A.

3.1.2 Validating the numerical scheme

The numerical method described in Appendix A converges provided it is stable and consistent (LeVeque, 1992). Stability is guaranteed provided the CFL (Courant et al., 1959) condition is satisfied, namely

$$C = \frac{u\Delta t}{\Delta X} \leq 1, \tag{3.18}$$

and similarly for $\Delta\bar{X}$, where $\Delta t = T/N$, $\Delta X = \lambda/K$, and $\Delta\bar{X} = (L-\lambda)/K$. C is called the Courant number. Our chosen values of K and N satisfy (3.18), where we use the maximum value of the initial condition on u to calculate C. Godunov's method is also proved to be consistent for any choice of flux function $\mathcal{U}$, with appropriate Lipschitz continuity (LeVeque, 1992), which we assume without proof in this work. The MATLAB routine `ode15s.m` selects the timesteps using inbuilt adaptivity, and then evaluates the result onto the specified (equispaced) timesteps we have imposed. The solutions produced at the specified points are of the same order of accuracy as the solutions computed at each internal step in the MATLAB routine. We have confirmed that the results for specified timesteps match the ones where the timesteps are chosen by the solver. Grid convergence was verified for the isothermal case, showing a linear convergence rate.

We first apply our numerical scheme to the isothermal case, for which we have the analytical steady solution calculated in §2.4.1 where $\theta \equiv 0$ and $\mu(\theta) \equiv 1$. We remove the temperature equations and impose simple initial conditions

$$A(x,0) = \frac{x}{\hat{\lambda}}(1-D) + D, \quad \lambda(0) = \hat{\lambda}, \tag{3.19}$$

where $0 < \hat{\lambda} < 1$ and $0 \leq x \leq \hat{\lambda}$, as we only require an initial condition for A up to $\hat{\lambda}$. We choose $\mathrm{St} = 25.5$, which for the isothermal case leads to $\lambda = 1$. We show the time evolution provided by our numerical scheme for the area and velocity as they converge to the steady state solution in Figures 3.1.1(a) and 3.1.1(b), respectively, where we used $\hat{\lambda} = 0.7$. In Figure 3.1.1(c), we see that the numerical scheme converges to the analytical solution $\lambda = 1$ for different values of $\hat{\lambda}$. We have used $K = 300$ equispaced points in x and $N = 8000$ equispaced points in t (satisfying (3.18)), for which the scheme converges quickly with discretisation errors of $\mathcal{O}(10^{-3})$.

We also compare the steady state of the numerical scheme described in §3.1.1 (full details in Appendix A) with the numerical method used in §2.4.2. We use simple initial conditions (3.19) with $\theta(X,0) = 0$ and $\Phi(\bar{X},0) = 0$. We show the results of this example in Figure 3.1.2, where the area, velocity, and temperature solutions differ by $\mathcal{O}(10^{-2})$. The steady state reached by the time dependent numerical scheme presented in this section corresponds to the solution to the steady problem presented in §2.4.2 with the full Heaviside function. Recall that for our previous numerical implementation from Chapter 2, we use an approximation of the Heaviside function in order to enforce the behaviour of A as x reaches λ, which depends on a smoothening parameter ζ. In this sense, although they produce the same qualitative results, we do not expect both methods

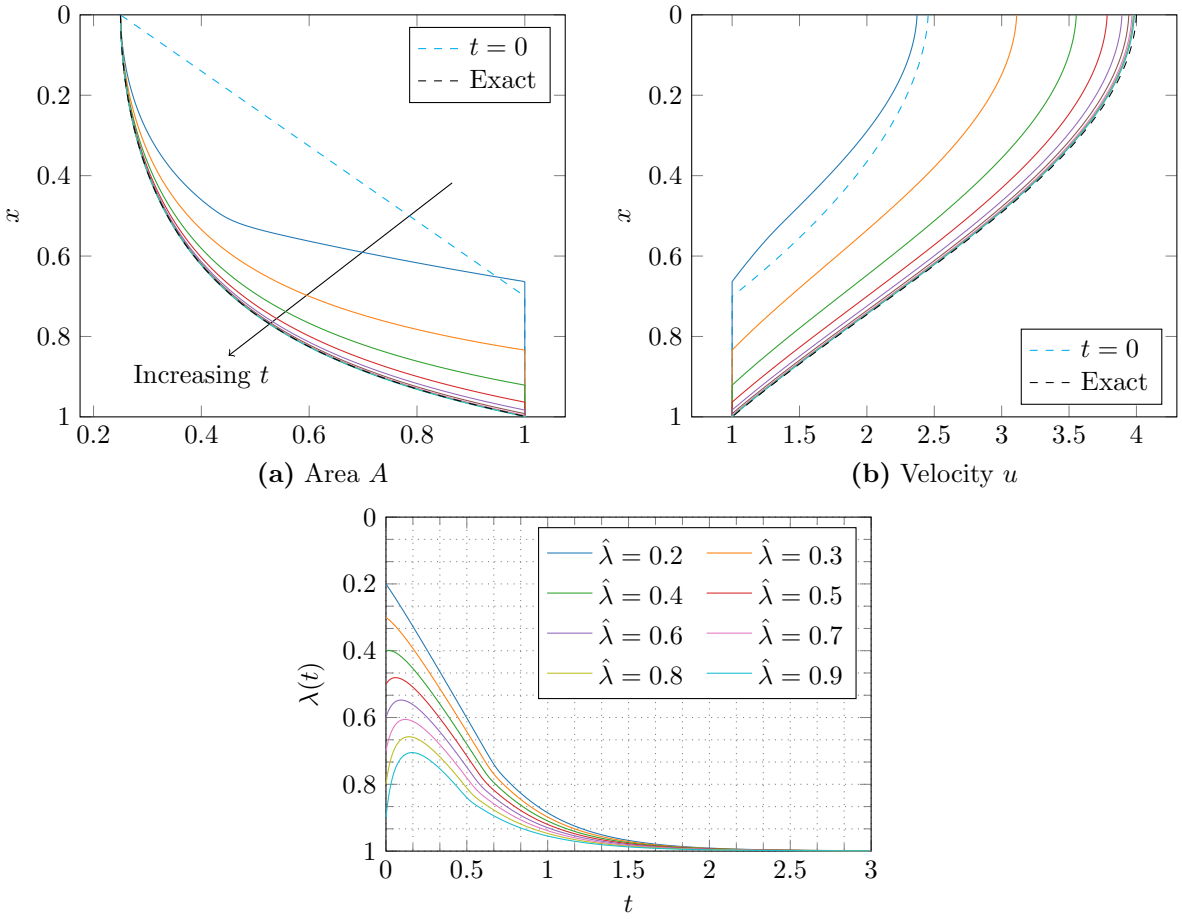

(a) Area A **(b)** Velocity u

(c) Free boundary $\lambda(t)$

Figure 3.1.1 – Solution to (3.4) and (3.8), with $\mu = 1$, where we show variation of the area, the velocity, and the free boundary position over time, from $t = 0$ to $t = 3$ with $K = 300$. We have used initial conditions (3.19), with $\bar{P}_{\text{in}} = 0.1$, D $= 0.25$ and St chosen such that $\lambda = 1$ (St $= 25.5$). Note that (a) and (b) have the same colour scheme, where each colour corresponds to one of 10 equispaced time-steps, and the dashed black curve shows the exact steady solution (2.57).

to reach the same steady state. For instance, our previous routine predicted $\lambda \approx 0.89$ with $\Gamma = 10$ and standard parameters from Table 1.3.1, whereas the unsteady solution converges to $\lambda \approx 0.87$. However, the steady state routine is much faster for these experiments, which has allowed us to perform the parameter sweeps in §2.4.3, but the time dependent scheme converges for larger values of the viscosity sensitivity Γ for which the steady problem is prohibitively stiff.

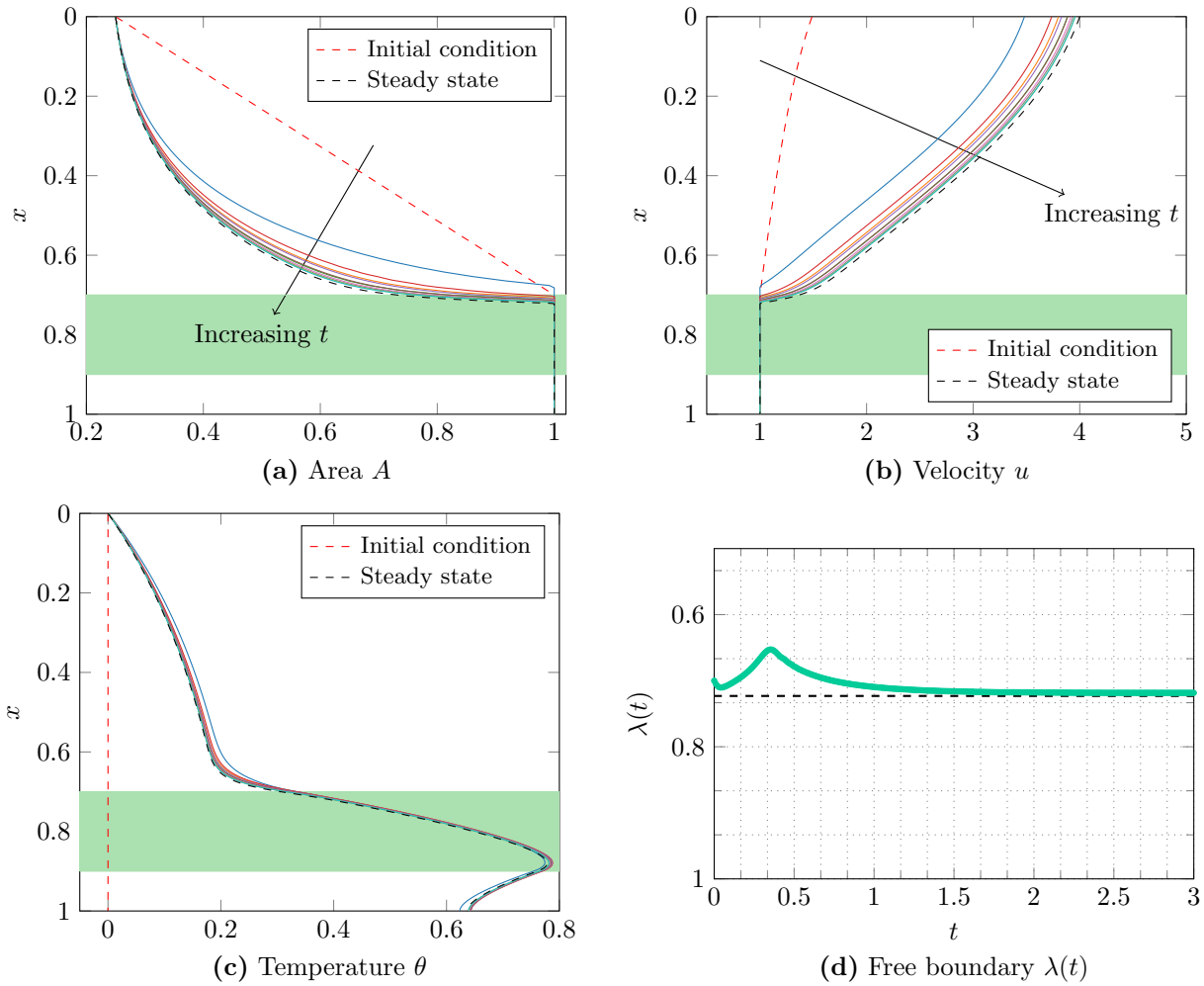

(a) Area A **(b)** Velocity u

(c) Temperature θ **(d)** Free boundary $\lambda(t)$

Figure 3.1.2 – Numerical results with parameters: Pe $= 27$, St $= 1$, $\bar{P}_{\text{in}} = 1$, Bi $= 58$, $\theta_{\text{a}} = 0.23$, $D = 0.25$, $\Gamma = 10$, $K = 800$, and $N = 20000$, using initial conditions (3.19), $\theta(X, 0) = 0$ and $(\bar{X}, 0) = 0$. Each colour represents a distinct equispaced timestep between 0 and 3 and the shaded green region corresponds to the domain where Q is non-zero.

3.2 Exploring P_{in} variation numerically

The applied load represents the weight of the paste cylinders added to the region above $x = 0$. Since these cylinders are in reality added at discrete time intervals, but are consumed continuously by the electrode, the weight of the cylinders above $x = 0$ varies through time. Later we will add a separate equation for the evolution of $P_{\text{in}}(t)$, forced by a prescribed rate of cylinder addition. However, to gain a general understanding of the effects of unsteadiness on the solution, we first impose a known sinusoidal form for the applied load that oscillates in time with average $\bar{P}_{\text{in}}$. We take

$$P_{\text{in}}(t) = \bar{P}_{\text{in}} + \Delta \sin(\omega t), \tag{3.20}$$

where Δ ($\leq \bar{P}_{\text{in}}$) controls the amplitude of the perturbation to $\bar{P}_{\text{in}}$, and ω is the dimensionless frequency of the variations. From Table 1.3.1 we find that the natural time-scale of the problem is

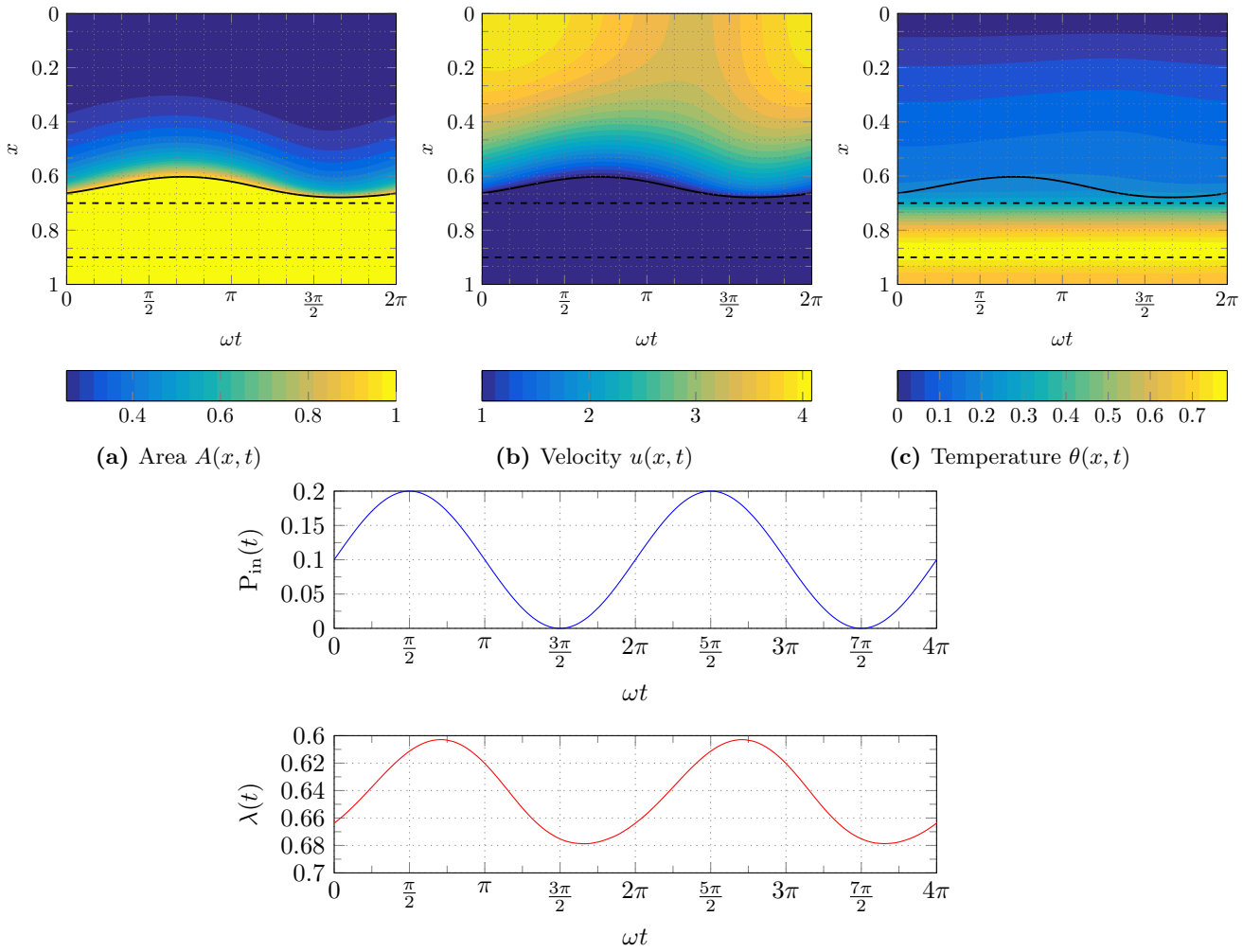

(a) Area $A(x,t)$ **(b)** Velocity $u(x,t)$ **(c)** Temperature $\theta(x,t)$

(d) Free boundary and applied load

Figure 3.2.1 – Numerical results with parameters: Pe = 27, St = 1, Bi = 58, constant air heating $\theta_a = 0.23$, $D = 0.25$, $\Gamma = 23$, $K = 300$, $\bar{P}_{in} = 0.1$, $\Delta = 0.1$, and $\omega = 2$. In (a)-(c) we superimpose λ on the contour plots in black, and we indicate the area where Q is applied by the dashed lines.

$\bar{L}/u_c \approx 1$ week, whereas the cylinders are added at least once daily (Nelson and Prins, 2004), so we expect ω to be relatively large.

After some transient behaviour, the system settles down to a time-periodic state. In Figure 3.2.1 we show the resulting variation of the area, velocity, and temperature using the sinusoidal applied load (3.20), with $\omega = 2$, $\Delta = 0.1$, and $P_{in} = 0.1$. In each contour plot we overlay the free boundary λ and the location of the heating Q. Note that there is a time delay in how pressure variations affect the solution for A and θ, but not the solution for u. Since u satisfies the quasi-steady problem (3.1b), $P_{in}(t)$ affects the velocity instantaneously, across the entire domain. As seen in Figure 3.2.1(b), the increase in P_{in} produces a velocity peak as the paste is being pushed down, causing it to reach the casing at a higher position, i.e. a smaller value of λ.

The temperature oscillations in Figure 3.2.1(c) are zero at the top as defined by the boundary

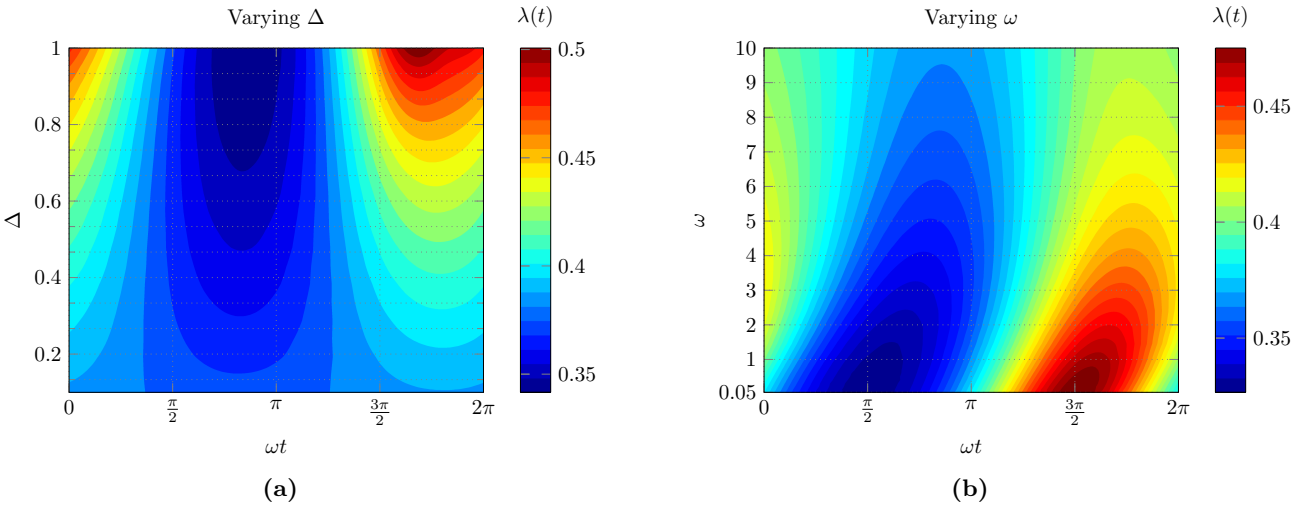

Figure 3.2.2 – Parametric sweep for (a) Δ, keeping $\omega = 1$ and $\bar{P}_{\text{in}} = 1$ and (b) ω, keeping $\Delta = 0.5$ and $\bar{P}_{\text{in}} = 1$. We have used the standard parameters $\text{Pe} = 27$, $\text{St} = 1$, $\text{Bi} = 58$, $\theta_{\text{a}} = 0.23$, $D = 0.25$, $\Gamma = 23$, and $K = 300$.

condition (3.1d), and then increase as the paste softens and flattens out further down the domain. The temperature in the induction heating region appears virtually unchanged from the case of a constant applied load.

In Figure 3.2.1(d) we show the imposed P_{in} and the corresponding λ variations, which present an offset of approximately $\pi/4$. This delay is caused by the time taken for variations in A to propagate through the domain, according to the hyperbolic equation (3.1a). In §3.4 we explore analytically the relationship between the fluctuations in the free boundary and the fluctuations in the applied load. We take these experiments a step further and explore how the solution depends on the parameters Δ and ω, i.e. the amplitude and frequency of the perturbation of $\bar{P}_{\text{in}}$. We show the variation of λ over a parameter sweep of Δ in Figure 3.2.2(a), keeping the remaining parameters fixed to the standard values indicated in the caption. Larger amplitudes of P_{in} oscillations produce larger variations in λ, as expected, while the lag between P_{in} and λ remains roughly constant. Similarly, we show the dependence of λ on ω in Figure 3.2.2(b). At very small values of ω, the problem becomes quasi-steady, with variations in P_{in} being transmitted instantaneously to λ. At large frequency, the system appears to converge to an oscillatory state with amplitude that decays with ω, and a fixed phase shift relative to the variations of P_{in}.

In the industrial problem, the applied load fluctuations are not sinusoidal or even smooth, as cylinders are added directly. To better describe the actual rate of cylinder addition, we need to refine our model to solve for the applied load instead of imposing it, and to investigate specific cylinder addition regimes that are relevant to the industrial problem. We describe this approach in the next section.

3.3 Control strategies with $P_{\text{in}}(t)$

We model the problem illustrated by the schematic in Figure 3.3.1, where we incorporate the daily addition of cylinders. In this generalised set-up, we find that it is possible for $\lambda(t)$ to exceed 1 so we extend the solution domain to $x = L > 1$.

In non-dimensional form, we relate P_{in} to the height of cylinders above $x = 0$, $h(t)$, with the ODE

$$\frac{\mathrm{d}P_{\text{in}}}{\mathrm{d}t} = \mathrm{DSt}\frac{\mathrm{d}h}{\mathrm{d}t}, \tag{3.21a}$$

where

$$\frac{\mathrm{d}h}{\mathrm{d}t} = \frac{\mathrm{d}C}{\mathrm{d}t} - u(0,t), \tag{3.21b}$$

and

$$\frac{\mathrm{d}C}{\mathrm{d}t} = h_c \sum_{j=1}^{J} n_j \delta\left(t - t_j\right), \tag{3.21c}$$

where $C(t)$ denotes the cumulative height of added cylinders and h_c is the non-dimensional height of one cylinder, typically 0.2, corresponding to 1 m (Nelson and Prins, 2004; Skjeldestad, 2019). Equation (3.21) describes an integer number n_j of cylinders being added at each discrete time t_j. Note that (3.21) requires setting an initial condition for both P_{in} and h. We set $h(0) = 0$ so that $P_{\text{in}}(0)$ accounts for any cylinders already present when the process starts at $t = 0$. In the industrial problem, the number of cylinders added each time is not necessarily the same. For example, it is common practice to add more cylinders before a weekend, when the furnace has fewer operators. We are interested in the differences between adding a constant rate of cylinders and adding them according to some pattern, which we explore by choosing n_j and t_j accordingly. We couple (3.21) with (3.1) numerically and allow the solutions to converge to a time-periodic state, under different addition regimes. We now explore some possible control strategies for the addition of cylinders.

3.3.1 Control strategy 1

We first consider control strategy 1 (CS 1), where we prescribe the number of cylinders to be added, n_j, but we do not prescribe the times of cylinder addition, t_j. These are automatically determined when P_{in} falls below a set tolerance tol_P. As a consequence, the addition frequency is an output of CS 1. As a starting point, we compute the time evolution for a constant value of cylinder addition, so that $n_j = 1$ for all j, and compare it to the case of a repeating pattern for the n_j, whose average value is 1. In particular, Elkem ASA are interested in patterns that would allow skipping addition days, for example public holidays, as this is a common occurrence in some production plants. A daily addition normally consists of 1, 2 or 3 cylinders of 1 m length. Therefore, we have used the repeating pattern $\{1, 1, 1, 1, 3\}$ to represent addition during a typical week. The results for CS 1 are shown in Figure 3.3.2, where the first addition times, t_1^{c} for the "constant" case and t_1^{p} for the "pattern" case, are the same.

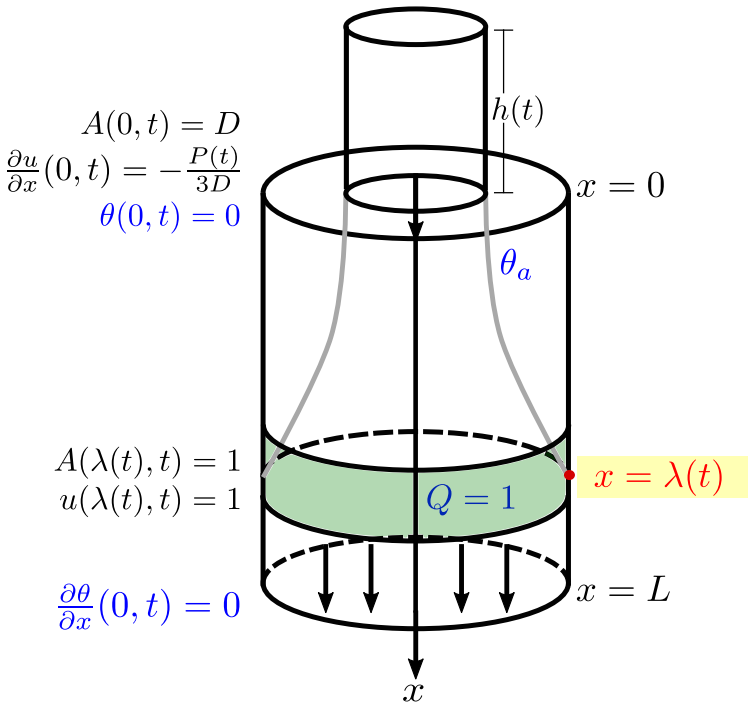

Figure 3.3.1 – Schematic of the time dependent model (3.21). The height of the column of cylinders above our solution domain is denoted by $h(t)$.

For the "constant" case, the system settles down to a periodic solution with constant $t^{\text{c}}_{j+1} - t^{\text{c}}_j = \Delta t^{\text{c}} = Dh_c \approx 0.05$, by net mass conservation. Each time a cylinder is added, it causes a jump in P_{in}, which then tapers off as the cylinder is gradually consumed. This in turn produces a slope discontinuity in λ, which suddenly starts to decrease (corresponding to the paste reaching the casing sooner). For the "pattern" case, mass conservation still holds over the whole cycle so we must have $t^{\text{p}}_{j+5} - t^{\text{p}}_j = 7\Delta t^{\text{c}}$, but individual time intervals can vary. When 3 cylinders are added together, the additional height causes them to descend more quickly, so $t^{\text{p}}_6 - t^{\text{p}}_5 < 3\Delta t^{\text{c}}$. It follows that the other time intervals must be slightly larger than Δt^{c}. The large peak in P_{in} when 3 cylinders are added leads to a noticeably larger average loading $\bar{P}_{\text{in}}$, which causes a decrease in the average value of λ. In either case, the amplitude of the oscillations in λ is rather small, due to the relatively small variations in P_{in} and high frequency of P_{in}, as noted in Figure 3.3.2(b).

In Figure 3.3.3 we show the effects of the two different cylinder addition regimes on the area, velocity, and temperature evolution. For reference, we overlay the resulting graph of $\lambda(t)$ onto each plot, as well as dashed lines to indicate where the heating Q is applied. In either case, the high frequency and low amplitude in the applied load P_{in} produced by the control strategy result in small variations in A and θ, which both remain quite close to their time-averaged values. There are large variations in the velocity u, which reacts instantaneously to the applied load through equation (3.1b). The largest velocities occur each time 3 cylinders are added, as seen in the bright yellow region in Figure 3.3.3(e). We have truncated the colourbar maximum for u to observe more contour levels in Figure 3.3.3(e); the actual maximum value of u is ≈ 11.1.

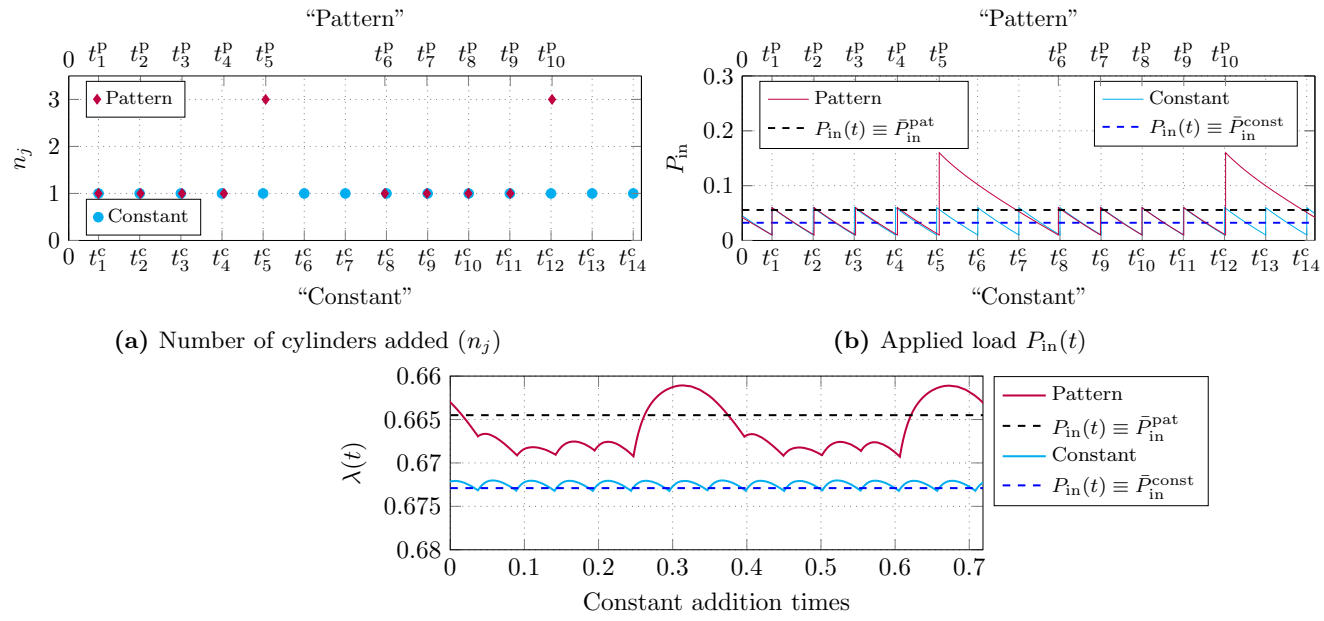

(a) Number of cylinders added (n_j)

(b) Applied load $P_{\text{in}}(t)$

(c) Free boundary $\lambda(t)$

Figure 3.3.2 – Oscillatory states produced by CS 1 in the two experiment cases: "pattern" and "constant". The first addition time t_1 is the same for both cases and the dashed lines indicate the results with no time variation in P_{in}, using the average value for the pattern and constant cases, respectively. Addition occurs when $P_{\text{in}} < \text{tol}_{\text{P}} = 0.01$. We have used the standard parameters Pe $= 27$, St $= 1$, Bi $= 58$, $\theta_{\text{a}} = 0.23$, $D = 0.25$, $\Gamma = 23$, and $K = 300$.

As with the sinusoidal case shown in Figure 3.2.1(c), the temperature in the induction heating zone delimited by the dashed lines is not much affected by varying the addition rate, but the fluctuations seen above this region reflect that the initial softening of the paste is sensitive to P_{in} variations. Although these are small effects, these observations suggest that under extreme conditions where the cylinder addition is rapidly increased, for example to compensate for no addition on weekends, hot paste may be present further up the casing, which may lead to increased segregation and a low quality in the baked electrode.

Finally, we note that the values of Δt given by CS 1 are smaller than a non-dimensional day $d \approx 0.1728$, suggesting a faster addition rate than is seen in the industrial setting for this cylinder size. This is partly due to the chosen pressure tolerance tol_{P}, whose purpose is to ensure that we never run out of cylinders. However CS 1 does not take into account that in practice the height $h(t)$ is kept above some non-zero constant level, illustrated in Figure 3.3.1. This industrial feature is included in the next control strategy, CS 2.

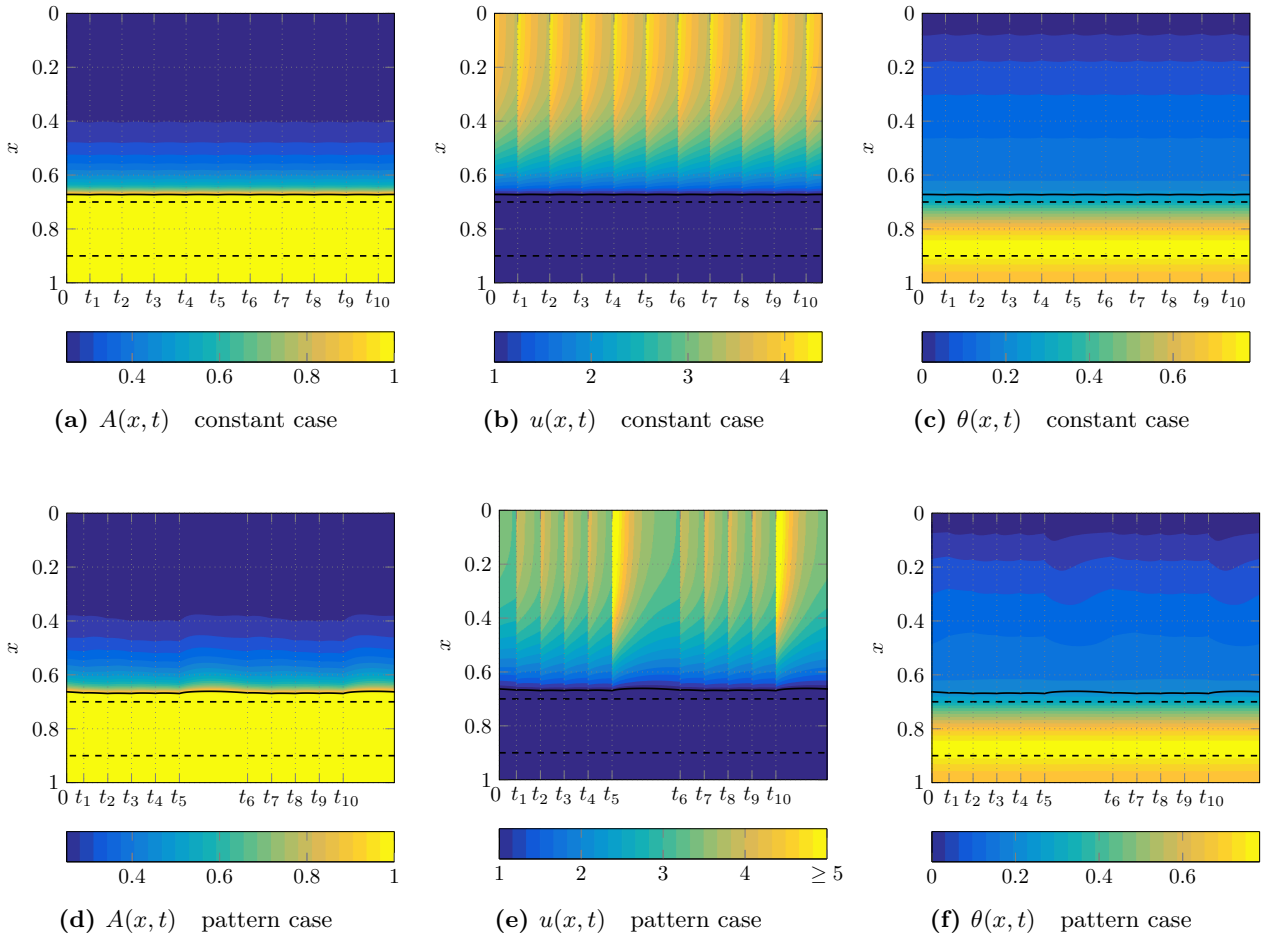

(a) $A(x,t)$ constant case **(b)** $u(x,t)$ constant case **(c)** $\theta(x,t)$ constant case

(d) $A(x,t)$ pattern case **(e)** $u(x,t)$ pattern case **(f)** $\theta(x,t)$ pattern case

Figure 3.3.3 – We show the evolution of the area profile $A(x,t)$, the velocity $u(x,t)$, and the temperature $\theta(x,t)$ for the "constant" case (top) and the "pattern" case (bottom). The position of the free boundary λ is plotted in black. We have used standard parameters: $\text{Pe} = 27$, $\text{St} = 1$, $\text{Bi} = 58$, $\theta_{\text{a}} = 0.23$, $D = 0.25$, $\Gamma = 23$, and $K = 300$.

3.3.2 Control strategies 2a and 2b

An alternative control strategy which is closer to Elkem ASA's actual practice, is to fix the timesteps t_j to correspond to non-dimensional days, but allow the numerical scheme to choose the cylinder addition n_j according to some specific constraints. In contrast with CS 1, we will now set a level $P_{\text{target}} = kd + \text{tol}_{\text{P}}$, which corresponds to the minimum level that we need P_{in} to be at each t_j such that we expect P_{in} never to fall below tol_{P} during the following time interval until the next addition. Here, $d = 0.1728$ is one non-dimensional day, and k is the number of days until the next addition (so every fifth t_j we take $k = 3$ in order to skip two days at the weekend). Under CS 2a we allow n_j to take whatever value is needed to make $P_{\text{in}} = P_{\text{target}}$ at time t_j. CS 2b is the more realistic case where we can only add integer numbers of cylinders, and we constrain n_j to be the smallest integer that makes $P_{\text{in}} \geq P_{\text{target}}$.

The differences between using CS 2a and CS 2b are small but noticeable when considering the predictions for P_{in} and the free boundary λ, shown in Figure 3.3.4. As before, we compare each

fluctuation case with its equivalent average $\bar{P}_{\text{in}}$ result for reference, and we also show the results of applying CS 1 with a larger load, corresponding to the pattern $n_j = \{3, 3, 3, 3, 10\}$. To reach a time-periodic solution, we require

$$\frac{Dh_c \sum_{j=1}^{5} n_j}{7\Delta t} = 1, \tag{3.22}$$

for net mass conservation. However, it is impossible to satisfy (3.22) when using CS 2b as it requires both Δt and n_j to be constrained. Thus, we expect that CS 1 and CS 2a result (eventually) in time-periodic solutions, whereas CS 2b does not. Ultimately, this suggests that the addition strategy used currently, which is closest to CS 2b where cylinders are added at a specific time in the day, requires a variation in n_j as it will not reach a time-periodic solution. In reality, the addition strategy is also affected by the electrode consumption which depends on daily production needs. The resulting number of cylinders n_j for CS 2a and 2b are shown in Figure 3.3.5(a), where we note a higher number of cylinders required for daily addition than the one used during normal operations. This is attributed to the many simplifying assumptions we have made to make the model tractable, but these results are illustrative about the kind of behaviour that can happen during cylinder addition. Since we are now adding a larger load each day, the variations in $P_{\text{in}}(t)$ have higher amplitude and lower frequency, and the free boundary fluctuations are therefore larger than the ones shown for CS 1 in the previous section. Another consequence of the increase in P_{in} is the existence of a local minimum as λ moves upwards with the addition of cylinders (around day 6 in Figure 3.3.4), which was absent for the addition considered in §3.3.1. In this example case we are considering a larger number of cylinders, and when a large number of cylinders are added on day 5, the velocity increases, drawing colder paste down from the top more rapidly, and causing λ to decrease (move upwards), which produces the initial change in λ. Because this paste is colder, however, it does not spread as easily, which causes λ to temporarily increase again, leading to the local minimum observed in Figure 3.3.4. The free boundary moves upward again as the heating acts on the colder paste. For the isothermal problem, there is no local minimum in λ, even for large cylinder additions.

In these examples we have used $h_c = 0.2$, corresponding to 1 m, which is the standard length of a paste cylinder. However, most plants incorporate briquette addition in between addition days, while some even use half cylinders as a standard, as described in Skjeldestad (2019). Although we do not incorporate the specific effects of using briquettes instead of cylinders, such as the final air/paste distribution as the briquettes soften into the casing (Fitt and Howell, 1998), we can effectively treat such alternative procedures by modifying h_c. As we vary the cylinder height, we notice that a precisely time-periodic state still cannot be reached, as seen for the half cylinders distribution in Figure 3.3.5(b).

The area, velocity, and temperature fluctuations for CS 2b with $h_c = 0.2$ are shown in Figure 3.3.6. Again, the time-dependence of the pressure exerted by the added cylinders has the most immediate

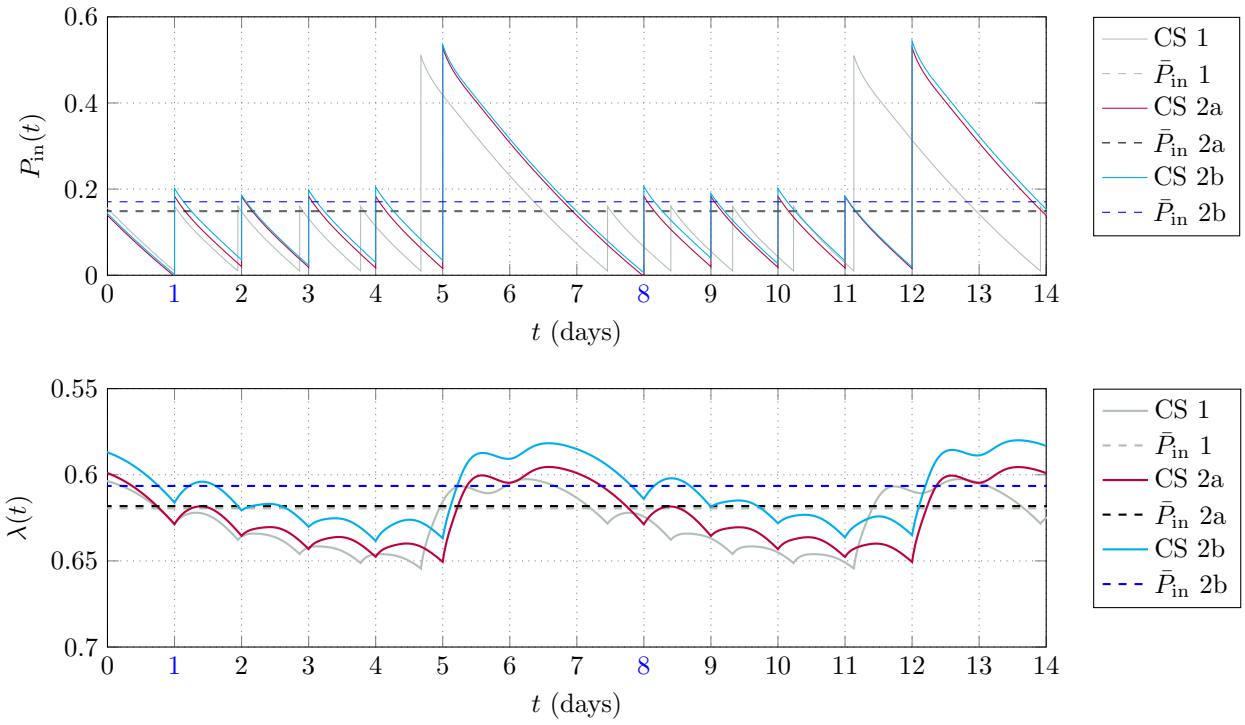

Figure 3.3.4 – Applied load $P_{\text{in}}(t)$ and free boundary position $\lambda(t)$ under control strategy CS 2. We use standard parameters: Pe $= 27$, St $= 1$, Bi $= 58$, $\theta_{\text{a}} = 0.23$, $D = 0.25$, $\Gamma = 23$, and $K = 300$. The days in blue mark the beginning of a new cycle. The dashed lines show the corresponding numerical results for $P_{\text{in}} = \bar{P}_{\text{in}}$, where this constant value is the average of each loading regime. The grey line shows the comparison with CS 1, where we have chosen an addition pattern $n = \{3, 3, 3, 3, 10\}$.

and dramatic effect on the velocity u. We have truncated the colourbar maximum for u to observe more contour levels in Figure 3.3.6(b); the actual maximum value of u is ≈ 11.68. In contrast, the profiles of A and θ indicate that the paste only begins to soften and deform significantly at around $x \approx 0.3$. There are relatively small but noticeable fluctuations in A and θ within each day and not only at the addition times. Furthermore, in Figure 3.3.6(c), the large additions every 5th day cause cold paste to be pushed downwards. As in the previous example with CS 1, when the induction heating region is reached, the fluctuations have flattened out and the heating profile is essentially unchanged from the constant P_{in} case (see Figure 3.1.2(c)).

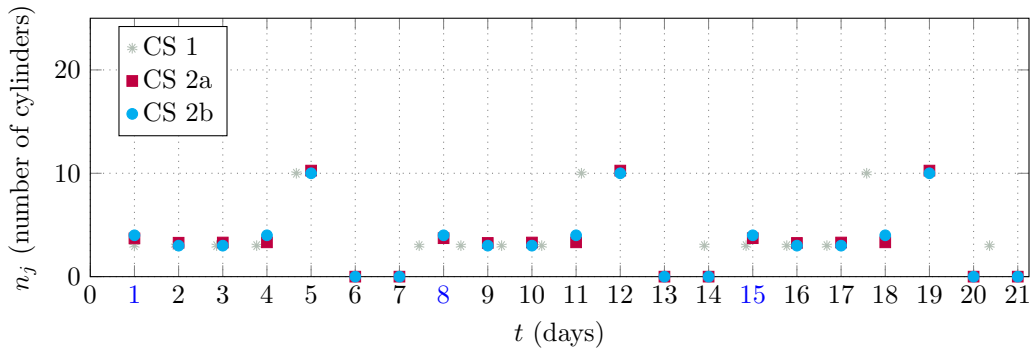

(a) Comparing non-integer and integer cylinder addition, where the height of a typical cylinder is 1 m.

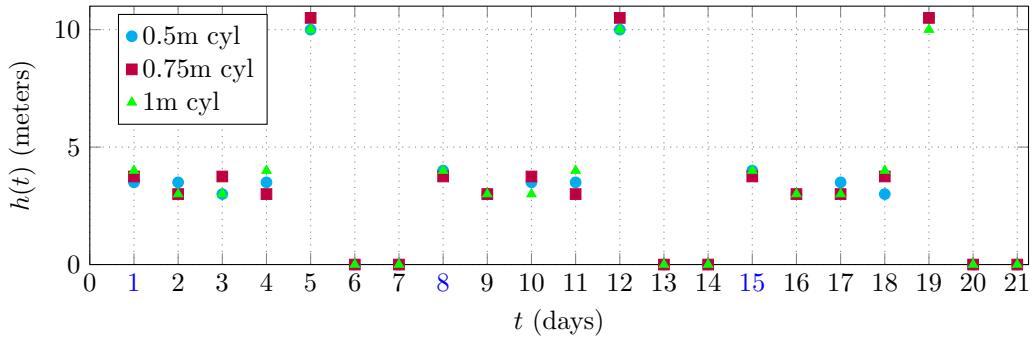

(b) Control strategy 2b applied using cylinders of different heights.

Figure 3.3.5 – Cylinder addition implemented with CS 2, i.e, at equally spaced time intervals which correspond to days. We use standard parameters: Pe = 27, St = 1, Bi = 58, $\theta_a = 0.23$, $D = 0.25$, $\Gamma = 23$, and $K = 300$.

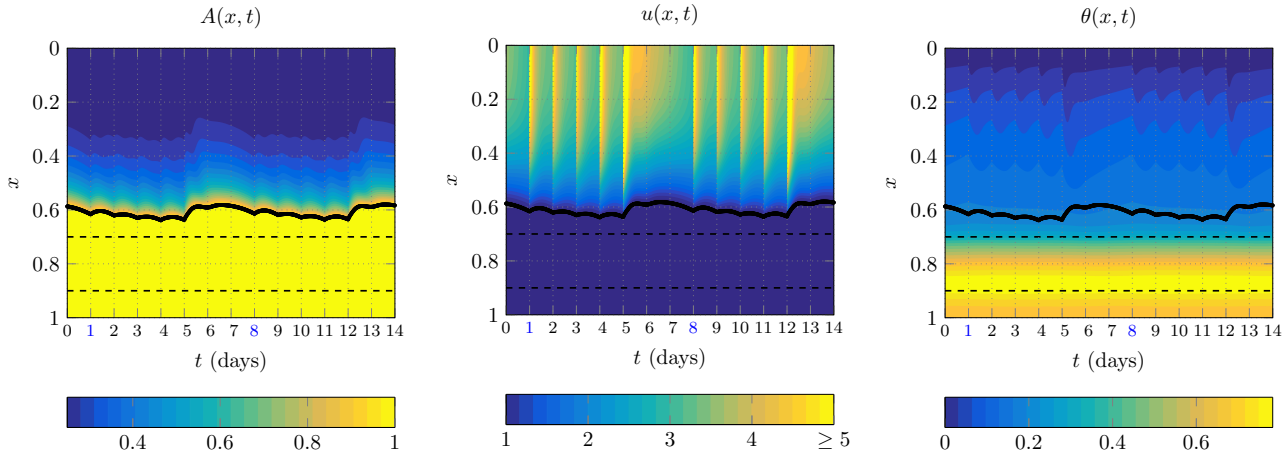

Figure 3.3.6 – Evolution of area, velocity, and temperature under control strategy CS 2b, i.e. integer cylinder addition at equally spaced time intervals which correspond to days. We use standard parameters: Pe = 27, St = 1, Bi = 58, $\theta_a = 0.23$, $D = 0.25$, $\Gamma = 23$, and $K = 300$.

3.3.3 Varying slipping velocity

Another important control mechanism for the Søderberg electrode is the *slipping rate* u_{c}, i.e. the rate at which the casing descends into the furnace, which is automatically adjusted based on assumed and calculated electrode consumption during operator shifts. In practice, slippage occurs through a series of relatively rapid 'drops', in between which the electrode is held still. We take u_{c} to be the average over such a slipping regime, which is $\mathcal{O}(10^{-5})$ m s^{-1}, and scale the governing equations accordingly. An alternative for this scaling is to use the velocity of the faster 'drops', which is $\mathcal{O}(10^{-3})$ m s^{-1} (Van Gorder et al., 2021), and may lead to some inertial effects as it increases the size of the Reynolds number.

We take advantage of our numerical solution to experiment with a changing slipping rate. The only change in the problem formulation (3.1) is the generalisation of boundary condition (3.1e) to

$$A = 1, \quad u = u_L(t) \quad \text{at} \quad x = \lambda(t). \tag{3.23}$$

By our choice of non-dimensionalisation, the dimensionless slipping velocity $u_L(t)$ must have time-average equal to 1. As an example we use a slipping rate equivalent to dropping the casing for 15 minutes every 6 hours, which in non-dimensional form is given by

$$u_L(t) = \begin{cases} 24 & \text{for} \quad \lfloor \frac{24t}{t_q} \rfloor = 0 \pmod{24} \\ 0 & \text{otherwise} \end{cases}, \tag{3.24}$$

where $t_q \approx 0.0432$ corresponds to 6 hours in dimensionless variables. We apply the cylinder addition strategy CS 2b, but replacing the downstream boundary condition with (3.24). The results, shown in Figure 3.3.7, qualitatively resemble the ones for $u_L = 1$, in Figure 3.3.6. The largest difference is perhaps appreciated in Figure 3.3.7(b), where the fast slips can be seen in the bright yellow acceleration lines which propagate instantaneously through the flow domain. As before, we have truncated the colourbar maximum for u to observe more contour levels in Figure 3.3.7(b); the actual maximum value of u is $\approx$ 33.78. However, the rapidly changing velocity does not significantly influence the temperature distribution in $x > \lambda(t)$. It is clear from this experiment that, since the slipping velocity changes on such a rapid timescale when compared to the flow, using an average velocity gives a good approximation for the flow properties of interest.

We compare this example directly to the $u_L = 1$ case in Figure 3.3.8, where we see that the u_L fluctuations produce only a small disturbance in the applied load P_{in}. The effects of variable slipping velocity are more noticeable in λ, where the free boundary exhibits fluctuations in phase with u_L, with constant amplitude. The local average over the oscillations in λ resembles the behaviour obtained when $u_L = 1$, so it is reasonable to expect that, for more realistic and more extreme slipping regimes, such as a 2-4 cm slip over 5 seconds every 45 minutes, the u_L fluctuations will still not affect greatly the qualitative behaviour of our variables of interest. However, we note that the

rapid timescale variations change the value of λ when imposing the average $\bar{P}_{\text{in}}$, as seen in the grey and blue dotted lines in the bottom panel of Figure 3.3.8. This problem is highly sensitive to P_{in} variations, as seen in Chapter 2, so the small change in $\bar{P}_{\text{in}}$ caused by imposing $u_L(t)$ predicts a λ at a lower position in the casing than when $u_L = 1$.

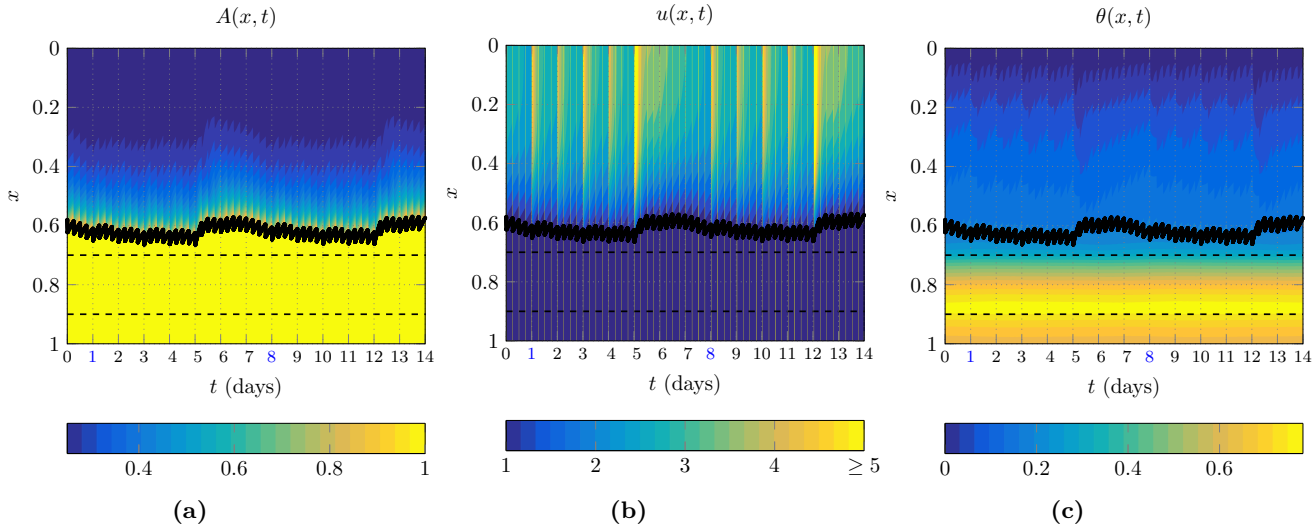

Figure 3.3.7 – Evolution of area, velocity and temperature using the slipping velocity (3.24) with patterned integer cylinder addition (CS 2b). We use standard parameters: Pe = 27, St = 1, Bi = 58, $\theta_{\text{a}} = 0.23$, $D = 0.25$, $\Gamma = 23$, and $K = 300$.

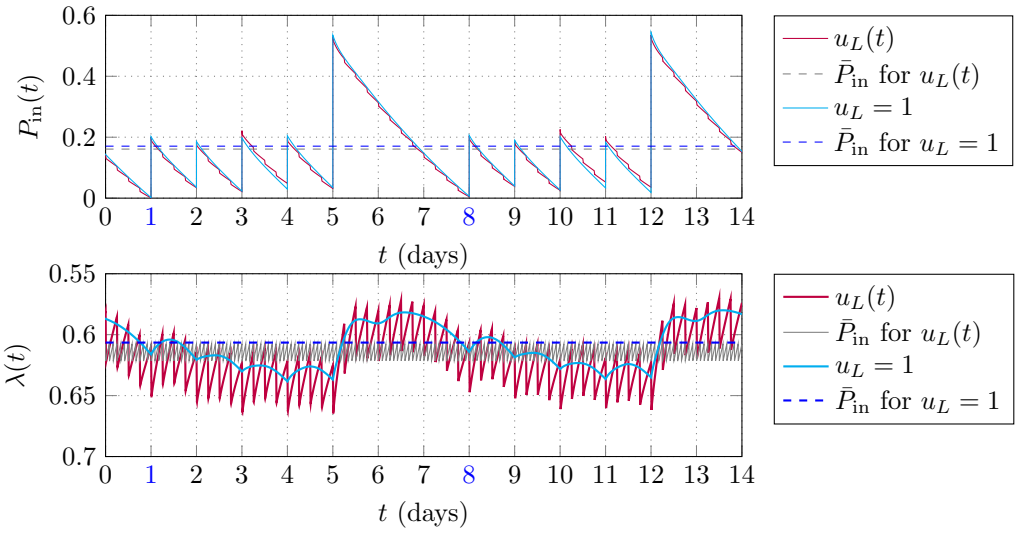

Figure 3.3.8 – Applied load P_{in} and free boundary position λ versus time t using CS 2b with slipping velocity $u_L \equiv 1$ and $u_L \equiv u_L(t)$ given by (3.24). We use standard parameters: Pe = 27, St = 1, Bi = 58, $\theta_{\text{a}} = 0.23$, $D = 0.25$, $\Gamma = 23$, and $K = 300$.

3.4 Exploring P_{in} variation analytically

The applied load P_{in} varies on a faster timescale than the characteristic time-scale of the flow which is reflected in the largeness of the dimensionless frequency ω. Figure 3.2.2(b) suggests that for large

ω we reach a time-periodic oscillatory state, whereas for small ω we reach a quasi-steady state. In this section, we investigate the asymptotic limit $\omega \to \infty$ analytically and compare it to our obtained numerical solutions. Our aim is to find how the oscillations in λ are related to the oscillations in P_{in} when ω is large.

3.4.1 Analysing fast oscillations

Let $\tau = \omega t$ where $\omega \gg 1$ is the dimensionless frequency of the P_{in} oscillations. Then, substituting into (3.1), we get

$$\omega A_\tau + (Au)_x = 0, \tag{3.25a}$$

$$(3\mu(\theta)Au_x)_x + \mathrm{St}A = 0, \tag{3.25b}$$

$$A\left(\omega\theta_\tau + u\theta_x\right) = \frac{1}{\mathrm{Pe}}\left(A\theta_x\right)_x - 2\frac{\mathrm{Bi}}{\mathrm{Pe}}\sqrt{A}\left(\theta - \theta_{\mathrm{a}}(x)\right) + Q(x)A, \tag{3.25c}$$

subject to

$$A = D, \quad u_x = -\frac{P_{\text{in}}(\tau)}{3D}, \quad \theta = 0 \qquad \text{at} \quad x = 0, \tag{3.25d}$$

$$A = u = 1 \qquad \text{at} \quad x = \lambda(\tau), \tag{3.25e}$$

$$\theta_x = 0 \qquad \text{at} \quad x = 1, \tag{3.25f}$$

and in fact $A = u = 1$ for $x > \lambda(\tau)$. We seek solutions in which all time-dependent variables are 2π- periodic functions of τ.

We assume the expansions

$$A \sim A^{(0)}(x,\tau) + \frac{1}{\omega}A^{(1)}(x,\tau) + \ldots, \tag{3.26a}$$

and similarly for u and θ together with

$$\lambda \sim \lambda^{(0)}(\tau) + \frac{1}{\omega}\lambda^{(1)}(\tau) + \ldots. \tag{3.26b}$$

We substitute the expansions (3.26) into (3.25a) to get to leading order

$$A^{(0)} \equiv A^{(0)}(x), \qquad \theta^{(0)} \equiv \theta^{(0)}(x). \tag{3.27}$$

Expanding (3.25a) to $\mathcal{O}\left(1/\omega\right)$, we find

$$A^{(1)}_\tau + \left(A^{(0)}u^{(0)}\right)_x = 0, \tag{3.28}$$

and since $A^{(1)}$ is required to be 2π-periodic with respect to τ, $\int_0^{2\pi} A^{(1)}_\tau \mathrm{d}\tau = 0$ so we can time-average to find

$$\left(A^{(0)}\bar{u}^{(0)}\right)_x = 0, \tag{3.29}$$

where, here and henceforth, the overbar denotes the time average, i.e.

$$\bar{u}^{(0)}(x) = \frac{1}{2\pi}\int_0^{2\pi} u^{(0)}(x,\tau)\mathrm{d}\tau. \tag{3.30}$$

We Taylor expand the boundary condition (3.1e) and find that,

$$A^{(0)}(0) = D, \quad A^{(0)}(\lambda^{(0)}) = 1, \tag{3.31}$$

which implies that $\lambda^{(0)}$ is a constant and $A^{(0)}\bar{u}^{(0)} \equiv 1$.

We evaluate (3.25c) to $\mathcal{O}(1/\omega)$ as

$$A^{(0)}\theta_\tau^{(1)} + A^{(0)}u^{(0)}\theta_x^{(0)} = \frac{1}{\mathrm{Pe}}\left(A^{(0)}\theta_x^{(0)}\right)_x - \frac{2\mathrm{Bi}}{\mathrm{Pe}}\sqrt{A^{(0)}}\left(\theta^{(0)} - \theta_\mathrm{a}\right) + QA^{(0)}. \tag{3.32}$$

Then, using (3.27) and assuming 2π-periodicity of $\theta^{(1)}$ with respect to τ, averaging (3.32) gives

$$\theta_x^{(0)} = \frac{1}{\mathrm{Pe}}\left(A^{(0)}\theta_x^{(0)}\right)_x - \frac{2\mathrm{Bi}}{\mathrm{Pe}}\sqrt{A^{(0)}}\left(\theta^{(0)} - \theta_\mathrm{a}\right) + QA^{(0)}. \tag{3.33}$$

Finally, the leading order problem for (3.25b) is given by

$$\left(3\mu(\theta^{(0)})A^{(0)}u_x^{(0)}\right)_x + \mathrm{St}A^{(0)} = 0, \tag{3.34a}$$

subject to

$$u_x^{(0)} = -\frac{P_\mathrm{in}(\tau)}{3D} \qquad \text{at} \quad x = 0, \tag{3.34b}$$

$$u^{(0)} = 1 \qquad \text{at} \quad x = \lambda^{(0)}, \tag{3.34c}$$

assuming $\mu(0) = 1$. Integrating (3.34) with respect to τ from 0 to 2π gives

$$\left(3\mu(\theta^{(0)})A^{(0)}\bar{u}_x^{(0)}\right)_x + \mathrm{St}A^{(0)} = 0, \tag{3.35a}$$

subject to

$$\bar{u}_x^{(0)} = -\frac{\bar{P}_\mathrm{in}}{3D} \qquad \text{at} \quad x = 0, \tag{3.35b}$$

$$\bar{u}^{(0)} = 1 \qquad \text{at} \quad x = \lambda^{(0)}. \tag{3.35c}$$

The average leading-order values $A^{(0)}$, $\bar{u}^{(0)}$, $\theta^{(0)}$, and $\lambda^{(0)}$ therefore satisfy the standard steady-state equations solved numerically in Chapter 2, with constant applied load given by the average of P_in.

We denote the fluctuations in P_{in} and $u^{(0)}$ as

$$\tilde{u}^{(0)}(x,\tau) = u^{(0)}(x,\tau) - \bar{u}^{(0)}(x), \quad \tilde{P}_{\text{in}}(\tau) = P_{\text{in}}(\tau) - \bar{P}_{\text{in}}, \tag{3.36}$$

so that the time-average of the fluctuations is zero. Then, combining (3.34) and (3.35) and integrating, we find that

$$\tilde{u}^{(0)}(x,\tau) = \frac{\tilde{P}_{\text{in}}(\tau)}{3} \int_x^{\lambda^{(0)}} \frac{\mathrm{d}s}{\mu(\theta^{(0)}(s))A^{(0)}(s)}. \tag{3.37}$$

We move on to determine the fluctuations in A, θ, and λ. We rewrite (3.28) in terms of the fluctuations and use (3.37) to find

$$A^{(1)}_{\tau} = -\frac{\tilde{P}_{\text{in}}(\tau)}{3} \frac{\mathrm{d}}{\mathrm{d}x} \left(A^{(0)} \int_x^{\lambda^{(0)}} \frac{\mathrm{d}s}{\mu(\theta^{(0)}(s))A^{(0)}(s)} \right), \tag{3.38}$$

and integrating with respect to τ gives

$$A^{(1)}(x,\tau) = \bar{A}^{(1)}(x) - \frac{1}{3} \frac{\mathrm{d}}{\mathrm{d}x} \left(A^{(0)}(x) \int_x^{\lambda^{(0)}} \frac{\mathrm{d}s}{\mu(\theta^{(0)}(s))A^{(0)}(s)} \right) \varphi(\tau), \tag{3.39}$$

where $\bar{A}^{(1)}$ denotes the time average of $A^{(1)}$ and

$$\varphi(\tau) = \int_0^{\tau} \tilde{P}_{\text{in}}(s)\mathrm{d}s + \frac{1}{2\pi} \int_0^{2\pi} \tau \tilde{P}_{\text{in}}(\tau)\mathrm{d}\tau. \tag{3.40}$$

The second term in this definition of φ is chosen such that $\bar{\varphi} = 0$. For the specific case $P_{\text{in}}(\tau) = \bar{P}_{\text{in}} + \Delta \sin\tau$, equation (3.40) simply gives $\varphi(\tau) = -\Delta\cos\tau$.

Similarly, using (3.33) in (3.32) and the definition (3.36), we find

$$A^{(0)}\theta^{(1)}_{\tau} = -A^{(0)}\tilde{u}^{(0)}\theta^{(0)}_x. \tag{3.41}$$

As we did for $A^{(1)}$, we integrate (3.41) with respect to τ, substitute with (3.37), and find

$$\theta^{(1)}(x,\tau) = \bar{\theta}^{(1)}(x) - \frac{\theta^{(0)}_x(x)}{3} \left(\int_x^{\lambda^{(0)}} \frac{\mathrm{d}s}{\mu(\theta^{(0)}(s))A^{(0)}(s)} \right) \varphi(\tau). \tag{3.42}$$

Hence, the fluctuations in $A^{(1)}$ and $\theta^{(1)}$ are determined in terms of the leading order solution and the known function $\varphi(\tau)$. To determine the corrections to the average values $\bar{A}^{(1)}$ and $\bar{\theta}^{(1)}$, we need to go to higher order, as shown below.

We also find a first approximation of the fluctuations in λ, using a Taylor expansion of the the

boundary condition (3.25e), to get

$$\bar{\lambda}^{(1)} + \tilde{\lambda}^{(1)}(\tau) = -\frac{A^{(1)}}{A_x^{(0)}}\Big|_{x=\lambda^{(0)}}. \tag{3.43}$$

We evaluate (3.39) at $x = \lambda^{(0)}$ and insert it into (3.43) to obtain an expression for the fluctuations of $\lambda^{(1)}$, namely

$$\tilde{\lambda}^{(1)} = \frac{-\varphi(\tau)}{3A_x^{(0)}(\lambda^{(0)})\mu(\theta^{(0)}(\lambda^{(0)}))}. \tag{3.44}$$

Thus, (3.39), (3.42), and (3.44) describe the lowest order fluctuations in $A^{(1)}$, $\theta^{(1)}$, and $\lambda^{(1)}$.

We can find the corrections to the average values $\bar{A}^{(1)}$, $\bar{u}^{(1)}$, $\bar{\theta}^{(1)}$, and $\bar{\lambda}^{(1)}$ by looking at the next order expansions of (3.25) and assuming 2π periodicity of higher order terms. For (3.25a), this is

$$A_\tau^{(2)} = \left(A^{(1)}u^{(0)} + A^{(0)}u^{(1)}\right), \tag{3.45}$$

which we integrate with respect to τ and get

$$\left[\overline{\left(A^{(1)}u^{(0)}\right)} + A^{(0)}\bar{u}^{(1)}\right]_x = 0. \tag{3.46}$$

Note that $\overline{\tilde{P}_{\text{in}}\varphi} = 0$ so, when we substitute (3.37) and (3.39) into (3.46), we get

$$\left(\bar{u}^{(0)}\bar{A}^{(1)} + A^{(0)}\bar{u}^{(1)}\right)_x = 0. \tag{3.47}$$

Then, the momentum equation (3.25b) is, to $\mathcal{O}(1/\omega)$,

$$3\left(\mu_x(\theta^{(0)})\theta^{(1)}A^{(0)}u_x^{(0)} + \mu(\theta^{(0)})A^{(1)}u_x^{(0)} + \mu(\theta^{(0)})A^{(0)}u_x^{(1)}\right)_x + \mathrm{St}A^{(1)} = 0. \tag{3.48}$$

We average (3.48) with respect to τ and, using the same simplifications as for (3.47), we obtain

$$3\left(\mu_x(\theta^{(0)})\bar{\theta}^{(1)}A^{(0)}\bar{u}_x^{(0)} + \mu(\theta^{(0)})\bar{A}^{(1)}\bar{u}_x^{(0)} + \mu(\theta^{(0)})A^{(0)}\bar{u}_x^{(1)}\right)_x + \mathrm{St}\bar{A}^{(1)} = 0. \tag{3.49}$$

Finally, we perform the same calculation for the energy equation (3.25c), which to $\mathcal{O}(1/\omega)$ is

$$\begin{aligned} A^{(1)}\theta_\tau^{(1)} + A^{(0)}\theta_\tau^{(2)} + A^{(1)}u^{(0)}\theta_x^{(0)} + A^{(0)}u^{(1)}\theta_x^{(0)} + A^{(0)}u^{(0)}\theta_x^{(1)} &= \frac{1}{\mathrm{Pe}}\left(A^{(1)}\theta_x^{(0)} + A^{(0)}\theta_x^{(1)}\right)_x \\ &\quad - \frac{2\mathrm{Bi}}{\mathrm{Pe}}\left[\frac{\left(\theta^{(0)} - \theta_{\mathrm{a}}\right)}{2\sqrt{A^{(0)}}}A^{(1)} + \sqrt{A^{(0)}}\theta^{(1)}\right] + QA^{(1)}. \end{aligned} \tag{3.50}$$

As before, we integrate with respect to τ and exploit 2π periodicity to find

$$\bar{A}^{(1)}\bar{u}^{(0)}\theta_x^{(0)} + A^{(0)}\bar{u}^{(1)}\theta_x^{(0)} + \bar{\theta}_x^{(1)} = \frac{1}{\text{Pe}}\left(\bar{A}^{(1)}\theta_x^{(0)} + A^{(0)}\bar{\theta}_x^{(1)}\right)_x - \frac{2\text{Bi}}{\text{Pe}}\left[\frac{\left(\theta^{(0)} - \theta_{\text{a}}\right)}{2\sqrt{A^{(0)}}}\bar{A}^{(1)} + \sqrt{A^{(0)}}\bar{\theta}^{(1)}\right] + Q\bar{A}^{(1)}. \quad (3.51)$$

In principle, (3.47), (3.49), and (3.51), together with boundary conditions

$$\bar{A}^{(1)} = 0, \quad \bar{u}_x^{(1)} = 0, \quad \bar{\theta}^{(1)} = 0 \qquad \text{at} \quad x = 0, \quad (3.52a)$$

$$\bar{\theta}_x^{(1)} = 0 \qquad \text{at} \quad x = 1, \quad (3.52b)$$

and (3.44), fully determine the first order corrections for the averages. In fact, they form a linear system of ODEs that is the homogeneous version of the system of ODEs solved by the steady states $A^{(0)}$, $\bar{u}^{(0)}$, and $\theta^{(0)}$. Writing the solution of $\bar{A}^{(1)}$, $\bar{\theta}^{(1)}$ and $\bar{u}^{(1)}$ as a linear combination of the steady states, and then using the boundary conditions (3.52), we find that $\bar{A}^{(1)} \equiv \bar{\theta}^{(1)} \equiv \bar{u}^{(1)} \equiv 0$.

To perform the numerical simulations, given that our approximations for A and u depend on the derivatives of the leading-order solution (so it is desirable to have smooth solutions), we set Q to be the Gaussian

$$Q(x) = \tilde{Q}_I \exp\left(-\frac{\left(x - \frac{x_1+x_2}{2}\right)^2}{2(x_2 - x_1)^2}\right), \quad (3.53)$$

with $\tilde{Q}_I$ chosen such that $\int_0^1 Q(x)\mathrm{d}x = 1$, with $x_1 = 0.7$, $x_2 = 0.9$.

We compare the predicted fluctuations with numerical results in Figure 3.4.1, where we have used $P_{\text{in}} = \bar{P}_{\text{in}} + \Delta\sin(\tau)$ with $\omega = 100$, $\Delta = 0.8$, $\theta_a = 0.23$, and $\text{Bi} = \text{Pe} = \text{St} = \bar{P}_{\text{in}} = \Gamma = 1$, for which we expect good agreement. We have subtracted the averages $\bar{A}$, $\bar{u}$, and $\bar{\theta}$ from the numerical solution to compare it with the asymptotic prediction. For A, u, and θ, the magnitude of the predicted oscillations approximates well the one obtained numerically. Particularly, in the case of the velocity, these two solutions are practically indistinguishable from each other, as seen in Figures 3.4.1(b) and 3.4.1(e). The area is approximated well near $x = \lambda^{(0)}$, but has a different behaviour near $x = 0$, where the numerical solution shows oscillations propagated downwards through the paste, as seen in Figure 3.4.1(d). This observation suggests that the oscillations in P_{in} create wave-like disturbances in A that propagate both in space and in time, and this motivates a multiple scales approach that we describe in §3.5. It is associated with the fact that the equation for $A^{(1)}$, (3.28), does not contain any spatial derivatives of $A^{(1)}$, and our solution for $A^{(1)}$ therefore does not (necessarily) satisfy the required boundary condition $A^{(1)}(0) = 0$. In contrast, the full equation for A, (3.25a), is hyperbolic, and can indeed be expected to propagate waves through the domain.

Finally, comparing the temperature solutions, we see from Figures 3.4.1(c) and 3.4.1(f) that the

asymptotic prediction recovers the resulting numerical behaviour, apart from a thin region near $x = 0$, where we have a diffusive boundary layer. Again, this is because the equation for $\theta^{(1)}$, (3.41), does not contain spatial derivatives of $\theta^{(1)}$ and is not able to satisfy the boundary condition $\theta^{(1)} = 0$ at $x = 0$. We explore this boundary layer behaviour for the temperature next.

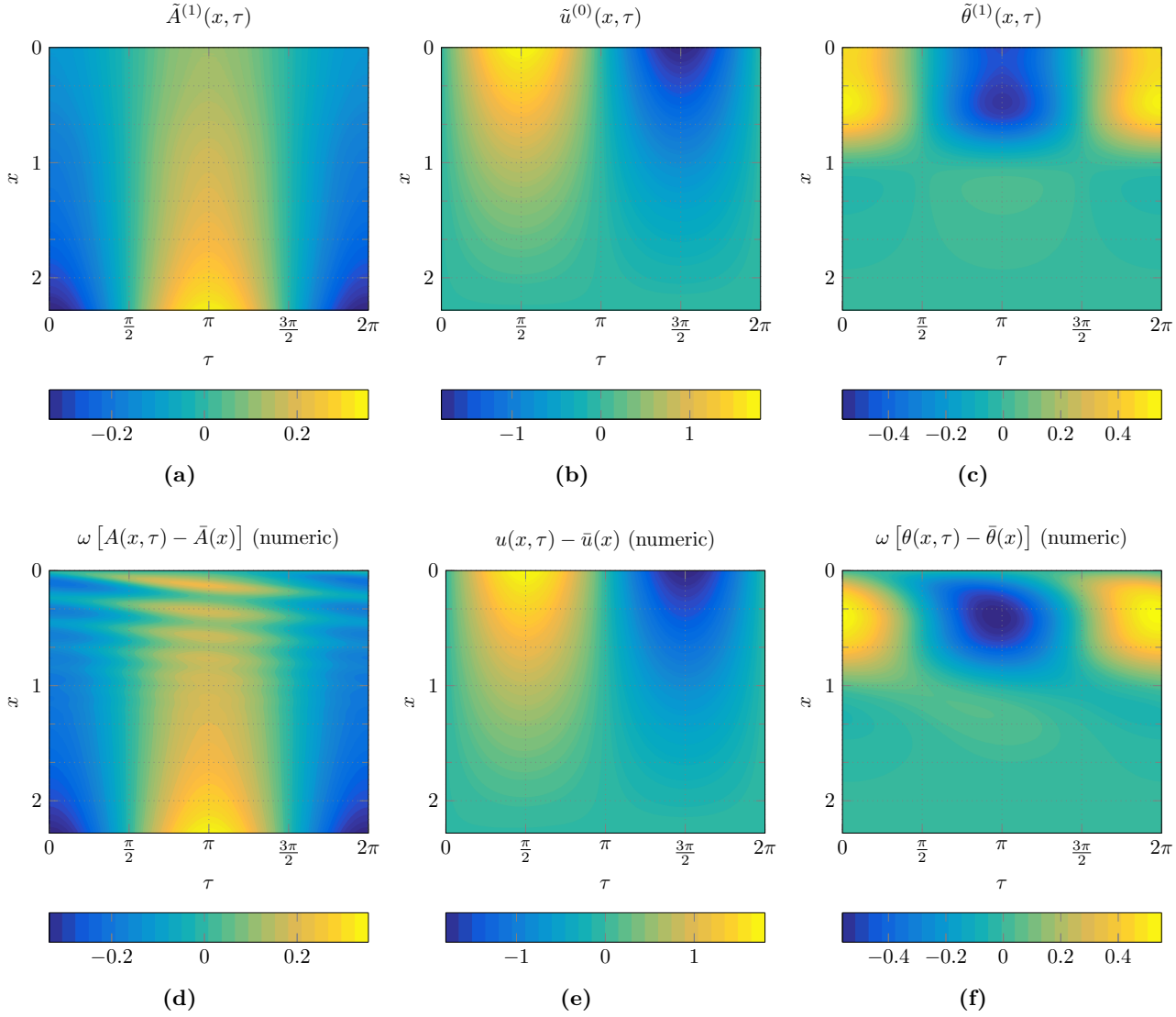

Figure 3.4.1 – Asymptotic predictions (a)-(c) of the fluctuations compared with their numerical counterparts (d)-(f), for area, velocity and temperature. We set $\mathrm{Bi} = \mathrm{Pe} = \Gamma = \mathrm{St} = \bar{P}_{\mathrm{in}} = 1$, $\theta_{\mathrm{a}} = 0.23$, $D = 0.25$, and $K = 300$ with $\omega = 100$ and $\Delta = 0.8$; $Q(x)$ is given by (3.53) with $x_1 = 0.7$ and $x_2 = 0.9$.

3.4.2 Thermal boundary layer

We proceed to explore the boundary layer near $x = 0$ by making the rescaling $x = \delta X$ (not to be confused with the previous X notation), with $\delta = 1/\sqrt{\omega} \ll 1$. We determine the matching conditions as $X \to \infty$ by expanding the outer solution in inner variables. Using the structure of

the fluctuations calculated in §3.4.1, we write the outer solution in the form

$$A \sim A^{(0)}(x) + \delta^2 \hat{A}^{(1)}(x)\varphi(\tau) + \dots, \tag{3.54a}$$

$$u \sim \bar{u}^{(0)}(x) + \hat{u}^{(0)}(x)\tilde{P}_{\text{in}}(\tau) + \delta^2 \tilde{u}^{(1)}(x,\tau) + \dots, \tag{3.54b}$$

$$\theta \sim \theta^{(0)}(x) + \delta^2 \hat{\theta}^{(1)}(x)\varphi(\tau) + \dots, \tag{3.54c}$$

$$\lambda \sim \lambda^{(0)} + \delta^2 \hat{\lambda}^{(1)}\varphi(\tau) + \dots. \tag{3.54d}$$

For $A(x,\tau)$, the outer expansion rewritten in inner variables is

$$A \sim A^{(0)}(0) + \delta X A_x^{(0)}(0) + \delta^2 \left(\frac{1}{2} X^2 A_{xx}^{(0)}(0) + \hat{A}^{(1)}(0)\varphi(\tau) \right) + \dots. \tag{3.55}$$

Note that we can evaluate some of these terms, as

$$A^{(0)}(0) = D, \quad A_x^{(0)}(0)\bar{u}^{(0)}(0) = \frac{\bar{P}_{\text{in}}}{3}, \tag{3.56a}$$

and

$$\hat{A}^{(1)}(0) = \frac{1}{3}\left(1 - A_x^{(0)}(0) \int_0^{\lambda^{(0)}} \frac{\mathrm{d}x}{\mu\left(\theta^{(0)}(x)\right) A^{(0)}(x)} \right). \tag{3.56b}$$

Note that the numerical solution estimates the integral term in (3.56b) to be small but not zero. We assume an inner expansion of the form $A(x,\tau) = \mathcal{A}(X,\tau)$, with

$$\mathcal{A}(X,\tau) \sim \mathcal{A}^{(0)}(X,\tau) + \delta \mathcal{A}^{(1)}(X,\tau) + \delta^2 \mathcal{A}^{(2)}(X,\tau) + \dots, \tag{3.57}$$

and the matching conditions are taken from (3.55), namely

$$\mathcal{A}^{(0)}(X,\tau) \to D \qquad \text{as} \quad X \to \infty, \tag{3.58a}$$

$$\mathcal{A}^{(1)}(X,\tau) \sim X A_x^{(0)}(0) \qquad \text{as} \quad X \to \infty, \tag{3.58b}$$

$$\mathcal{A}^{(2)}(X,\tau) \sim \frac{1}{2} X^2 A_{xx}^{(0)}(0) + \frac{1}{3}\left(1 - A_x^{(0)}(0) \int_0^{\lambda^{(0)}} \frac{\mathrm{d}x}{\mu\left(\theta^{(0)}(x)\right) A^{(0)}(x)} \right) \varphi(\tau) \quad \text{as} \quad X \to \infty. \tag{3.58c}$$

For θ, the outer expansion in inner variables gives

$$\theta \sim \delta X \theta_x^{(0)}(0) + \delta^2 \left[\frac{1}{2} X^2 \theta_{xx}^{(0)}(0) + \hat{\theta}^{(1)}(0)\varphi(\tau) \right] + \dots, \tag{3.59}$$

which suggests an inner expansion $\theta(x,\tau) = \delta\Theta(X,\tau)$, with

$$\Theta(X,\tau) \sim \delta\Theta^{(0)}(X,\tau) + \delta^2 \Theta^{(1)}(X,\tau) + \dots, \tag{3.60}$$

and matching conditions

$$\Theta^{(0)}(X,\tau) \sim X\theta_x^{(0)}(0) \qquad \text{as} \quad X \to \infty, \tag{3.61a}$$

$$\Theta^{(1)}(X,\tau) \sim \frac{1}{2}X^2\theta_{xx}^{(0)}(0) + \hat{\theta}^{(1)}(0)\varphi(\tau) \qquad \text{as} \quad X \to \infty. \tag{3.61b}$$

Finally, using a similar method for u gives us the outer expression

$$u \sim \bar{u}^{(0)}(0) + \hat{u}^{(0)}(0)\tilde{P}_{\text{in}}(\tau) + \delta X\left[\bar{u}_x^{(0)} + \hat{u}_x^{(0)}(0)\tilde{P}_{\text{in}}\right] + \delta^2\left[\frac{1}{2}X^2\left(\bar{u}_{xx}^{(0)}(0) + \hat{u}_{xx}^{(0)}\tilde{P}_{\text{in}}\right) + \tilde{u}^{(1)}(0,\tau)\right] + \ldots, \tag{3.62}$$

where we can use our solutions from §3.4 to evaluate some terms, as

$$\bar{u}^{(0)}(0) = \frac{\bar{P}_{\text{in}}}{3A_x^{(0)}(0)}, \qquad \hat{u}^{(0)}(0) = \frac{1}{3}\int_0^{\lambda^{(0)}} \frac{\mathrm{d}x}{\mu\left(\theta^{(0)}(x)\right)A^{(0)}(x)}, \tag{3.63a}$$

$$\bar{u}_x^{(0)}(0) = -\frac{\bar{P}_{\text{in}}}{3D}, \qquad \hat{u}_x^{(0)}(0) = -\frac{1}{3D}. \tag{3.63b}$$

Thus, we assume an inner expansion $u(x,\tau) = U(X,\tau)$ with

$$U(X,\tau) \sim U^{(0)}(X,\tau) + \delta U^{(1)}(X,\tau) + \delta^2 U^{(2)}(X,\tau) + \ldots, \tag{3.64}$$

and matching conditions

$$U^{(0)}(X,\tau) \to \frac{\bar{P}_{\text{in}}}{3A_x^{(0)}(0)} + \frac{1}{3}\int_0^{\lambda^{(0)}} \frac{\mathrm{d}x}{\mu\left(\theta^{(0)}(x)\right)A^{(0)}(x)}\tilde{P}_{\text{in}}(\tau) \qquad \text{as} \quad X \to \infty, \tag{3.65a}$$

$$U^{(1)}(X,\tau) \sim -X\frac{\bar{P}_{\text{in}} + \tilde{P}_{\text{in}}}{3D} \qquad \text{as} \quad X \to \infty, \tag{3.65b}$$

$$U^{(2)}(X,\tau) \sim \frac{1}{2}X^2\left[\bar{u}_{xx}^{(0)}(0) + \hat{u}_{xx}^{(0)}(0)\tilde{P}_{\text{in}}\right] + \tilde{u}^{(1)}(0,\tau) \qquad \text{as} \quad X \to \infty. \tag{3.65c}$$

Then, the problem (3.25) in terms of inner variables is given by

$$\frac{1}{\delta^2}\mathcal{A}_\tau + \frac{1}{\delta}\left(\mathcal{A}U\right)_X = 0, \tag{3.66a}$$

$$\frac{1}{\delta^2}\left(3\mu(\Theta)\mathcal{A}U_X\right)_X + \mathrm{St}\mathcal{A} = 0, \tag{3.66b}$$

$$\mathcal{A}\left(\frac{1}{\delta^2}\Theta_\tau + \frac{1}{\delta}U\Theta_X\right) = \frac{1}{\delta^2\mathrm{Pe}}\left(\mathcal{A}\Theta_X\right)_X - 2\frac{\mathrm{Bi}}{\mathrm{Pe}}\sqrt{\mathcal{A}}\left(\Theta - \theta_{\mathrm{a}}(\delta X)\right) + Q(\delta X)\mathcal{A}, \tag{3.66c}$$

subject to

$$\mathcal{A} = D, \quad U_X = -\delta\frac{P_{\text{in}}(\tau)}{3D}, \quad \Theta = 0 \qquad \text{at} \quad X = 0, \tag{3.66d}$$

and matching conditions (3.58), (3.61), and (3.65).

To leading order, we get the system of equations

$$\mathcal{A}^{(0)}_\tau = 0, \tag{3.67a}$$
$$\left(\mathcal{A}^{(0)} U^{(0)}_X\right)_X = 0, \tag{3.67b}$$
$$\mathcal{A}^{(0)}\Theta^{(0)}_\tau = \frac{1}{\mathrm{Pe}}\left(\mathcal{A}^{(0)}\Theta^{(0)}_X\right)_X, \tag{3.67c}$$

with

$$\mathcal{A}^{(0)} = D, \quad U^{(0)}_X = 0, \quad \text{and} \quad \Theta^{(0)} = 0 \quad \text{at} \quad X = 0, \tag{3.67d}$$

and conditions (3.58a), (3.61a), and (3.65a) as $X \to \infty$. The solution to (3.67) is found trivially to correspond to the matching conditions, namely

$$\mathcal{A}^{(0)} \equiv D, \tag{3.68a}$$
$$U^{(0)} = \frac{\bar{P}_{\text{in}}}{3A^{(0)}_x(0)} + \frac{1}{3}\int_0^{\lambda^{(0)}} \frac{\mathrm{d}x}{\mu\left(\theta^{(0)}(x)\right) A^{(0)}(x)} \tilde{P}_{\text{in}}(\tau), \tag{3.68b}$$
$$\Theta^{(0)} = X\theta^{(0)}_x(0). \tag{3.68c}$$

The next order problem is given by

$$\mathcal{A}^{(1)}_\tau = 0 \tag{3.69a}$$
$$U^{(1)}_{XX} = 0, \tag{3.69b}$$
$$\Theta^{(1)}_\tau - \frac{1}{\mathrm{Pe}}\Theta^{(1)}_{XX} = c_1 + c_2\tilde{P}_{\text{in}}(\tau), \tag{3.69c}$$

where

$$c_1 = \frac{1}{D\mathrm{Pe}}\left[A^{(0)}_x(0)\theta^{(0)}_x(0) + 2\mathrm{Bi}\theta_a\sqrt{D}\right] - \frac{\theta^{(0)}_x(0)\bar{P}_{\text{in}}}{3A^{(0)}_x(0)}, \tag{3.69d}$$
$$c_2 = -\frac{\theta^{(0)}_x(0)}{3}\int_0^{\lambda^{(0)}} \frac{\mathrm{d}x}{\mu\left(\theta^{(0)}(x)\right) A^{(0)}(x)}. \tag{3.69e}$$

We find that

$$\mathcal{A}^{(1)} = XA^{(0)}_x(0), \tag{3.70}$$
$$U^{(1)} = \frac{-P_{\text{in}}(\tau)}{3D}X, \tag{3.71}$$

and it just remains to solve (3.69c) for $\Theta^{(1)}$, subject to $\Theta^{(0)}(0,\tau) = 0$ and the far-field behaviour given by (3.61b). To simplify the problem, we subtract (3.61b) from (3.69c), which gives the

boundary-value problem for $\mathcal{T} = \left(1/\hat{\theta}^{(1)}(0)\right)\left[\Theta^{(1)} - \frac{1}{2}X^2\theta^{(0)}_{xx}(0) - \hat{\theta}^{(1)}(0)\varphi(\tau)\right]$ as

$$\mathcal{T}_\tau - \frac{1}{\mathrm{Pe}}\mathcal{T}_{XX} = 0 \qquad \text{for} \quad 0 \le \tau < 2\pi, \quad 0 \le X < \infty, \tag{3.72a}$$

$$\mathcal{T} = -\varphi(\tau) \qquad \text{at} \quad X = 0, \tag{3.72b}$$

$$\mathcal{T} \to 0 \qquad \text{as} \quad X \to \infty, \tag{3.72c}$$

with $\mathcal{T}$ also required to be 2π-periodic in τ.

In the simple case where $\tilde{P}_{\mathrm{in}}(\tau) = \Delta\sin(\tau)$ and $\varphi(\tau) = -\Delta\cos(\tau)$, the solution of (3.72) is easily found to be given by

$$\mathcal{T} = \Delta e^{-X\sqrt{\frac{\mathrm{Pe}}{2}}}\cos\left(\tau - \sqrt{\frac{\mathrm{Pe}}{2}}X\right). \tag{3.73}$$

Since (3.72) is linear, the solution for arbitrary $\varphi(\tau)$ can in principle be found by superimposing solutions like (3.73) and using Fourier series. Then, the composite solution $\theta^{(1)}_c(x,\tau)$ (in outer variables) for the temperature oscillations is

$$\theta^{(1)}_c(x,\tau) = \hat{\theta}^{(1)}(x)\varphi(\tau) + \hat{\theta}^{(1)}(0)\Delta e^{-x\sqrt{\frac{\omega\mathrm{Pe}}{2}}}\cos\left(\tau - x\sqrt{\frac{\omega\mathrm{Pe}}{2}}\right), \tag{3.74}$$

with $\hat{\theta}^{(1)}(x)$ from (3.42). We compare the numeric result with the composite solution in Figure 3.4.2, where we see good agreement between the two. In this example, we are looking at one period of a very fast oscillation ($\omega = 100$), which limits the resolution of the result shown leading to the slight shift seen in the numerical method as compared to the composite solution, near $x = 0$.

The next order problem for conservation of mass (3.66a) is

$$\mathcal{A}^{(2)}_\tau + \left(\mathcal{A}^{(0)}U^{(1)}\right)_X + \left(\mathcal{A}^{(1)}U^{(0)}\right)_X = 0, \tag{3.75}$$

or equivalently

$$\mathcal{A}^{(2)}_\tau = \frac{1}{3}\tilde{P}_{\mathrm{in}}(\tau)\left(1 - A^{(0)}_x(0)\int_0^{\lambda^{(0)}}\frac{\mathrm{d}x}{\mu\left(\theta^{(0)}(x)\right)A^{(0)}(x)}\right), \tag{3.76}$$

where we used (3.68a), (3.68b), (3.70), and (3.71). Using the matching condition (3.58c), we find that

$$\mathcal{A}^{(2)}(X,\tau) = \frac{1}{2}X^2A^{(0)}_{xx}(0) + \frac{1}{3}\left(1 - A^{(0)}_x(0)\int_0^{\lambda^{(0)}}\frac{\mathrm{d}x}{\mu\left(\theta^{(0)}(x)\right)A^{(0)}(x)}\right)\varphi(\tau), \tag{3.77}$$

so $\mathcal{A}^{(2)}(X,\tau)$ is just equal to its far-field behaviour, and it does not satisfy the boundary condition (3.66d) at $X = 0$, i.e. $\mathcal{A}^{(2)}(0,\tau) = 0$. This inconsistency is indicative of another, smaller, boundary layer which allows the boundary condition $A(0,t) = D$ to be satisfied. However, the hyperbolic nature of the equation (3.25a) for A appears to be such that, rather than a boundary-layer structure, the solution for A exhibits rapidly varying waves that propagate into the domain from $x = 0$. We

are therefore led in the next section to consider a multiple-scales solution for A. The analysis turns out to be rather involved and so, for simplicity, we now focus on the isothermal problem.

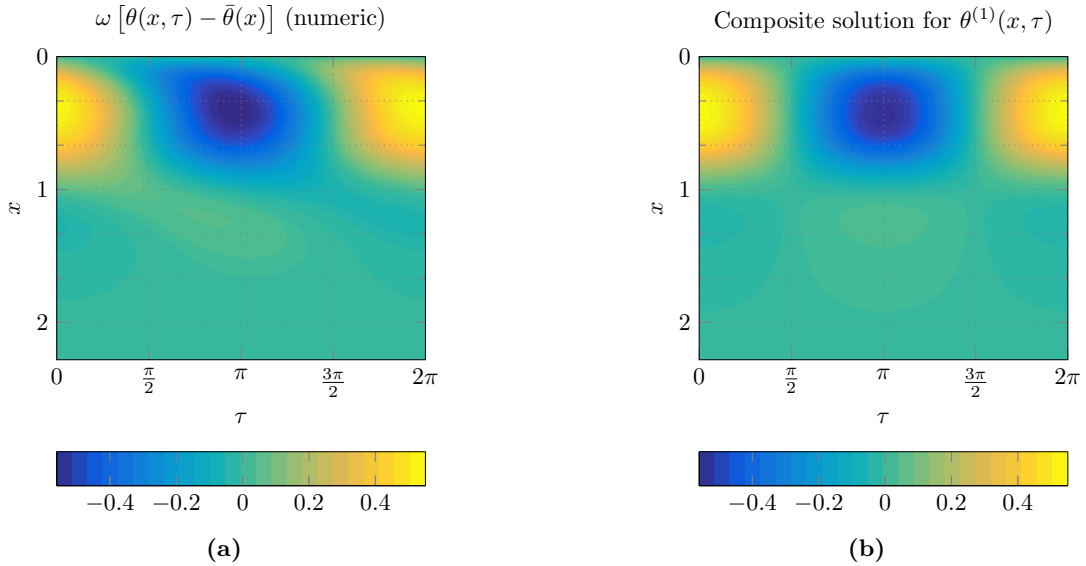

Figure 3.4.2 – Comparison of the numerical solution for the fluctuations in θ with its asymptotic approximation, incorporating the boundary layer by using the composite solution (3.73). We set $\mathrm{Bi}=\mathrm{Pe}=\Gamma=\mathrm{St}=\bar{P}_{\mathrm{in}}=1$, $\theta_{\mathrm{a}}=0.23$, $D=0.25$, and $K=300$ for this example, with $\omega=100$ and $\Delta=0.8$; $Q(x)$ is as in (3.53), with $x_1=0.7$ and $x_2=0.9$.

3.5 Multiple scales structure for isothermal problem

In this section, we focus on the isothermal problem, where we assume a multiple-scales solution for A, motivated by the oscillations propagated downwards through the domain seen in the numerical solution in Figure 3.4.1(d). A similar structure is seen in numerical solutions of the isothermal problem, as will be shown shortly, suggesting that temperature-dependence is not fundamental to creating these oscillations.

We write the isothermal version of the governing equations (3.25) as the first order system of partial differential equations

$$\omega A_\tau + (Au)_x = 0, \tag{3.78a}$$

$$3Au_x + P = 0, \tag{3.78b}$$

$$P_x - \mathrm{St}A = 0. \tag{3.78c}$$

As in §3.4, we denote the forcing pressure fluctuations by $\dot{\varphi}(\tau)$, where φ is defined to be a 2π periodic

function that satisfies $\bar{\varphi} = \frac{1}{2\pi}\int_0^{2\pi} \varphi(\tau)\mathrm{d}\tau = 0$. The boundary conditions can thus be written as

$$A = D, \quad P = \bar{P}_{\text{in}} + \dot{\varphi}(\tau) \qquad \text{at} \quad x = 0, \tag{3.78d}$$

$$u = A = 1 \qquad \text{at} \quad x = \lambda(\tau), \tag{3.78e}$$

where we have used that $\tilde{P}_{\text{in}}(\tau) = \dot{\varphi}(\tau)$ to simplify our notation.

Before proceeding with the multiple-scales analysis, we note a net conservation law that will be useful later. By integrating (3.78a) with respect to τ and imposing 2π-periodicity, we deduce that $\overline{Au} = \frac{1}{2\pi}\int_0^{2\pi} A(x,\tau)u(x,\tau)\,\mathrm{d}\tau$ is a constant. Moreover, because we know that $A = u = 1$ for $x > \lambda(t)$, we must have

$$\overline{Au} = 1. \tag{3.79}$$

Motivated by the solution structure seen for example in Figure 3.4.1(d), we suppose that there are two length-scales, namely a long scale x and a short scale $\hat{X} = \omega\psi(x)$; the function $\psi(x)$ is, for now, arbitrary, but will be determined by enforcing 2π periodicity of the solution with respect to $\hat{X}$. Then, by the chain rule, we have

$$\frac{\partial}{\partial x} \mapsto \frac{\partial}{\partial x} + \omega\psi'(x)\frac{\partial}{\partial \hat{X}}, \tag{3.80}$$

so the rescaled governing equations (3.78) become

$$\omega A_\tau + \psi'\left(Au\right)_{\hat{X}} + \frac{1}{\omega}\left(Au\right)_x = 0, \tag{3.81a}$$

$$3A\left(\psi' u_{\hat{X}} + \frac{1}{\omega}u_x\right) = -\frac{1}{\omega}P, \tag{3.81b}$$

$$\psi' P_{\hat{X}} + \frac{1}{\omega}P_x = \frac{1}{\omega}\mathrm{St}A. \tag{3.81c}$$

We seek the solutions as asymptotic expansions of the form

$$A(x,\hat{X},\tau) \sim A^{(0)}(x,\hat{X},\tau) + \frac{1}{\omega}A^{(1)}(x,\hat{X},\tau) + \frac{1}{\omega^2}A^{(2)}(x,\hat{X},\tau) + \ldots, \tag{3.82a}$$

with likewise for u and P, and similarly

$$\lambda(\tau) \sim \lambda^{(0)}(\tau) + \frac{1}{\omega}\lambda^{(1)}(\tau) + \frac{1}{\omega^2}\lambda^{(2)}(\tau) + \ldots. \tag{3.83}$$

Then, the leading order problem is

$$A^{(0)}_\tau + \psi'\left(A^{(0)}u^{(0)}\right)_{\hat{X}} = 0, \tag{3.84a}$$

$$u^{(0)}_{\hat{X}} = 0, \tag{3.84b}$$

$$P^{(0)}_{\hat{X}} = 0, \tag{3.84c}$$

so $u^{(0)} = u^{(0)}(x,\tau)$ and $P^{(0)} = P^{(0)}(x,\tau)$. In fact, it transpires that $A^{(0)} = A^{(0)}(x)$ and $\lambda^{(0)}$ is constant, and we will simplify the analysis by anticipating these results from now.

Then, at $\mathcal{O}(1/\omega)$

$$A^{(1)}_\tau + \psi'\left(u^{(0)}A^{(1)}_{\hat{X}} + A^{(0)}u^{(1)}_{\hat{X}}\right) = -\left(A^{(0)}u^{(0)}\right)_x, \tag{3.85a}$$

$$3A^{(0)}\psi' u^{(1)}_{\hat{X}} + 3A^{(0)}u^{(0)}_x = -P^{(0)}, \tag{3.85b}$$

$$\psi' P^{(1)}_{\hat{X}} + P^{(0)}_x = \mathrm{St}A^{(0)}, \tag{3.85c}$$

Averaging (3.85b) and (3.85c) with respect to $\hat{X}$ gives $u^{(1)}_{\hat{X}} = P^{(1)}_{\hat{X}} = 0$, so $u^{(1)} = u^{(1)}(x,\tau)$, $P^{(1)} = P^{(1)}(x,\tau)$, and

$$3A^{(0)}u^{(0)}_x = -P^{(0)}, \tag{3.86a}$$

$$P^{(0)}_x = \mathrm{St}A^{(0)}. \tag{3.86b}$$

As in §3.4, we decompose the leading-order velocity as $u^{(0)}(x,\tau) = \bar{u}^{(0)}(x) + \hat{u}^{(0)}(x)\dot{\varphi}(\tau)$ and similarly $P^{(0)}(x,\tau) = \bar{P}^{(0)}(x) + \dot{\varphi}(\tau)$. Therefore our multiple scales approach is around a steady problem, where we are only considering rapid fluctuations about the mean. Then by separating the time averaged and fluctuating terms in (3.86) we obtain

$$3A^{(0)}\bar{u}^{(0)}_x = -\bar{P}^{(0)}, \tag{3.87a}$$

$$3A^{(0)}\hat{u}^{(0)}_x = -1, \tag{3.87b}$$

$$\bar{P}^{(0)}_x = \mathrm{St}A^{(0)}, \tag{3.87c}$$

with

$$A^{(0)} = D, \quad \bar{P}^{(0)} = \bar{P}_{\mathrm{in}} \qquad \text{at} \quad x = 0, \tag{3.87d}$$

$$\bar{u}^{(0)} = A^{(0)} = 1, \quad \hat{u}^{(0)} = 0 \qquad \text{at} \quad x = \lambda^{(0)}. \tag{3.87e}$$

It follows that

$$\hat{u}^{(0)}(x) = \frac{1}{3}\int_x^{\lambda^{(0)}} \frac{\mathrm{d}s}{A^{(0)}(s)}, \tag{3.88}$$

is determined once we have solved for $A^{(0)}$ and $\lambda^{(0)}$.

Now we turn to equation (3.85a) for $A^{(1)}$, which simplifies to

$$A^{(1)}_\tau + \psi' u^{(0)}A^{(1)}_{\hat{X}} = -\left(A^{(0)}u^{(0)}\right)_x. \tag{3.89}$$

To ensure periodicity with respect to both $\hat{X}$ and τ, we now choose

$$\psi'(x) = \frac{1}{\bar{u}^{(0)}(x)}. \tag{3.90}$$

To specify ψ uniquely, we take $\psi(0) = 0$ so that

$$\psi(x) = \int_0^x \frac{\mathrm{d}s}{\bar{u}^{(0)}(x)} = \frac{1}{\mathrm{St}} \left(\bar{P}^{(0)} - \bar{P}_{\mathrm{in}} \right). \tag{3.91}$$

Then (3.89) becomes

$$A^{(1)}_{\tau} + \left(1 + v^{(0)}(x)\dot{\varphi}(\tau) \right) A^{(1)}_{\hat{X}} = - \left(A^{(0)} u^{(0)} \right)_x, \tag{3.92}$$

where we have introduced the shorthand

$$v^{(0)}(x) = \frac{\hat{u}^{(0)}(x)}{\bar{u}^{(0)}(x)}. \tag{3.93}$$

To facilitate the solution of the linear hyperbolic PDE (3.92), let $\eta = \hat{X} - \tau - v^{(0)}(x)\varphi(\tau)$. We perform the change of variables $\left(x, \hat{X}, \tau \right) \mapsto (x, \eta, \tau)$, such that

$$\frac{\partial}{\partial \tau} \mapsto \frac{\partial}{\partial \tau} - \left(1 + v^{(0)}(x)\dot{\varphi}(\tau) \right) \frac{\partial}{\partial \eta}, \tag{3.94a}$$

$$\frac{\partial}{\partial x} \mapsto \frac{\partial}{\partial x} - v^{(0)}_x(x)\varphi(\tau) \frac{\partial}{\partial \eta}, \tag{3.94b}$$

$$\frac{\partial}{\partial \hat{X}} \mapsto \frac{\partial}{\partial \eta}, \tag{3.94c}$$

and so (3.92) becomes

$$A^{(1)}_{\tau} = - \left[A^{(0)} \left(\bar{u}^{(0)} + \hat{u}^{(0)}\dot{\varphi} \right) \right]_x. \tag{3.95}$$

Imposing 2π periodicity with respect to τ gives

$$\left(A^{(0)} \bar{u}^{(0)} \right)_x = 0, \tag{3.96}$$

which finally closes the problem for $A^{(0)}$, $\bar{u}^{(0)}$, and $\bar{P}^{(0)}$. The system (3.87) and (3.96) corresponds to the steady isothermal problem, for which we have analytical solutions (see §2.4.1). Then, we can write the general solution of (3.95) for $A^{(1)}$ as

$$A^{(1)}(x, \eta, \tau) = -v^{(0)}_x(x)\varphi(\tau) + G_1(x, \eta), \tag{3.97}$$

where $G_1(x, \eta)$ is to be determined.

Imposing $A^{(1)} = 0$ at $x = 0$, we find that

$$G_1 \left(0, -\tau - D\hat{u}^{(0)}(0)\varphi(\tau) \right) = v^{(0)}_x(0)\varphi(\tau), \tag{3.98}$$

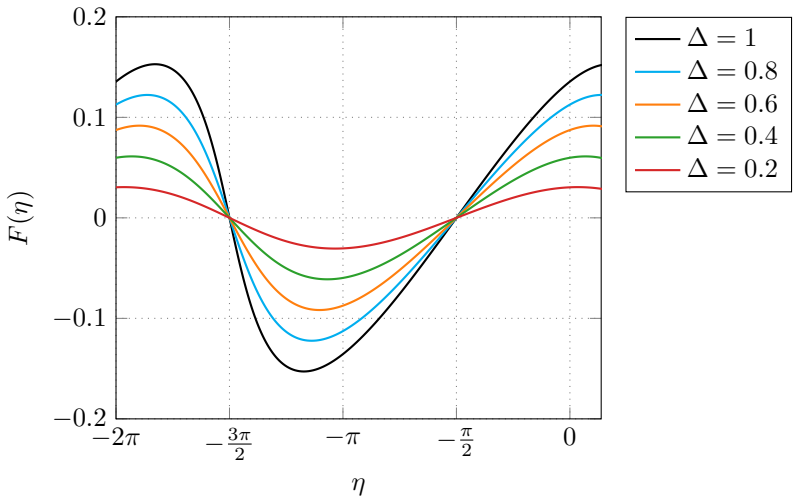

Figure 3.5.1 – We plot $F(\eta)$ defined in (3.99), using $P_{\text{in}} = 1 + \Delta \sin\tau$, St $= 1$, $D = 0.25$, for different Δ.

where we can evaluate $v_x^{(0)}(0) = \frac{1}{3}\left(\bar{P}_{\text{in}} D\hat{u}^{(0)}(0) - 1\right)$ with $\hat{u}^{(0)}(0)$ determined from (3.88). We can therefore write $G_1(0,\eta) = F(\eta)$ where F satisfies the implicit equation

$$F\left(-\tau - D\hat{u}^{(0)}(0)\varphi(\tau)\right) = v_x^{(0)}(0)\varphi(\tau). \tag{3.99}$$

Equation (3.99) can be inverted in principle provided $1 + D\hat{u}^{(0)}(0)\varphi(\tau) \geq 0$, which is the condition for characteristics of (3.92) to be travelling into the solution domain at $\hat{X} = 0$. This inequality also implies that $\Delta = 1$ is the largest value we can set, as $\Delta > 1$ allows $P_{\text{in}} < 0$ and makes $F(\eta)$ non-invertible. In Figure 3.5.1 we show typical behaviour of $F(\eta)$ when $P_{\text{in}}(\tau) = 1 + \Delta\sin\tau$ and we see how the sinusoidal forcing is distorted by the dynamics and how the amplitude increases for increasing Δ. Note that

$$\int_0^{2\pi} F(\eta)\mathrm{d}\eta = \int_0^{2\pi} F\left(-\tau - D\hat{u}^{(0)}(0)\varphi(\tau)\right)\left(-1 - D\hat{u}^{(0)}(0)\dot{\varphi}(\tau)\right)\mathrm{d}\tau = 0, \tag{3.100}$$

by (3.99) and so $\bar{G}_1(0) = 0$ where $\bar{G}_1(x) = \frac{1}{2\pi}\int_0^{2\pi} G_1(x,\eta)\mathrm{d}\eta$.

To obtain an equation for $G_1(x,\eta)$, we must proceed to $\mathcal{O}\left(1/\omega^2\right)$, where we find

$$\frac{u_{\hat{X}}^{(2)}}{\bar{u}^{(0)}} = -u_x^{(1)} - \frac{P^{(1)}}{3A^{(0)}} + \frac{P^{(0)}A^{(1)}}{3\left(A^{(0)}\right)^2}, \tag{3.101a}$$

$$\frac{P_{\hat{X}}^{(2)}}{\bar{u}^{(0)}} = -P_x^{(1)} + \text{St}A^{(1)}. \tag{3.101b}$$

As before, we use (3.94) to write (3.101) in terms of (x, η, τ) as

$$\frac{u_\eta^{(2)}}{\bar{u}^{(0)}} = -u_x^{(1)} - \frac{P^{(1)}}{3A^{(0)}} + \frac{1}{A^{(0)}}\left(\bar{u}_x^{(0)} + \hat{u}_x^{(0)}\dot{\varphi}(\tau)\right)\left(v_x^{(0)}\varphi(\tau) - G_1\right), \tag{3.102a}$$

$$\frac{P_\eta^{(2)}}{\bar{u}^{(0)}} = -P_x^{(1)} + \mathrm{St}A^{(1)}. \tag{3.102b}$$

We average (3.102) with respect to η and find

$$u_x^{(1)} + \frac{P^{(1)}}{3A^{(0)}} = \frac{1}{A^{(0)}}\left(\bar{u}_x^{(0)} + \hat{u}_x^{(0)}\dot{\varphi}(\tau)\right)\left(v_x^{(0)}\varphi(\tau) - \bar{G}_1\right), \tag{3.103a}$$

$$P_x^{(1)} = \mathrm{St}\left(\bar{G}_1 - v_x^{(0)}\varphi(\tau)\right). \tag{3.103b}$$

Next, we average (3.103) with respect to τ and get

$$\bar{P}^{(1)} = -3\left(A^{(0)}\bar{u}_x^{(1)} + \bar{G}_1\bar{u}_x^{(0)}\right), \tag{3.104a}$$

$$\bar{P}_x^{(1)} = \mathrm{St}\bar{G}_1, \tag{3.104b}$$

with $\bar{P}^{(1)} = \bar{G}^{(1)} = 0$ at $x = 0$.

The equation for $A^{(2)}$ is

$$A_\tau^{(2)} + \frac{1}{\bar{u}^{(0)}}\left(A^{(0)}u^{(2)} + A^{(1)}u^{(1)} + A^{(2)}u^{(0)}\right)_{\hat{X}} + \left(A^{(1)}u^{(0)} + A^{(0)}u^{(1)}\right)_x = 0. \tag{3.105}$$

We change variables to (x, η, τ) and get

$$A_\tau^{(2)} + \frac{u^{(1)}}{\bar{u}^{(0)}}G_{1\eta} + A^{(0)}\left[-u_x^{(1)} - \frac{P^{(1)}}{3A^{(0)}} + \frac{1}{A^{(0)}}\left(\bar{u}_x^{(0)} + \hat{u}^{(0)}\dot{\varphi}\right)\left(v_x^{(0)}\varphi - G_1\right)\right] + \left(A^{(0)}u^{(1)}\right)_x + \left[\left(\bar{u}^{(0)} + \hat{u}^{(0)}\dot{\varphi}\right)\left(-v^{(0)}\varphi + G_1\right)\right]_x - v_x^{(0)}\varphi\left[\left(\bar{u}^{(0)} + \hat{u}^{(0)}\dot{\varphi}\right)\left(-v^{(0)}\varphi + G_1\right)\right]_\eta, \tag{3.106}$$

which we average with respect to τ and find

$$\frac{\bar{u}^{(1)}}{\bar{u}^{(0)}}G_{1\eta} - \frac{\bar{P}^{(1)}}{3} + \bar{u}^{(1)}A_x^{(0)} + \bar{u}^{(0)}G_{1x} = 0. \tag{3.107}$$

Next, we average (3.107) with respect to η to find

$$\bar{P}^{(1)} = 3\left(\bar{u}^{(1)}A_x^{(0)} + \bar{u}^{(0)}\bar{G}_{1x}\right), \tag{3.108}$$

which together with (3.104a) gives

$$A^{(0)}\bar{u}^{(1)} + \bar{u}^{(0)}\bar{G}_1 = q, \tag{3.109}$$

where q is a constant to be determined.

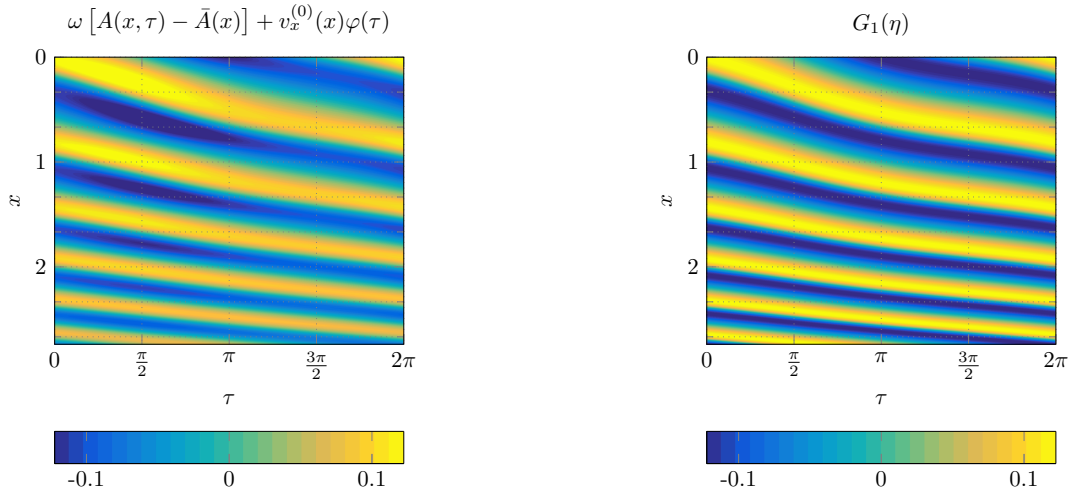

(a) Numeric **(b)** Analytic

Figure 3.5.2 – Numerical results for area fluctuations compared with the multiple scales prediction, with $P_{\text{in}} = 1 + \Delta \sin \tau$, $\text{St} = 1$, $D = 0.25$, $L = 3$, $\Delta = 0.8$, and $\omega = 30$. The simulation was run for 20 periods to allow for convergence, where we show only the last period, for which $N = 500$ and $K = 1500$.

By considering the net conservation equation (3.79) at $\mathcal{O}(1/\omega)$, we deduce q must equal zero. Thus (3.104) becomes a homogeneous first-order system for $(\bar{G}_1, \bar{P}^{(1)})$, namely

$$\left(\bar{u}^{(0)}\bar{G}_1\right)_x = \frac{1}{3}\bar{P}^{(1)}, \tag{3.110a}$$

$$\bar{P}_x^{(1)} = \text{St}\bar{G}_1. \tag{3.110b}$$

Given the boundary conditions $\bar{G}_1 = \bar{P}^{(1)} = 0$ at $x = 0$, we can only have the trivial solution $\bar{P}^{(1)} = \bar{G}_1 = \bar{u}^{(1)} = 0$. Hence the governing equation (3.107) for G_1 reduces to $G_{1x} = 0$, and the solution is

$$G_1(x, \eta) = F(\eta). \tag{3.111}$$

Finally, to obtain an equation for the correction $\lambda^{(1)}$ to the position of the free boundary, we impose the downstream boundary condition $A = 1$ at $x = \lambda$. Note that $x = \lambda$ corresponds to $\psi(x) = \Lambda$, say, where $\Lambda(\tau) \sim \Lambda^{(0)} + 1/\omega\ \lambda^{(1)}(\tau) + \ldots$ and $\Lambda^{(0)} = \int_0^{\lambda^{(0)}} A^{(0)}(x)\ \mathrm{d}x$ is a (known) constant. We therefore have $\lambda^{(1)}A_x^{(0)} + A^{(1)} = 0$ at $x = \lambda^{(0)}$, $\eta = \omega\Lambda(\tau) - \tau$, which reduces to

$$\bar{u}_x^{(0)}(\lambda^{(0)})\lambda^{(1)}(\tau) = \frac{1}{3}\varphi(\tau) + F\left(\omega\Lambda^{(0)} + \lambda^{(1)}(\tau) - \tau\right), \tag{3.112}$$

a transcendental equation for $\lambda^{(1)}(\tau)$.

In summary, the results of the multiple-scales analysis are as follows. In the limit $\omega \to \infty$:

- The leading-order area $A^{(0)}(x)$, average velocity $\bar{u}^{(0)}(x)$ and free boundary position $\lambda^{(0)}$ satisfy the steady isothermal problem (2.52) analysed in Chapter 2.
- The velocity undergoes $\mathcal{O}(1)$ fluctuations whose amplitude $\hat{u}^{(0)}(x)$ is fully determined by (3.88)

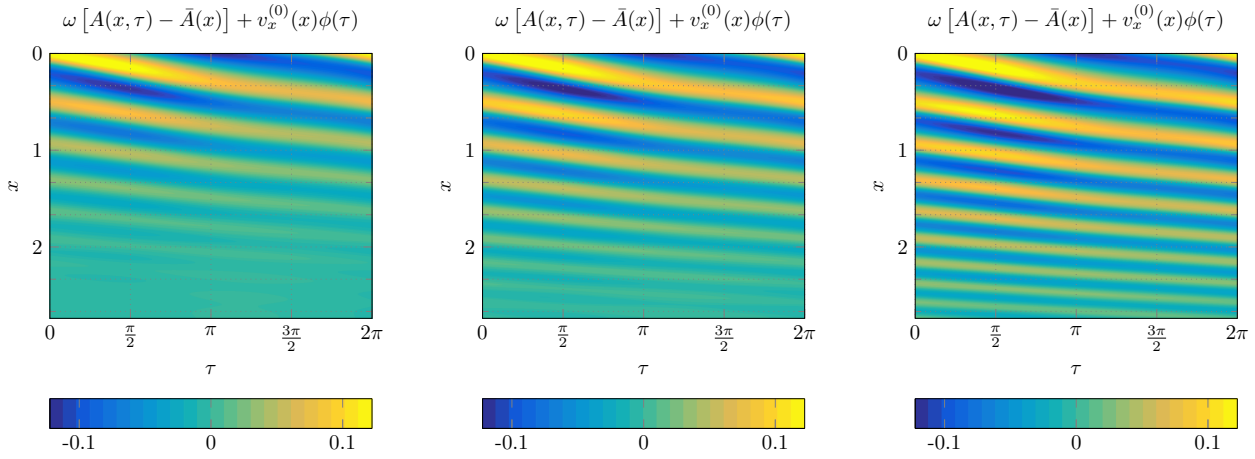

(a) $K = 300$ **(b)** $K = 500$ **(c)** $K = 1000$

Figure 3.5.3 – Numerical results for area fluctuations with $P_{\text{in}} = 1 + \Delta \sin\tau$, $\text{St} = 1$, $D = 0.25$, $L = 3$, $\omega = 50$, $\Delta = 0.8$, and different spatial discretisations K. The simulation was run for 20 periods to allow for convergence, where we only show the last period, with $N = 500$.

in terms of the known leading order solution.

- The fluctuations in the area A are smaller, of order $1/\omega$. They propagate along the characteristics of the PDE (3.89) without attenuation, with a wave form $F(\eta)$ that satisfies the functional equation (3.99).
- The fluctuations in the position of the free boundary λ are also $\mathcal{O}(1/\omega)$ and satisfy a similar implicit equation (3.112).

We show the comparison between the multiple scales approximation and the numerical solution in Figure 3.5.2, for $\omega = 30$. We have isolated the propagating waves in $A(x,\tau)$ by subtracting the average $\bar{A}(x)$ and the known perturbation $-v_x^{(0)}(x)\varphi(\tau)$. As seen in Figure 3.5.2(a), the numerical solution captures the position of the propagating waves, but shows a decreasing amplitude as $x \to \lambda^{(0)}$, which is absent in the multiple scales solution in Figure 3.5.2(b). This is likely due to unwanted numerical dissipation effects caused by the finite difference approximation used for the hyperbolic equation (3.1a) for A, which are common for the numerical method we have used (LeVeque, 1992). We highlight this in Figure 3.5.3, where, as we increase the discretisation points in K, the amplitude attenuation decreases from the resulting fluctuations.

In Figure 3.5.4, we compare the two asymptotic solutions we have for the $\lambda^{(1)}(\tau)$ fluctuations, namely the fast oscillations solution (3.44) and the multiple scales correction (3.112), with the numerical result, where we have subtracted the average $\bar{\lambda}$. For the first two examples in the top two panels we show some agreement between the numerical solution and the multiple scales approximation, whereas the original asymptotics are out of phase. However, as we increase ω in the bottom two panels, we see very close agreement between the original asymptotics (3.44) and the numerical solution. The difference between the two asymptotic solutions is the correction term given by F in (3.112), whose effect is attenuated by the numerical dissipation in our numerical scheme. A more

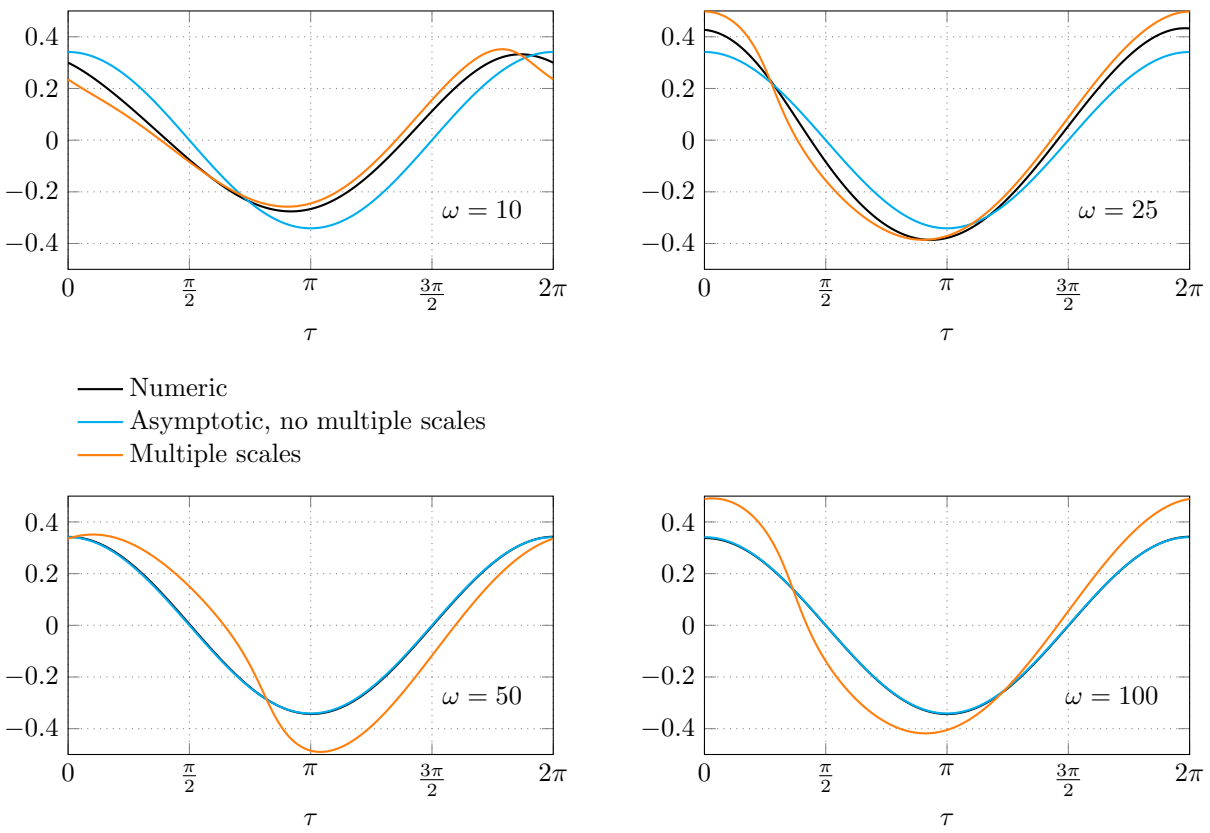

Figure 3.5.4 – Numerical results for $\lambda^{(1)}(\tau)$ fluctuations, as computed numerically (black), using asymptotic approximation (3.44) (blue), and using the multiple scales correction (3.112) (orange). We have used $P_{\text{in}} = 1 + \Delta \sin \tau$, St $= 1$, $D = 0.25$, $\Delta = 0.8$, and $K = 1500$, for different ω. The simulation was run for 20 periods to allow for convergence, with L $= 3$. We only show the last period, with $N = 500$.

sophisticated hyperbolic solver is necessary to tackle this dissipation and resolve the behaviour of the oscillations as $x \to \lambda^{(0)}$.

3.6 Concluding remarks

In this chapter, we have presented numerical solutions as well as asymptotic approximations to the unsteady quasi-one-dimensional coupled flow and temperature problem which describes paste softening in the top region of a Søderberg electrode. In §3.1, we use a finite volume numerical scheme, described in Appendix A, that calculates the area $A(x,t)$, the velocity $u(x,t)$, the temperature $\theta(x,t)$, and the position of the free boundary $\lambda(t)$, which denotes where the paste touches the casing for the first time. The implementation was performed by rescaling the spatial domain and splitting it into two regions, the one above $x = \lambda$ and the one below, which are joined with the appropriate continuity conditions.

After validating the numerical scheme, in §3.2 we performed numerical experiments by varying the applied compressive load, P_{in}, which represents the addition of cylinders in the industrial problem. We proposed two possible control strategies that mimic the cylinder addition patterns used during

normal operations at Elkem ASA, including the skipping of addition days and its consequences on the paste softening profile.

- In CS 1 we fix the number of cylinders added while allowing the addition times to be automatically determined by imposing a minimum P_{in} which prevents the applied load from becoming negative.
- In CS 2, we instead fix daily addition times, but allow the number of added cylinders to vary, which is closer to the industrial case. We found that the additional weight required to skip two days in the imposed patterns leads to two distinct peaks in λ fluctuations: the first caused by the specific addition event and the second by the effects of the cold paste descending more rapidly into the casing. The system can reach a periodic state when arbitrary cylinder addition is allowed, but not when only integer numbers of cylinders can be used.
- We also varied the casing velocity u_L to represent a more realistic slipping regime and incorporated it to the cylinder addition problem. We find that, since u_L varies on a faster timescale than both P_{in} and the flow, the resulting fast oscillations in λ do not significantly alter the qualitative behaviour in the rest of the domain.

In §3.4, we considered the asymptotic limit where the addition frequency $\omega \gg 1$ to explore the cylinder addition problem analytically, and thus obtained asymptotic approximations to the relationship between the fluctuations in P_{in} and the ones in A, u, θ, and λ. The analytical approximations for sinusoidal P_{in} show a boundary layer for θ near $x = 0$, which we analyse in §3.4.2, as well as additional oscillations in the area that are propagated through the domain, which we investigated using the method of multiple scales for the isothermal problem in §3.5. Our multiple scales solution for the area correctly predicts the position of the propagating oscillations, but not the spatial attenuation observed in the numerical solutions. This was shown to be at least partially due to numerical diffusion effects and the numerical and asymptotic results converge as we refine the mesh.

An extension to these asymptotic solutions for the propagating oscillations is to use the multiple scales approach for the coupled problem, using the isothermal solutions as a guide. Although they do not appear in the temperature and velocity solutions, it is likely that the position and amplitude of the oscillations in the area are affected by the other parameters in our problem, such as Γ, Bi, and Pe. We can also extend our results for a non-sinusoidal $P_{\text{in}}(t)$, with the assumption that this function is periodic. This would allow us to impose a form that is closer to the industrial practice of adding cylinders, similar to the P_{in} evolution resulting from the control strategies shown in §3.3. We could also perform a stability analysis, first for the constant P_{in} case and then extend the results to the problem presented in §3.3, where $P_{\text{in}}(t)$ is determined as part of the solution. Finally, the numerical scheme described in Appendix A can be modified, for example by using an alternative for the discretisation of λ (3.4). Additionally, we can use a Godunov-type method that specifically tackles numerical dissipation issues, such as the central second-order method proposed by Kurganov

and Tadmor (2000) and further refined in Kurganov and Lin (2007).

In the next chapter, we shall relax the assumption of a small aspect ratio and numerically solve a two-dimensional or axisymmetric model using finite elements.

Chapter 4

Two-dimensional axisymmetric CFD model with FEniCS

The full free boundary problem (2.4)-(2.16) can in principle be solved numerically using finite element methods. The free boundary could be implemented for example by using a phase field method (Fasano and Primicerio, 1983) or an Arbitrary Lagrangian-Eulerian method for a deformed mesh (Sawo and Bernard, 2009; Selim, 2012). However, in this chapter we take a simplified approach that is easier to implement and describes the main features present in the industrial problem.

Unlike the one-dimensional problem solved in §2.2, the full axisymmetric formulation allows us to capture the presence of the paste pool, shown by the red shaded region in Figure 1.1.2, corresponding to hotter, and hence less viscous paste that is present at the inlet. The pool manifests as a recirculating region of hotter paste in our model, and we are interested in how the pool will behave as we change the boundary conditions and other operating parameters. We interpret the recirculation region as being responsible for the accumulation of hot paste where the cylinders are introduced, which matches the observations by Elkem ASA of Søderberg electrodes, where a viscous pool can be seen at the top of the casing (Skjeldestad, 2019). We obtain initial simulations by 'cutting' the domain of interest, considering only the top part of the casing and 'flattening' the free boundary (see Figure 4.1.1). A physical interpretation of this approach might be that gravitational effects are sufficiently strong to keep the surface of the paste pool effectively flat.

To solve the resulting model, we use FEniCS (Langtangen and Logg, 2017), a Python based CFD solver, which requires us to formulate the problem in variational form, as shown in §4.1. After describing the boundary conditions used, we look at initial results for the isothermal problem in §4.2, where we also perform a convergence test for a known solution. We discuss corner singularities and their effects on our results in §4.2.3 as well as different meshing options in §4.2.4. In §4.3 we move onto the coupled problem (i.e. for flow and temperature) which we solve in both Cartesian

and cylindrical coordinates. In §4.4 we investigate the effects of varying the heating parameters and the inlet velocity on the recirculation of hot paste near the casing wall. We conclude the numerical experiments of this chapter in §4.5 with a simple approach for relating the weight of the added cylinders to our results, first with unsteady solutions and then by varying the free surface height within the framework of our reduced problem. Finally, we discuss conclusions in §4.6.

Before continuing, we give a brief review of other numerical studies of the Søderberg electrode. Some of the earliest numerical schemes used to solve mathematical models for Søderberg electrodes were the 2D iterative solvers for general elliptic equations, for example in Olsen et al. (1972) and Innvaer and Olsen (1979). Only the bottom part of the electrode was considered (regions 3, 4, and 5 in Figure 1.1.2), as the main quantity of interest was the baking isotherm and the Ohmic heating from the clamps. The density, thermal conduction, electrical conductivity, and heat capacity were taken as temperature-dependent material properties. Specific numerical tools were developed on the basis of this method, namely the steady numerical methods Elkem S for direct current (no skin effects) and Elkem X for alternating current (Innvaer and Olsen, 1979), and the dynamic models Elkem D and Elkem T, the latter of which also computes thermal stresses (Larsen, 2012).

Skjeldestad et al. (2015) implemented an axisymmetric model for the temperature of a Søderberg electrode in Comsol for the heat transport without fins and slipping, combining the heat transfer in solids and heat transfer in fluids (i.e. the conjugated heat transfer module) to model the effect of air heating. Induction from the copper tubes and the water cooling from the clamps were included in the model as functions of axial position, which were chosen to fit experimental data. It was found that additional heat transfer is required to match the temperatures from the data, highlighting the need for including the casing fins in future modelling efforts aimed at understanding the baking zone.

The electrical problem for the Søderberg electrode has been studied as a thermistor problem, which describes the heat produced in a conductor by an electric current. A 3D finite element thermistor model was presented in Jonsson and Ingason (1998) for calculating the time-dependent temperature distribution near the contact clamps, using alternating current. The resulting temperature is non-uniform across the electrode, with its maximum in the centre. This model was used as a framework for the model in Palsson and Jonsson (2000), which is reduced to a 2D finite element model for the cross-section of the furnace, allowing the inclusion of all three electrodes, to estimate proximity and skin effects. It was found that the proximity of the other electrodes in the furnace produce symmetry breaking temperature profiles across the cross-section near the baking zone, with a casing up to three times hotter when suffering from proximity effects. A similar 2D finite element model is shown in Bermúdez et al. (1998) for alternating current electrodes. Thermal runaway as a route to blow-up in the time-dependent form of these problems was further elucidated by Lacey (1995). Finite element modelling has also been used to investigate the position of the baking zone (Meyjes et al., 2010; Van Gorder et al., 2021) and to assist in casing design (McDougall et al., 2004). We

focus our current finite element efforts to understand the paste softening near the top of the electrode column, where the cylinders are added.

4.1 Governing equations and boundary conditions

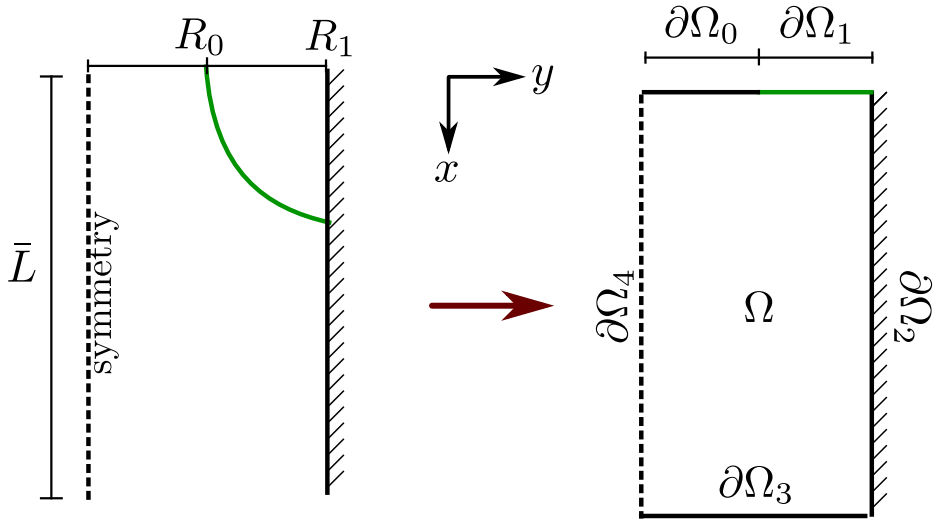

(a) Axisymmetric model with free boundary

(b) FEniCS model

Figure 4.1.1 – (a) Schematic of full problem with the free boundary (shown in green), dimensional length $\bar{L}$, cylinder radius R_0, and electrode casing radius R_1. (b) Geometry used for the FEniCS model, where the free boundary (shown in green) is treated as flat. Both a two-dimensional Cartesian geometry and an axisymmetric geometry are considered (y is replaced with radius r in the latter case).

In Figure 4.1.1, we depict the domain Ω used in FEniCS simulations and compare it to the axisymmetric geometry described Chapter 2. The labels $\partial\Omega_i$, for $i = 0, \dots 4$ denote the boundaries where the various boundary conditions will be applied. We use x for downward vertical direction and y in the transversal direction, with the origin $x = 0$ at the top of the domain (y is replaced with r when we consider an axisymmetric geometry). We solve the steady Stokes flow equations,

$$\nabla p = \nabla \cdot \left[\mu(T)\left(\nabla \boldsymbol{u} + (\nabla \boldsymbol{u})^T\right)\right] + \boldsymbol{f} \qquad \text{in} \quad \Omega, \tag{4.1a}$$

$$\nabla \cdot \boldsymbol{u} = 0 \qquad \text{in} \quad \Omega, \tag{4.1b}$$

where $\boldsymbol{f} = (\rho g, 0)$ is the external forcing which corresponds to gravitational effects, and the viscosity μ depends on the temperature T with the exponential relationship (1.2) described in Chapter 1. We couple (4.1) with the heat equation

$$\rho c \boldsymbol{u} \nabla T = k \nabla^2 T + Q \qquad \text{in} \quad \Omega, \tag{4.1c}$$

where $Q(x)$ describes the inductive heating. We model $Q(x)$ using the Gaussian function (1.5) from

Chapter 1 that depends on the vertical position on the casing, namely

$$Q(x) = Q_I \exp\left(-\frac{\left(x - \frac{x_1+x_2}{2}\right)^2}{2(x_2 - x_1)^2}\right), \tag{4.2}$$

where x_1 and x_2 determine the width of the Gaussian and the position of its peak.

We denote the outward normal unit vector $\boldsymbol{n}$ and stress tensor $\boldsymbol{\sigma} = \mu\left(\nabla \boldsymbol{u} + (\nabla \boldsymbol{u})^T\right) - pI$, where I is the identity matrix. Then, the applied boundary conditions are

$$\boldsymbol{u} = (\hat{u}_{\text{in}}, 0)\,, \qquad T = T_{\text{in}} \qquad \text{on} \quad \partial\Omega_0, \tag{4.3a}$$

$$\text{(see below)}, \qquad \nabla T \cdot \boldsymbol{n} = 0 \qquad \text{on} \quad \partial\Omega_1, \tag{4.3b}$$

$$\boldsymbol{u} = (u_{\text{c}}, 0)\,, \qquad k\nabla T \cdot \boldsymbol{n} = -h\,(T - T_{\text{a}}) \qquad \text{on} \quad \partial\Omega_2, \tag{4.3c}$$

$$\boldsymbol{u} = (u_{\text{c}}, 0)\,, \qquad \nabla T \cdot \boldsymbol{n} = 0 \qquad \text{on} \quad \partial\Omega_3, \tag{4.3d}$$

$$\boldsymbol{u} \cdot \boldsymbol{n} = 0, \qquad \nabla T \cdot \boldsymbol{n} = 0 \qquad \text{on} \quad \partial\Omega_4. \tag{4.3e}$$

As in Chapter 2, the input velocity $\hat{u}_{\text{in}}$ (where we use the hat notation to distinguish it from its non-dimensional form) and the casing velocity u_{c} are related through net mass conservation by

$$\frac{\hat{u}_{\text{in}} R_0}{u_{\text{c}} R_1} = 1 \quad \text{or} \quad \frac{\hat{u}_{\text{in}} R_0^2}{u_{\text{c}} R_1^2} = 1, \tag{4.4}$$

depending on whether we are considering the Cartesian or axisymmetric geometry.

Although in this model we are imposing the inlet velocity, in reality we are interested in imposing the weight of the cylinders added. To recover this information from our model, we will relate the inlet velocity to the integral of the normal stress on $\partial\Omega_0$ in §4.5.1. A more general approach would be to develop a time dependent model, and allow the addition of cylinders to result in a transient behaviour similar to Chapter 3. In principle, a similar extension is possible for the finite element model presented in this chapter, and this is discussed in Chapter 6.

The zero conductive heat flux condition on the free boundary, (4.3b), is chosen for simplicity, to circumvent modelling the temperature in the air above. However heat transfer at the outer walls is accounted for in (4.3c), where the hot air *outside* the electrode casing T_{a} is included as the linear function

$$T_{\text{a}}(x) = \frac{T_{\text{bot}} - T_{\text{top}}}{\bar{L}} x + T_{\text{top}}, \tag{4.5}$$

where $T_{\text{top}} = 80$ °C and $T_{\text{bot}} = 120$ °C (these values are chosen as an example and are consistent with the data from Skjeldestad (2019)). The heat transfer coefficient h represents the efficacy of the heat transfer across the casing.

Note that in this flattened free surface problem, the paste is already touching the casing at $x = 0$. This is different to the work done in Chapter 2 and Chapter 3, where we had that the free surface

was allowed to deform towards the casing. Given that the hot air heating T_a is applied on the wall, the boundary $\partial\Omega_1$ in our current model is now in contact with air that is not heated by T_a, as it corresponds to the air above the free surface. For simplicity, we assume no heating or cooling effects from this air by imposing the no heat flux condition (4.3b). Also note that the situation where the free surface is flat occurs in real electrodes, so in principle, we could use real measurement data to either impose a heat flux or a temperature for this region.

We have yet to define fluid boundary conditions on $\partial\Omega_1$, the flat free surface in our problem. Ideally, we would like to impose both kinematic and dynamic conditions, but our domain simplification allows for only two boundary conditions to be imposed on $\partial\Omega_1$. We consider two cases

$$\underline{\text{Case 1}} \qquad \text{zero normal stress :} \qquad \boldsymbol{t}\cdot\boldsymbol{\sigma}\cdot\boldsymbol{n} = \boldsymbol{n}\cdot\boldsymbol{\sigma}\cdot\boldsymbol{n} = 0 \qquad \text{on} \quad \partial\Omega_1, \quad \text{or} \tag{4.6a}$$

$$\underline{\text{Case 2}} \qquad \text{zero normal flow :} \qquad \boldsymbol{t}\cdot\boldsymbol{\sigma}\cdot\boldsymbol{n} = \boldsymbol{u}\cdot\boldsymbol{n} = 0 \qquad \text{on} \quad \partial\Omega_1, \tag{4.6b}$$

where $\boldsymbol{t}$ denotes the unit tangent vector. In case 1, $\partial\Omega_1$ is not a kinematic boundary so paste can flow in and out. In case 2, there may be a non-zero stress along this boundary. We will discuss the results of both cases above in the numerical examples in this chapter. Note that the combination of boundary conditions (4.3) and (4.6) leads to a pressure solution where the hydrostatic pressure can be subtracted, so in this case our solution is independent of the gravitational term $\boldsymbol{f}$ in (4.1a), and we include it in the definition of the pressure.

4.1.1 Non-dimensionalisation and variational problem formulation

We non-dimensionalise with respect to the length $\bar{L}$ and the vertical velocity u_c with the scalings $\boldsymbol{x} = \bar{L}\boldsymbol{x}'$, $\boldsymbol{u} = u_c\boldsymbol{u}'$, $p = \frac{u_c\mu_0}{\bar{L}}p'$, $\mu = \mu_0\mu'$, $T = T_\mathrm{in} + \Delta T\theta$, $T_a = T_{in} + \Delta T\theta_a$, and $Q = \bar{Q}Q'$, where ΔT is chosen as in Chapter 2 and $\bar{Q} = \frac{1}{\bar{L}}\int_0^{\bar{L}} Q(x)\mathrm{d}x$ denotes the average volumetric heating. This gives the non-dimensionalised governing equations (dropping primes)

$$\nabla p = \nabla\cdot\left[\mu(\theta)\left(\nabla\boldsymbol{u} + (\nabla\boldsymbol{u})^T\right)\right] \qquad \text{in} \quad \Omega, \tag{4.7a}$$

$$\nabla\cdot\boldsymbol{u} = 0 \qquad \text{in} \quad \Omega, \tag{4.7b}$$

$$\boldsymbol{u}\cdot\nabla\theta = \frac{1}{\mathrm{Pe}}\nabla^2\theta + Q \qquad \text{in} \quad \Omega, \tag{4.7c}$$

with

$$\boldsymbol{u} = (1/D, 0)\,, \qquad \theta = 0 \qquad \text{on} \quad \partial\Omega_0, \tag{4.8a}$$

$$\text{case 1 or case 2,} \qquad \nabla\theta\cdot\boldsymbol{n} = 0 \qquad \text{on} \quad \partial\Omega_1, \tag{4.8b}$$

$$\boldsymbol{u} = (1, 0)\,, \qquad \nabla\theta\cdot\boldsymbol{n} = -\overline{\mathrm{Bi}}\,(\theta - \theta_a) \qquad \text{on} \quad \partial\Omega_2, \tag{4.8c}$$

$$\boldsymbol{u} = (1, 0)\,, \qquad \nabla\theta\cdot\boldsymbol{n} = 0 \qquad \text{on} \quad \partial\Omega_3, \tag{4.8d}$$

$$\boldsymbol{u}\cdot\boldsymbol{n} = 0, \qquad \nabla\theta\cdot\boldsymbol{n} = 0, \qquad \text{on} \quad \partial\Omega_4, \tag{4.8e}$$

and either (4.6a) or (4.6b), with non-dimensional parameters

$$\mathrm{Pe} = \frac{\rho c u_c \bar{L}}{k}, \quad \overline{\mathrm{Bi}} = \frac{h\bar{L}}{k}, \quad \text{and} \quad D = \frac{u_\mathrm{c}}{\hat{u}_\mathrm{in}}. \tag{4.9}$$

Note that we have used an overbar in the Biot number definition to distinguish it from the reduced Biot number used in Chapters 2 and 3.

We pose the problem in weak form using the notation

$$\langle \boldsymbol{u}, \boldsymbol{v} \rangle = \int_\Omega \boldsymbol{u} \cdot \boldsymbol{v} \, \mathrm{d}\boldsymbol{x} \quad \text{and} \quad \langle \boldsymbol{u}, \boldsymbol{v} \rangle_{\partial\Omega} = \int_{\partial\Omega} \boldsymbol{u} \cdot \boldsymbol{v} \, \mathrm{d}s. \tag{4.10}$$

We consider the test function space $W = V \times \hat{Q} \times S$, such that $\boldsymbol{u} \in V$, $p \in \hat{Q}$, and $\theta \in S$. Furthermore, we choose $V_0 = \{\boldsymbol{v} \in V \mid \boldsymbol{v} = \boldsymbol{0} \text{ on } \partial\Omega \backslash \partial\Omega_1\}$ and $S_0 = \{s \in S \mid s = 0 \text{ on } \partial\Omega_0\}$ to incorporate the Dirichlet boundary conditions (4.8). Then, we multiply (4.7) and (4.8) by test functions (with slight abuse of notation) $(v, q, s) \in W = V_0 \times \hat{Q} \times S_0$, and integrate over Ω to find the variational form

$$\begin{aligned} 2\langle \mu(\theta)\, \epsilon(\boldsymbol{u}), \nabla \boldsymbol{v} \rangle - \langle p, \nabla \cdot \boldsymbol{v} \rangle - \langle \nabla \cdot \boldsymbol{u}, q \rangle + \langle \boldsymbol{u} \cdot \nabla\theta, s \rangle + \frac{1}{\mathrm{Pe}} \langle \nabla\theta, \nabla s \rangle - \langle Q, s \rangle \\ + \frac{\mathrm{Bi}}{\mathrm{Pe}} \langle \theta - \theta_a, s \rangle_{\partial\Omega_2} - \langle \mu\epsilon(\boldsymbol{u}) - pI, \boldsymbol{v} \rangle_{\partial\Omega \backslash \partial\Omega_1} = 0, \end{aligned} \tag{4.11}$$

with $\epsilon(\boldsymbol{u}) = \frac{1}{2}\left(\nabla \boldsymbol{u} + (\nabla \boldsymbol{u})^T\right)$, $\mu(\theta) = \exp(-\Gamma\theta)$, $\theta_a(x) = x$, and

$$Q(x) = \widetilde{Q}_I \exp\left(-\frac{\left(x - \frac{x_1 + x_2}{2}\right)^2}{2(x_2 - x_1)^2} \right), \tag{4.12}$$

where $\widetilde{Q}_I = Q_I / \bar{Q} \approx 2.371$, $x_1 = 0.7$, and $x_2 = 0.9$. We implement (4.11) in FEniCS using Taylor-Hood mixed elements to pose our problem in weak form, which are a standard approach for solving Stokes equations with finite elements (Elman et al., 2014).

4.2 Isothermal problem

In the first instance, we solve the isothermal problem where $\theta \equiv 0$. We use Cartesian coordinates (x, y), with x in the direction of the flow, as depicted in Figure 4.1.1 and a mesh with a crossed triangle pattern. We solve the equations on a rectangular domain $\Omega : [0, 1] \times [0, 0.2]$ to represent the long and relatively thin geometry of our problem, basing our FEniCS implementation on the work in Terrel et al. (2016). To test our numerical scheme we first perform an example with a known manufactured solution.

4.2.1 Convergence test for a manufactured solution

We consider the manufactured solution adapted from Fehn et al. (2017)

$$\boldsymbol{u}_e = \begin{pmatrix} -\sin\left(2\pi(1-x)\right) \\ \sin\left(2\pi y\right) \end{pmatrix}, \; p_e = -\cos\left(2\pi y\right)\cos\left(2\pi(1-x)\right), \tag{4.13, 4.14}$$

which gives the forcing term

$$\boldsymbol{f}_e = \begin{pmatrix} 2\pi\left[\cos\left(2\pi(1-x)\right)\sin\left(2\pi y\right) - 2\pi\sin\left(2\pi(1-x)\right)\right] \\ 2\pi\left(\sin\left(2\pi y\right) + \cos\left(2\pi y\right)\sin\left(2\pi(1-x)\right)\right) \end{pmatrix}. \tag{4.15}$$

We specify the velocity on $\partial\Omega \backslash \partial\Omega_1$ and the normal stress on $\partial\Omega_1$ consistent with the approach in case 1 in (4.6a). We solve (4.1) with $\boldsymbol{f} = \boldsymbol{f}_e$ on an initial mesh consisting of 8×8 rectangular cells, each split into 4 triangles, shown in 4.2.1(a). Then, we iteratively solve the problem on a finer mesh up to a final configuration of 320×320 rectangular cells. We show the numerical solution on this final mesh in Figures 4.2.1(b) and 4.2.1(c), where we have used the ParaView software (Ayachit, 2015) to visualise the results. We note that for the form of $\boldsymbol{u}_e$ in (4.13), the transition between $\partial\Omega_0$ and $\partial\Omega_1$ is smooth and continuous so these different boundaries are not discernible on the figure (they each occupy half of the top boundary in this example). This is not the case for our actual boundary conditions as discussed in §4.2.2.

We are also interested in evaluating the normal stress on $\partial\Omega_1$ to verify that the Neumann boundary condition is correctly imposed. We show the numerical result compared with the analytic solution for the normal stress on $\partial\Omega_0 \cup \partial\Omega_1$ in Figure 4.2.2(a), where we have used a projection onto piecewise linear functions to evaluate the numerical solution for $\boldsymbol{\sigma} \cdot \boldsymbol{n}$. Note that there are different ways of calculating this quantity during post-processing, including a direct evaluation of the solution of $\boldsymbol{u}$ and p, but this is in general a computationally expensive calculation which is sensitive to mesh construction. We shall therefore use the projection method to evaluate the normal stress in all calculations, unless stated otherwise.

Finally, in Figure 4.2.2(b) we show the convergence results for this example by comparing the error between the numerical solution evaluated at the vertices and the analytical expressions (4.13) and (4.14) as we refine the mesh. The h value corresponds to the minimum cell size, and we note that we obtain quadratic convergence with respect to the sum of the H^1 norm for the velocity and the L_2 norm for the pressure, which is an appropriate *a posteriori* error estimate for mixed finite elements (Banki and Welfert, 1991).

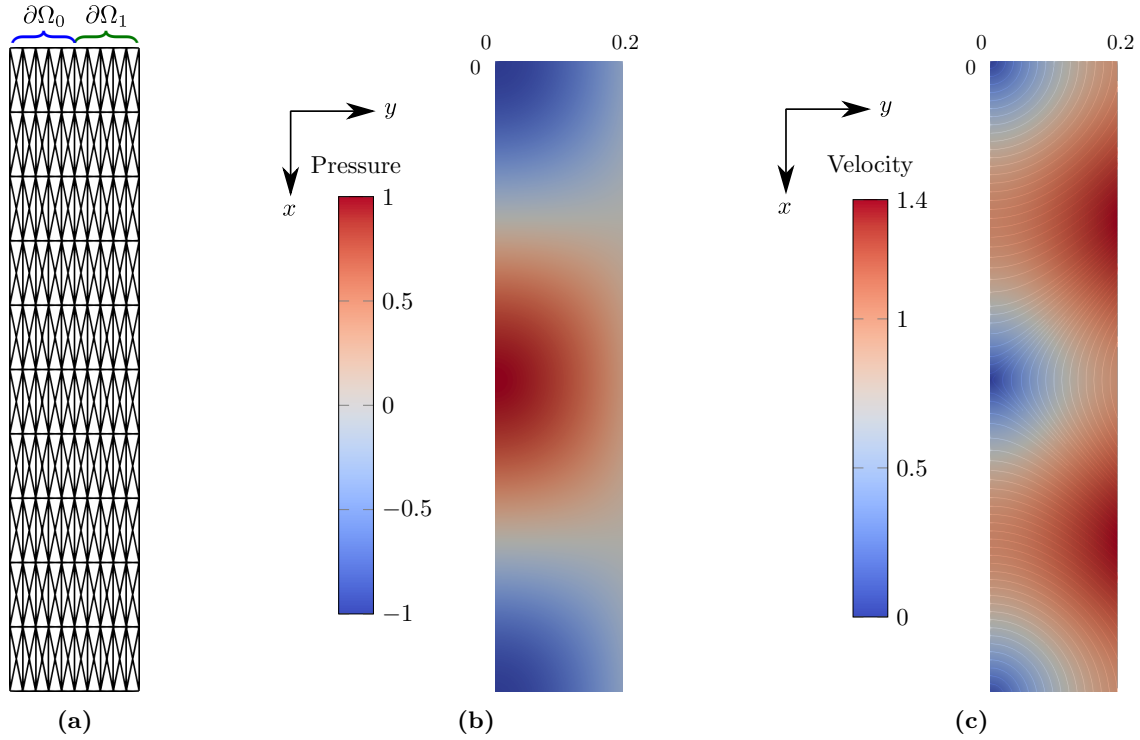

Figure 4.2.1 – (a) The initial mesh for the manufactured solution, consisting of 8×8 rectangles, each split into four triangles. (b) Pressure and (c) Velocity from the numerical solution of (4.1). We use forcing function (4.15), we specify the velocity (4.13) on $\partial\Omega \backslash \partial\Omega_1$ and the normal stress consistent with (4.13) and (4.14) on $\partial\Omega_1$. The white lines in (c) represent the streamlines.

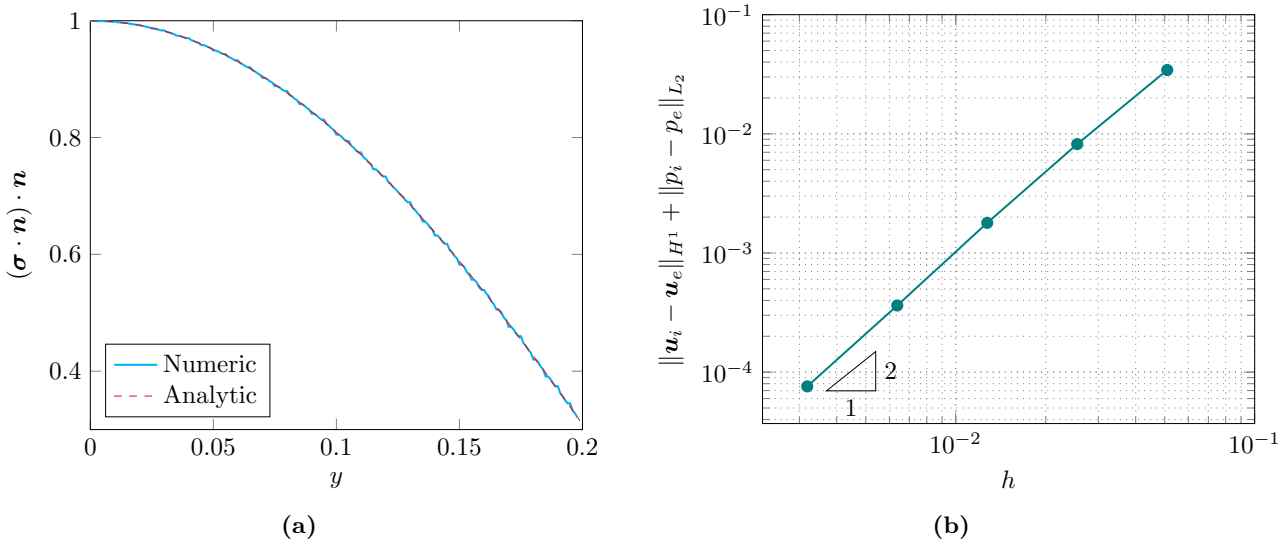

Figure 4.2.2 – (a) We compare the numerical and analytical results for the normal stress evaluated on $\partial\Omega_0 \cup \partial\Omega_1$. In (b), we show the quadratic convergence of the numerical method, where we compare the mesh size h to the appropriate mixed H^1-L_2 norm of the vertex values of the results.

4.2.2 Electrode isothermal problem

We now focus on the numerical solution of the non-dimensional isothermal problem, namely (4.7)-(4.8) with $\mu(\theta) = 1$ and θ ignored. We show the numerical solution for the velocity in Cartesian coordinates in Figure 4.2.3, where we look at the resulting streamlines for both cases of the boundary conditions on $\partial\Omega_1$ defined in (4.6), with velocity ratio $D = 0.5$. Although both choices of boundary conditions provide similar streamlines, the zero normal stress condition allows material to flow out of $\partial\Omega_1$. As a measure of the amount of flow across $\partial\Omega_1$, we calculate the normal velocity flux $\int\int_{\partial\Omega_1} |\boldsymbol{u} \cdot \boldsymbol{n}|^2 \mathrm{d}s \approx 0.025$. Conversely, the zero normal flow condition causes $\partial\Omega_1$ to act as a lid, preventing flow of material through it. As a consequence, the resulting stress is non-zero on this boundary, and there is a non integrable singularity at the intersection between $\partial\Omega_0$ and $\partial\Omega_1$, which we investigate in §4.2.3. Note that global mass conservation is satisfied in both cases as $\int_{\partial\Omega_1} \boldsymbol{u} \cdot \boldsymbol{n} \, \mathrm{d}s = 0$. The real physical problem, with a free boundary that is not exactly flat, consists of a combination of the behaviours seen with these two cases of boundary conditions, and it is not entirely clear at this point which one provides a better approximation. We have more flexibility to perform numerical experiments with the zero normal stress problem and will primarily pursue this condition for the coupled problem in §4.3.

The squared velocity flux on $\partial\Omega_1$ for the zero normal stress problem provides an indication of the size of the recirculation zone shown at the top right part of the casing which draw paste up towards the top. This is clearly seen in Figure 4.2.3(a), whereas it is not seen for the zero normal flow problem in Figure 4.2.3(b) as it is very small and near the point where the two top boundaries meet.

The boundary condition imposed at the outlet requires the downstream velocity to match the velocity at the wall. In practice, we observe that the system rapidly develops into a plug flow near the top of the domain, and appears insensitive to the downstream conditions imposed. To test this hypothesis, we solve the isothermal problem on differently sized domains. The results of this exercise are shown in Figure 4.2.4, where we evaluate the vertical velocity at discrete values of x for domains of different length. The resulting plots are indistinguishable from one another, so we conclude that the outlet condition does not affect the behaviour near the top even for a shorter domain, as the flow quickly becomes fully developed.

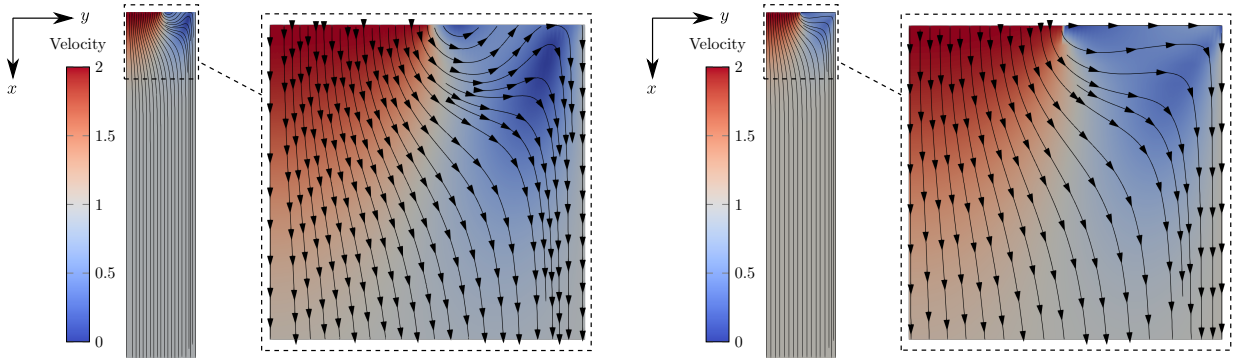

(a) $(\boldsymbol{\sigma} \cdot \boldsymbol{n}) \cdot \boldsymbol{n} = 0$ on $\partial\Omega_1$ **(b)** $\boldsymbol{u} \cdot \boldsymbol{n} = 0$ on $\partial\Omega_1$

Figure 4.2.3 – Numerical solution of Stokes equations (4.7) and the boundary condition indicated in the individual captions above, both for the full domain $\Omega : [0,1] \times [0,0.2]$ and the zoomed domain $[0,0.2] \times [0,0.2]$ using $D = 0.5$ with a mesh consisting of 80×80 rectangular cells split into four triangles.

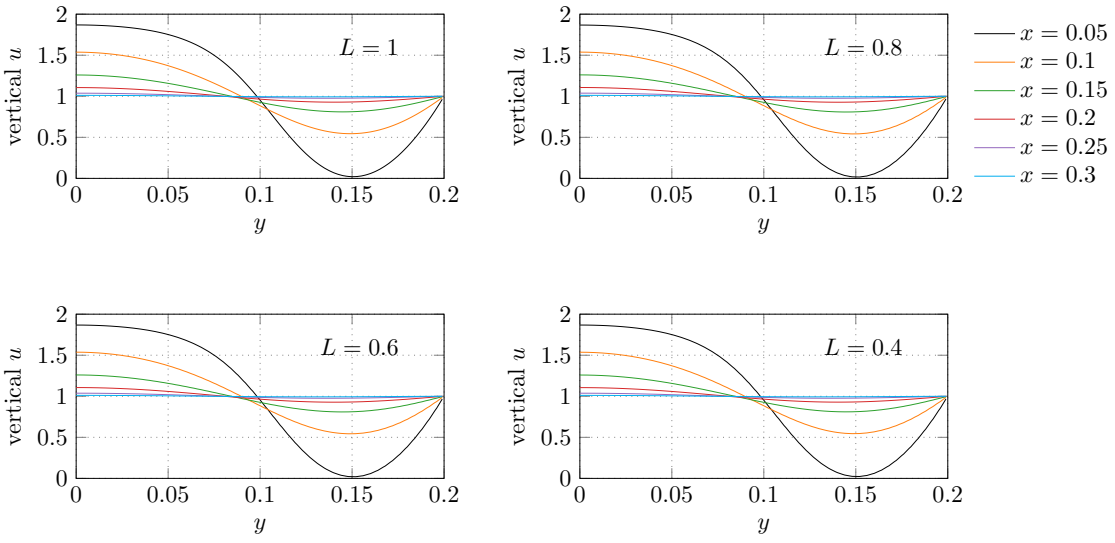

Figure 4.2.4 – Vertical velocity solutions for each reduced domain, of length indicated in each panel, at discrete points along x. The solutions are essentially identical, with the velocity having approached $u \approx 1$ by $x = 0.3$ in all cases, indicating that the length of the domain (provided it is large enough) is unimportant for this problem.

4.2.3 Normal stress calculation and corner singularities

The Stokes flow problem has a pressure singularity near the upper right corner ($x = 0$, $y = 0.2$ in Figure 4.2.3) which is a well known feature of this type of problem and is ubiquitous in the literature (Elman et al., 2014). However, due to our choice of boundary conditions, there exists another singularity in the pressure at the point ($x = 0$, $y = 0.1$ in Figure 4.2.3) separating $\partial\Omega_0$ and $\partial\Omega_1$, for both cases 1 and 2 discussed above. We are interested in computing the normal stress on $\partial\Omega_0$ to ultimately relate the inlet velocity to the corresponding weight of cylinders added at the top; however we must first verify that our code correctly resolves this singularity at edge of $\partial\Omega_0$. We show the results for the numerical integral of the normal stress on in Figure 4.2.5, where we see approximate convergence for the zero normal stress case (case 1) and apparent divergence for the zero normal flow case (case 2) as the minimum cell size h is decreased. To produce better estimates of this quantity and to gain some insight on this behaviour, we first investigate the local solution near the singularity point analytically following the same approach as Dean and Montagnon (1949).

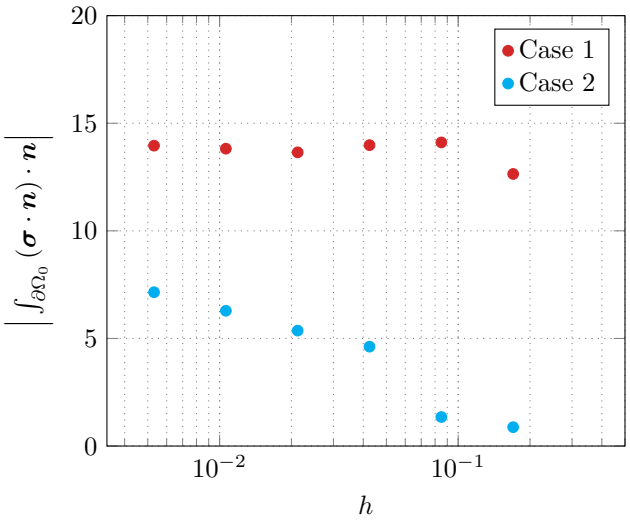

Figure 4.2.5 – We vary the mesh size h and show the integral of the normal stress on $\partial\Omega_0$ for both case 1, where we impose $(\boldsymbol{\sigma}\cdot\boldsymbol{n})\cdot\boldsymbol{n} = 0$ on $\partial\Omega_1$ and case 2, where we impose $\boldsymbol{u}\cdot\boldsymbol{n} = 0$ on $\partial\Omega_1$. This numerical integral converges for case 1 and diverges for case 2, as the mesh size is reduced.

We use polar coordinates (r, θ) such that $\theta = 0$ corresponds to $\partial\Omega_0$ and $\theta = \pi$ corresponds to $\partial\Omega_1$ as seen in the schematic in Figure 4.2.6, where we have rotated the frame of reference from Figure 4.1.1 so that the x axis is now pointing upwards. We introduce the stream function $\psi(r, \theta)$ such that $\boldsymbol{u} = \left(\frac{1}{r}\frac{\psi}{\partial\theta}, -\frac{\partial\psi}{\partial r}\right)$. Then ψ satisfies the biharmonic equation

$$\left(\frac{\partial^2}{\partial r^2} + \frac{1}{r}\frac{\partial}{\partial r} + \frac{1}{r^2}\frac{\partial^2}{\partial\theta^2}\right)^2 \psi = 0, \tag{4.16}$$

and p satisfies

$$\frac{\partial p}{\partial r} = \frac{1}{r}\frac{\partial}{\partial\theta}\left(\nabla^2\psi\right), \qquad \frac{1}{r}\frac{\partial p}{\partial\theta} = -\frac{\partial}{\partial r}\left(\nabla^2\psi\right). \tag{4.17}$$

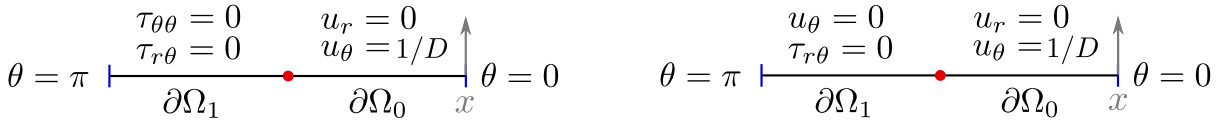

(a) $(\boldsymbol{\sigma}\cdot\boldsymbol{n})\cdot\boldsymbol{n} = 0$ on $\partial\Omega_1$ **(b)** $\boldsymbol{u}\cdot\boldsymbol{n} = 0$ on $\partial\Omega_1$

Figure 4.2.6 – Corner schematics showing the boundary conditions close to the corner singularity for case 1 and case 2, in local polar coordinates, rotated so that the x axis is pointing upwards. These are expanded in terms of the stream function ψ in (4.18) and (4.19).

Then, the boundary conditions for case 1 (zero normal stress) in terms of ψ are

$$\psi = -\frac{r}{D}, \qquad \frac{\partial\psi}{\partial\theta} = 0 \qquad \text{at} \quad \theta = 0, \tag{4.18a}$$

$$\frac{1}{r^2}\frac{\partial^2\psi}{\partial\theta^2} - \frac{\partial^2\psi}{\partial r^2} + \frac{1}{r}\frac{\partial\psi}{\partial r} = 0, \qquad -p + \frac{2}{r^2}\frac{\partial\psi}{\partial\theta} - \frac{2}{r}\frac{\partial^2\psi}{\partial\theta\partial r} = 0 \qquad \text{at} \quad \theta = \pi. \tag{4.18b}$$

Similarly, the boundary conditions for case 2 (zero normal flow) in terms of ψ are

$$\psi = -\frac{r}{D}, \qquad \frac{\partial\psi}{\partial\theta} = 0 \qquad \text{at} \quad \theta = 0, \tag{4.19a}$$

$$\psi = 0, \qquad \frac{\partial^2\psi}{\partial\theta^2} = 0 \qquad \text{at} \quad \theta = \pi. \tag{4.19b}$$

Using the results from Moffatt (1964), applying (4.18) we find that a particular solution for case 1 is given by

$$\psi(r,\theta) = -\frac{r}{D}\cos\theta, \tag{4.20a}$$

$$p(r,\theta) = 0, \tag{4.20b}$$

and we find that for case 2 the boundary conditions (4.19) require a solution of the form

$$\psi(r,\theta) = -\frac{r}{D\pi}\left[(\pi-\theta)\cos\theta + \sin\theta\right], \tag{4.21a}$$

$$p(r,\theta) = \frac{2\cos\theta}{D\pi r}. \tag{4.21b}$$

Hence, for case 2 there is a non-integrable $\frac{1}{r}$ singularity in p at $\theta = 0$, but in case 1 there is not. Furthermore, there is an infinite set of eigenfunctions in each case, which can be written as

$$\psi(r,\theta) = C_n r^{n+\frac{1}{2}}\left[\cos\left(\left(n+\frac{1}{2}\right)\theta\right) - \cos\left(\left(n-\frac{3}{2}\right)\theta\right)\right], \tag{4.22a}$$

$$p(r,\theta) = 2C_n\left(2n-1\right)r^{n-\frac{3}{2}}\sin\left(\left(n-\frac{3}{2}\right)\theta\right), \tag{4.22b}$$

for $n \in \mathbb{Z}$. We find that the minimal singularity selected by the system in our case corresponds to $n = 1$, producing an integrable $r^{-\frac{1}{2}}$ singularity in p for case 1. The actual weight C_n applied to each of these eigensolutions can only be found by matching with the behaviour away from the corner, i.e., it does not come from just analysing the local behaviour.

We plot the expected pressure singularity for each case in Figure 4.2.7 and compare it to the obtained numerical solution when solved on a regular 80×80 mesh. For case 1, we have fitted the eigenfunction (4.22b) with $n = 1$ to the numerical solution for over the range at $0.1-y \in [0.003, 0.01]$, right before it begins to diverge. Closer to the singularity, the local analytical solution (4.22b) provides a better estimate than the numerical solution. In principle, this suggests that for case 1 we can choose a point δ, close to the singularity, which defines a cut-off length-scale after which we switch to the analytical prediction to estimate the integral.

We show the resulting pressure on $\partial\Omega_0$ for case 2 in Figure 4.2.7(b), where the non-integrable singularity (4.21b) is shown in the red dashed line. Hence, for this case, the integral of the normal stress on $\partial\Omega_0$ does not exist, consistent with the behaviour shown in Figure 4.2.5 where this numerical integral diverges as the mesh is refined. Therefore, we cannot use this boundary condition to estimate the weight of added cylinders on $\partial\Omega_0$.

Another approach to improve the estimate of the integral of the normal stress is to look at different mesh constructions, which we describe in the next section.

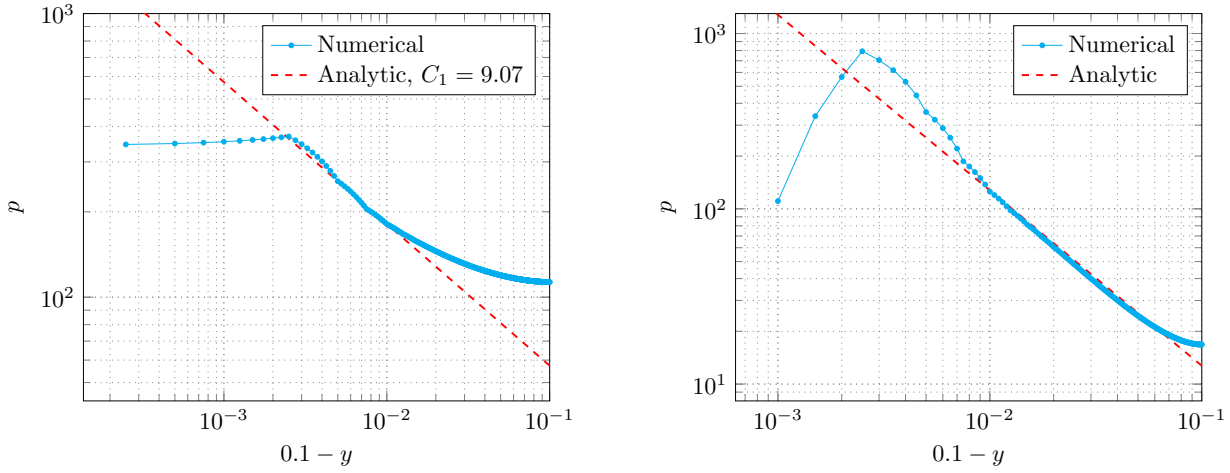

(a) $(\boldsymbol{\sigma}\cdot\boldsymbol{n})\cdot\boldsymbol{n} = 0$ on $\partial\Omega_1$ **(b)** $\boldsymbol{u}\cdot\boldsymbol{n} = 0$ on $\partial\Omega_1$

Figure 4.2.7 – The numerically computed pressure on $\partial\Omega_0$ close to $y = 0.1$ on the top boundary. The result for (a) case 1 is coupled with the eigenfunction (4.22b) with $n = 1$ and coefficient $C_1 = 8.92$ to fit the prediction of the singularity for $0.1 - y \in [0.003, 0.01]$; for (b) case 2, we use the form (4.20a) for the analytical comparison.

4.2.4 Alternative mesh constructions

Recall that our domain of interest is $\Omega \in [0, 1] \times [0, 0.2]$. A standard mesh option available in FEniCS is a rectangular domain split into 'crossed' rectangular cells, which we have used in all

examples so far. In Figure 4.2.8(a) we show the top part of this regular mesh for $x \in [0, 0.2]$. We now look at other mesh options to tackle the singularities at the top boundary described in §4.2.3 by using a mesh that is especially designed for our boundary conditions. We present here three such possibilities.

The first approach is a naive mesh refinement where the top boundaries are on a finer grid than the rest of the mesh, leaving a coarser mesh after the flow is fully developed. We call this mesh *top refined* and we show an example in Figure 4.2.8(b), for $x \in [0, 0.2]$. The second approach is simply having a finer discretisation in the horizontal direction than in the vertical direction, which we simply call *refined*. In fact there are many combinations of these two refinements that could also be attempted, but the principle is similar.

The third approach makes use of the goal oriented adaptivity available in FEniCS. This technique works by introducing an *a-posteriori* estimator for the error, based on a current evaluation of the numerical solution. The adaptivity procedure follows the local values of the estimator to add or remove mesh nodes to the domain, in such a way that the estimator is kept below a certain tolerance throughout the whole domain. For our purposes, we use a tolerance of 10^{-8}. Additional details can be found in Logg et al. (2012). We call this mesh *adaptive*, and an example of it is shown in Figure 4.2.8(c).

We compare the pressure evaluated at $\partial\Omega_0$ for different meshes in Figure 4.2.9 for both cases of boundary conditions, where the grey dashed lines correspond to the analytical predictions found in §4.2.3. The solution for the adaptive mesh is indistinguishable from the analytical prediction in case 1, and very close in case 2, whereas the regular mesh has the worst performance in both cases. It is not sufficient to refine near the top or to have more cells discretised in the horizontal direction, as shown by the red and green curves. Therefore, in all further computations we use adaptive meshes both for the isothermal problem and for the coupled problem.

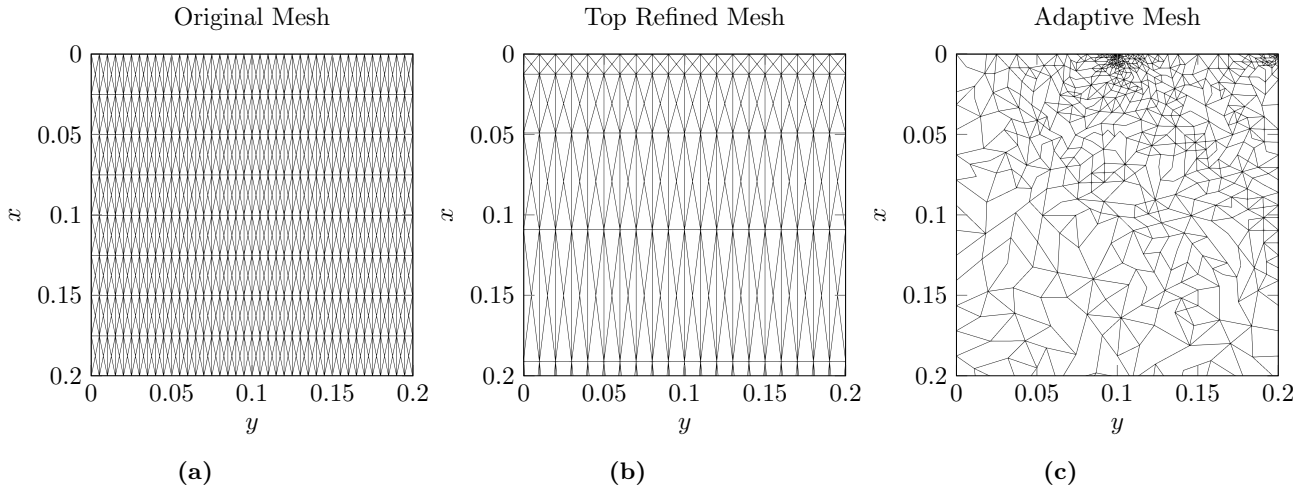

Figure 4.2.8 – Mesh examples used for the isothermal problem, where (a) consists of 40×40 cells, (b) consists of 20×20 cells with top refinement and (c) consists of an adaptive mesh obtained using the adaptive linear variational solver in FEniCS, with a starting mesh of 40×40 cells and a tolerance of 10^{-6}. Note that we show a coarser discretisation for visualisation purposes, and the actual mesh sizes used for the experiments have four times as many cells for (a) and (b), as well as a smaller tolerance of 10^{-8} for (c).

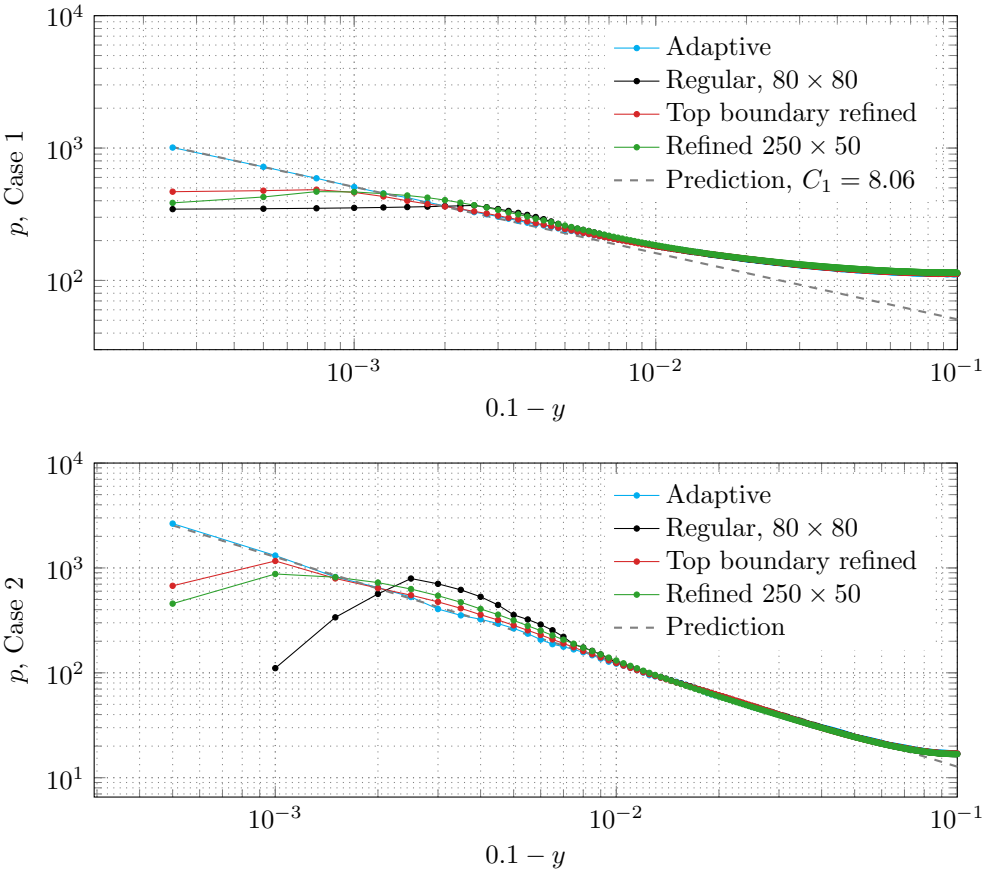

Figure 4.2.9 – Pressure p on the inlet boundary $\partial\Omega_0$ plotted versus distance from the singularity for the different meshes shown in Figure 4.2.8, as well as an additional refined mesh of 250×50 cells. The singularity at $y = 0.1$ is approximated with the prediction (4.22b) with $n = 1$ and fitted prefactor $C_1 = 8.06$ and (4.21b) for cases 1 and 2, respectively. The prefactor is chosen to fit the adaptive mesh curve for $0.1 - y \in [10^{-4}, 10^{-3}]$.

4.3 Coupled problem

We approach the non-dimensional coupled temperature and flow problem (4.7) using the lessons learned from the isothermal problem, namely by adopting an adaptive mesh and a careful consideration of the various singularities intrinsic to the problem. We discuss different coordinate systems and the two options for the boundary condition on $\partial\Omega_1$.

4.3.1 Varying coordinate systems

The variational form (4.11) can be adapted to different coordinate systems, and one of the goals of this chapter is to explore the difference between a 2D Cartesian geometry and an axisymmetric geometry. (The earlier Chapters 2 and 3 assumed axisymmetry, whereas the work in Chapter 5 will be based in two dimensions for simplicity).

We use the parameter values in Table 1.3.1 and perform all calculations in non-dimensional variables. We compare the velocity solutions for both coordinate systems in Figure 4.3.1 for the zero normal stress boundary condition (case 1), where we plot the streamlines and the velocity magnitude for the upper section of the domain, $[0, 0.2] \times [0, 0.2]$. The top panels show the results for the coupled problem and the bottom panels show the results for the isothermal problem, both using the adaptive mesh. In both coordinate systems, the inlet velocity is chosen to keep mass balance, resulting in $D = 0.5$ for the Cartesian case and $D = 0.25$ for the cylindrical case. The resulting integral of the square of the fluid flux on $\partial\Omega_1$ is also shown in the figures, where we note that the Cartesian case gives a lower value than across the cylindrical case, but not zero. This quantity gives an indication of how close we are to satisfying the true free boundary problem, which would have zero normal flux as well as zero normal stress. By approximating the free boundary as flat we cannot hope to satisfy this, but it is interesting to investigate how close we are. The upper right region present near the wall, where the fluid recirculates to match the wall velocity, is similar in both coordinate systems, although we note that in the cylindrical case this is slightly narrower, as seen in Figure 4.3.1(b). Since the cylindrical geometry is closer to the real industrial problem, we will favour this configuration in following examples. We also note that the small changes in temperature near the top boundary in the coupled problem lead to larger recirculation zones when compared to the isothermal case, although these differences are small. Consequently, the coupled problem presents a smaller boundary layer near the casing wall than its isothermal counterpart.

For comparison, we show the results of the coupled problem for the zero normal flow boundary condition (case 2) in Figure 4.3.2 where, as with the isothermal example, the paste seems to spread more rapidly towards $\partial\Omega_1$, although there is a small recirculating region seen near $r = 0.1$ in Figure 4.3.2(b). For this case, the small temperature changes near the top boundary do not lead to significant differences in the streamlines, as the recirculation occurs very close to the top, only slightly visible in the coupled cylindrical case.

Although the coordinate system and choice of boundary conditions significantly influences the flow, the temperature field is affected much less, as shown in Figure 4.3.3, where the qualitative behaviour is similar among all four examples. As Pe is large, diffusion effects are small, leading to the largest temperature contrast occurring near the induction heating zone $x \in [x_1, x_2] = [0.7, 0.9]$ at the bottom of the domain. The larger inlet velocity for the cylindrical case results in higher convective heat transport, as seen by comparing for example the contours in Figures 4.3.3(a) and 4.3.3(b), but in most cases the maximum temperature is reached at the bottom of the domain, near the centreline as the hot air heating acts as a cooling mechanism from the sides near the bottom.

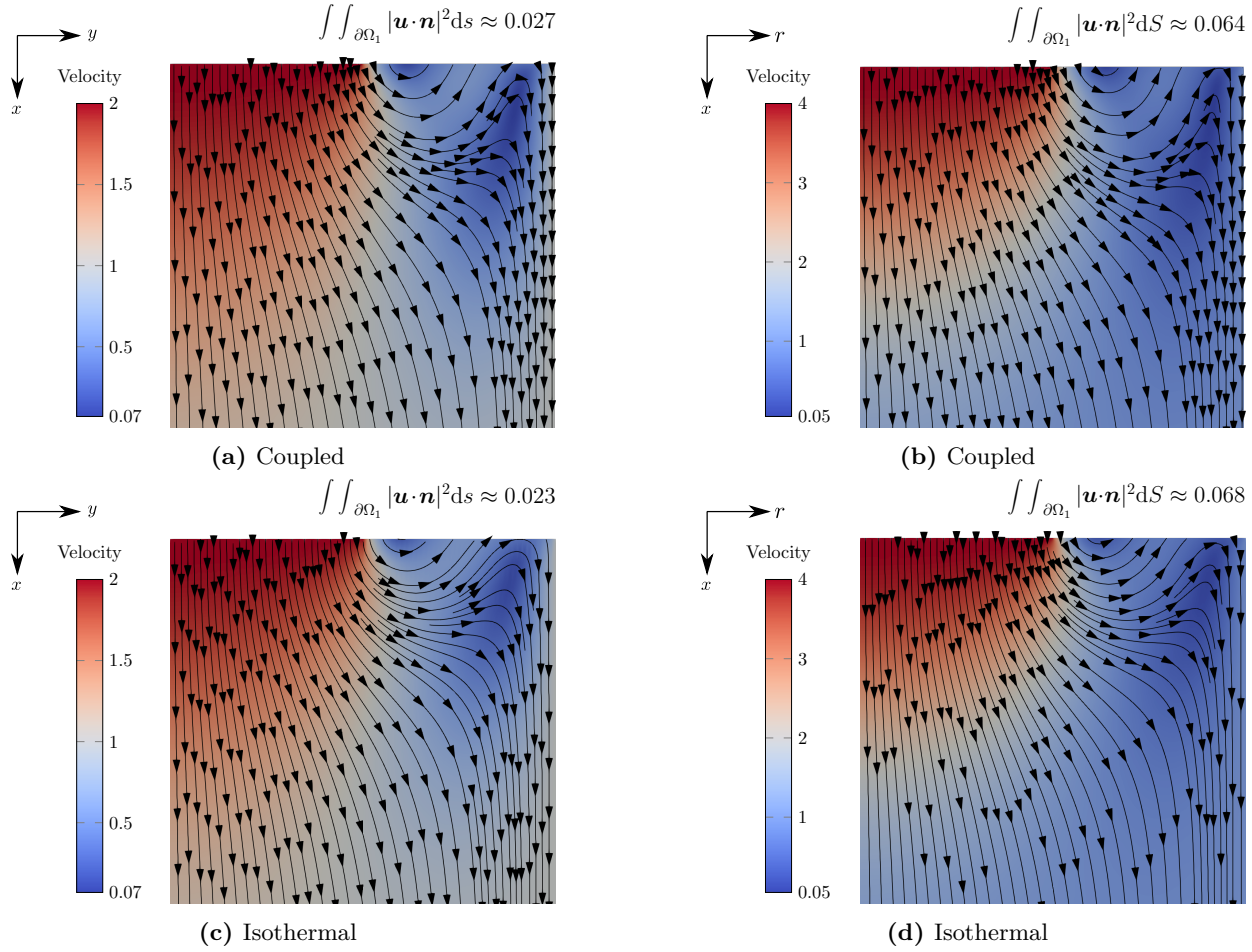

(a) Coupled **(b)** Coupled

(c) Isothermal **(d)** Isothermal

Figure 4.3.1 – Velocity streamlines shown for $x \in [0, 0.2]$ for the Cartesian (left) and cylindrical (right) coordinate cases, for the coupled (top) and isothermal problem (bottom) using parameter values from Table 1.3.1 and imposing boundary condition (4.6a). Here, $\bar{\mathrm{Bi}} = 11.6$, $\mathrm{Pe} = 27$, induction heating is given by (4.12), $\theta_a = x$, and (a) $D = 0.5$, (b) $D = 0.25$.

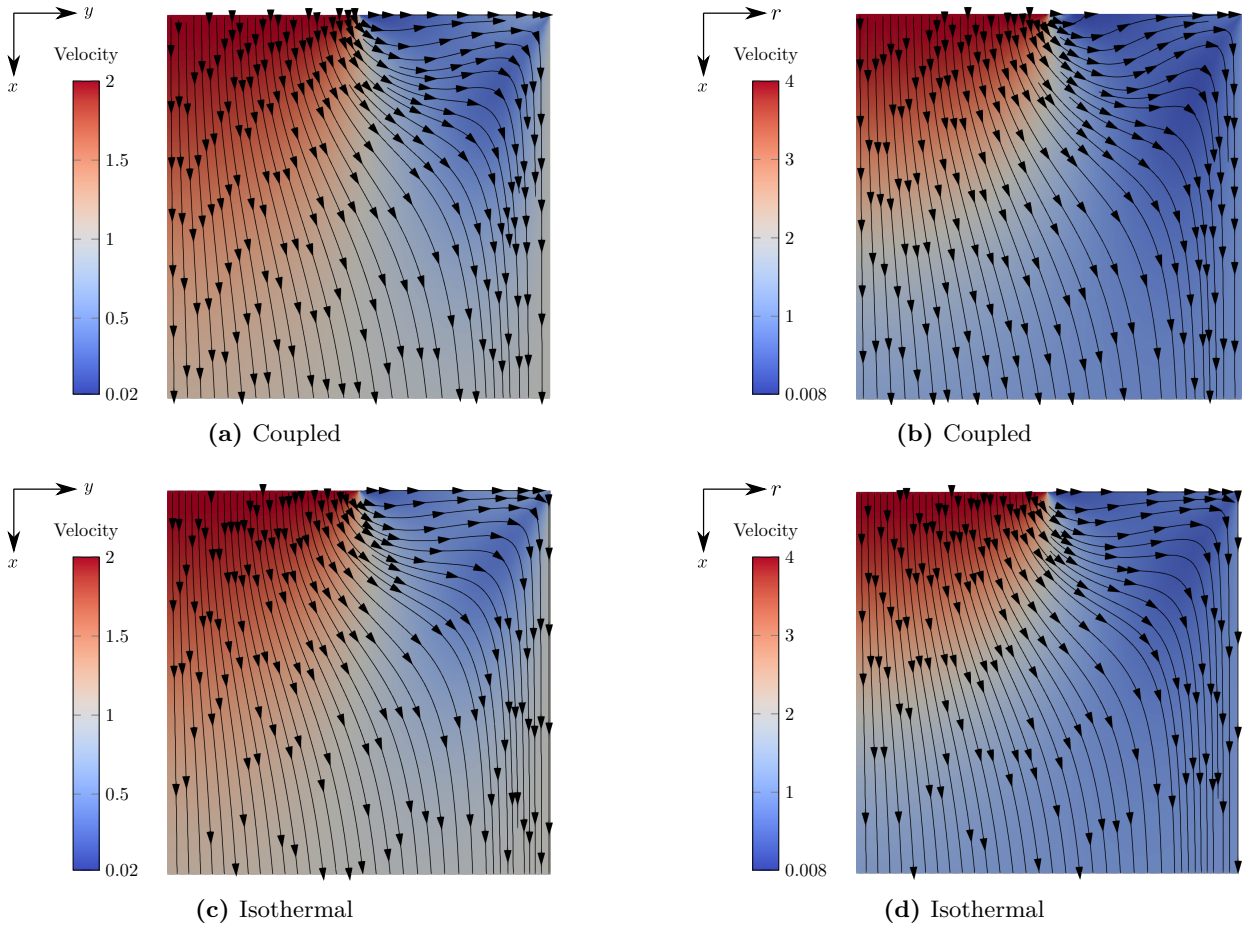

(a) Coupled **(b)** Coupled

(c) Isothermal **(d)** Isothermal

Figure 4.3.2 – Velocity streamlines shown for $x \in [0, 0.2]$ for the Cartesian (left) and cylindrical (right) coordinate cases, for the coupled (top) and isothermal problem (bottom) using parameter values from Table 1.3.1 and imposing boundary condition (4.6b). Here, St $= 1$, Bi $= 11.6$, Pe $= 27$, induction heating is given by (4.12), $\theta_a = x$, and (a) $D = 0.5$, (b) $D = 0.25$.

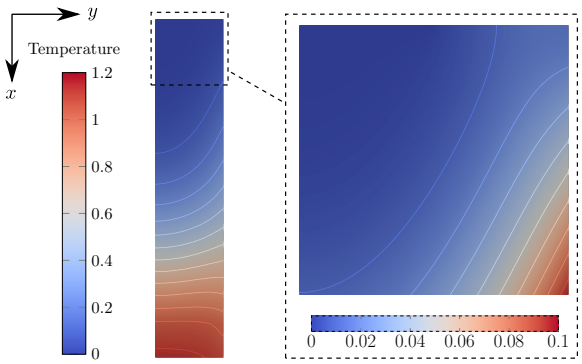

(a) Zero normal stress, Cartesian

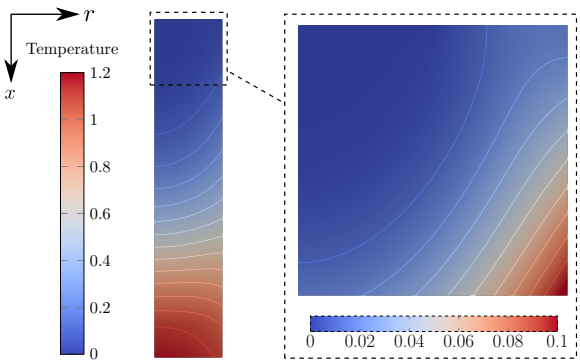

(b) Zero normal stress, cylindrical

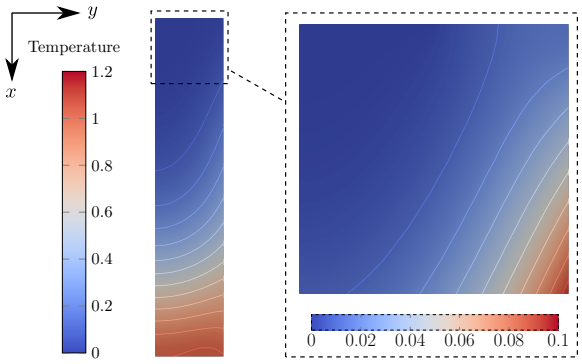

(c) Zero normal flow, Cartesian

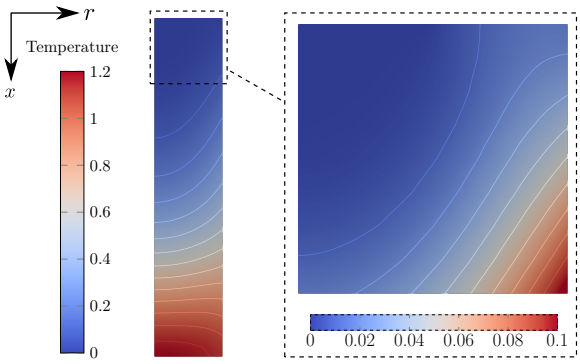

(d) Zero normal flow, cylindrical

Figure 4.3.3 – Temperature for the problem in Cartesian (left) and cylindrical (right) coordinates for both cases of boundary conditions on $\partial\Omega_1$ using parameter values from Table 1.3.1. Here, St $= 1$, $\bar{\text{Bi}} = 11.6$, Pe $= 27$, induction heating is given by (4.12) with $x_1 = 0.7$ and $x_2 = 0.9$, $\theta_a = x$, and $D = 0.5$ for the Cartesian case and $D = 0.25$ for the cylindrical case.

4.4 Investigating parameters

The circulation zones in the flow act to transport hot paste to the surface, which has been observed empirically in Elkem ASA as an indication of paste segregation, leading to a lower electrode quality (in terms of thermal and physical strength) after baking and increasing the risk of breakages; a correct temperature distribution is essential in electrode control (Olsen et al., 1972; Ray et al., 2007; Skjeldestad, 2019). The hotter the paste, the less viscous it is and the larger the recirculation zones are. If the paste is not sufficiently viscous in the recirculation zones it could lead to the uncontrolled sinking of paste cylinders, as depicted in Figure 1.1.2. In this section, we explore the effects of the parameters in the problem on the recirculation region of paste. We use the zero normal stress boundary condition (4.6a), unless stated otherwise, and solve in a cylindrical geometry.

4.4.1 Dependence on heating parameters

In the industrial problem, the heat transfer coefficient is a function of position, as it depends on whether the paste is in contact with the air, with the casing fins or with the metal casing itself. In our simplification we have imposed it as constant, and the role of the wall heating is investigated by changing $\overline{\mathrm{Bi}}$, whose value is 11.6 under normal operating conditions (i.e. using parameter values in Table 1.3.1). We compare three cases of $\overline{\mathrm{Bi}}$ in Figure 4.4.1, where we show the resulting velocity streamlines as well as the corresponding viscosity profiles. Figures 4.4.1(a) and 4.4.1(c) are extreme cases where the heat transfer coefficient at the wall is very small or very large.

In the absence of heat transfer from the wall, with $\overline{\mathrm{Bi}} = 0$, the only heating source is given by the induction heating Q. Since the Péclet number is large, the effect of induction heating does not significantly propagate upstream. In Figure 4.4.1(a), the viscosity appears close to constant, which results in smaller recirculation zones as the paste is harder to move. A larger viscosity contrast near the top of the domain is present in Figure 4.4.1(c), where the wall heating results in a hotter and hence less viscous paste pool at the upper right. The recirculating zone is slightly larger in this case.

Another practical aspect of our problem is that, although the paste is highly conductive after it is baked, it has low thermal conductivity when it is softening, which is precisely our region of interest. The heat diffusion effects are incorporated into the Péclet number, which in turn affects the impact of the induction heating Q. We investigate the dependence of the solution on this parameter in Figure 4.4.2, where a larger recirculation region is produced by a lower Pe, as expected since more heat conducts upwards from the induction heating zone in this case. In Figure 4.4.2(a) there is a small region near $\partial\Omega_0$ where most of the viscosity change occurs, which in practice would mean the presence of liquid paste through a large part of the domain above the baking region.

In our examples, we use a viscosity function (2.51) that allows the paste to soften quickly with temperature changes, but we have not incorporated the baking, which would begin to occur at

around 330°C. In the situation of Figure 4.4.2(a), we would expect baking to occur too close to the top of the domain and therefore breakage to occur. The Péclet number is also proportional to the casing velocity, which is an operating parameter that varies from plant to plant, and depends on operator experience and required production rates, which allows for some flexibility. The results in Figure 4.4.2 suggest that the casing velocity is an important control parameter for the size of the hot viscous pool near the casing wall, with a lower value associated with larger recirculation zones. This observation is in agreement with results found in the literature, where the casing velocity and the induction heating are identified as the main causes for electrode breakages, for example in Innvaer and Olsen (1979), Innvær et al. (1985), and Andersen et al. (2001).

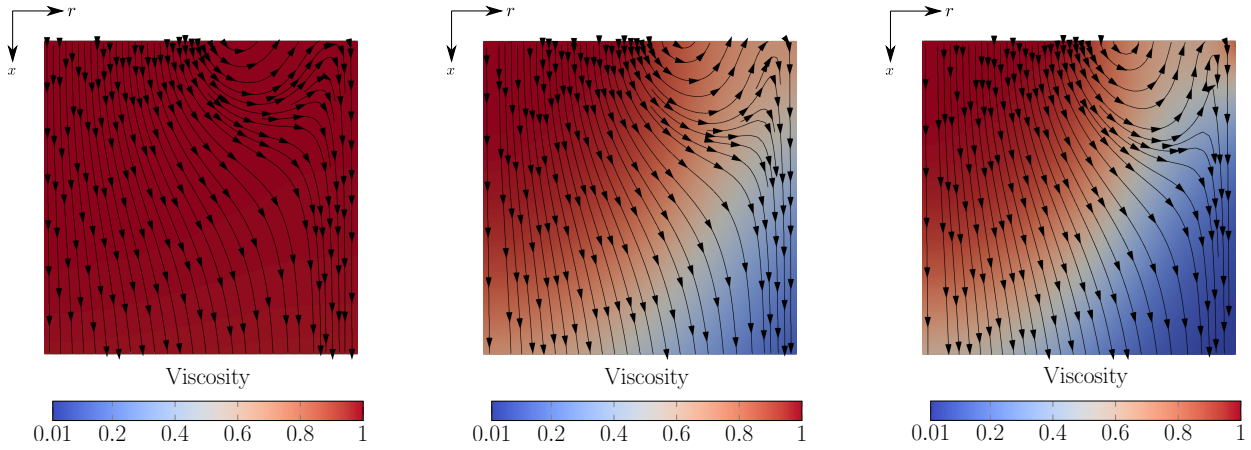

(a) $\overline{\text{Bi}} = 0$ **(b)** $\overline{\text{Bi}} = 12$ **(c)** $\overline{\text{Bi}} = 200$

Figure 4.4.1 – Velocity streamlines with background colour showing viscosity, for different $\overline{\text{Bi}}$. We show the top part of the domain $[0, 0.2] \times [0, 0.2]$. Cylindrical coordinates were used, with the zero stress boundary condition on $\partial\Omega_1$ as well as parameter values from Table 1.3.1, which give $\text{Pe} = 27$, induction heating given by (4.12), $\theta_a = x$, and $D = 0.25$.

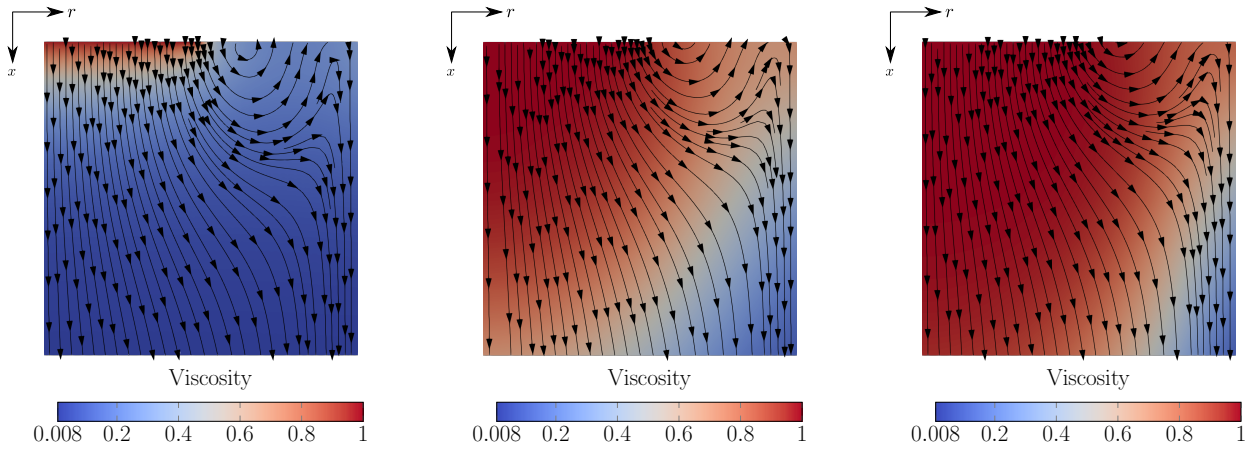

(a) $\text{Pe} = 0.1$ **(b)** $\text{Pe} = 27$ **(c)** $\text{Pe} = 60$

Figure 4.4.2 – Velocity streamlines with background colour showing viscosity, for different Pe. Cylindrical coordinates were used, with the zero stress boundary condition on $\partial\Omega_1$ as well as parameter values from Table 1.3.1, which give $\overline{\text{Bi}} = 11.6$, induction heating given by (4.12), $\theta_a = x$, and $D = 0.25$.

4.5 Relationship to weight of added cylinders

Cylinder addition is a transient behaviour, and our current model does not describe this process, which was investigated in detail in the time dependent model in Chapter 3. However, to approach this problem in an approximate way in our current model we propose two different strategies. In §4.5.1 we look at unsteady solutions by imposing an inlet velocity $u_{\text{in}} \neq 1/D$. In §4.5.2 we look at steady solutions (i.e. with $u_{\text{in}} = 1/D$) but with a displaced free surface, which is accounted for by shifting our coordinates appropriately. In each case we show the resulting integral of the normal stress on $\partial\Omega_0$, which is rescaled to show the equivalent number of cylinders.

4.5.1 Unsteady solutions with $u_{\text{in}} \neq 1/D$

We introduce a general (non-dimensional) inlet velocity

$$\boldsymbol{u} = (u_{\text{in}}, 0) \quad \text{on} \quad \partial\Omega_0, \tag{4.23}$$

which allows us to choose values away from the steady state, i.e. where $u_{\text{in}} \neq 1/D$. Recall that $D = 0.25$ (for the axisymmetric case) was chosen such that the inlet mass flux of the cylinders matches the outflow flux imposed by velocity of the wall. As we change u_{in} we are no longer matching the flux into and out of the domain. In reality, this means the free boundary $\partial\Omega_1$ must be moving upwards or downwards to accommodate the changing mass. The situation can be accommodated in our setup when prescribing zero stress on $\partial\Omega_1$ (case 1 in (4.6)), and in that case it results in a non-zero net flux across $\partial\Omega_1$, that can be associated with the upwards/downwards movement of the free surface.

This is seen in Figure 4.5.1, where for $u_{\text{in}} < 4$ we have a negative net flux, indicating that the paste domain must shrink, and conversely a positive net flux for $u_{\text{in}} > 4$ indicating that the paste domain must grow. The dashed line indicates the exact value of the average normal velocity calculated as $(u_{\text{in}}D - 1)/(1 - D)$. An example of this approach used to estimate numbers of cylinders is shown in Figure 4.5.2, where the inlet velocity is varied and the integral of the normal stress on $\partial\Omega_0$ is calculated. Supposing we specify the weight of cylinders added, we can use this to infer the velocity at which the cylinders sink into the paste. We convert the non-dimensional stress to an equivalent number of cylinders noting that the weight of one cylinder is approximately 14.2×10^3 N, and using a reference viscosity $\mu_0 = 1 \times 10^8$ Pa·s, appropriate for this particular simplification of the problem where we would expect that the material entering the domain has undergone some softening by the hot air above the domain. With these values, we estimate that approximately 2.8 cylinders will sink at the steady-state velocity $u_{\text{in}} = 1/D$, with $D = 0.25$, which is within the expected range of one to three cylinders that are normally added per day (Skjeldestad, 2019). The fact that this is a non-integer value is related in part to the irregular cylinder addition used in practice and discussed in Chapter 3 where we explored various cylinder addition patterns.

This method could provide us a way to model observations made by Elkem ASA regarding the hot paste level increasing as paste cylinders are being stacked on top and decreasing as the height of cylinders then gradually decreases. This is an alternative to the cylinder addition investigated in Chapter 3, where we describe how the softened paste reaches the casing for the first time at $x = \lambda(t)$. The results shown in Figure 4.5.1 are consistent with our results from Chapter 3, where we had that cylinder addition causes $\lambda(t)$ to move upwards, which corresponds to the observation that the domain must grow for positive net flux.

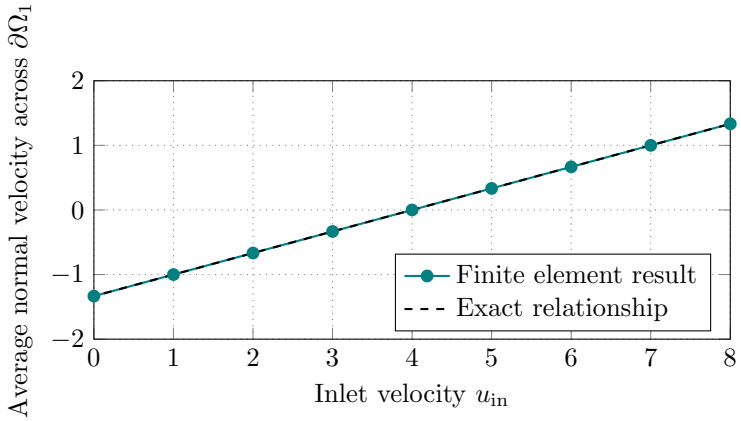

Figure 4.5.1 – Average normal velocity across $\partial\Omega_1$, for different inlet velocity u_{in} imposed at $\partial\Omega_0$. We use cylindrical coordinates with domain $[0, 1] \times [0, 0.2]$ and standard parameters from Table 1.3.1, which give $\text{Pe} = 27$, $\overline{\text{Bi}} = 11.6$, induction heating given by (4.12), $\theta_a = x$, and $D = 0.25$. The dashed line shows the exact value for the average normal velocity at this boundary, $(u_{\text{in}}D - 1)/(1 - D)$.

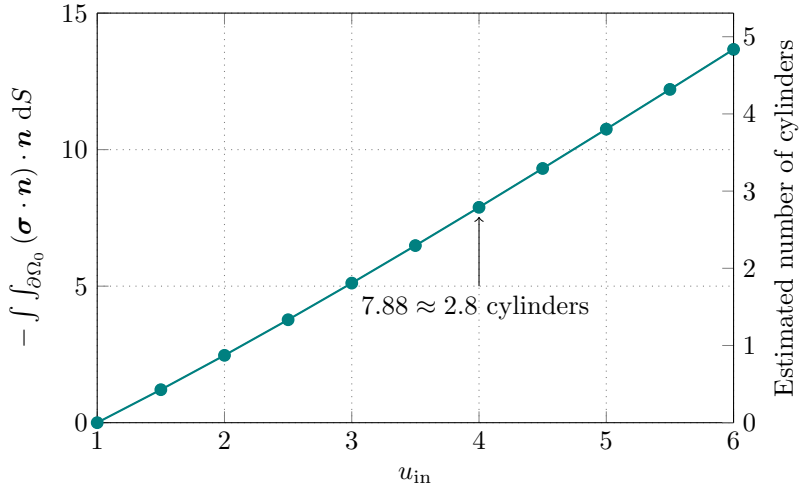

Figure 4.5.2 – Integral of the normal stress on $\partial\Omega_0$, along with an estimate of the corresponding number of cylinders with a specified inlet velocity u_{in}. $u_{\text{in}} = 1/D = 4$ corresponds to the steady state. We have used standard parameters from Table 1.3.1, which give $\text{Pe} = 27$, $\overline{\text{Bi}} = 11.6$, induction heating given by (4.12), $\theta_a = x$, and $D = 0.25$.

4.5.2 Steady solutions with a displaced free surface

In the previous section we saw that only one particular value of the weight of the added cylinders could correspond to $u_{\text{in}} = 1/D$ and a steady position of the free surface. Other values result in the free surface moving up or down. We now investigate steady states for different weights once the free surface has been allowed to adjust its position. Such solutions can be found in our model by simply shifting the coordinates. Using coordinates in which $x = 0$ still corresponds to the location of the free surface, this is equivalent to modifying the heating terms to

$$Q = \tilde{Q}_I \exp\left(-\frac{\left(x - \frac{x_1+x_2}{2} - X\right)^2}{2\left(x_2 - x_1\right)^2}\right), \tag{4.24}$$

and

$$\theta_a = \begin{cases} 0 & \text{for} \quad x \leq X, \\ x - X & \text{for} \quad X \leq x \leq 1 + X, \\ 1 & \text{for} \quad x \geq 1 + X, \end{cases} \tag{4.25}$$

where X is the value of the shift. The problem is described in the schematic in Figure 4.5.3, where $X > 0$ indicates that the free surface has moved upward and $X < 0$ indicates that the free surface has moved downward relative to the fixed position of the heating elements. We are essentially moving where the top of our domain is, keeping the same velocity condition at the outlet (which is also moved, since we keep the same length of domain, but which should not affect the behaviour in our region of interest as seen in §4.2.1). Since we are working in a steady state, we perform the computation for a given X and evaluate the integral of the normal stress on $\partial\Omega_0$, and the result is shown in Figure 4.5.4, for different $\overline{\text{Bi}}$.

As we did in §4.5.1, we relate the height of the free surface to the estimated number of cylinders added, shown in Figure 4.5.4, on the right y axis. When the free surface has moved downward ($X < 0$), it supports a lower number of cylinders, which is consistent with observations. When the free surface has moved upward ($X > 0$), the number of cylinders increases until its height is far enough from the heating terms that the changes in normal stress with any further change in X are small. In particular, we note that a higher free surface (larger X) is required if $\overline{\text{Bi}}$ is higher (see Figure 4.5.4) for the the same number of cylinders, as a higher $\overline{\text{Bi}}$ requires the free surface to be increased so that the paste is viscous enough to provide the required stress.

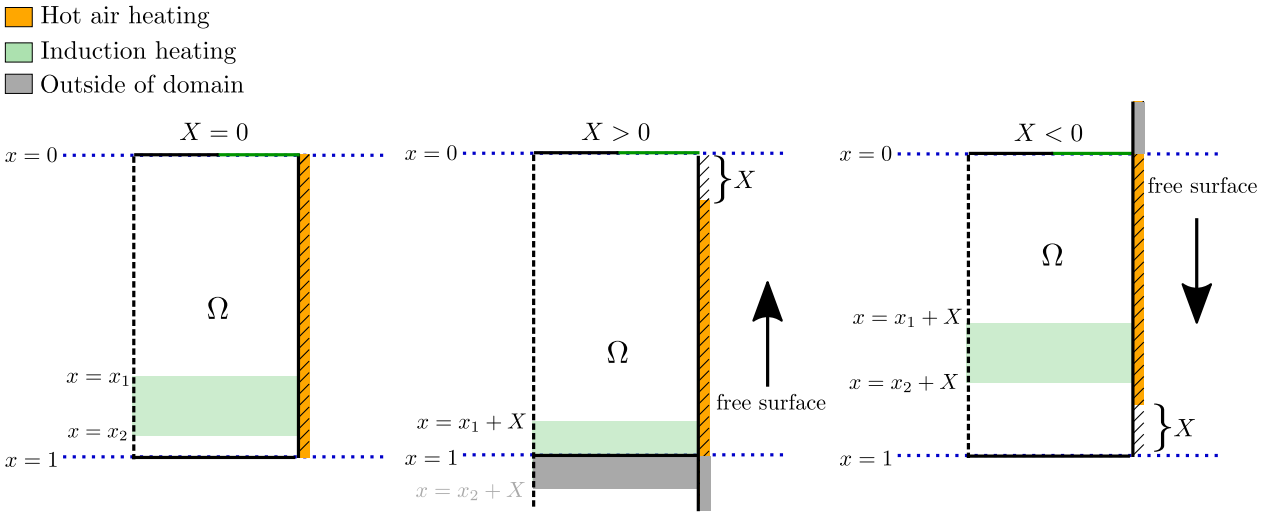

Figure 4.5.3 – Schematic for the vertical displacement X of the free surface, where $x = 0$ corresponds to a different height in each case. When $X > 0$, the free surface is shifted upwards and when $X < 0$ it is shifted downwards.

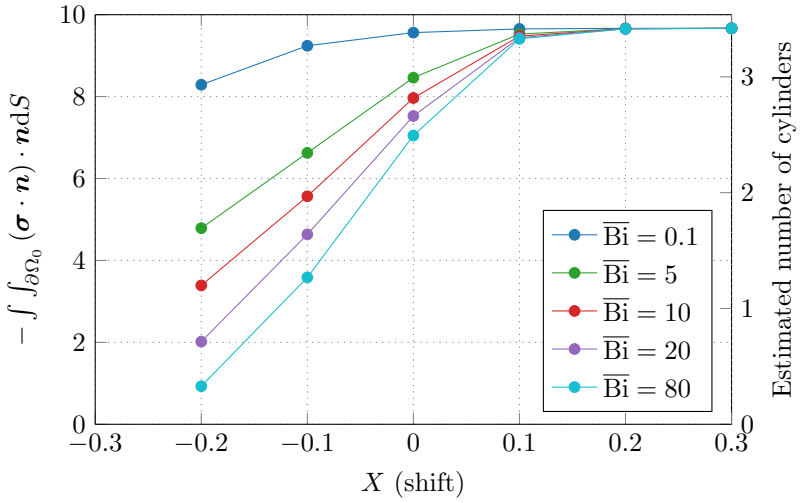

Figure 4.5.4 – Integral of the normal stress on $\partial\Omega_0$ for each position of the flat free surface, and for different values of $\overline{\mathrm{Bi}}$, with $X > 0$ reflecting a shift upwards, and $X < 0$ a shift downwards. We have used cylindrical coordinates and parameter values in table 1.3.1, which give, $D = 0.25$, $\mathrm{Pe} = 27$ and $\overline{\mathrm{Bi}} = 11.6$. We have used (4.24) for induction heating and (4.25) for θ_a.

4.6 Concluding remarks

In this chapter we have formulated an idealised boundary-value problem for the flow in the region where the paste is in contact with the casing. In §4.1 we described the domain and the mathematical problem and discussed the possibility of two different boundary conditions on the top right boundary, namely zero normal stress and zero normal flow. We looked at the top part of the casing, above the contact clamps and hence without any baking effects. We used the open source CFD software FEniCS to obtain numerical solutions in each case.

In §4.2 we solved the isothermal problem, performed a convergence test for a known manufactured solution, and discussed the differences between imposing a zero normal stress or a zero normal flow boundary condition on the top right boundary of the domain. We identified recirculation zones in the paste indicating the upwards transport of relatively hot paste to the surface. In §4.2.3 we identified corner singularities in the flow which make computations of the pressure and normal stress difficult. We created an adaptive mesh in §4.2.4 to tackle some of these difficulties.

In §4.3 we solved for the coupled temperature and flow problem in Cartesian and cylindrical coordinates, and we showed that, although the latter is closer to the real geometry of the problem, both frameworks provide similar numerical results. This observation allows us to compare with the results from Chapter 2.

In §4.4 we investigated the effect of varying the heating parameters, $\overline{\mathrm{Bi}}$ and Pe, as well as the inlet velocity. In particular, a higher $\overline{\mathrm{Bi}}$, and therefore increasing the effects of heating on the casing wall, leads to a greater viscosity change in the paste closer to the wall and allows for larger recirculation zones. Similarly, a smaller Pe, related to higher conduction and lower casing velocity, results in larger recirculation zones. In §4.5.1 we presented a naive approach to the dynamic free surface problem by allowing the inlet velocity to differ from the steady state value, and calculating the corresponding weight of cylinders above the domain. In §4.5.2 we return to steady states but vary the wall heating and induction heating in such a way to represent the free surface having moved upwards or downwards. We have effectively related the change of the free surface position to the weight of the cylinders on $\partial\Omega_0$, showing that a higher level of hot paste near the wall corresponds to a greater weight of cylinders on top.

To make the problem tractable, we have simplified the boundary conditions significantly. We replaced the free surface between the paste and the surrounding air by a flat boundary where zero shear stress and zero heat conduction boundary conditions are imposed, as well as a given form for the inductive heat flux Q to represent the induction caused by the copper tubes that lead to the clamps. Despite all of these artificial simplifications, our model produces encouraging results, in particular predicting the presence of a recirculation zone which transports relatively hot paste upwards, potentially giving rise to the observed pool of less viscous paste at the surface, and to segregation. Our model allows us to explore how the strength and structure of the recirculation

zone depend on the control parameters. Nevertheless, to obtain more physically realistic results it may be necessary to make the boundary conditions more realistic.

In the next chapter we attempt to understand some more of the flow structures observed in the simulations by asymptotic analysis in the limit where the casing is long and thin and the viscosity varies dramatically across its width.

Chapter 5

A coupled temperature and flow problem with extreme transverse viscosity variation

In this chapter, we simplify the full problem in steady state described in Chapter 4 by exploiting the small aspect ratio of the geometry. Usually, this results in one of two possible distinguished limits: either lubrication theory if no slip conditions are applied at the wall (Langlois and Deville, 2014), or extensional flow if the boundary of the problem is stress-free (Ockendon and Ockendon, 1995), as was done in Bergstrøm et al. (1989) and as we did in Chapter 2. However, when there are extreme viscosity variations across the fluid layer, there is an alternative hybrid limit, with extensional flow in the centre and lubrication flow towards the edge of the domain. In this chapter, we simplify the calculations by considering a two-dimensional geometry, with the fluid occupying a rectangular domain, but in principle an analogous approach will work for the axisymmetric geometry relevant to a Søderberg electrode.

We begin our approach for the extreme viscosity variation modelling by deriving a general 2D model for fluid occupying a rectangular domain. In §5.1 we analyse problem where the temperature profile is known and the resulting flow is to be determined. In §5.1.1 we formulate a two-dimensional model, which is then non-dimensionalised and scaled in a form analogous to the two-dimensional extensional flow formulation, (see e.g. Howell, 1994). This model is then reduced asymptotically in a distinguished limit where the viscosity near the walls is much smaller than that in the bulk of the flow. The leading-order model comprises an outer extensional (plug) flow with lubrication layers near the walls. By approximating integrals of the temperature profile using Laplace's method, the problem is reduced to a system dependent solely on the values of the temperature and temperature gradients at the wall and the centre-line.

In §5.2 we look at the complementary problem for the temperature (the heat equation), assuming

a given velocity profile. In §5.3 we describe the numerical solution for a constant velocity away from the walls. We find that rapid reverse flow in the boundary layers near the walls leads to a novel thermal boundary condition that propagates information upstream, whose effects we analyse in §5.4.

In §5.5 we describe a numerical method to solve the coupled flow and temperature problem, taking advantage of the approximations calculated in previous sections and we explore the dependence of the solutions on the parameters of the problem in §5.6. We discuss the conclusions to these approaches in §5.7.

Before we begin to describe our approach, we first comment on some relevant literature. The effects of a temperature dependent viscosity in fluid flow have been studied extensively over the years with diverse applications such as glass re-drawing (O'Kiely et al., 2015), polymer production Pearson (1977), and the study of magma transport (Morris, 1982) and planetary mantles (Khaleque et al., 2015). Lubrication theory is used to model Newtonian incompressible fluids with an exponential or algebraic viscosity-temperature dependence. Most notably, Ockendon and Ockendon (1977) considered (Newtonian) fluid flow in a channel that is suddenly heated or cooled, ignoring inertia effects and viscous dissipation. The downstream viscosity at the channel wall is assumed to differ by an order of magnitude from that in the upstream flow. Asymptotic solutions were shown for an exponential viscosity function for the 2D case and discussed for the axisymmetric case. Morris (1982) followed a similar approach for the slow flow past a sphere with a large viscosity contrast which produced regions where the flow shows qualitatively isoviscous behaviour, as the essential viscosity variations occur over a distance much shorter than the lengthscale of the temperature.

In our model, viscous dissipation effects are considered to be small, but there are numerous studies on extreme viscosity contrasts where these effects are dominant. Pearson (1977) calculated asymptotic solutions for the flow and temperature behaviour in fluids with rapidly varying exponential viscosity where viscous dissipation is entirely responsible for temperature variations. Ockendon (1979) extended these results by showing the boundary layer structure of a 2D heated channel with exponential viscosity and dissipative heating. Further relevant studies in heated channels with high viscosity-temperature dependence with dissipative heating are Joseph (1964), Wylie and Lister (1995), and Costa and Macedonio (2005), who also investigated the associated instabilities which can trigger secondary flows due to viscosity stratification. Most recently, Sloman et al. (2020) studied thermally driven dripping of a highly viscous fluid in a cylinder with applications to Elkem ASA pilot furnaces. An axisymmetric geometry was used, with a long and thin asymptotic reduction, and the formation of a crust inside the furnace was studied. In all these studies, lubrication theory was used to reduce the problem, whereas in our approach we find the hybrid limit with extensional flow in the centre and lubrication flow towards the wall.

A similar distinguished limit was found by Stewart et al. (2015) in the study of extreme viscosity contrast in a planar free liquid film with applications to surfactants. Their main focus was on

instabilities that lead to the rupture of the film and the hybrid limit was briefly discussed, where extensional flow is present in the top layer and lubrication equations describe the bottom layer. Across the interface between the two layers, continuity of stress and continuity of velocity is assumed. However, they do not consider temperature variations in their model as we do in §5.2 and §5.5, for the coupled problem.

5.1 Flow problem with known temperature

5.1.1 Governing equations and boundary conditions

We consider the general problem of a two-dimensional slow-flow of a Newtonian fluid with viscosity highly dependent on the temperature. This is similar to what we did in Chapter 2, but now in the domain where the paste is fully in contact with the casing and with significant temperature variation in the transverse direction as well as the flow direction. The geometry is represented in the schematic in Figure 5.1.1. We consider a rectangular domain in the (x, y) plane, with the casing wall at $y = H$ and a symmetry line at $y = 0$. Paste flows in through the boundary at $x = 0$, and we denote by $\bar{L}$ the length-scale in the x-direction.

The flow is governed by the two-dimensional steady state Stokes equations, which we write in Cartesian coordinates, as

$$u_x + v_y = 0, \tag{5.1a}$$

$$p_x = \left[\mu\left(u_y + v_x\right)\right]_y + \left(2\mu u_x\right)_x, \tag{5.1b}$$

$$p_y = \left[\mu\left(u_y + v_x\right)\right]_x + \left(2\mu v_y\right)_y. \tag{5.1c}$$

The boundary conditions are as depicted in Figure 5.1.1. At the casing wall $y = H$ we have no slip, with a specified casing velocity u_c. We also impose symmetry conditions at the centre-line $y = 0$. We defer discussion of the boundary conditions to be imposed at the up- and downstream ends of the domain until we have derived our leading-order model.

We are interested in situations where the viscosity $\mu(x, y)$ varies dramatically across the domain. We consider two regions, shown in Figure 5.1.1, where region (i) consists of high viscosity paste and region (ii) consists of softened paste. On the interface between the two regions, $y = h(x)$, we have the continuity conditions

$$[\boldsymbol{\sigma} \cdot \mathbf{n}] = 0, \tag{5.2a}$$

$$[\mathbf{u}] = 0, \tag{5.2b}$$

where $[\cdot]$ denotes the jump across the interface and $\mathbf{n}$ is a vector normal to the interface, written as

$$\mathbf{n} = \frac{1}{\sqrt{1+h_x^2}} \begin{pmatrix} -h_x \\ 1 \end{pmatrix}, \tag{5.3}$$

and $\boldsymbol{\sigma}$ is the stress tensor, written as

$$\boldsymbol{\sigma} = \begin{pmatrix} -p + 2\mu u_x & \mu\left(u_y + v_x\right) \\ \mu\left(u_y + v_x\right) & -p + 2\mu v_y \end{pmatrix}. \tag{5.4}$$

In reality we expect the viscosity to vary continuously, although rapidly, across the domain, so the location of the boundary $y = h(x)$ between the "high viscosity" and "softened" paste may not be uniquely defined; however, we will find below that the leading-order behaviour does not depend on the precise definition of $h(x)$.

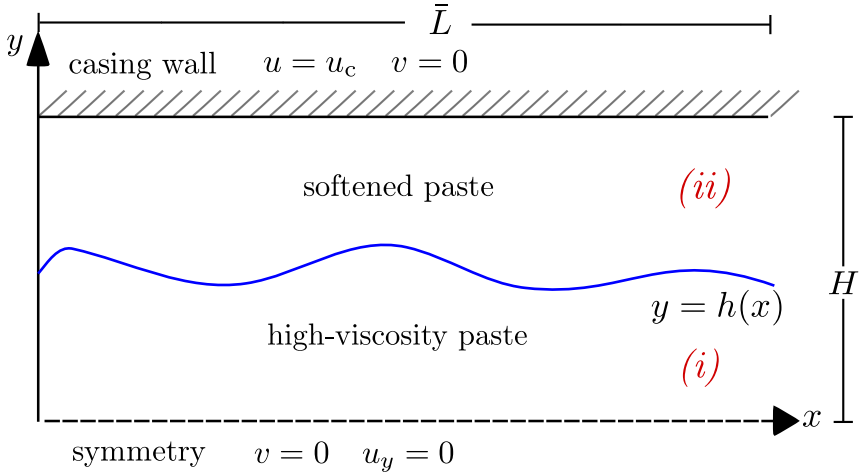

Figure 5.1.1 – Sketch of the dimensional geometry and boundary conditions.

5.1.2 Non-dimensionalisation and scaling

For the scaling of the system (5.1) we assume a small aspect ratio, $\epsilon = \frac{H}{\bar{L}} \ll 1$, which allows us to use a version of lubrication theory. With this assumption, we choose the scalings

$$x = Lx', \quad y = \epsilon L y', \quad u = u_c u', \quad v = \epsilon u_c v', \quad h = \epsilon \bar{L} h', \quad p = \frac{u_c \mu_0}{\bar{L}} p', \quad \mu = \mu_0 \mu', \tag{5.5}$$

where the viscosity has been normalised with its maximum value μ_0. We consider a distinguished limit in which the dimensionless viscosity μ' varies by a factor of $\mathcal{O}\left(\epsilon^2\right)$ across the channel.

Specifically we assume

$$\text{region (i):} \qquad \mu' = \mathcal{O}(1) \quad \text{for} \quad 0 < y < h(x), \tag{5.6a}$$

$$\text{region (ii):} \qquad \frac{\mu'}{\epsilon^2} = M = \mathcal{O}(1) \quad \text{for} \quad h(x) < y < 1. \tag{5.6b}$$

The difference in the scaling for μ' across the channel allows us to write differently scaled 2D Stokes equations for each region. We henceforth neglect the primes on the dimensionless variables.
For *(i)* we have an *extensional flow* scaling,

$$u_x + v_y = 0, \tag{5.7a}$$

$$\epsilon^2 p_x = \left[\mu\left(u_y + \epsilon^2 v_x\right)\right]_y + 2\epsilon^2 \left(\mu u_x\right)_x, \tag{5.7b}$$

$$p_y = \left[\mu\left(u_y + \epsilon^2 v_x\right)\right]_x + 2\left(\mu v_y\right)_y, \tag{5.7c}$$

in $0 < y < h(x)$, with

$$v = u_y = 0 \quad \text{at } y = 0. \tag{5.8}$$

For *(ii)* we have a *lubrication* scaling,

$$U_x + V_y = 0, \tag{5.9a}$$

$$P_x = \left[M\left(U_y + \epsilon^2 V_x\right)\right]_y + 2\epsilon^2 \left(M U_x\right)_x, \tag{5.9b}$$

$$P_y = \epsilon^2 \left[M\left(U_y + \epsilon^2 V_x\right)\right]_x + 2\epsilon^2 \left(M V_y\right)_y, \tag{5.9c}$$

in $h(x) < y < 1$, with

$$V = 0, \quad U = 1 \quad \text{at } y = 1. \tag{5.10}$$

Note that in order to distinguish the variables in each region, the velocity, pressure and viscosity notation is capitalised in region *(ii)*. At $y = h(x)$ we impose conditions (5.2) of continuity of velocity and stress, namely

$$u = U, \quad v = V, \tag{5.11}$$

for the continuity of velocity, and

$$\left(1 + \epsilon^2 h_x^2\right) p + 2\mu\left(1 - \epsilon^2 h_x^2\right) u_x + 2\mu h_x \left(u_y + \epsilon^2 v_x\right) = \left(1 + \epsilon^2 h_x^2\right) P + 2\epsilon^2 M \left(1 - \epsilon^2 h_x^2\right) U_x + 2\epsilon^2 M h_x \left(U_y + \epsilon^2 V_x\right), \tag{5.12a}$$

$$\mu\left(u_y + \epsilon^2\left(1 - \epsilon^2 h_x^2\right) v_x - 4\epsilon^2 h_x u_x - \epsilon^2 h_x^2 u_y\right) = \epsilon^2 M \left(U_y + \epsilon^2\left(1 - \epsilon^2 h_x^2\right) V_x - 4\epsilon^2 h_x U_x - \epsilon^2 h_x^2 U_y\right), \tag{5.12b}$$

at $y = h(x)$ for the continuity of stress. A schematic of the dimensionless version of the problem is shown in Figure 5.1.2.

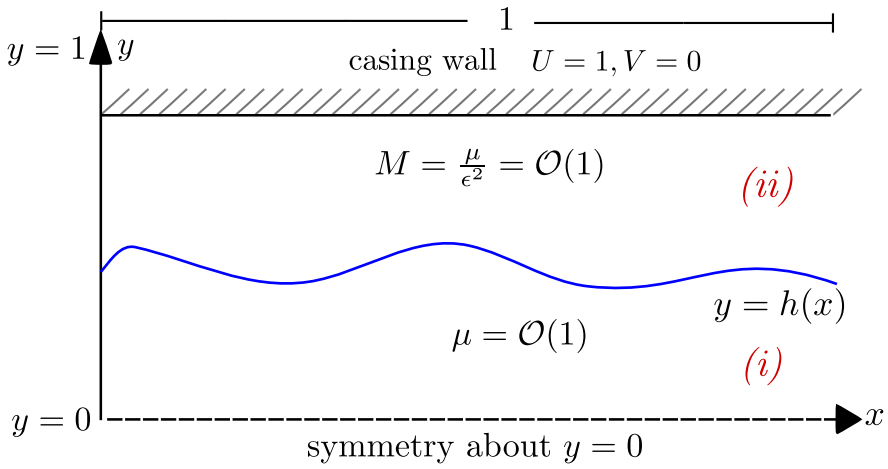

Figure 5.1.2 – Schematic of the problem in non-dimensional form.

5.1.3 Asymptotic expansions

We expand in asymptotic expansions in powers of ϵ^2, i.e.

$$u \sim u^{(0)} + \epsilon^2 u_1 + \ldots, \quad v \sim v^{(0)} + \epsilon^2 v_1 + \ldots, \quad p \sim p^{(0)} + \epsilon^2 p_1 + \ldots, \tag{5.13}$$

and similarly for U, V, and P. We take $\mu(x, y)$ and $h(x)$ as known (for the moment) so they are not expanded. Then in region *(i)*, the leading order solution is

$$u^{(0)} = u^{(0)}(x), \quad v^{(0)} = -y u_x^{(0)}(x), \tag{5.14}$$

so we have extensional flow to leading order. For the pressure we have that

$$p^{(0)}(x, y) = -2\mu(x, y)\ u_x^{(0)}(x) + g(x), \tag{5.15}$$

where $g(x)$ is an arbitrary function of x representing the normal stress exerted by the lubrication flow region *(ii)* on the extensional flow region *(i)*. By integrating (5.15) with respect to y, we can write $g(x)$ as

$$g(x) = \bar{p}^{(0)}(x) + 2\bar{\mu}(x)\ u_x^{(0)}(x), \tag{5.16}$$

where the overbar notation denotes the average, $\bar{\mu}(x) = \frac{1}{h}\int_0^h \mu(x, y)\mathrm{d}y$, and similarly for $\bar{p}^{(0)}(x)$. Then we can rewrite (5.15) as

$$p^{(0)}(x, y) = \bar{p}^{(0)}(x) + 2\left(\bar{\mu}(x) - \mu(x, y)\right) u_x^{(0)}(x). \tag{5.17}$$

Then, from (5.7b) at $\mathcal{O}(\epsilon^2)$ we get

$$\mu\left(u_y^{(1)} + v_x^{(0)}\right) = y\left(\bar{p}^{(0)} + 2\bar{\mu}u_x^{(0)}\right)_x - 4\left(u_x^{(0)}\int_0^y \mu \mathrm{d}\eta\right)_x, \tag{5.18}$$

for $0 < y < h(x)$.

In the second region $h(x) < y < 1$, where we have the lubrication scaling, we find that

$$P^{(0)} = P^{(0)}(x), \tag{5.19a}$$

$$U^{(0)}(x,y) = 1 - P_x^{(0)}(x)\int_y^1 \frac{(\eta-1)\,\mathrm{d}\eta}{M(x,\eta)} - B(x)\int_y^1 \frac{\mathrm{d}\eta}{M(x,\eta)}, \tag{5.19b}$$

where $B(x) = M(x,1)\ U_y^{(0)}(x,1)$ is the shear stress on the wall. Then the transverse velocity is given by

$$V^{(0)}(x,y) = \int_y^1 U_x^{(0)}(x,\eta)\mathrm{d}\eta. \tag{5.20}$$

Now we apply continuity conditions so that

$$u^{(0)} = U^{(0)}, \qquad v^{(0)} = V^{(0)}, \tag{5.21a}$$

$$p^{(0)} + 2\mu u_x^{(0)} = P^{(0)}, \qquad \mu\left(u_y^{(1)} + v_x^{(0)} - 4h_x u_x^{(0)}\right) = MU_y^{(0)}, \tag{5.21b}$$

at $y = h$ and thus

$$P^{(0)}(x) = \bar{p}^{(0)} + 2\bar{\mu}u_x^{(0)}, \tag{5.22a}$$

$$u^{(0)}(x) = 1 - P_x^{(0)}\int_h^1 \frac{(y-1)\,\mathrm{d}y}{M(x,y)} - B\int_h^1 \frac{\mathrm{d}y}{M(x,y)}. \tag{5.22b}$$

From the continuity of v we can also obtain the net mass conservation equation

$$u^{(0)}(x)h(x) + \int_h^1 U^{(0)}(x,y)\mathrm{d}y = q, \tag{5.23}$$

where q is the constant average velocity of the fluid.

We integrate (5.19b) to obtain

$$\int_h^1 U^{(0)}\mathrm{d}y = 1 - h - P_x^{(0)}\int_h^1 \frac{(y-h)(y-1)}{M(x,y)}\mathrm{d}y - B\int_h^1 \frac{(y-h)\mathrm{d}y}{M(x,y)}, \tag{5.24}$$

which we substitute into (5.23) to get

$$q - 1 + (1-u^{(0)})h = -P_x^{(0)}\int_h^1 \frac{(y-h)(y-1)}{M(x,y)}\mathrm{d}y - B\int_h^1 \frac{(y-h)\mathrm{d}y}{M(x,y)}. \tag{5.25}$$

Combining with (5.22b), this becomes

$$q-1=-P_x^{(0)}\int_h^1\frac{y\,(y-1)}{M(x,y)}\mathrm{d}y-B\int_h^1\frac{y\mathrm{d}y}{M(x,y)}. \tag{5.26}$$

The continuity of shear stress gives

$$h\Big(\bar{p}^{(0)}+2\bar{\mu}u_x^{(0)}\Big)_x-4\int_0^h\Big(\mu u_x^{(0)}\Big)\,x\mathrm{d}y-4\mu\big|_{y=h}h_xu_x^{(0)}=(h-1)P_x^{(0)}+B, \tag{5.27}$$

which simplifies to

$$\Big(4h\bar{\mu}u_x^{(0)}\Big)_x=P_x^{(0)}-B, \tag{5.28}$$

an axial force balance, analogous to that in the Trouton model (Dewynne et al., 1989), but in this case including the shear stress, B, applied to layer *(i)* by layer *(ii)*.

In summary, if the viscosity profile is specified, so that $M(x,y)$, $\bar{\mu}(x)$ and $h(x)$ are all known functions, then equations (5.22b), (5.26), and (5.28) provide a closed system for the core axial velocity $u^{(0)}(x)$, lubrication pressure $P^{(0)}(x)$, and shear stress $B(x)$.

Now, since $M=\frac{\mu}{\epsilon^2}=\mathcal{O}(\frac{1}{\epsilon^2})$ for $y<h$, we have

$$\int_h^1\frac{y^k\mathrm{d}y}{M(x,y)}\sim\int_0^1\frac{y^k\mathrm{d}y}{M(x,y)}\quad\text{for } k=0,1,2, \tag{5.29}$$

so all of the integrals involving M in the above equations are asymptotically independent of h. Similarly, since $\mu=\mathcal{O}(\epsilon^2)$ for $y>h$,

$$h\bar{\mu}=\int_0^h\mu(x,y)\mathrm{d}y\sim I_4(x):=\int_0^1\mu(x,y)\mathrm{d}y \tag{5.30}$$

is likewise independent of h. With the approximations in (5.29) and (5.30), we can solve (5.22b) and (5.26) simultaneously and get, to leading order,

$$B=\frac{1}{\Delta}\left[(1-u^{(0)})I_3+(q-1)I_2\right], \tag{5.31a}$$

$$-P_x^{(0)}=\frac{1}{\Delta}\left[(1-u^{(0)})I_2-(u^{(0)}-q)I_1\right], \tag{5.31b}$$

where

$$I_1(x)=\int_0^1\frac{\mathrm{d}y}{M(x,y)},\qquad I_2(x)=\int_0^1\frac{(y-1)\,\mathrm{d}y}{M(x,y)},\qquad I_3(x)=\int_0^1\frac{y\,(y-1)\,\mathrm{d}y}{M(x,y)}, \tag{5.32}$$

and Δ is the determinant of the system, defined as

$$\Delta(x)=\left(\int_0^1\frac{\mathrm{d}y}{M(x,y)}\right)\left(\int_0^1\frac{y^2\mathrm{d}y}{M(x,y)}\right)-\left(\int_0^1\frac{y\mathrm{d}y}{M(x,y)}\right)^2. \tag{5.33}$$

Note that $\Delta(x) > 0$ by the Cauchy-Schwartz inequality.

If we know $\mu(x,y)$ and $M(x,y)$, then all of the integrals $I_k(x)$ are known and (5.31a), (5.31b), and (from (5.28)),

$$\begin{aligned}\left(4u_x^{(0)}I_4\right)_x &= P_x^{(0)} - B \\ &= \frac{1}{\Delta}\left[(I_1+I_2+I_3)\left(u^{(0)}-1\right) - (I_1+I_2)(q-1)\right]\end{aligned} \tag{5.34}$$

in principle determine $u^{(0)}(x)$, $P^{(0)}(x)$, and $B(x)$. This is a hybrid model that combines elements of extensional flow and lubrication theory in situations where the viscosity varies by $\mathcal{O}\left(\epsilon^{-2}\right)$ across the domain.

For the purposes of plotting the velocity field, we can combine the leading order solution for $u(x)$ in region *(i)* with the solution in region *(ii)*, equations (5.14) and (5.22b) respectively. This gives a leading order approximation for $u(x)$ valid everywhere (i.e. for both u and U), namely

$$u(x,y) \sim u^{(0)} + P_x^{(0)}\int_0^y \frac{(\eta-1)\,\mathrm{d}\eta}{M(x,\eta)} + B\int_0^y \frac{\mathrm{d}\eta}{M(x,\eta)}. \tag{5.35}$$

Similarly for v, we have that

$$v(x,y) = -\int_0^y \frac{\partial u}{\partial x}(x,\eta)\mathrm{d}\eta, \tag{5.36}$$

and, substituting for u from (5.35), we obtain

$$v \sim -yu_x^{(0)} - \int_0^y (\eta-1)(y-\eta)\frac{\partial}{\partial x}\left(\frac{P_x^{(0)}(x)}{M(x,\eta)}\right)\mathrm{d}\eta - \int_0^y (y-\eta)\frac{\partial}{\partial x}\left(\frac{B(x)}{M(x,\eta)}\right)\mathrm{d}\eta, \tag{5.37}$$

where we have used the explicit notation for partial derivatives for clarity.

5.1.4 Laplace's method for integrals

In order to make analytic progress in the problem described in §5.1.3, we again assume that the viscosity is an exponential function of the dimensionless temperature θ, namely

$$M(x,y) = \frac{\mathrm{e}^{-\Gamma\theta(x,y)}}{\epsilon^2}, \tag{5.38}$$

where $\Gamma \gg 1$, reflecting the fact that the viscosity varies very strongly with temperature. We are considering the small aspect ratio limit, $\epsilon \ll 1$ so from the initial assumptions in (5.6) we must also have that $M = \mathcal{O}(1)$ as $\epsilon \to 0$. Assume for the moment that we know $\theta(x,y)$ everywhere, and that it satisfies the symmetry condition $\theta_y(x,0) = 0$. Additionally, we assume that $\theta(x,y)$ is an increasing function of y, i.e. (for a given x) $\theta(x,y)$ attains its maximum value at $y = 1$. This assumption is consistent with the data presented in Chapter 1, as the paste is hottest at the casing and is coldest at the inlet, where the cylinders are added. Letting $\Gamma \to \infty$ in (5.38) then allows

us to use Laplace's method to obtain leading order approximations for the integrals in (5.30) and (5.32).

The approximations to $\mathcal{O}(1/\Gamma)$ are

$$I_1(x) \sim \Lambda(x)\left(1 + \frac{\theta_{yy}(x,1)}{\Gamma\theta_y(x,1)^2} + \mathcal{O}\left(\frac{1}{\Gamma^2}\right)\right), \tag{5.39a}$$

$$I_2(x) \sim \Lambda(x)\left(-\frac{1}{\Gamma\theta_y(x,1)} + \mathcal{O}\left(\frac{1}{\Gamma^2}\right)\right), \tag{5.39b}$$

$$I_3(x) \sim \Lambda(x)\left(-\frac{1}{\Gamma\theta_y(x,1)} + \mathcal{O}\left(\frac{1}{\Gamma^2}\right)\right), \tag{5.39c}$$

$$I_4(x) \sim \left(\frac{\pi}{2\Gamma\theta_{yy}(x,0)}\right)^{1/2} e^{-\Gamma\theta(x,0)} + \mathcal{O}\left(\frac{1}{\Gamma^2}\right), \tag{5.39d}$$

where we define

$$\Lambda(x) = \frac{\epsilon^2 e^{\Gamma\theta(x,1)}}{\Gamma\theta_y(x,1)}. \tag{5.40}$$

Note that the approximations in (5.39) all have the same prefactor $\Lambda(x)$ apart from (5.39d), since the integrand here reaches its maximum at $y = 0$. Furthermore $\theta_y(x,0) = 0$ due to our boundary conditions, so higher order terms in the Taylor expansion of $\theta(x,y)$ must be taken when approximating I_4. Substituting (5.39a)-(5.39c) into (5.33) gives us, to leading order, $\Delta \simeq 0$. Hence, we must use even higher order approximations of the integrals I_1 to I_3 to obtain

$$\Delta(x) \sim \left(\frac{\Lambda(x)}{\Gamma\epsilon^2\theta_y(x,1)}\right)^2 = \frac{e^{2\Gamma\theta(x,1)}}{\Gamma^4\theta_y(x,1)^4}. \tag{5.41}$$

Then we substitute with our leading order approximations (5.39) and (5.41) for $\Delta(x)$ and the integrals into (5.31a), (5.31b), and (5.34) to obtain the system of equations

$$P_x^{(0)} = \beta(u^{(0)} - q), \tag{5.42a}$$

$$B = \frac{\beta}{\Gamma\theta_y(x,1)}(u^{(0)} - q), \tag{5.42b}$$

$$\frac{\mathrm{d}}{\mathrm{d}x}\left(\alpha u_x^{(0)}\right) = \beta\left(u^{(0)} - q\right) \tag{5.42c}$$

where

$$\beta(x) = \frac{\Gamma^3\theta_y(x,1)^3}{\epsilon^2 e^{\Gamma\theta(x,1)}}, \tag{5.43a}$$

$$\alpha(x) = 4\left(\frac{\pi}{2\Gamma\theta_{yy}(x,0)}\right)^{\frac{1}{2}} e^{-\Gamma\theta(x,0)}. \tag{5.43b}$$

In principle, the temperature $\theta(x,y)$ is determined by coupling (5.42) with the heat equation. For the moment, we simplify the problem by taking $\theta(x,y)$ to be a known function, and then examine

the behaviour of solutions of the system (5.42). With $\theta(x, y)$ known, (5.42c) is a second-order ODE for the core velocity $u^{(0)}(x)$. As typical boundary conditions, we expect to set $u^{(0)}(0)$ to be the incoming cylinder velocity and to specify either the velocity or the extensional stress at the downstream end of the domain. In addition, either we specify the net flux q, in which case (5.42a) gives the corresponding pressure gradient, or we specify the net pressure jump across the domain, in which case integration of (5.42a) with respect to x in principle determines q. As is typical in lubrication problems, by imposing either the flux or the pressure jump one can determine the other. If the domain is semi-infinite in the x-direction, then we expect the solution ultimately to approach a fully-developed state in which $u^{(0)}$ becomes independent of x, and we explore this possibility next.

5.1.5 Fully developed flow

We note that the governing equation (5.42c) contains two small parameters: ϵ and $1/\Gamma$. The left- and right-hand sides of (5.42c) balance if those parameters satisfy the relation

$$\epsilon^2 = \Gamma^{7/2} \exp\left(-\Gamma\left[\theta(x,1) - \theta(x,0)\right]\right). \tag{5.44}$$

The value of the aspect ratio defined by (5.44) implies a length-scale over which the flow is expected to develop. On much shorter length-scales (i.e. larger values of ϵ), the right-hand side of (5.42c) is negligible and we have a pure extensional flow. On the other hand, on a length-scale much longer than the one implied by (5.44), the flow ultimately becomes fully developed, so that $u^{(0)}$ is independent of x and the right-hand side of (5.42c) is set to zero, i.e.

$$0 = \beta(u^{(0)} - q) = P_x^{(0)}. \tag{5.45}$$

We assume that $\beta(x)$, defined by (5.43a), is non-zero, since $\theta(x, y)$ is an increasing function of y. Hence, we must have that

$$u^{(0)} = q \tag{5.46}$$

everywhere and the pressure gradient is equal to zero to leading order. In the leading-order fully-developed flow, the central core expands to fill most of the domain and thus fully accounts for the flux q, while the pressure gradient tends to zero.

5.1.6 Solutions dependent on x

When there is non-zero stress between layers (i) and (ii), i.e. $B(x) \neq 0$, we have to solve the system (5.42). We solve the problem on a finite domain $0 < x < 1$ with conditions imposed on the inlet and outlet core velocities, namely

$$u^{(0)}(0) = u_{\text{in}}, \qquad u^{(0)}(1) = q, \tag{5.47}$$

so the flow is fully developed at the downstream end.

Once the system (5.42) has been solved for $u^{(0)}(x)$, $P^{(0)}(x)$, and $B(x)$, we can evaluate the flow field throughout the domain by using Laplace's method on the approximations (5.35)-(5.37) for $u(x,y)$ and $v(x,y)$. We find that $u(x,y) \sim u^{(0)}(x)$ outside a boundary layer of thickness $\mathcal{O}(1/\Gamma)$ at the wall, and therefore introduce the local stretched variable

$$Y = \Gamma(1-y). \tag{5.48}$$

This substitution allows us to simplify equation (5.35) as

$$u(x,y) \sim u^{(0)}(x) + \epsilon^2 P_x^{(0)}(x) \int_0^{1-Y/\Gamma} (\eta - 1)\, e^{\Gamma\theta(x,\eta)} \mathrm{d}\eta + \epsilon^2 \Gamma^2 B(x) \int_0^{1-Y/\Gamma} e^{\Gamma\theta(x,\eta)} \mathrm{d}\eta, \tag{5.49}$$

where $P_x^{(0)}(x)$ and $B(x)$ are given by (5.42a) and (5.42b), respectively. To calculate the behaviour of the velocity in the boundary layer, we use Laplace's method to approximate the integrals as

$$\int_0^{1-Y/\Gamma} (\eta - 1)\, e^{\Gamma\theta(x,\eta)} \mathrm{d}\eta \sim \frac{-\exp\left(-\theta_y(x,1)Y + \Gamma\theta(x,1)\right)\left(1 + \theta_y(x,1)Y\right)}{\Gamma^2 \theta_y(x,1)^2} + \mathcal{O}\left(\frac{1}{\Gamma^3}\right), \tag{5.50}$$

$$\int_0^{1-Y/\Gamma} e^{\Gamma\theta(x,\eta)} \mathrm{d}\eta \sim \frac{\exp\left(-\theta_y(x,1)Y + \Gamma\theta(x,1)\right)}{\Gamma\theta_y(x,1)} + \mathcal{O}\left(\frac{1}{\Gamma^2}\right). \tag{5.51}$$

Then our boundary layer approximation for $u(x,y)$ is

$$\begin{aligned} u(x,y) \sim{}& \Gamma \mathrm{e}^{-Y\theta_y} \theta_y^2 Y \left(q - u^{(0)}(x)\right) + u^{(0)}(x) + \\ & \mathrm{e}^{-Y\theta_y} \left[\left(q - u^{(0)}(x)\right)\left(-5\theta_{yy} Y + \theta_y \theta_{yy} Y^2 + \frac{\theta_y^2 \theta_{yy} Y^3}{2}\right) + \left(1 - u^{(0)}(x)\right)\left(1 - \theta_y Y\right)\right] + \mathcal{O}\left(\frac{1}{\Gamma}\right), \end{aligned} \tag{5.52}$$

and the corresponding form for $v(x,y)$ is

$$v(x,y) \sim \left(1 + \theta_y Y - \mathrm{e}^{Y\theta_y}\right) \mathrm{e}^{-Y\theta_y} u_x^{(0)}(x) + \theta_y \theta_{xy} Y^2 \mathrm{e}^{-Y\theta_y} \left(q - u_x^{(0)}(x)\right) + \mathcal{O}\left(\frac{1}{\Gamma}\right), \tag{5.53}$$

where all the derivatives of θ are evaluated at $y = 1$ and Y is defined in (5.48).

Note that the asymptotic approximations (5.52) and (5.53) for u and v satisfy the boundary conditions at the wall, namely $u = 1$, $v = 0$ at $y = 1$, and the matching conditions $u \to u^{(0)}(x)$ and $v \to -u_x^{(0)}(x)$ as $Y \to \infty$. Except in the fully developed flow where $u^{(0)}(x) = q$, (5.52) shows that there is a fast-moving jet, with $u = \mathcal{O}(\Gamma)$, in the boundary layer. The jet flows in the same direction as the wall motion if $q > u^{(0)}$ or in the reverse direction if $u^{(0)} > q$.

Equation (5.52) gives a uniformly valid leading-order approximation for $u(x,y)$ across the flow domain. The expression (5.53) does not satisfy the boundary condition $v = 0$ at $y = 0$ but can be

combined with (5.14) to give the uniformly valid approximation

$$v(x,y) \sim -yu_x^{(0)}(x) + (1+\theta_y Y)\,\mathrm{e}^{-Y\theta_y}u_x^{(0)}(x) + \theta_y\theta_{xy}Y^2\mathrm{e}^{-Y\theta_y}\left(q-u_x^{(0)}(x)\right) + \mathcal{O}\left(\frac{1}{\Gamma}\right), \tag{5.54}$$

where the derivatives of θ are again evaluated at $y=1$, with Y defined in (5.48).

5.1.7 Example with known temperature quadratic in y

In order to visualize the solution structure, we first solve the system (5.42) for a quadratic temperature profile θ_{Q} independent of x, namely

$$\theta_{\mathrm{Q}}(y) = y^2. \tag{5.55}$$

Then, α and β, defined in (5.43) are constants. We fix the length-scale L by imposing the relationship (5.44) between the aspect ratio ϵ and the small parameter $1/\Gamma$, specifically

$$\epsilon^2 = 4\Gamma^{7/2}e^{-\Gamma}. \tag{5.56}$$

We solve the ODE (5.42) subject to the boundary conditions (5.47) and get the solutions

$$u^{(0)}(x) = \frac{(u_{\mathrm{in}}-q)\left(e^{2-x}-e^x\right)}{e^2-1} + q, \tag{5.57a}$$

$$P^{(0)}(x) = \frac{2\sqrt{\pi/\Gamma}(q-u_{\mathrm{in}})\left(e^{2-x}+e^x\right)}{e^2-1} + P_0, \tag{5.57b}$$

$$B(x) = \frac{\sqrt{\pi}(u_{\mathrm{in}}-q)\left(e^{2-x}-e^x\right)}{\Gamma^{\frac{3}{2}}\left(e^2-1\right)}, \tag{5.57c}$$

where P_0 is an arbitrary constant. Substituting with our assumed quadratic form (5.55) for θ, we find that the approximations (5.52) and (5.54) for the velocity components become

$$\begin{aligned} u(x,y) \sim{}& 4\Gamma Y e^{-2Y}\left(q-u^{(0)}(x)\right) + u^{(0)}(x) + \\ & e^{-2Y}\left[\left(q-u^{(0)}(x)\right)\left(-10Y+4Y^2+4Y^3\right) + \left(1-u^{(0)}(x)\right)(1-2Y)\right] + \mathcal{O}\left(\frac{1}{\Gamma}\right), \end{aligned} \tag{5.58}$$

and

$$v(x,y) \sim -yu_x^{(0)} + (2Y+1)\mathrm{e}^{-2Y}u_x^{(0)} + \mathcal{O}\left(\frac{1}{\Gamma}\right). \tag{5.59}$$

With the outer flow $u^{(0)}$ now determined by (5.57a), the resulting streamlines for a quadratic temperature are shown in Figure 5.1.3, where the flow regime depends on the sign of $q-u_{\mathrm{in}}$. When $q < u_{\mathrm{in}}$, we observe the behaviour shown in 5.1.3(a), where significant backflow occurs in region (*ii*), i.e. in the boundary layer, but the boundary layer dissipates as x increases and the flow approaches the fully developed profile. This is the industrially relevant problem, as the cylinders are pushed in at the top faster than the casing, and we expect the less viscous paste to recirculate closer to the

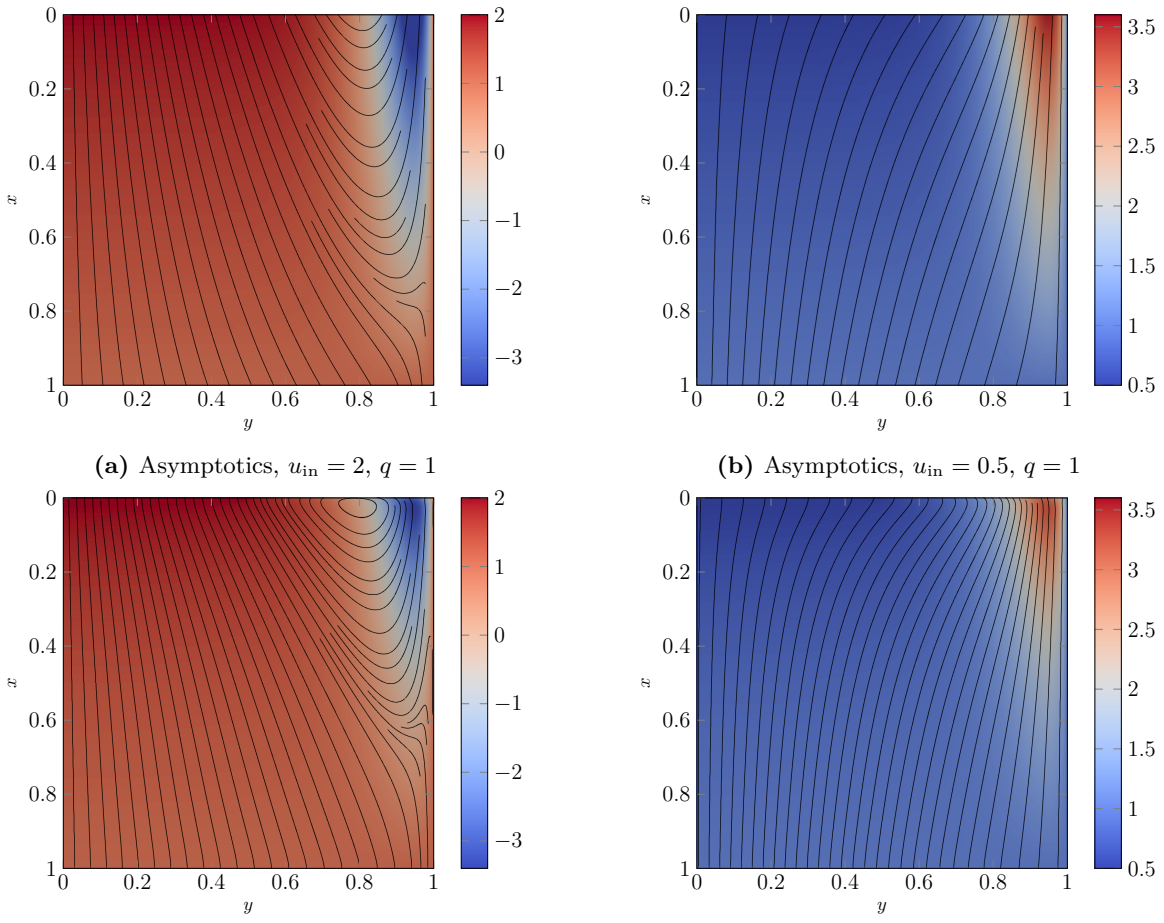

(a) Asymptotics, $u_{\text{in}} = 2$, $q = 1$

(b) Asymptotics, $u_{\text{in}} = 0.5$, $q = 1$

(c) FEniCS, $u_{\text{in}} = 2$, $q = 1$

(d) FEniCS, $u_{\text{in}} = 0.5$, $q = 1$

Figure 5.1.3 – Flow profile using viscosity parameter $\Gamma = 10$ and aspect ratio $\epsilon = 0.76$, comparing asymptotic approximation (5.58) (top) with results from finite element simulation described in Chapter 4 (bottom). For the finite element simulations we have used $\Gamma = 10$ for consistency, and imposed $\boldsymbol{u} = (u_{\text{in}}, 0)$ on $\partial\Omega_0$, $(\boldsymbol{\sigma} \cdot \boldsymbol{n}) = \boldsymbol{0}$ on $\partial\Omega_1$, $\boldsymbol{u} = (1, 0)$ on $\partial\Omega_2 \cup \Omega_3$, and symmetry on $\partial\Omega_4$ (see Figure 4.1.1 for reference). The colourbars indicate values of the vertical velocity component $u(x, y)$. Note that the region of downward flow near the wall is so narrow (see Figure 5.1.4(a)) that the corresponding streamlines are not visible.

casing. In Figure 5.1.3(b) we show the case when $q > u_{\text{in}}$. In this case the core of the fluid must be accelerated so as to move faster than the inlet speed (and that of the wall), so the streamlines converge towards the centre. Note that in the industrial problem we have $q = 1$ so the paste is ultimately moving with the casing, but our model allows for more general fluxes to be imposed.

For comparison, we use the finite element simulation described in Chapter 4 to compute the velocity profile for a temperature θ_Q given by (5.55) in Cartesian coordinates with $\Gamma = 10$. We impose $\boldsymbol{u} = (u_{\text{in}}, 0)$ on $\partial\Omega_0$, the boundary where the cylinders are added, $(\boldsymbol{\sigma} \cdot \boldsymbol{n}) = \boldsymbol{0}$ on the flat free surface $\partial\Omega_1$, and $\boldsymbol{u} = (q, 0)$ on $\partial\Omega_2 \cup \partial\Omega_3$, the wall and outlet boundaries respectively (see Figure 4.1.1 for reference), with $q = 1$. The FEniCS results shown for $u_{\text{in}} > 1$ in Figure 5.1.3(c), and for $u_{\text{in}} < 1$ in Figure 5.1.3(d) are qualitatively similar to the asymptotic solution. Focusing on the industrially relevant problem where $u_{\text{in}} > 1$, we see that the width of the boundary layer is similar in both

cases, but the finite element simulation predicts a slightly shorter jet of hot paste coming out of the domain, shown in the blue regions in Figure 5.1.3(a) and Figure 5.1.3(c), respectively. In the numerical simulation, we must specify the width of the region $\partial\Omega_0$ where the cylinders are added and the boundary conditions to be imposed on the free surface $\partial\Omega_1$, but in the asymptotic problem we specify only the inlet velocity u_{in}. Nevertheless, the results shown in Figure 5.1.3 suggest that the asymptotic solution gives a good approximation of the overall structure of the flow, including the upwards flow near the casing and the recirculation zones. Thus reassured, we focus now on studying the predictions of the asymptotic model. The behaviour of the vertical velocity component u predicted by (5.58) versus the scaled horizontal coordinate Y is shown in Figure 5.1.4 for different values of x and Γ. We show the case for $u_{\text{in}} = 1.5$ and $q = 1$, so the jet velocity is higher than the flux, as in the industrial problem. At the wall, the velocity satisfies the boundary condition $u = 1$. As we move further away from the wall, we observe significant backflow of the hot paste in region (ii) caused by the more viscous paste in region (i). The magnitude of the backflow increases with increasing Γ, shown in Figure 5.1.4(b), as this represents the width of the boundary layer at the wall.

Figure 5.1.5 shows what happens when the flux q does not match the casing velocity 1, in which case we are effectively driving the flow with an imposed pressure gradient, in addition to the forcing from the input cold paste at $x = 0$. As noted above, whether or not there is backflow in the boundary layer depends on the sign of $u_{\text{in}} - q$, as demonstrated in Figure 5.1.5(a) for $\Gamma = 10$ and $x = 0$. As we move further along the casing, the outer velocity $u^{(0)}(x)$ approaches its far-field value of q, and the velocity change at the boundary layer becomes less dramatic, as seen in Figure 5.1.5(b) for $x = 1$.

As we increase u_{in}, keeping $q = 1$ we note the complementary behaviour to the previous case, as when $u_{\text{in}} > q$, the boundary layer velocity is in the opposite direction of the flow, slowing it down so that it reaches an outflow of q. In Figure 5.1.6(a) for $x = 0$ and $\Gamma = 10$, we observe a large return flow to compensate for a larger velocity at the inlet, and the flow approaches a plug flow with $u = q = 1$ as we move further along the casing, as seen in Figure 5.1.6(b) for $x = 0.99$.

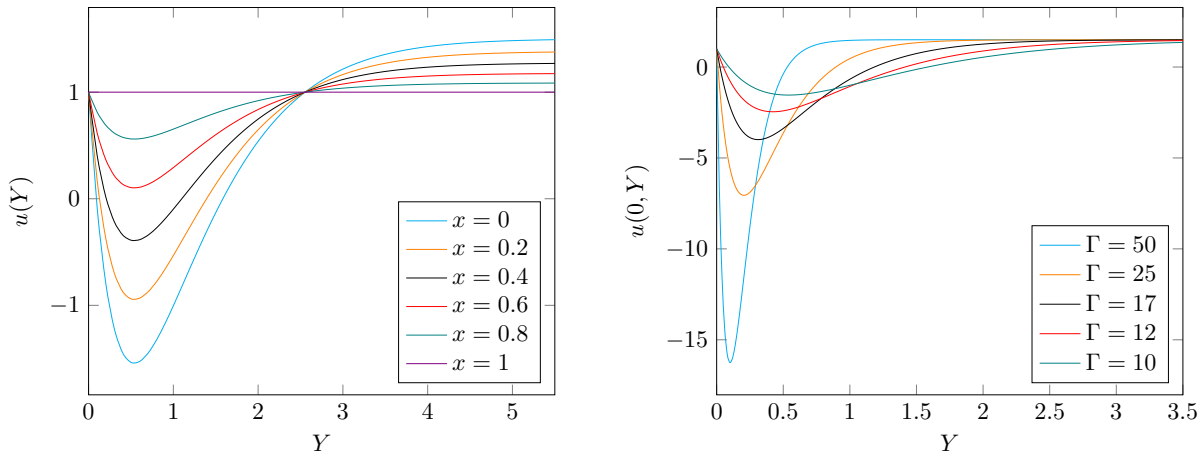

(a) **(b)**

Figure 5.1.4 – Solutions for the vertical velocity $u(Y)$, for $\theta(x, y) = y^2$, $u_{\text{in}} = 1.5$, $q = 1$ and (a) $\Gamma = 10$ at different values of x, (b) $x = 0$ at different values of Γ.

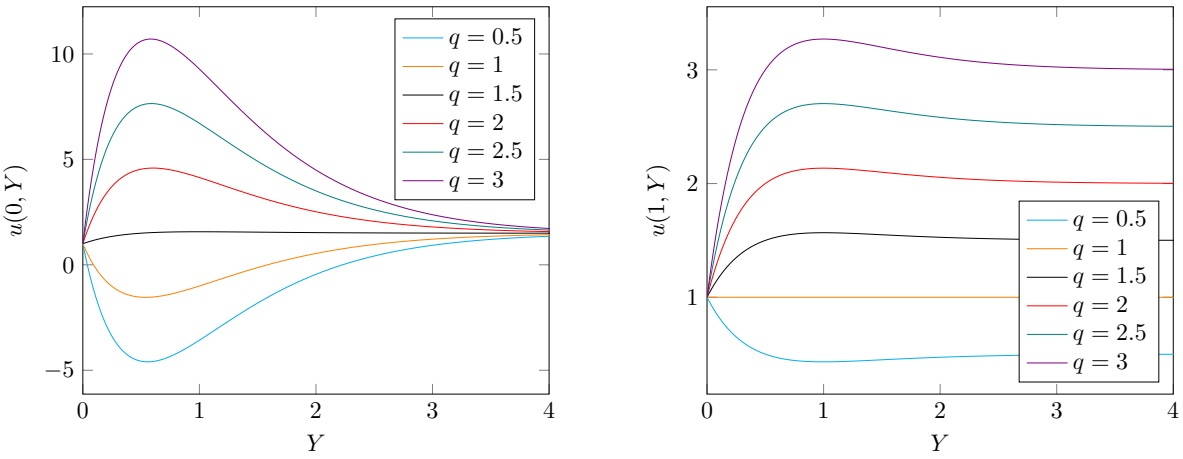

(a) **(b)**

Figure 5.1.5 – Solutions for the vertical velocity $u(Y)$, for $\theta(x, y) = y^2$, $u_{\text{in}} = 1.5$, $\Gamma = 10$, and varying q, at (a) $x = 0$, (b) $x = 1$.

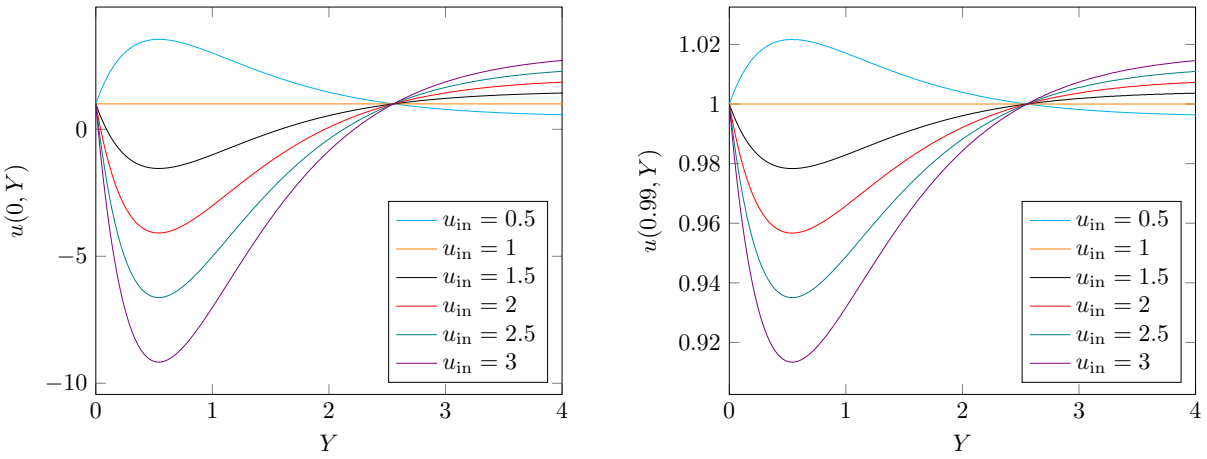

(a) **(b)**

Figure 5.1.6 – Solutions for the vertical velocity $u(Y)$ in the boundary layer, for $\theta(x, y) = y^2$, $q = 1$, and $\Gamma = 10$ varying u_{in}, at (a) $x = 0$, (b) $x = 0.99$.

5.1.8 Examples with known temperature dependent on x

Next consider a temperature profile θ_{H} of the form

$$\theta_{\mathrm{H}}(x, y) = 1 + \left(y^2 - 1\right) e^{-x}, \tag{5.60}$$

which models a case where the temperature increases with x and ultimately approaches a uniform profile. This is more like the temperature profile we anticipate when we couple the flow with the heat equation for the industrial setting in §5.5. Now both α and β are functions of x, namely

$$\alpha(x) = 2\sqrt{\frac{\pi}{\Gamma}} \exp\left(\frac{x}{2} - \Gamma\left(1 - e^{-x}\right)\right), \tag{5.61a}$$

$$\beta(x) = 2\sqrt{\frac{\pi}{\Gamma}} e^{-3x}, \tag{5.61b}$$

where we have again chosen the scaling (5.56), such that $\beta(0) = \alpha(0)$.

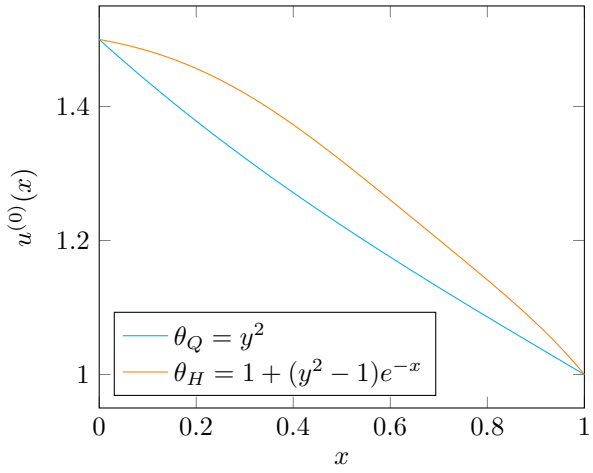

Figure 5.1.7 – Leading order velocity $u^{(0)}(x)$ for two different temperature profiles: θ_Q and θ_H, with $\Gamma = 10$, $\epsilon = 0.76$, $u_{\mathrm{in}} = 1.5$, and $q = 1$.

We solve the problem (5.42c), (5.43), and (5.47) numerically for this case on $x \in [0, 1]$ using the MATLAB built-in ODE solver `bvp4c`, a finite difference code which uses Simpson's method (Kierzenka and Shampine, 2001). The resulting leading-order core velocity $u^{(0)}(x)$ is shown in Figure 5.1.7, where it is compared to the solution obtained with θ_{Q}, using $\Gamma = 10$, $u_{\mathrm{in}} = 1.5$, and $q = 1$. We use these numerical results in the expressions (5.52) and (5.53) to visualise the flow profile for both temperature examples, shown in Figure 5.1.8(a) and Figure 5.1.8(b), respectively. Although the streamlines have the same qualitative behaviour in both solutions, we observe that including x dependence in the temperature pushes the recirculation zone further up the domain, causing the streamlines to converge more quickly towards the wall than in the x-independent case.

As we did for the quadratic temperature in the previous section, we compare with the asymptotic results with the finite element simulation described in Chapter 4 for $\theta = \theta_Q$ in Figure 5.1.8(c) and for $\theta = \theta_H$ in Figure 5.1.8(d), with the boundary conditions indicated in the caption. We observe

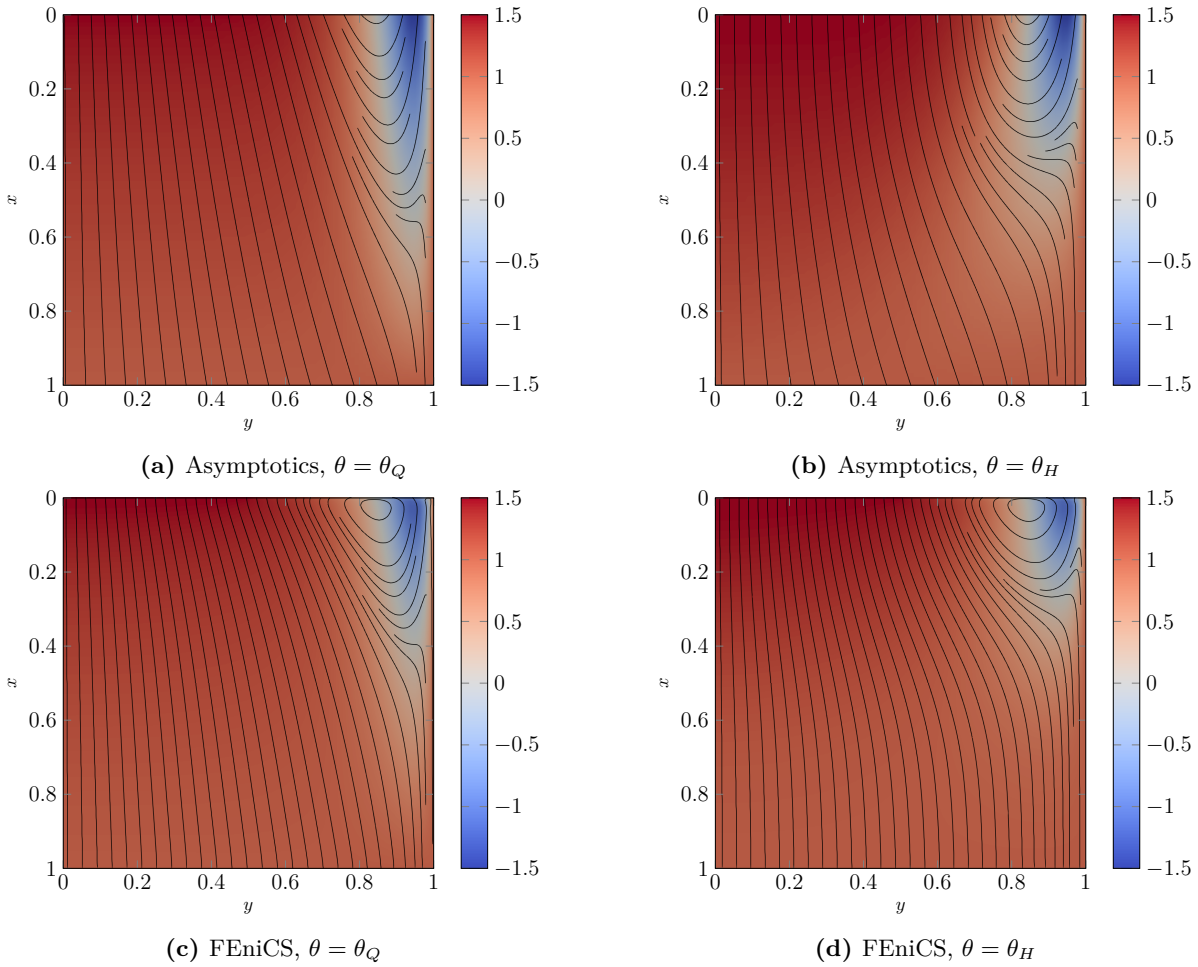

(a) Asymptotics, $\theta = \theta_Q$

(b) Asymptotics, $\theta = \theta_H$

(c) FEniCS, $\theta = \theta_Q$

(d) FEniCS, $\theta = \theta_H$

Figure 5.1.8 – Velocity profile described by the asymptotic solution (top) and finite element simulations (bottom), for $\Gamma = 10$, $\epsilon = 0.76$ and different imposed temperature, namely $\theta_Q = y^2$ (left) and $\theta_H = 1 + (y^2 - 1)e^{-x}$. For the asymptotics, we have used $u_{\text{in}} = 1.5$, and $q = 1$. For the finite element simulations we have imposed $\boldsymbol{u} = (1.5, 0)$ on $\partial\Omega_0$, $(\boldsymbol{\sigma} \cdot \boldsymbol{n}) = \boldsymbol{0}$ on $\partial\Omega_1$, $\boldsymbol{u} = (1, 0)$ on $\partial\Omega_2 \cup \Omega_3$, and symmetry on $\partial\Omega_4$ (see Figure 4.1.1 for reference). The colourbars indicate values of the vertical velocity component $u(x, y)$.

that the asymptotic prediction of the streamlines and the finite element solution are still similar when the temperature varies with x and y, despite neither ϵ nor $1/\Gamma$ being exceptionally small. As before, we note that our asymptotic solution provides a good prediction for the width of the boundary layer, although we over-estimate the length of the jet of hot paste, which occurs over a shorter lengthscale in the finite element simulations.

In this section we have demonstrated that, given a prescribed temperature field, our asymptotic solution captures well the flow of a paste with highly temperature-dependent viscosity in a narrow channel. We next go on to solve for the temperature in the paste, initially assuming that the velocity field is known. The fully coupled problem in which we must solve simultaneously for the velocity and the temperature will be discussed below in §5.5.

5.2 Temperature problem with known flow

In contrast to §5.1, in this section we focus on the temperature problem assuming a known velocity profile. We formulate and non-dimensionalise the general problem in §5.2.1 and, since we have shown that the velocity field has a boundary layer structure in §5.1, we exploit a similar structure for the temperature problem in §5.2.2. The structure of the velocity field results in an 'outer' temperature problem that has a very unusual boundary condition (matching condition) at the outer wall, due to the advection caused by the reverse flow in the boundary layer.

5.2.1 Problem statement

We start with the dimensional steady state heat transfer problem in 2D Cartesian coordinates,

$$\rho c\left(uT_x + vT_y\right) = k\left(T_{xx} + T_{yy}\right) \qquad \text{for} \quad 0 < x < \bar{L}, \quad 0 < y < H, \tag{5.62}$$

with boundary conditions

$$T = T_{\text{in}} \qquad \text{at} \quad x = 0, \tag{5.63a}$$

$$T_y = 0 \qquad \text{at} \quad y = 0, \tag{5.63b}$$

$$-kT_y = h\left(T - T_{\text{a}}(x)\right) \qquad \text{at} \quad y = H. \tag{5.63c}$$

Strictly speaking, the inlet boundary condition (5.63a) is imposed only on the core region of the flow where the paste is flowing into the domain. However, we note that (as in lubrication theory), there are inner regions near the inlet and outlet of the domain where the asymptotic theory breaks down and the flow is fully two-dimensional, and (5.63a) could also be viewed as a matching condition with the inner region at $x = 0$. The downstream boundary condition to be imposed on the temperature will be discussed below.

In (5.63c) Newton's law of cooling is imposed at the external boundary, with ambient temperature $T_{\text{a}}(x)$ (for now) a linear function of x,

$$T_{\text{a}}(x) = \frac{T_{\text{bot}} - T_{\text{top}}}{\bar{L}}x + T_{\text{top}}, \tag{5.64}$$

where T_{top} and T_{bot} correspond to the temperature at the top and bottom of the air column. We rescale consistently with the flow problem, i.e. $x = \bar{L}x'$, $y = \epsilon\bar{L}y'$, $u = u_{\text{c}}u'$, $v = \epsilon u_{\text{c}}v'$, and for the temperature we choose

$$T = T_{\text{top}} + \Delta T\theta, \qquad T_{\text{a}} = T_{\text{top}} + \Delta T\theta_{\text{a}}, \tag{5.65}$$

where $\Delta T = T_{\text{bot}} - T_{\text{top}}$. For simplicity, we assume that the temperature at the inlet is in equilibrium with the air column temperature, i.e. $T_{\text{in}} = T_{\text{top}}$.

The non-dimensional problem is (dropping primes)

$$(u\theta_x + v\theta_y) = \frac{1}{\mathrm{Pe}^*}\left(\epsilon^2\theta_{xx} + \theta_{yy}\right) \qquad \text{for} \quad 0 < x < 1, \quad 0 < y < 1, \tag{5.66}$$

with boundary conditions

$$\theta = 0 \qquad \text{at} \quad x = 0, \tag{5.67a}$$

$$\theta_y = 0 \qquad \text{at} \quad y = 0, \tag{5.67b}$$

$$\theta_y = -\mathrm{Bi}^*\left(\theta - \theta_\mathrm{a}\right) \qquad \text{at} \quad y = 1, \tag{5.67c}$$

where the non-dimensional parameters are defined in Table 5.2.1 and the dimensionless heating due to the air column is given by

$$\theta_\mathrm{a} = x. \tag{5.68}$$

Notation	Parameter Group	Definition	Typical Value
ϵ	Aspect ratio	$\frac{H}{L}$	0.2
Pe^*	Reduced Péclet number	$\epsilon^2\frac{\rho c u_\mathrm{c} L}{k}$	1.1
Bi^*	Reduced Biot number	$\epsilon^2\frac{L^2 h}{Hk}$	2.3

Table 5.2.1 – Nondimensional parameters calculated with dimensional parameter values given in Table 1.3.1.

5.2.2 Boundary layer asymptotics for the temperature problem

From §5.1, we know that the velocity field has a boundary layer structure, with an extensional type flow when $y = \mathcal{O}(1)$ and a lubrication-type flow when $1 - y = \mathcal{O}(1/\Gamma)$. Now we exploit this structure to simplify the thermal problem.

For the outer problem, we expand in asymptotic expansions in powers of ϵ^2, i.e.

$$\theta \sim \theta^{(0)} + \epsilon^2\theta^{(1)} + \ldots. \tag{5.69}$$

Additionally, we use the forms for u and v obtained in §5.1, namely $u \sim u^{(0)}(x)$ and $v \sim -yu_x^{(0)}$.

Then to $\mathcal{O}(1)$ in ϵ^2:

$$u^{(0)}\theta_x^{(0)} - yu_x^{(0)}\theta_y^{(0)} = \frac{1}{\mathrm{Pe}^*}\theta_{yy}^{(0)} \tag{5.70}$$

with boundary conditions

$$\theta_y^{(0)} = 0 \qquad \text{at} \quad y = 0, \tag{5.71a}$$

$$\theta^{(0)} = 0 \qquad \text{at} \quad x = 0. \tag{5.71b}$$

We cannot in general make any analytical progress with the outer problem, as $u^{(0)}$ additionally

satisfies the ODE (5.42c).

For the inner problem, we introduce the stretched variable

$$Y = \Gamma\,(1-y)\,, \tag{5.72}$$

where $\Gamma \gg 1$. Furthermore, we assume $u \sim \Gamma U^{(0)}$ and $v \sim V^{(0)}$, as obtained in (5.52), (5.53). Let

$$\Theta(x,Y) \sim \Theta^{(0)} + \frac{1}{\Gamma}\Theta^{(1)} + \dots \tag{5.73}$$

where $\theta(x,y) = \Theta(x,Y)$. Then the inner problem is

$$\frac{1}{\Gamma}U^{(0)}\Theta_x^{(0)} - \frac{1}{\Gamma}V^{(0)}\Theta_Y^{(0)} = \frac{1}{\mathrm{Pe}^*}\left(\frac{\epsilon^2}{\Gamma^2}\Theta_{xx}^{(0)} + \Theta_{YY}^{(0)}\right), \tag{5.74}$$

with boundary condition

$$\Theta_Y = \frac{1}{\Gamma}\mathrm{Bi}^*\,(\Theta - \theta_a) \quad \text{at} \quad Y = 0. \tag{5.75}$$

Since $\epsilon \ll 1$ and $\Gamma \gg 1$, the Θ_{xx} diffusion term is always negligible in this inner region. At leading order we have

$$\frac{1}{\mathrm{Pe}^*}\Theta_{YY}^{(0)} = 0 \qquad \text{for} \quad Y > 0, \tag{5.76a}$$

$$\Theta_Y^{(0)} = 0 \qquad \text{at} \quad Y = 0. \tag{5.76b}$$

This gives us that

$$\Theta^{(0)} \equiv \Theta^{(0)}(x). \tag{5.77}$$

To next order, the governing equations become

$$U^{(0)}\Theta_x^{(0)} - V^{(0)}\Theta_Y^{(0)} = \frac{1}{\mathrm{Pe}^*}\Theta_{YY}^{(1)} \qquad \text{for} \quad Y > 0, \tag{5.78a}$$

$$\Theta_Y^{(1)} = \mathrm{Bi}^*\left(\Theta^{(0)} - \theta_{\mathrm{a}}\right) \qquad \text{at} \quad Y = 0. \tag{5.78b}$$

This is an inhomogeneous version of the leading order problem satisfied by $\Theta^{(0)}$. Therefore, the Fredholm alternative implies that this problem will have no solutions for $\Theta^{(1)}$ unless a solvability condition is satisfied. We substitute (5.77) into (5.78a) and integrate with respect to Y to obtain the condition

$$\int_0^\infty \mathrm{Pe}^* U^{(0)}\Theta_x^{(0)}\mathrm{d}Y = {\Theta^{(1)}}_Y\Big|_0^\infty. \tag{5.79}$$

We use the form for $U^{(0)}$ from (5.52). Then the solvability condition (5.79) gives

$$\lim_{Y\to\infty}\Theta_Y^{(1)}(x,Y) = \mathrm{Bi}^*\left(\Theta^{(0)} - \theta_{\mathrm{a}}\right) + \mathrm{Pe}^*\Theta_x^{(0)}\left(q - u^{(0)}\right). \tag{5.80}$$

This result gives us the effective boundary condition (the matching condition) for the outer problem

(5.70), to account for the boundary layer described by the inner problem (5.74). To leading order in $1/\Gamma$, this boundary condition is

$$\theta_y^{(0)}(x,0) = -\lim_{Y\to\infty} \Theta_Y^{(1)}(x,Y) = -\mathrm{Bi}^*\left(\theta^{(0)} - \theta_\mathrm{a}\right) - \mathrm{Pe}^*\theta_x^{(0)}\left(q - u^{(0)}\right), \tag{5.81}$$

where we have used (5.77) and (5.72) to rewrite the inner solution in terms of y. The resulting outer problem to leading order in $1/\Gamma$ and ϵ is, removing superscripts,

$$u\theta_x - yu_x\theta_y = \frac{1}{\mathrm{Pe}^*}\theta_{yy} \qquad \text{for} \quad 0<x<1, \quad 0<y<1, \tag{5.82a}$$

$$\theta = 0 \qquad \text{at} \quad x = 0, \tag{5.82b}$$

$$\theta_y = 0 \qquad \text{at} \quad y = 0, \tag{5.82c}$$

$$\theta_y = -\mathrm{Bi}^*\left(\theta - \theta_\mathrm{a}\right) + \mathrm{Pe}^*(u-q)\theta_x \qquad \text{at} \quad y = 1, \tag{5.82d}$$

where $u \equiv u^{(0)}(x)$ is the solution to (5.42c).

In the limit $\epsilon \to 0$, thermal diffusion in the x-direction is negligible and the simplified heat equation (5.82a) appears to require no downstream boundary condition for θ. However, we will discover that the unconventional heat transfer condition (5.82d) *does* require some information about the downstream temperature to be imposed. To help build understanding of the problem, we first analyse a simple special case where the velocity u is constant.

5.3 Solutions for constant u

5.3.1 Equations and boundary conditions

We first consider the problem (5.82) with constant u, namely

$$\theta_x = \frac{1}{u\mathrm{Pe}^*}\theta_{yy} \qquad \text{for} \quad 0<x<1, \quad 0<y<1, \tag{5.83a}$$

$$\theta = 0 \qquad \text{at} \quad x = 0, \tag{5.83b}$$

$$\theta_y = 0 \qquad \text{at} \quad y = 0, \tag{5.83c}$$

$$\theta_y = -\mathrm{Bi}^*\left(\theta - \theta_\mathrm{a}\right) + (u-q)\mathrm{Pe}^*\theta_x \qquad \text{at} \quad y = 1. \tag{5.83d}$$

In light of the unconventional boundary condition (5.83d), before we describe the numerical scheme used to solve (5.83), we make some comments on its well-posedness. To examine uniqueness we

assume $\theta_1(x,y)$ and $\theta_2(x,y)$ are two distinct solutions to (5.83). Then $\omega = \theta_1 - \theta_2$ satisfies

$$\omega_x = \frac{1}{u\mathrm{Pe}^*}\omega_{yy} \qquad \text{for} \quad 0<x<1, \quad 0<y<1, \tag{5.84a}$$

$$\omega = 0 \qquad \text{at} \quad x = 0, \tag{5.84b}$$

$$\omega_y = 0 \qquad \text{at} \quad y = 0, \tag{5.84c}$$

$$\omega_y + \mathrm{Bi}^*\omega = (u-q)\mathrm{Pe}^*\omega_x \qquad \text{at} \quad y = 1. \tag{5.84d}$$

We multiply by ω and integrate with respect to y over $[0,1]$, to obtain

$$\int_0^1 \omega\omega_x \mathrm{d}y = \frac{1}{u\mathrm{Pe}^*}\int_0^1 \omega\omega_{yy}\mathrm{d}y. \tag{5.85}$$

Computing the integrals and substituting with (5.84c), (5.84d) gives

$$\frac{\mathrm{d}f}{\mathrm{d}x} = -\left[\frac{2}{u\mathrm{Pe}^*}\int_0^1 \omega_y^2 \mathrm{d}y + \frac{2\mathrm{Bi}^*}{u\mathrm{Pe}^*}\omega^2|_{y=1}\right] \leq 0, \tag{5.86}$$

where

$$f(x) = \int_0^1 \omega(x,y)^2 \mathrm{d}y - \frac{u-q}{u}\omega(x,1)^2. \tag{5.87}$$

Note that, for $u \leq q$, $f(x) \geq 0$ and $f(0) = 0$ by (5.84b). Hence, f is bounded above and below by 0, therefore for this case $\omega \equiv 0$ and hence the solution to (5.83) is unique. However, we cannot make the same conclusion if $u > q$, and in fact we claim that (5.83) is ill-posed in this case.

In the industrial setting, we encounter the case $u > q$, as the cylinders are effectively *pushing* down on the already softened paste, displacing it. This forces a jet of softened paste to flow upwards along the wall, in the opposite direction to the central plug flow. The final term in (5.83d) captures the convective transport of heat caused by this jet. To determine the temperature in this wall flow, we have to specify the 'upstream' temperature at $x = 1$. Therefore in order to investigate solutions for $u > q$, we additionally impose

$$\theta = \theta_0 \quad \text{at} \quad x = 1, \quad y = 1, \tag{5.88}$$

with θ_0 a given constant. In the following numerical examples, we take $\theta_0 = 1$ unless otherwise specified. In principle, (5.88) can be replaced by a zero-conduction condition $\theta_x(1,1) = 0$ similar to (2.16); however, as in Chapter 2, we will see that the details of the boundary condition imposed are felt only in a small neighbourhood of $x = 1$.

5.3.2 Numerical method and validation

To solve (5.83), we discretise using central differences in the y-direction and backward Euler in the x-direction, leading to

$$\frac{\theta_n^k - \theta_n^{k-1}}{\Delta x} = \frac{1}{u\mathrm{Pe}^*}\frac{\theta_{n+1}^k - 2\theta_n^k + \theta_{n-1}^k}{\Delta y^2}, \tag{5.89}$$

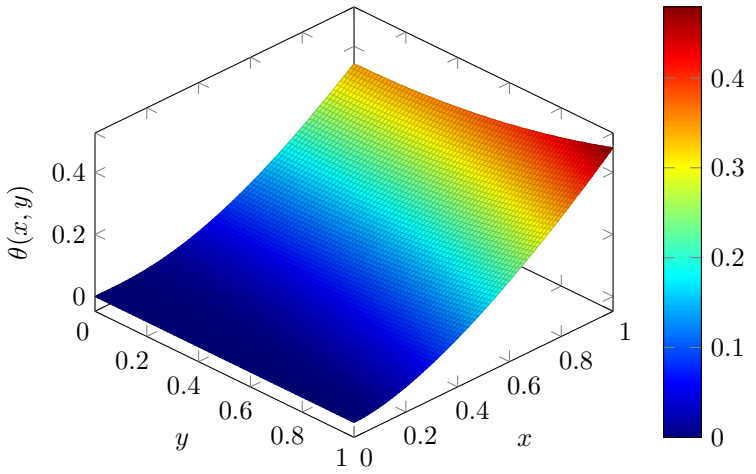

Figure 5.3.1 – Temperature contours for problem (5.83), with $u = 1$, $q = 2$, $\mathrm{Pe}^* = 0.4$, and $\mathrm{Bi}^* = 1.1$, and $\theta_\mathrm{a} = x$.

for all $n < 0 < N$ and $0 < k \leq K$ where $k = 0, \ldots, K$ denotes the discretisation in x and $n = 0, \ldots, N+1$ denotes the discretisation in y. For $k = 0$ ($x = 0$) we specify the inlet temperature $\theta_n^0 = 0$ for $n = 0, \ldots, N+1$. For $n = 0$ ($y = 0$) we have a Neumann boundary condition where we use a second order finite difference approximation

$$\frac{\theta_0^k - \theta_0^{k-1}}{\Delta x} = \frac{1}{u\mathrm{Pe}^*} \frac{2\theta_1^k - 2\theta_0^k}{\Delta y^2}. \tag{5.90}$$

Recall that the sign of $u - q$ affects the causality of the propagation of information (heat) along the boundary at $y = 1$, so we have different solution behaviours for positive and negative values of $u - q$. We discretise the boundary condition at $n = N$ ($y = 1$) as

$$\frac{\theta_N^k - \theta_{N-1}^k}{\Delta y} + \mathrm{Bi}^* \left(\theta_N^k - \theta_a^k\right) - \mathrm{Pe}^* (u - q) \left(\frac{\theta_N^k - \theta_N^{k-1}}{\Delta x}\right) = 0 \tag{5.91}$$

for $k = 1, \ldots K-1$. For $k = K$ ($x = 1$), we set

$$\text{for } u \leq q: \qquad \frac{\theta_N^K - \theta_{N-1}^K}{\Delta y} + \mathrm{Bi}^* \left(\theta_N^K - \theta_a^K\right) - \mathrm{Pe}^* (u - q) \left(\frac{\theta_N^K - \theta_N^{K-1}}{\Delta x}\right) = 0, \tag{5.92}$$

$$\text{for } u > q: \qquad \theta_N^K = \theta_0, \tag{5.93}$$

where θ_0 is the imposed end temperature. In the following numerical examples, we take $\theta_0 = 1$ unless otherwise specified.

In Figure 5.3.1, we use this numerical scheme to illustrate the effect of the heating by the air column function $\theta_\mathrm{a}(x) = x$ for the case $u < q$ with $\mathrm{Pe}^* = 0.4$, and $\mathrm{Bi}^* = 1.1$. We note that the numerical scheme is working satisfactorily and boundary conditions (5.83b), (5.83c), (5.83d) are resolved.

The result of solving (5.83) with $u > q$ is shown in Figure 5.3.2. We note that the backward

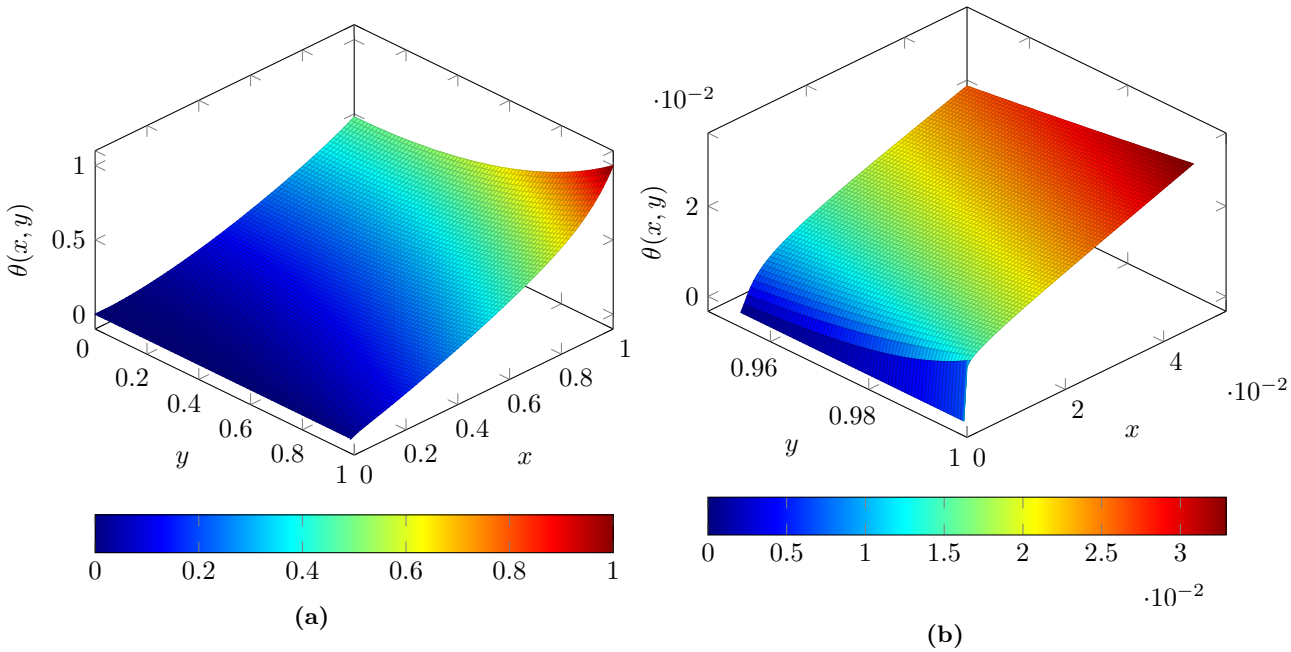

Figure 5.3.2 – (a) Temperature contours for problem (5.83), with $u = 2$, $q = 1$, $\mathrm{Pe}^* = 0.4$, $\mathrm{Bi}^* = 1.1$, $\theta_0 = 1$, and $\theta_\mathrm{a} = x$, (b) zooming into the region near $x = 0$, $y = 1$.

advection in (5.83d) caused by $u - q$ being positive results in a discontinuity in the solution near $(0, 1)$, as shown in Figure 5.3.2(b). This is a result of the conflict between the boundary conditions (5.83b), (5.83d) at that point. We summarise the behaviour of this discontinuity as we vary $u - q$ in Figure 5.3.3(a), where for $u - q < 0$ it remains zero, and for $u - q > 0$ it increases as we increase the value of this difference. In §5.3.5 we explore this behaviour by analysing the discontinuity at $(0, 1)$ analytically.

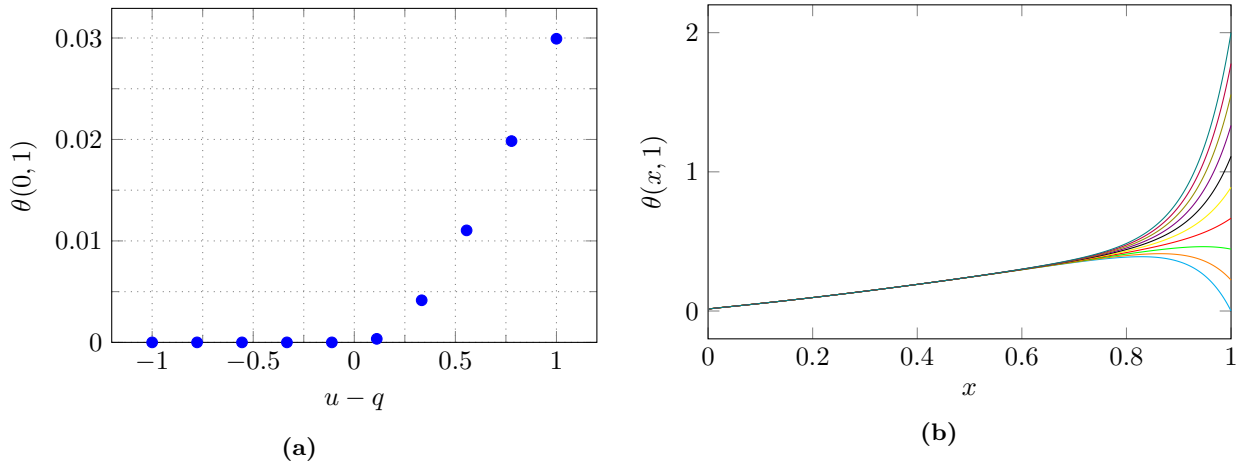

Figure 5.3.3 – (a) Temperature evaluated at the discontinuity $(0, 1)$ with $q = 1$, $\mathrm{Pe}^* = 0.4$, $\mathrm{Bi}^* = 1.1$, and $\theta_\mathrm{a} = x$, varying u from 0 to 2. (b) Temperature at the wall, $\theta(x, 1)$ from (5.83), with $u = 2$, $q = 1$, $\mathrm{Pe}^* = 0.4$, $\mathrm{Bi}^* = 1.1$, and $\theta_\mathrm{a} = x$, with for $\theta(1, 1) = \theta_0$. Each line corresponds to the solution for a different θ_0.

The numerical results confirm that imposing an end condition on θ at $(1, 1)$ gives a well-posed problem when $u > q$. The effect of varying $\theta(1, 1) = \theta_0$ while keeping other parameters fixed

is illustrated in Figure 5.3.3(b), where we plot the wall temperature $\theta(x,1)$. We observe that the solution adopts a universal profile away from $x = 1$, with a non-zero (though small) initial temperature $\theta(0,1)$, giving rise to the discontinuity highlighted in Figure 5.3.2. The temperature then adjusts near to $x = 1$ to fit the imposed end value θ_0. This behaviour will be analysed in more detail in §5.4. Note that the green curve in Figure 5.3.3(b) suggests that imposing a zero flux condition rather than an imposed temperature would also lead to a unique solution.

5.3.3 Comparing with an exact solution

To check that our numerical method converges to the correct solution we compare it with an exact solution where the temperature is known using a form of manufactured solution. In order to do this, we pose a simple form for θ, namely

$$\theta_e(x,y) = \frac{2}{u\mathrm{Pe}^*}x + y^2, \tag{5.94}$$

and substitute into (5.83) and find that now

$$\theta = y^2 \quad \text{at} \quad x = 0, \tag{5.95}$$

and the remaining equations (5.83a) (5.83c) and (5.83d) are automatically satisfied, provided

$$\theta_\mathrm{a} = 1 + 2\frac{\mathrm{Pe}^* q + \mathrm{Bi}^* x}{\mathrm{Bi}^*\mathrm{Pe}^* u}. \tag{5.96}$$

Note that, as before, when $u > q$ we must additionally impose

$$\theta = \theta_e(1,1) = \frac{2}{u\mathrm{Pe}^*} + 1 \qquad \text{at} \quad x = 1, \quad y = 1. \tag{5.97}$$

We use the discretisation described in §5.3.2 to solve (5.83a) with (5.95) and the appropriate form (5.96) for θ_a for both the $u > q$ and $u < q$ cases. The results are shown in Figure 5.3.4, where both solutions match, indicating that our numerical method indeed recovers θ_e. Furthermore, we present the results of a convergence test in Figure 5.3.5, where the maximum error norm is computed as a square mesh is refined from 20 to 1000 points. We observe quadratic convergence for N and a linear convergence for K, in accordance with convergence results for the finite difference schemes we have used. These results validate our numerical approach for solving (5.83).

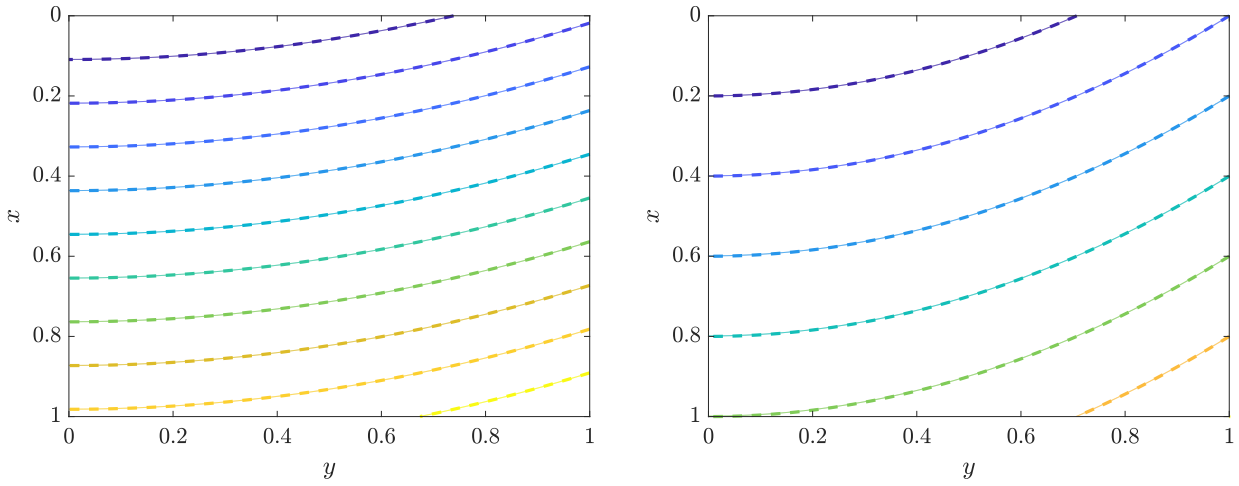

Figure 5.3.4 – Manufactured solution (5.94) (dashed line) compared to solution obtained with the numerical method described in §5.3.2 (solid line) with conditions (5.83c), (5.83d), (5.94) and θ_a given by (5.96), using $N = K = 1500$, and setting (a) $u = 1$, $q = 2$, (b) $u = 2$, $q = 1$.

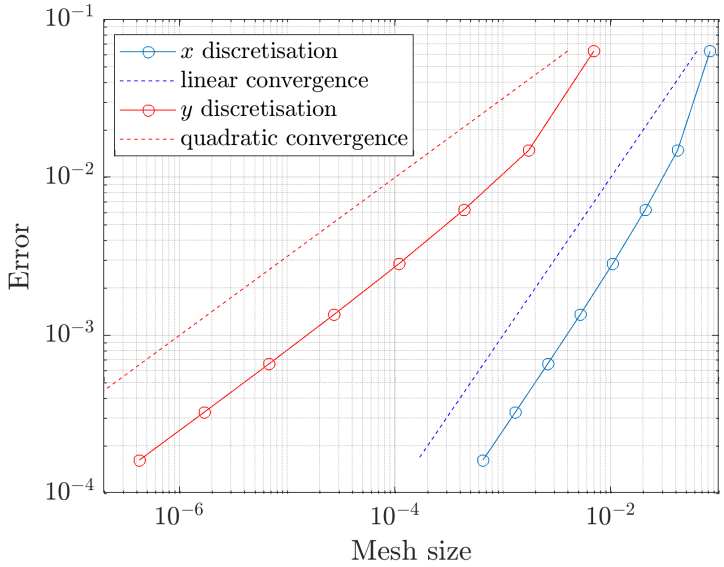

Figure 5.3.5 – Convergence measured in the maximum norm (i.e. L_∞) when a square mesh is refined in a regular way from 20 to 1000 gridpoints and reference lines for linear and quadratic convergence. We have used standard values $u = 2$, $q = 1$, $\mathrm{Pe}^* = 0.4$, $\mathrm{Bi}^* = 1.1$, $\theta_0 = 1$, and $\theta_\mathrm{a} = x$.

5.3.4 Regularising with diffusion in x

Another way to regularise our numerical method is to add a small amount of diffusion in the x-direction, so we can prescribe the temperature everywhere along the outflow boundary $x = 1$. Thus

we consider

$$\theta_x = \frac{1}{u\mathrm{Pe}^*}\left(\theta_{yy} + \varepsilon_D\theta_{xx}\right) \qquad 0 \le x \le 1, \quad 0 \le y \le 1, \tag{5.98a}$$

$$\theta = 0 \qquad \text{at} \quad x = 0, \quad 0 \le y \le 1, \tag{5.98b}$$

$$\theta_y = 0 \qquad \text{at} \quad y = 0, \quad 0 \le x < 1, \tag{5.98c}$$

$$\theta = \theta_0 \qquad \text{at} \quad x = 1, \quad 0 \le y \le 1, \tag{5.98d}$$

$$\theta_y = -\mathrm{Bi}^*\left(\theta - \theta_a\right) + (u-q)\mathrm{Pe}^*\theta_x + \varepsilon_D\theta_{xx} \qquad \text{at} \quad y = 1, \quad 0 < x < 1, \tag{5.98e}$$

where ε_D is a small regularising parameter. The advantage of this approach is that the problem is well-posed regardless of the sign of $u - q$, and we should obtain the solution to (5.83) as the limiting case of (5.98) when we take ε_D to zero. We modify our numerical method by adding the discretisation for $\varepsilon_D\theta_{xx}$ to (5.89) and (5.91), using

$$\theta_{xx} \approx \frac{\theta_n^{k+1} - 2\theta_n^k + \theta_n^{k-1}}{\Delta x^2}, \tag{5.99}$$

no longer applying any of the discrete equations at $k = K$ (since $\theta_n^K = 1$ is now prescribed for all n by (5.98d)).

In principle, the value of the temperature θ_0 imposed at the diffusion end of the domain should not affect the global solution outside a boundary layer at $x = 1$ in the limit $\varepsilon_D \to 0$. Hence, we set $\theta_0 = \theta_a^{\max} = 1$ for both the $u < q$ and $u > q$ cases. In this way, we are able to compare consistent solutions for either sign of $u - q$.

We show the behaviour of $\theta(x, 1)$ in Figure 5.3.6, for both $u < q$ and $u > q$, as we decrease ε_D, where the dashed line corresponds to $\varepsilon_D = 0$, the problem without diffusion in x (imposing $\theta_0 = 1$ at $x = 1$, $y = 1$ only for the case $u > q$). In both cases, as we decrease ε_D, the solution collapses onto the no x diffusion case, confirming that the numerical method we have used renders the solution of (5.83) as a limiting case of (5.98) as $\varepsilon_D \to 0$, as anticipated. In Figure 5.3.6(a) we see the boundary layer near $x = 1$ which decreases with decreasing ϵ_D, as required.

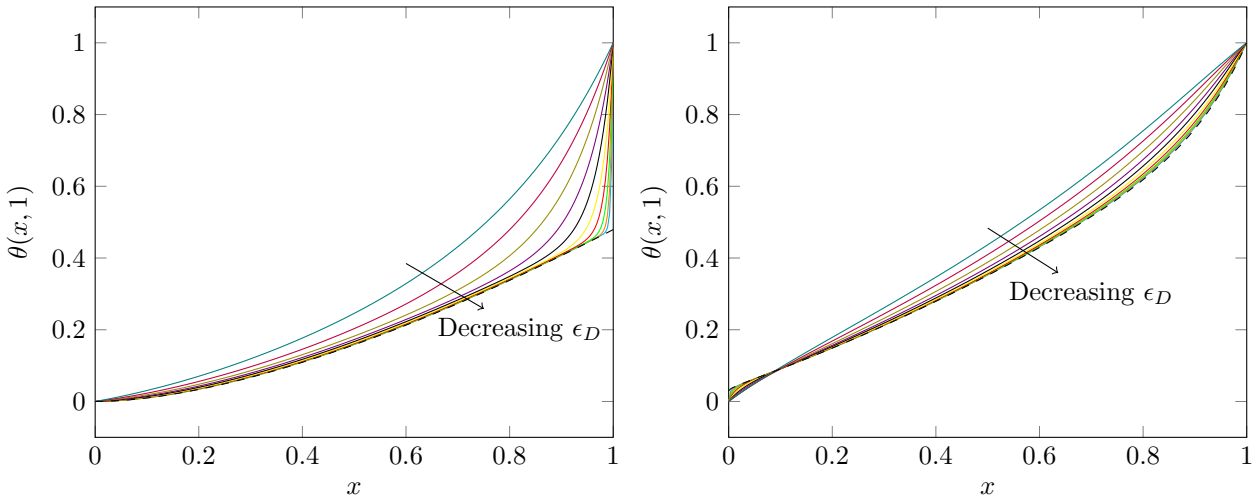

Figure 5.3.6 – Behaviour of the temperature at the wall, $\theta(x,1)$, comparing the solution to (5.98) as we decrease ε_D to the solution to (5.83) (dashed line) with $\mathrm{Pe}^* = 0.4$, $\mathrm{Bi}^* = 1.1$, $N = K = 1000$, $\theta_\mathrm{a} = x$, $\theta_0 = 1$, and (a) $q = 2$, $u = 1$, (b) $q = 1$, $u = 2$ (in which case (5.83) is supplemented by (5.88)). The parameter ε_D ranges logarithmically from 10^{-3} to 10^{-1}.

5.3.5 Local solutions near the corner $(0,1)$

From Figure 5.3.2, we observe that the discontinuity in the boundary conditions (5.83b) and (5.83d) at $(0,1)$ leads to a specific local behaviour of the solution, which we now proceed to investigate.

As is common in problems involving the heat equation, the behaviour near the discontinuity suggests the scaling:

$$y = 1 - \xi^{1/2}\bar{Y}, \tag{5.100a}$$

$$x = \xi\bar{X}, \tag{5.100b}$$

where $\xi \ll 1$. We let $\theta(x,y) = \bar{\Theta}(\bar{X},\bar{Y})$, and we expand

$$\bar{\Theta} \sim \bar{\Theta}^{(0)} + \xi^{1/2}\bar{\Theta}^{(1)} + \xi\bar{\Theta}^{(2)} + \dots, \tag{5.101}$$

with $\bar{X}$ and $\bar{Y}$ of $\mathcal{O}(1)$. Then, the problem (5.83) to lowest order in ξ is

$$\bar{\Theta}^{(0)}_{\bar{X}} = a\bar{\Theta}^{(0)}_{\bar{Y}\bar{Y}} \qquad \text{for} \quad \bar{X} > 0, \quad \bar{Y} > 0, \tag{5.102a}$$

$$\bar{\Theta}^{(0)} = 0 \qquad \text{at} \quad \bar{X} = 0, \tag{5.102b}$$

$$\bar{\Theta}^{(0)}_{\bar{X}} = 0 \qquad \text{at} \quad \bar{Y} = 0, \tag{5.102c}$$

$$\bar{\Theta}^{(0)}_{\bar{Y}} \to 0 \qquad \text{as} \quad \bar{Y} \to \infty, \tag{5.102d}$$

where $a = \frac{1}{u\mathrm{Pe}^*}$, assuming $\mathrm{Pe}^*\,(u-q) \neq 0$. We find the similarity solution to (5.102) of the form

$$\bar{\Theta}^{(0)}(\bar{X},\bar{Y}) = A_1 \mathrm{erfc}\left(\frac{\bar{Y}}{2\sqrt{a\bar{X}}}\right), \tag{5.103}$$

where A_1 is a constant and $\mathrm{erfc}(\cdot)$ is the complementary error function. Note that we cannot obtain the value of A_1 from this solution, and it should come from the matching to the problem away from the corner.

At next order in ξ, we have the problem

$$\bar{\Theta}^{(1)}_{\bar{X}} = a\bar{\Theta}^{(1)}_{\bar{Y}\bar{Y}} \qquad \text{for} \quad \bar{X} > 0, \quad \bar{Y} > 0, \tag{5.104a}$$

$$\bar{\Theta}^{(1)} = 0 \qquad \text{at} \quad \bar{X} = 0, \tag{5.104b}$$

$$\bar{\Theta}^{(1)}_{\bar{X}} = \frac{A_1\bar{X}^{-1/2}}{(u-q)\sqrt{a\pi}} \qquad \text{at} \quad \bar{Y} = 0, \tag{5.104c}$$

$$\bar{\Theta}^{(1)}_{\bar{Y}} \to 0 \qquad \text{as} \quad \bar{Y} \to \infty. \tag{5.104d}$$

As we did to solve (5.102), we rewrite (5.104) in terms of the grouped variable $\bar{Y}/\sqrt{a\bar{X}}$, and find that the similarity solution of the system (5.104) is of the form

$$\bar{\Theta}^{(1)}(\bar{X},\bar{Y}) = \frac{2A_1\bar{X}^{1/2}}{\mathrm{Pe}^*\,(u-q)\sqrt{a\pi}}\left[\frac{\bar{Y}}{2}\sqrt{\frac{\pi}{a\bar{X}}}\left(\mathrm{erf}\left(\frac{\bar{Y}}{2\sqrt{a\bar{X}}}\right)-1\right)+\exp\left(-\frac{\bar{Y}^2}{4a\bar{X}}\right)\right]. \tag{5.105}$$

We combine (5.103), (5.105), and undo the scaling to find the asymptotic solution for θ at $y = 1$ as

$$\theta(x,1) \sim A_1\left[1 + 2\left(\frac{u}{\pi\mathrm{Pe}^*}\right)^{1/2}\frac{1}{u-q}x^{1/2}\right] + \mathcal{O}(x). \tag{5.106}$$

The value of A_1 cannot be predicted locally but must be determined globally. Unless it is zero, the expansion (5.106) predicts a discontinuity in θ at $(0,1)$ with $\theta(0,y) = 0$, but $\theta(x,1) \to A_1$, as $x \to 0$, in agreement with Figure 5.3.2, when $u - q > 0$.

We compare our calculated local solution (5.106) with the numerical solution at $y = 1$ in Figure 5.3.7 where the small x behaviour approaches the expression (5.106), regardless of the value of $u-q$ used. We can also show that this is true for varying Pe^*, Bi^*, and discretisation level. Hence, the singular behaviour shown in Figure 5.3.2 is intrinsic to the equation we are solving and is correctly resolved by the numerical method.

The local analysis carried out in this section provides no way to calculate A_1, which in general depends on Pe^* and Bi^*, as well as $u - q$ (as will be shown later in Figures 5.4.2 and 5.4.3). In particular, we know from our previous numerical results that $A_1 = 0$ (so the inlet temperature is continuous) whenever $u < q$ but A_1 is positive when $u > q$, as seen in Figure 5.3.3(a). To understand this behaviour, we next perform an asymptotic analysis in the limit of small $u - q$.

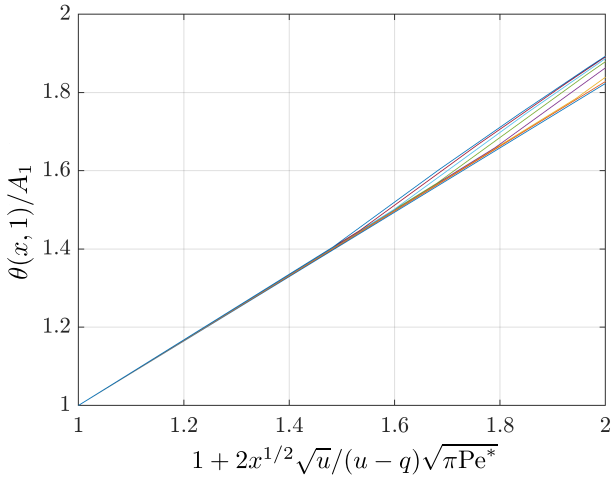

Figure 5.3.7 – Behaviour of the normalised wall temperature with $q = 1$, $\mathrm{Pe} = 0.4$, $\mathrm{Bi}^* = 1.1$, $N = K = 1500$, $\theta_\mathrm{a} = x$, and $\theta_0 = 1$, varying u such that $u - q = \{0.01, 0.02, \ldots, 0.1\}$. The value of A_1 in each case is taken from the numerical solution of the limiting value of $\theta(x, 1)$ as x approaches 0.

5.4 Asymptotics for $u \approx q$

Our problem is sensitive to the sign of $u - q$, as $u > q$ corresponds to the case where the velocity at which the paste is being pushed into the casing in faster than the downstream velocity, which produces recirculation zones at the sides. Naturally, this behaviour does not occur for $u < q$, where the paste velocity increases along the casing to match the specified flux. However, it is not clear what happens when $u - q$ is small, as it transitions from one case to the other. In this section, it is our aim to understand the behaviour of the temperature in the asymptotic limit where $u \approx q$.

We investigate this scenario by setting

$$\delta = u - q, \tag{5.107}$$

and exploring the behaviour with $0 < \delta \ll 1$. From the numerical results, we know that it is necessary to impose a condition on $\theta(1, 1)$ in order to obtain well-defined solutions. The problem to consider is therefore (5.83) with the additional end condition (5.88). We begin by solving the outer problem in §5.4.1 for small $u-q$ and we investigate an inner region near $(1, 1)$ in §5.4.2 to impose θ_0. In §5.4.3, we conclude by consolidating our new asymptotic results with the small x-approximation previously obtained in §5.3.5.

5.4.1 The outer problem

For the outer problem, we perform a regular expansion in powers of δ, so $\theta \sim \theta^{(0)} + \delta\theta^{(1)} + \ldots$, keeping x and y with their original scalings. Then, the leading order outer problem is

$$\theta^{(0)}_x = \frac{1}{u\mathrm{Pe}^*}\theta^{(0)}_{yy} \qquad \text{for} \quad 0 \le x \le 1, \quad 0 \le y \le 1, \tag{5.108a}$$

$$\theta^{(0)} = 0 \qquad \text{at} \quad x = 0, \quad 0 \le y \le 1 \tag{5.108b}$$

$$\theta^{(0)}_y = 0 \qquad \text{at} \quad y = 0, \quad 0 \le x \le 1, \tag{5.108c}$$

$$\theta^{(0)}_y = -\mathrm{Bi}^* \left(\theta - \theta_a\right) \qquad \text{at} \quad y = 1, \quad 0 \le x < 1. \tag{5.108d}$$

This outer problem is solved using the method of separation of variables by setting $\theta^{(0)}(x, y) = X(x)Y(y)$, and solving the associated spectral problem. After applying boundary conditions, we find the exact solution of (5.108) in terms of the generalised Fourier series

$$\theta^{(0)}_{\mathrm{outer}}(x, y) = \sum_{k=1}^{\infty} \zeta_k \cos \mu_k y \left(\theta_a(x) - \int_0^x \frac{1}{u\mathrm{Pe}^*} \mu_k^2 \theta_a(s) \exp\left(-\frac{\mu_k^2 \left(x - s\right)}{u\mathrm{Pe}^*} \right) \mathrm{d}s \right) + \theta_a(x), \tag{5.109a}$$

where

$$\zeta_k = \frac{-2 \sin \mu_k}{\sin \mu_k \cos \mu_k + \mu_k} \qquad \text{and} \qquad \mu_k = \frac{\mathrm{Bi}^*}{\tan \mu_k}. \tag{5.109b}$$

5.4.2 Zooming into the $(1, 1)$ corner

The leading-order outer problem (5.108) does not contain the term proportional to δ that describes transport along the wall. The outer solution (5.109) is fully determined by the ambient temperature θ_{a}, and it is therefore impossible to impose the additional constraint $\theta(1, 1) = \theta_0$. To resolve this problem, we must consider an inner region near $(1, 1)$. We introduce stretched coordinates

$$x = 1 - \frac{\mathrm{Pe}^*}{u}\delta^2 X \qquad \text{and} \qquad y = 1 - \frac{\delta}{u} Y, \tag{5.110}$$

where $X \in [0, \infty)$, $Y \in [0, \infty)$. Additionally, we rescale $\theta = \theta_\infty + (\theta_0 - \theta_\infty)\,\bar{\theta}$ and $\theta_a = \theta_\infty + (\theta_0 - \theta_\infty)\,\bar{\theta_a}$, where θ_∞ is given by $\theta^{(0)}_{\mathrm{outer}}(1, 1)$. Then, at leading order (5.83) becomes

$$-\bar{\theta}^{(0)}_X = \bar{\theta}^{(0)}_{YY}, \qquad \text{for} \quad X > 0, \quad Y > 0, \tag{5.111a}$$

$$\bar{\theta}^{(0)}_X = \bar{\theta}^{(0)}_Y \qquad \text{at} \quad Y = 0, \quad X > 0, \tag{5.111b}$$

$$\bar{\theta}^{(0)} = 1 \qquad \text{at} \quad X = 0, \quad Y = 0, \tag{5.111c}$$

$$\bar{\theta}^{(0)} \to 0, \qquad \text{as} \quad X, Y \to \infty. \tag{5.111d}$$

The leading order inner problem (5.111) has solution $\bar{\theta} = e^{-X-Y}$ so, rescaling for θ, we have

$$\theta^{(0)}_{\mathrm{inner}}(X, Y) = \theta_\infty + (\theta_0 - \theta_\infty) e^{-X-Y}, \tag{5.112}$$

where X and Y here are defined by (5.110).

Equations (5.109) and (5.112) allow us to see what happens to θ as the velocity difference δ becomes small. We compare these asymptotic solutions to the numerical solution in Figure 5.4.1, where we show that as we look closer to the $(1,1)$ corner, the inner problem begins to approximate the solution, with the outer solution providing a good approximation elsewhere. The boundary layer is quite small because its thickness scales with δ^2. Given the close agreement shown in Figure 5.4.1, the asymptotic solution provides us with a way to understand the temperature profile as $u \to q$. In particular, it confirms the structure observed previously in Figure 5.3.3(b), of a universal outer solution (5.109) that adjusts to the imposed end temperature θ_0 over a small boundary layer near $x = 1$.

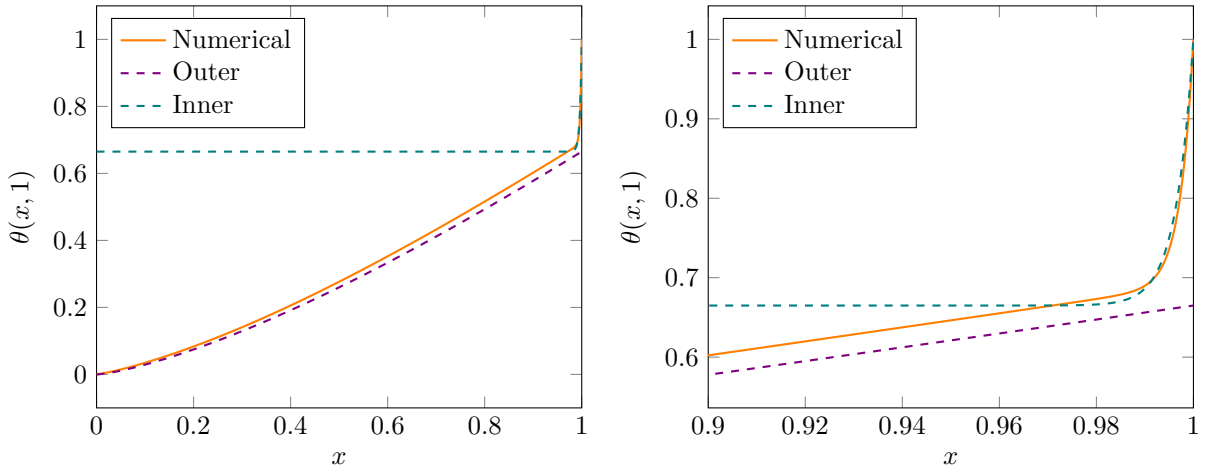

Figure 5.4.1 – Temperature at the wall $\theta(x,1)$, comparing numerical and asymptotic solutions, with $q = 1$, $u = 1.05$ (so $\delta = 0.05$), $\mathrm{Pe}^* = 0.4$, and $\mathrm{Bi}^* = 1.1$, $N = K = 1500$, $\theta_\mathrm{a} = x$, and $\theta_0 = 1$. Panel (b) shows a close up near $x = 1$.

5.4.3 Zooming into the $(0,1)$ corner

We now seek to understand the behaviour of θ as we consolidate the small-x approximation in §5.3.5 and the small δ approximation in §5.4.1. In particular, we note the presence of $(u - q)$ in the denominators of the small-x expansion (5.106), indicating a conflict in the limits $x \to 0$ and $\delta \to 0$. We obtain a distinguished limit when $x \sim \mathcal{O}(\delta^2)$ which retains the contributions from the air column heating $\theta_a(x) = x$ as well as the θ_x term in the boundary condition (5.83d) for the heat flux at $y = 1$.

For the inner problem, we use the rescalings

$$x = \frac{\mathrm{Pe}^*\delta^2}{u}X, \qquad y = 1 - \frac{\delta Y}{u}, \qquad \theta = \frac{\mathrm{Bi}^*\mathrm{Pe}^*\delta^3}{u^2}\bar{\theta} \tag{5.113}$$

and substitute into (5.83). To leading order in δ, the problem to solve is

$$\bar{\theta}^{(0)}_X = \bar{\theta}^{(0)}_{YY} \qquad \text{for} \quad X > 0, \quad Y > 0, \tag{5.114a}$$

$$\bar{\theta}^{(0)} = 0 \qquad \text{at} \quad X = 0, \quad Y > 0, \tag{5.114b}$$

$$\bar{\theta}^{(0)}_Y = -X - \bar{\theta}^{(0)}_X \qquad \text{at} \quad Y = 0, \quad X > 0. \tag{5.114c}$$

Let $F(s,Y) = \int_0^\infty \bar{\theta}^{(0)}(X,Y)e^{-sX}\mathrm{d}X$ be the Laplace transform of $\bar{\theta}$. Then the general solution of (5.114) in transformed variables is given by

$$F(s,Y) = A(s)e^{-Y\sqrt{s}} + B(s)e^{Y\sqrt{s}}, \tag{5.115}$$

where $A(s)$ and $B(s)$ are arbitrary functions. We take $\sqrt{s}$ to have a positive real part, and $B(s)$ must therefore be zero to avoid exponential growth as $Y \to \infty$.

Then we impose (5.114c) to (5.115) and find

$$F(s,Y) = \frac{\left(\bar{A}_1 - \frac{1}{s^2}\right)}{s - \sqrt{s}} e^{-Y\sqrt{s}}, \tag{5.116}$$

where $\bar{A}_1$ is the value of $\bar{\theta}^{(0)}$ at $X = Y = 0$.

We observe that $F(s,Y)$ has a singularity with $F(s,Y) \sim s^{-5/2}$ as $s \to 0$, corresponding to $\bar{\theta}$ growing like $\bar{X}^{3/2}$ as $\bar{X} \to \infty$. There is also a pole at $s = 1$, corresponding to exponential growth in $\bar{X}$. To suppress the exponential growth, we remove the pole by selecting $\bar{A}_1 = 1$. By reversing the scaling in (5.113), we obtain the following estimate for the constant A_1 introduced earlier in §5.3.5

$$\lim_{x \to 0} \theta(x,1) = A_1 \sim \frac{\mathrm{Bi}^*\mathrm{Pe}^*\delta^3}{u^2} \quad \text{as} \quad \delta \searrow 0. \tag{5.117}$$

We compare the numerically obtained A_1 with its predicted scaling (5.117) while varying Pe^* and Bi^* in Figures 5.4.2 and 5.4.3, respectively. For each case, we demonstrate that the value of A_1 produced by our numerical solution converges to the asymptotic prediction as δ decreases towards zero. In general, the value of the constant A_1 depends on the global solution, in particular on the imposed end temperature θ_0. However, we have shown that A_1 can be locally determined when δ is small. This result is consistent with Figure 5.3.3(b), where we see that the solution becomes insensitive to the value of θ_0 outside a neighbourhood of $x = 1$, even with $\delta = 1$. Furthermore, (5.117) shows that $A_1 \to 0$ as $\delta \to 0$ from above, which is consistent with our expectation that A_1 should be zero when $\delta \leq 0$.

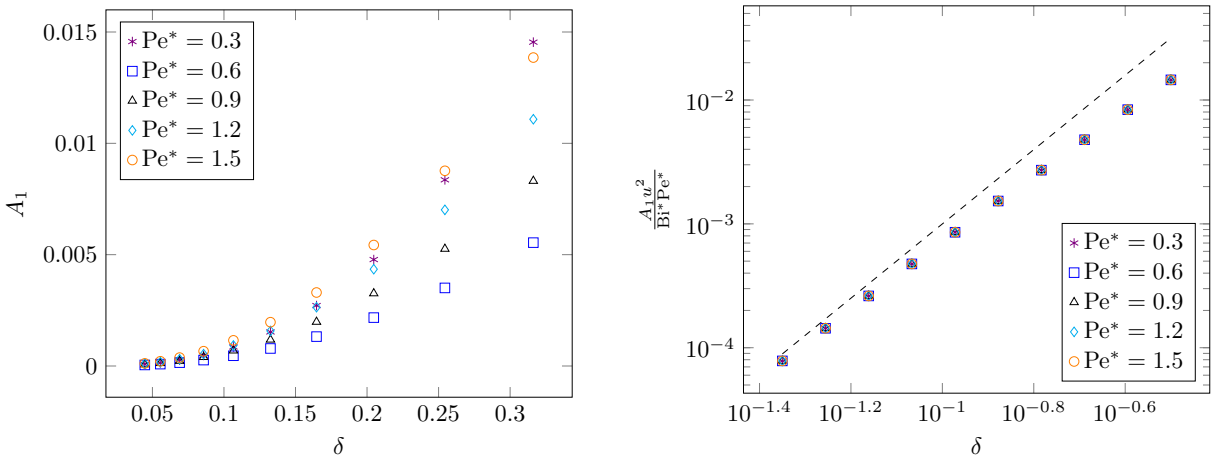

(a) **(b)**

Figure 5.4.2 – Behaviour of $A_1 = \lim_{x \to 0} \theta(x, 1)$ as we change $\delta \in (0.04, 0.3)$ for different values of Pe^*, with $\mathrm{Bi}^* = 1.1$ (a) unscaled, (b) applying the scaling (5.117). We have used 10 values of δ. As $\delta \to 0$, the solutions approach the dashed line, showing the predicted scaling δ^3.

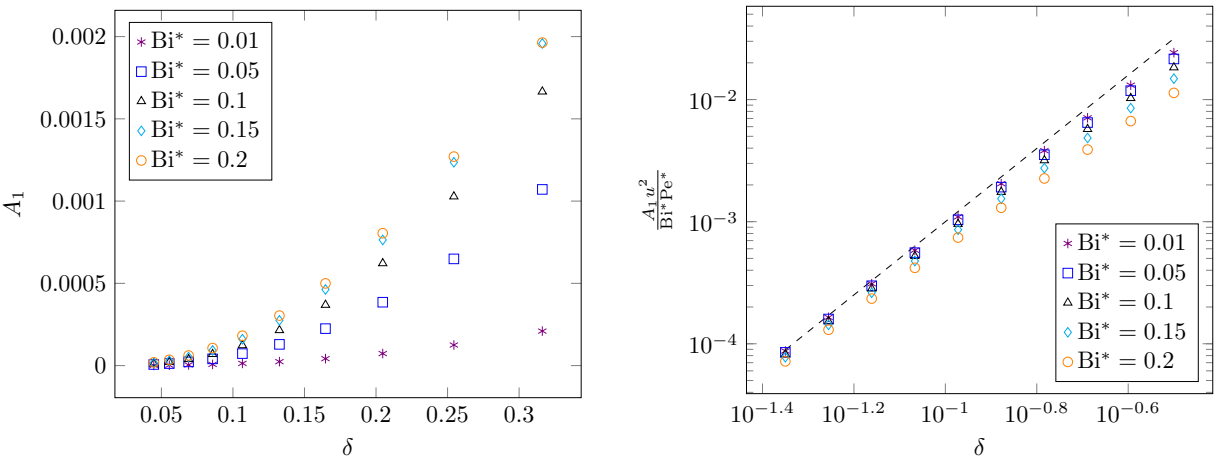

(a) **(b)**

Figure 5.4.3 – Behaviour of $A_1 = \lim_{x \to 0} \theta(x, 1)$ as we change $\delta \in (0.04, 0.3)$ for different values of Bi^*, with $\mathrm{Pe}^* = 0.4$ (a) unscaled, (b) applying the scaling (5.117). We have used 10 values of δ. As $\delta \to 0$, the solutions approach the dashed line, showing the predicted scaling δ^3.

5.5 Fully coupled flow and temperature problem

Now that we have looked at what happens to the flow problem for known temperature, and the temperature problem for known flow, it is clear that the last step is to understand the fully coupled flow and temperature problem. Although the complexity of this system prevents us from obtaining analytic solutions, we can investigate it numerically. In this section we present the necessary modifications to the discretisation method presented in §5.3.2 to take into account that $u(x)$ is not a constant, but the solution of a second order differential equation with coefficients that depend on θ, as in §5.1.4. However, the inaccuracies in the approximations generated using Laplace's method (5.43) which we used for these coefficients in §5.1 are not robust enough to use for this fully coupled problem. In particular, $\theta_{yy}(x,0)$ is very small near $x=0$, which causes the approximation for α in (5.43) to break down. In cases where we are interested specifically in the behaviour as we increase Γ, it is beneficial to directly discretise the integrals (5.31a), (5.31b), and (5.34) rather than using the approximations generated using Laplace's method. Therefore, in this section we describe a numerical method that uses the integral expressions (5.31a), (5.31b), and (5.34) directly.

We first describe the full coupled problem and then explain the iterative procedure used for the coupling.

5.5.1 Numerical method

The problem is to solve the temperature and the velocity problem as a PDE coupled with an ODE, namely

$$u\theta_x - yu_x\theta_y = \frac{1}{\mathrm{Pe}^*}\theta_{yy} \qquad \text{for} \quad 0<x<1, 0<y<1, \tag{5.118a}$$

$$\theta = 0 \qquad \text{at} \quad x=0, \tag{5.118b}$$

$$\theta_y = 0 \qquad \text{at} \quad y=0, \tag{5.118c}$$

$$\theta = \theta_0 \qquad \text{at} \quad x=1,\ y=1, \tag{5.118d}$$

$$\theta_y = -\mathrm{Bi}^*\left(\theta-\theta_\mathrm{a}\right) + \mathrm{Pe}^*\theta_x\left(u-q\right) \qquad \text{at} \quad y=1. \tag{5.118e}$$

In the examples in this section, we use $\theta_a(x)=x$ and $u(x)$ satisfies the system

$$\frac{\mathrm{d}}{\mathrm{d}x}\left(\hat{\alpha}u_x\right) = \beta_1\left(1-u\right) - \beta_2\left(1-q\right) \qquad \text{for} \quad 0<x<1, \tag{5.119a}$$

$$u = u_\mathrm{in} \qquad \text{at} \quad x=0, \tag{5.119b}$$

$$u = q + \varepsilon_q \qquad \text{at} \quad x=1, \tag{5.119c}$$

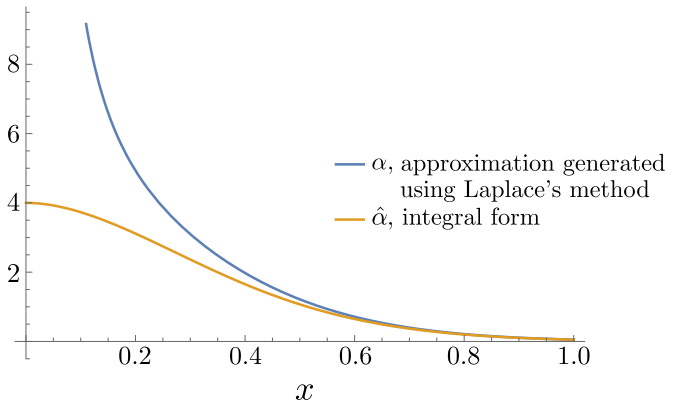

Figure 5.5.1 – Approximation generated using Laplace's method α compared with integral form $\hat{\alpha}$, using (5.109).

where

$$\hat{\alpha}(x) = 4\int_0^1 e^{-\Gamma\theta(x,y)}\mathrm{d}y, \tag{5.120a}$$

$$\beta_1(x) = -\frac{\epsilon^2}{\Delta(x)}\int_0^1 y^2 e^{\Gamma\theta(x,y)}\mathrm{d}y, \tag{5.120b}$$

$$\beta_2(x) = -\frac{\epsilon^2}{\Delta(x)}\int_0^1 y e^{\Gamma\theta(x,y)}\mathrm{d}y, \tag{5.120c}$$

and where $\Delta(x)$ is given by

$$\Delta(x) = \epsilon^4\left[\int_0^1 e^{\Gamma\theta(x,y)}\mathrm{d}y\int_0^1 y^2 e^{\Gamma\theta(x,y)}\mathrm{d}y - \left(\int_0^1 y e^{\Gamma\theta(x,y)}\mathrm{d}y\right)^2\right]. \tag{5.121}$$

We have used the simple exponential viscosity-temperature relationship in (5.38). As a validity check, in Figure 5.5.1 we compare the integral formulation $\hat{\alpha}(x)$, with its approximation generated using Laplace's method $\alpha(x)$ given by (5.43b) using the analytic expressions for θ in (5.109). Note that, despite the fact that α only depends on the temperature and temperature gradient evaluated at $y = 0$, the approximation becomes more accurate as we move further down the electrode column. This approximation breaks down near $x = 0$, where θ_{yy} tends to zero.

We are interested in situations where $u_{\text{in}} > q$, and therefore include the condition (5.118d) as discussed in §5.3. In principle we should impose a plug flow with $u = q$ at the downstream end, but to avoid the singularity in the limit $u = q$, we instead add a small positive perturbation ε_q in the boundary condition (5.119c).

To be consistent with the method used in §5.3 for the constant u problem, we discretise the additional transverse advection term in (5.118a) with centered differences, namely

$$\theta_y = \frac{\theta^k_{n+1} - \theta^k_{n-1}}{2\Delta y} \tag{5.122}$$

for each k, as before, and $0 < n < N$. We write the discretised form of (5.119) as,

$$\frac{\hat{\alpha}^k}{\Delta x^2}u^{k+1} + \left(\frac{\hat{\alpha}^{k+1} - \hat{\alpha}^{k-1}}{2\Delta x^2} + \beta_1^k - 2\frac{\hat{\alpha}^k}{\Delta x^2}\right)u^k + \left(\frac{\hat{\alpha}^k}{\Delta x^2} - \frac{\hat{\alpha}^{k+1} - \hat{\alpha}^{k-1}}{2\Delta x^2}\right)u^{k-1} = \beta_1^k - \beta_2^k\,(1-q)\,, \tag{5.123}$$

for $0 < k < K$, where we have used centered differences for the derivative of $\hat{\alpha}$ with respect to x. This is a boundary value problem, with $u^0 = u_{\text{in}}$ and $u^K = q + \varepsilon_q$.

Parameter	**Description**	**Value**
ϵ	Aspect ratio	0.5
Γ	Viscosity dependence with temperature	varies
ε_{tol}	Stopping criterion for iterative procedure	10^{-8}
u_{in}	Initial velocity, related to weight of cylinders	2
q	Velocity of the casing	1
ε_q	Perturbation to end condition for $u(x)$	0.1
Pe^*	Reduced Péclet number	0.4
Bi^*	Reduced Biot number	1.1

Table 5.5.1 – Typical parameters used for the numerical solutions described in §5.5.1.

In order to couple the two systems (that for θ and that for u) together, we take an iterative approach. We compute θ with a guess for u following the approach described in §5.3 and then solve equation (5.119) for u with this calculated θ.

The coupling can be described by the following iterative procedure:

1. Solve the discretised version of (5.118) with an initial guess for u, e.g.

$$u(x) = u_{\text{in}} + (q + \varepsilon_q - u_{\text{in}})\,x. \tag{5.124}$$

   This gives ${\theta_n^k}^{(0)}$.
2. Solve (5.123), using ${\theta_n^k}^{(0)}$ to define the coefficients $\hat{\alpha}$, β_1, and β_2. The required first and second derivatives of θ are computed with finite differences. This gives us ${u^k}^{(1)}$.
3. Solve the discretised version of (5.118) using ${u^k}^{(1)}$.
4. Continue to solve the u problem and the θ problem iteratively, until

$$\mathrm{e}^i = \left\|(\theta)^{(i)} - (\theta)^{(i-1)}\right\| < \varepsilon_{\text{tol}}, \tag{5.125}$$

   where ε_{tol} is some set tolerance.

The values for the numerical parameters introduced above are shown in Table 5.5.1. The integrals (5.120b) and (5.120c) are computed with `trapez.m`, an inbuilt MATLAB routine for the trapezoidal rule for integration. The results are shown in Figure 5.5.2, where we show the coefficients $\hat{\alpha}$, β_1,

and β_2, and the converged solution for $u(x)$. The numerical method converges quickly, taking 4 iterations for each value of Γ.

Note that for smaller values of Γ, the leading order velocity $u(x)$ gradually reaches the end condition $q + \varepsilon_q$, whereas for larger Γ, $u(x)$ is characterised by a sharp deceleration near $x = 1$. The latter behaviour corresponds to the cylinders moving at the constant inlet speed u_{in} throughout most of length the casing and only spreading near the bottom of the domain due to the hot paste recirculating near the wall. Furthermore, the coefficients β_1 and β_2 approach each other as we increase Γ, consistent with the approximations in (5.39), as $\theta_y(x, 1)$ becomes smaller. Additionally, in Figures 5.5.3(a) to 5.5.3(d) we note that a larger Γ results in hotter paste near the top of the casing wall, which is then cooled down by $\theta_a(x)$, resulting in the presence of colder paste near the bottom. For the largest Γ case in Figure 5.5.3(d), the temperature reaches the end condition $\theta_0 = 1$ very close to the corner, and it is not noticeable in this figure. We note that the resulting temperature distributions are mostly very similar, suggesting that the coupling from the flow to the temperature is quite weak, whereas the converse coupling is much stronger, as seen in §5.1.

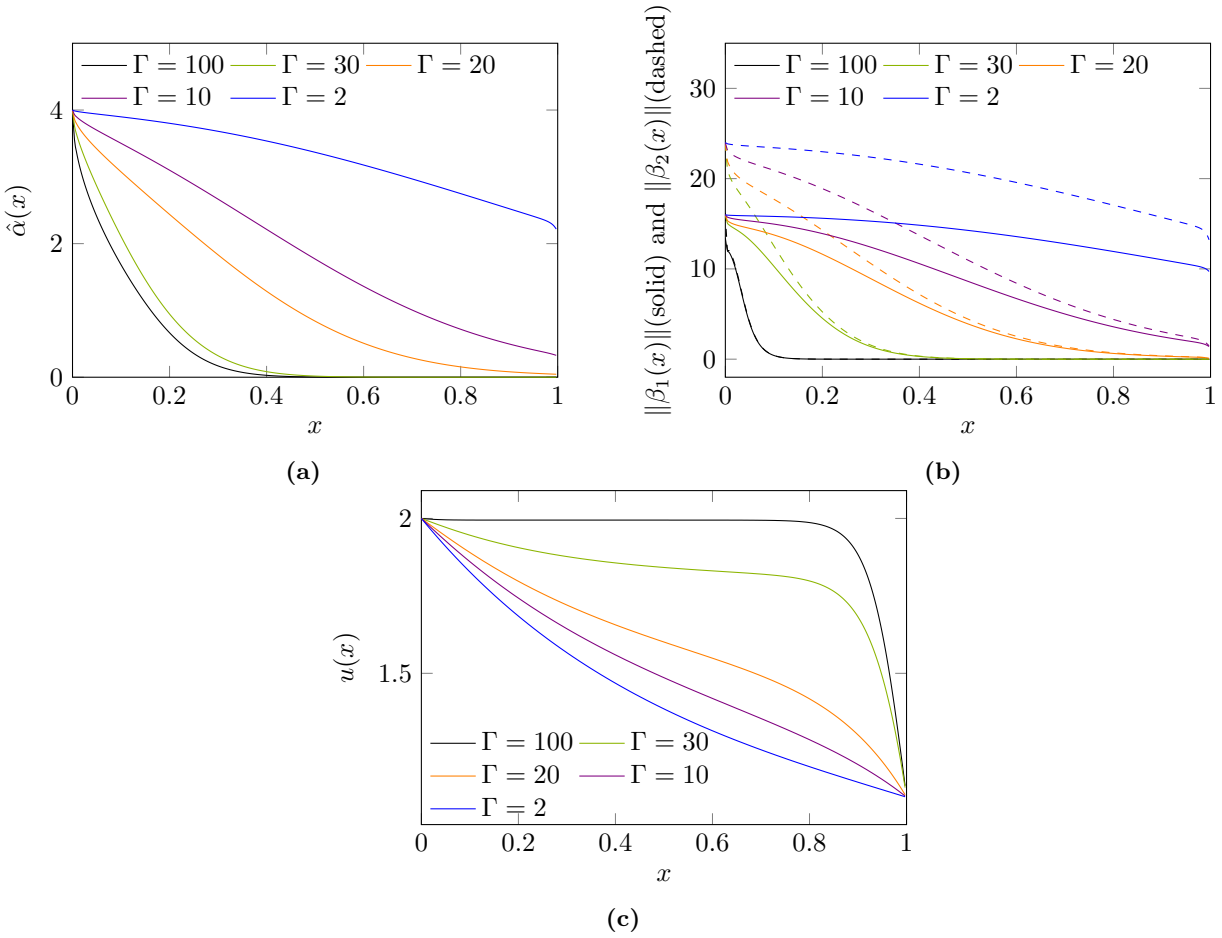

Figure 5.5.2 – Results of the coupled problem (5.118) for the coefficients (a) $\hat{\alpha}$, (b) β_1, and β_2, given by (5.120) and (c) velocity obtained with (5.119a), for different values of Γ.

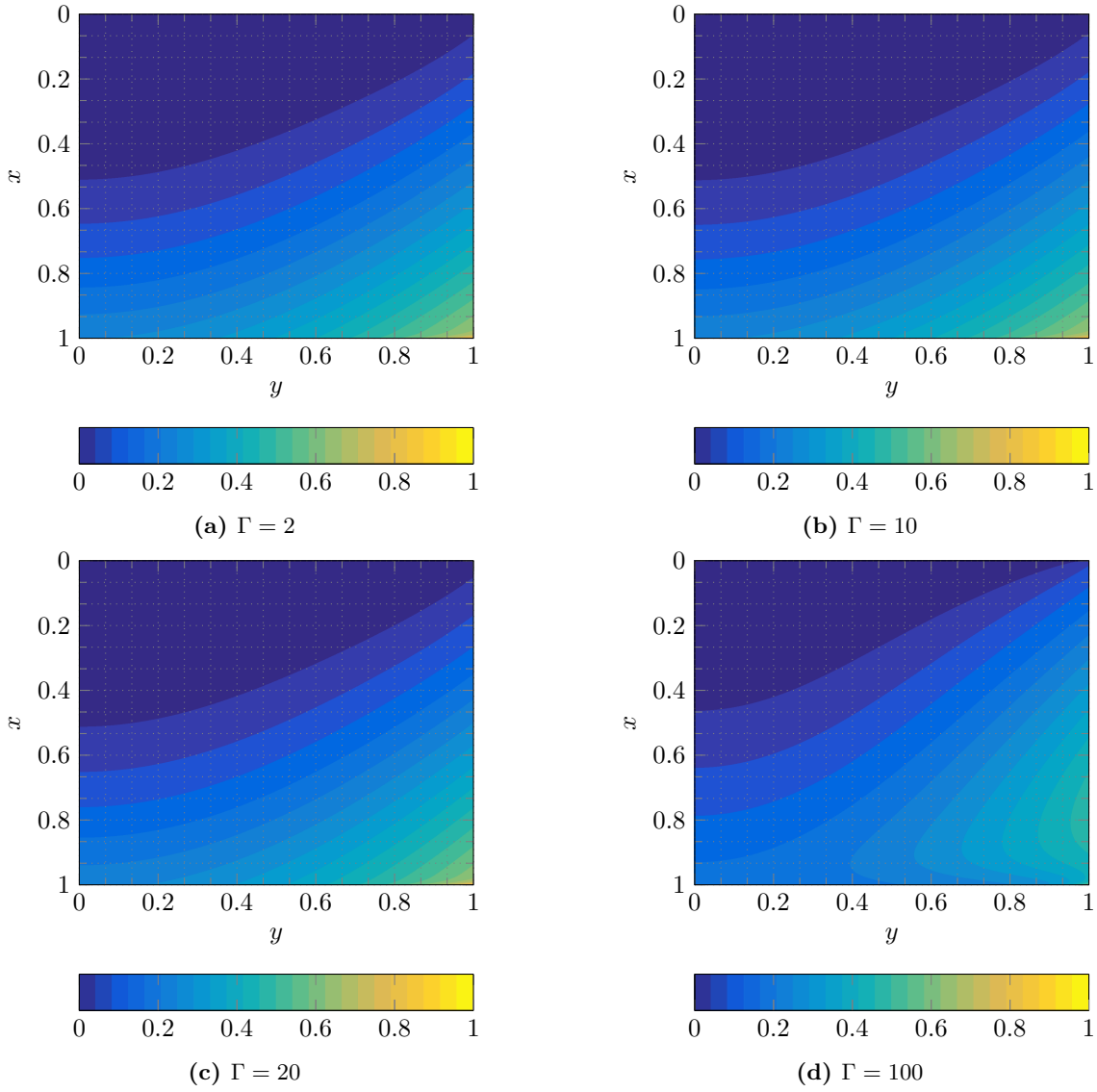

(a) $\Gamma = 2$ **(b)** $\Gamma = 10$

(c) $\Gamma = 20$ **(d)** $\Gamma = 100$

Figure 5.5.3 – Corresponding temperature contours for the results in Figure 5.5.2, given by the solution to (5.118) are shown in (a)-(d), using parameter values in Table 5.5.1 for different values of Γ.

5.6 Dependence of solutions on parameters

The problem (5.118) and (5.119) has a number of important parameters that are interesting to explore, in particular the effect of the reduced Péclet number Pe^*, the reduced Biot number Bi^*, and the inlet velocity u_{in}. We continue to focus our attention to cases where $u_{\mathrm{in}} > q$ with $q = 1$, as this is the industrially relevant problem. The coupling between the temperature and velocity is determined by Γ, and for all simulations in this section, we have used a constant value of $\Gamma = 30$, which it is sufficiently large to show a coupling between the two problems, and sufficiently small so that we can visualise the flow behaviour in the boundary layer close to the wall. We have also used the integral formulations for the coefficients given by (5.120). The colourmap is fixed to vary from 0 to 1, so the colour scale is the same in all the figures.

We begin by exploring Pe^*, which determines how strong the diffusive term is in (5.118a). We expect that for smaller Pe^*, the wall heating has greater effect and the temperature increases more rapidly with x, which is observed in Figure 5.6.1. The streamlines indicate that the width of the boundary layer at the wall decreases as we increase Pe^* as this confines the temperature variations closer to the wall. This means that electrode paste with a larger thermal conductivity coefficient k will experience greater recirculation of paste near the casing wall. Conversely, increasing the casing speed (which increases Pe^*) will produce flow profiles similar to the ones shown in Figure 5.6.1(c) with a more confined recirculating region.

Next, we explore variations in Bi^*, an indicator of how strong the heating term $\theta_a(x)$ is when imposed at $y = 1$. In the extreme case where there is no heat transfer from the wall, i.e. when $\mathrm{Bi}^* = 0$, the paste only softens near the bottom of our domain, where we have imposed $\theta(1, 1) = 1$, as this is the only heating term left in the problem, as seen in Figure 5.6.2(a). As we increase Bi^* in Figure 5.6.2, the heating from the air column becomes more dominant in boundary condition (5.118e), so the recirculation zone becomes larger. In this case, as in the case with small Pe^* in Figure 5.6.1, the recirculating hot paste prevents the cold paste from spreading as easily towards the wall, and the majority of the spreading happens further down the domain. Note that we have imposed that $u = q + \varepsilon_q$ at $x = 1$ (with $\varepsilon_q = 0.1$), whereas in reality u reaches q at a position controlled by the baking that occurs beyond the end of our domain.

Finally, we look at variations in u_{in} in Figure 5.6.3. For a smaller u_{in}, once the paste spreading has occurred, the flow profile approaches a plug flow outside of the boundary layer, as seen in Figures 5.6.3(a) and 5.6.3(b). As expected, increasing u_{in} allows for the formation of the recirculation zones, which form when $u_{\mathrm{in}} = 2$ in Figure 5.6.3(c), close to the casing wall.

Note that the flow profiles with recirculation zones, such as the ones shown in Figure 5.6.1, Figure 5.6.2(c), and Figure 5.6.3(c), qualitatively match to the ones observed for the imposed temperature cases shown in, for example, Figure 5.1.8. This brings value to studying the flow problem separately from the temperature one, as it appears that the general flow behaviour is

captured by (5.52) and (5.53) imposing a temperature profile that reaches its maximum at $y = 1$. Furthermore, the results shown in this section correspond well with the behaviour seen in the full finite element simulations described in Chapter 4, in particular when comparing the dependence on heating parameters shown in §4.4.1 and the inlet velocity shown in §4.5.1 . The simplifications carried out throughout this chapter therefore retain enough information to describe important features of both the flow and the temperature behaviour of paste at the top part of the electrode.

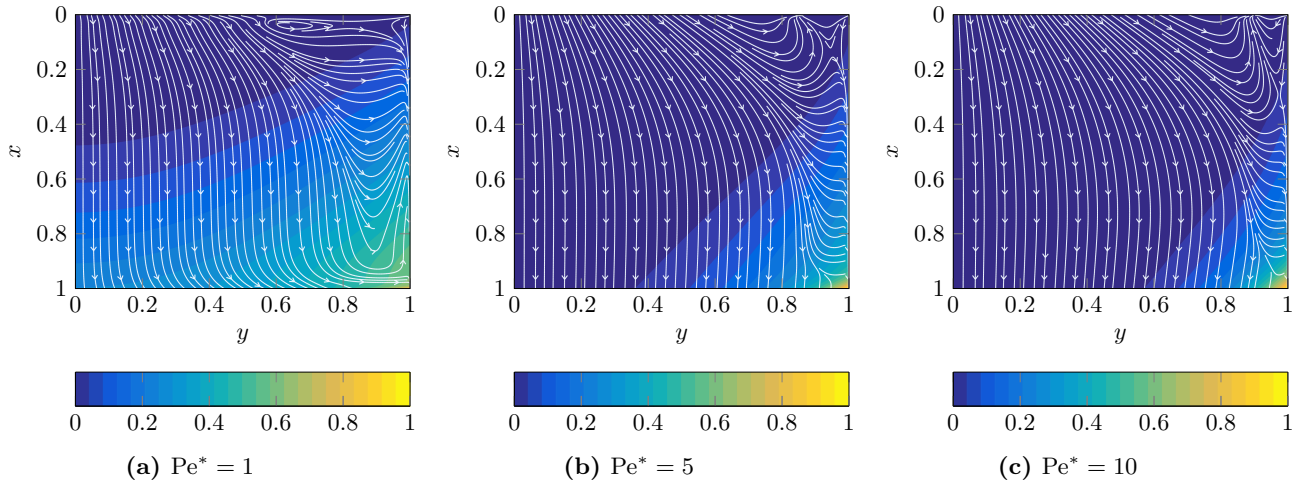

(a) $\mathrm{Pe}^* = 1$ **(b)** $\mathrm{Pe}^* = 5$ **(c)** $\mathrm{Pe}^* = 10$

Figure 5.6.1 – Temperature profiles given by solving (5.118) coupled with (5.119a), and streamlines obtained with the full velocity profiles (5.52) and (5.53). We have used $\theta_a = x$, $\theta_0 = 1$, $\Gamma = 30$, $\mathrm{Bi}^* = 2.3$, $N = 1000$, $K = 600$, $u_{\mathrm{in}} = 2$, and $q = 1$, as we increase Pe^*.

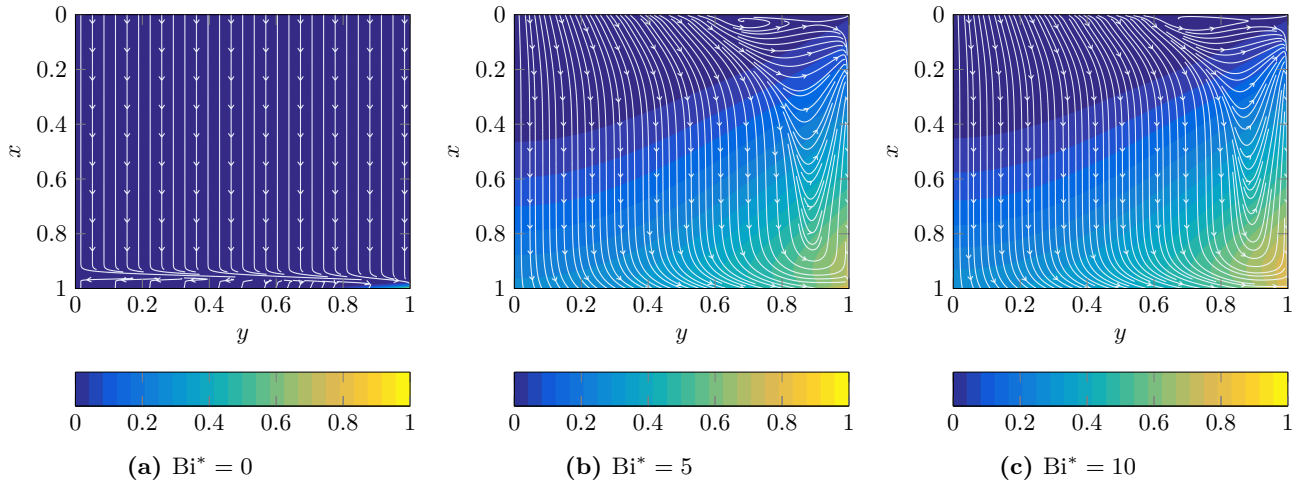

(a) $\mathrm{Bi}^* = 0$ **(b)** $\mathrm{Bi}^* = 5$ **(c)** $\mathrm{Bi}^* = 10$

Figure 5.6.2 – Temperature profiles given by solving (5.118) coupled with (5.119a), and streamlines obtained with the full velocity profiles (5.52) and (5.53). We have used $\theta_a = x$, $\theta_0 = 1$, $\Gamma = 30$, $\mathrm{Pe}^* = 1.1$, $N = 1000$, $K = 600$, $u_{\mathrm{in}} = 2$, and $q = 1$, as we increase Bi^*.

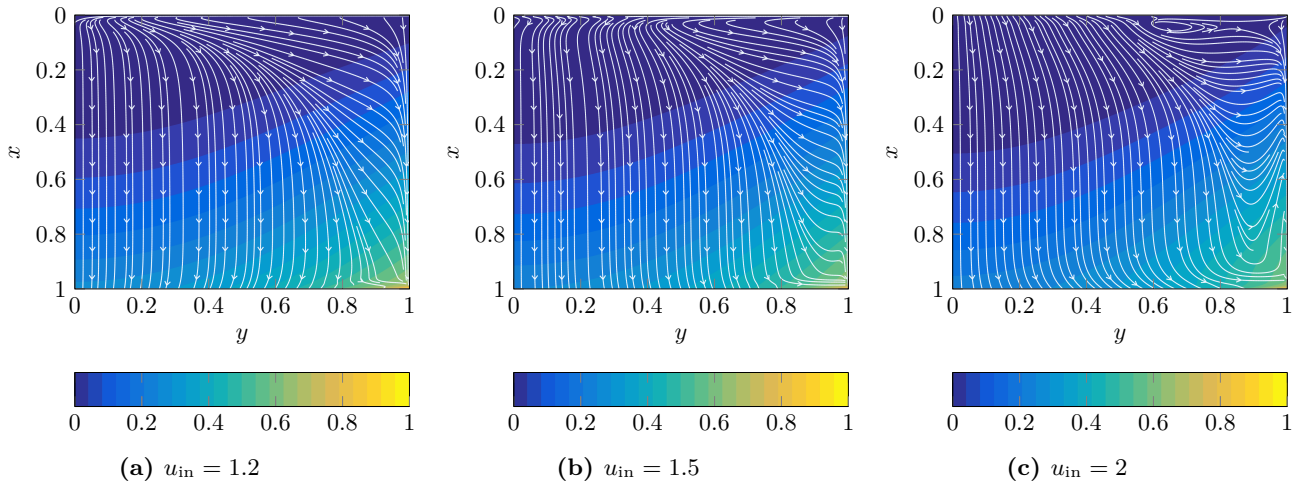

(a) $u_{\text{in}} = 1.2$ **(b)** $u_{\text{in}} = 1.5$ **(c)** $u_{\text{in}} = 2$

Figure 5.6.3 – Temperature profiles given by solving (5.118) coupled with (5.119a), and streamlines obtained with the full velocity profiles (5.52) and (5.53). We have used $\theta_a = x$, $\theta_0 = 1$, $\Gamma = 30$, $\text{Pe}^* = 1.1$, $N = 1000$, $K = 600$, $\text{Bi}^* = 2.3$, $q = 1$, and $\varepsilon_q = 0.1$ as we increase u_{in}

5.7 Concluding remarks

In this chapter our aim has been to exploit the small aspect ratio ϵ of the electrode and the strong temperature-dependent viscosity to derive a simplified model. We have found that a new distinguished limit emerges when the viscosity variation across the domain is of order $1/\epsilon^2$. The result is a new hybrid model that contains elements of both lubrication theory and extensional flow. The model describes an approximate plug flow of the cold cylinders down the centre of the domain while hotter low-viscosity paste flows along the sides, in qualitative agreement with the full numerical results obtained in Chapter 4.

As a first test, in §5.1 we used the model to analyse the flow problem with a known temperature profile and a viscosity that varies exponentially with temperature. In §5.1.4, using Laplace's method, we showed that the flow of softened paste can be treated as a boundary layer near the casing which exerts a drag on the colder central plug flow. The flow problem can then be reduced to a single ODE for the central paste velocity, with coefficients that depend on the temperature field.

We solved these approximations for a fully developed flow that is independent of x in §5.1.5, leading to a pressure profile dependent on the temperature at the wall. In particular, for a constant temperature at the wall we obtained a small constant pressure gradient. The equations were also solved for a developing flow in §5.1.7, and the form of the solution was explored for a quadratic temperature profile that is independent of x in §5.1.7, and varying with x in §5.1.8. Backflow may be present in the boundary layer, providing a mechanism for the hot paste at the wall to transport heat to the incoming paste cylinders. This backflow occurs when $u_{\text{in}} > q$, where u_{in} is the velocity at the inlet, and q is the flux, which can be set to 1, for the industrially relevant problem. We compared the asymptotic solutions with the finite element simulations described in Chapter 4, and found that the asymptotic flow profile is a good approximation of key features of the finite element

solutions.

Next, we considered the heat transport problem in §5.2. By exploiting the boundary layer structure of the velocity field, we reduced the problem to a one-dimensional heat equation with a novel boundary condition at the casing, which captures both heat transfer with the casing wall and heat transport by the flow of softened paste in the boundary layer.

To understand the effect of this new boundary condition we analysed the thermal problem with a known constant velocity in §5.3. We found that the interaction with the boundary layer at the casing wall is characterised by the parameter $\delta = u - q$. If $\delta < 0$, then the boundary layer flow is in the same direction as the cylinder velocity, while if $\delta > 0$ then they are in opposite directions. In this latter case, which is the one relevant to the industrial process, we found that it is necessary to impose a very unusual downstream boundary condition on the wall temperature to obtain a well-posed problem. We also showed that the temperature field develops some discontinuities and boundary layers at the corners of the domain and analysed how these depend on the parameters, in particular on the sign of δ.

Having studied the flow and temperature problem in isolation, we couple the two problems in §5.5. We solved the fully coupled problem numerically in §5.5.1 by iterating between flow and the temperature numerical schemes computing the full viscosity integrals numerically rather than using the approximations generated using Laplace's method. This iterative procedure converges very quickly.

Finally, we used the numerical method for the fully coupled problem to explore the effect of the relevant parameters in the problem, namely Pe^*, Bi^*, and u_{in}. We find that larger recirculation zones occur for smaller Pe^*, larger Bi^* or larger u_{in}. These have the tendency to cause the paste to spread towards the casing lower in the domain. Thus, although the necessary heating and softening of the paste is facilitated by the upwards transport of heat in these recirculating regions, they also have competing influences on the location of the spreading, hinting at the very sensitive conditions under which the electrodes operate. Additionally, we found that the hot air column is essential for the softening and deformation of the paste cylinders, as for $\mathrm{Bi}^* = 0$, recirculation is caused by setting $u_{\mathrm{in}} > q$ and the cylinders sink towards the centre instead of softening.

Chapter 6

Conclusions

In this chapter, we summarise the main conclusions derived from the mathematical models developed and described in this thesis. We highlight the specific conclusions for each chapter in §6.1, together with how they can be translated into industrial recommendations for Elkem ASA. In §6.2 we discuss some potential extensions to our work, and we conclude with some closing remarks in §6.3.

6.1 Summary of results and industrial recommendations

We treated Søderberg electrode paste as a Newtonian incompressible fluid with a temperature-dependent viscosity whose sensitivity is determined by the parameter Γ. We focused our modelling efforts towards the top part of the electrode column, where the paste softening occurs. We included the heating from the hot air supplied by the air fan on the electrode casing and the induction heating caused by the proximity of the current tubes to the metal casing.

In Chapter 2, we derived a coupled flow and temperature model for paste softening, neglecting inertia and the hot paste pool that may appear near the top of the electrode. The temperature was assumed to be uniform across the cross-section and the position where the paste touches the casing for the first time, $x = \lambda$, was an output of the model. We proceeded to asymptotically reduce this 2D model to a one-dimensional extensional flow model coupled to temperature, which described the behaviour of the paste averaged over the cross-sectional area. We restricted our domain to $0 < x < 1$, and interpreted a resulting $\lambda > 1$ as a failure of the industrial process as the paste does not reach the casing in the appropriate region. In this chapter we only considered steady state solutions, with a constant air heating θ_{a} and a piecewise linear function for the induction heating $Q(x)$. The parameter Γ, describing the strength of the viscosity-temperature dependence, is estimated to be around 23 based on industrial experiments, which made our steady numerical method prohibitively stiff. To circumvent this issue, we used $\Gamma = 10$ in all the simulations in this chapter which still represents a very significant temperature dependence. Elkem ASA are interested in the scalability of their electrodes, in particular how increasing the casing radius may affect the

softening profile of the paste. We found that increasing the radius of the casing while keeping the radius of the cylinders fixed (decreasing the area ratio D) lowers the position of λ. Therefore, if it is required to produce Søderberg electrodes with a large radius, it will be necessary to modify for example the weight or radius of the cylinders at the top, the hot air along the casing wall, and the slipping rate. We found that the position of λ depends sensitively on the applied compressive load P_{in}, which motivated the examples investigated in Chapter 3 for the time dependent case. We also found that the heating from the air along the casing, θ_{a}, contributes significantly to the softening of paste, as the conduction of heat to the upper part of the electrode is weak. Therefore, we determined that the role of θ_{a} alternates between a heating and a cooling mechanism, with the switch occurring when θ becomes larger than θ_{a}.

In Chapter 3, we extended the model presented in Chapter 2 to the unsteady case, with the same constant θ_{a} and piecewise linear $Q(x)$. We used a finite volume scheme to calculate the time evolution of the area, the velocity, the temperature, and the position of the free boundary, $\lambda(t)$. This scheme allowed for the use of a larger value of $\Gamma = 23$, but it was much slower to converge than the one used for steady solutions in Chapter 2. Our main interest was to understand how changes in $P_{\text{in}}(t)$ propagate through time and affect the free boundary $\lambda(t)$. We proposed two possible control strategies that mimic the cylinder addition patterns used during normal operations at Elkem ASA, including the skipping of addition days and its consequences on the paste softening profile. We found that the additional weight required to skip days leads to two distinct peaks in λ fluctuations: the first caused by the specific addition event and the second by the effects of the cold paste descending more rapidly into the casing. We explored these control strategies for both integer and non-integer cylinder addition and found that the system can reach a periodic state when arbitrary cylinder addition was allowed, but not when we restricted the problem to integer number of cylinders. We also varied the casing velocity and found that since it varies on a faster timescale than both P_{in} and the flow, the resulting fast oscillations in λ did not significantly alter the qualitative behaviour in the rest of the domain, thus confirming that using a constant casing velocity was appropriate for the model we have developed. We also explored the addition problem analytically, by assuming a large addition frequency ω, obtaining asymptotic approximations for the fluctuations in P_{in}, the area, the velocity, the temperature, and λ. For these solutions, we used a Gaussian form for the induction heating function $Q(x)$. We saw that the temperature had a boundary layer structure near the top of the domain, $x = 0$, for which we also showed analytical solutions. The area presented additional oscillations propagated through the domain, which we investigated using the method of multiple scales. We found that our approximation predicts the position of the propagating oscillations, but not the spatial attenuation present in the numerical solution, which we attributed to numerical dissipation effects intrinsic to the numerical scheme we used.

In Chapter 4, we presented finite element simulations using the Python based CFD solver FEniCS, for a simplified version of the free boundary problem in steady state, which was easier to implement

and described the features present in the industrial problem. Unlike the models shown in Chapter 2 and Chapter 3, in this chapter we used the full axisymmetric formulation, which allowed us to capture the presence of the paste pool, corresponding to hotter and hence less viscous paste that is present near the inlet. We used a simple linear hot air heating function $\theta_{\mathrm{a}}(x)$ and a Gaussian form for the induction heating $Q(x)$. We obtained initial simulations by 'cutting' the region of interest. We considered two different possibilities for the boundary condition imposed at the flattened free boundary, either zero normal stress or zero normal flow. We identified corner singularities in the flow making computations of the pressure and normal stress difficult, which we tackled by using an adaptive mesh. We solved the problem using both a Cartesian and an axisymmetric geometry, and found that although the latter is closer to the real geometry of the problem, both frameworks provide similar numerical results. We identified recirculation zones in the paste indicating the upwards transport of relatively hot paste to the surface. We investigated the effect of varying the heating parameters and the inlet velocity, and found that increasing the effects of the heating on the casing wall lead to a greater viscosity change in the paste closer to the wall, allowing for larger recirculation zones. Similarly, a paste with a larger thermal conductivity and using a lower casing velocity resulted in larger recirculation zones. As we are ultimately interested in the addition of cylinders and how this affects the flow, we described two approaches that are easily implemented in our finite element simulations. The first was a naive approach to the dynamic free surface problem where we allowed the inlet velocity to differ from its steady state value, and calculated the corresponding weight of cylinders above the domain. The second approach was kept at steady state, but the wall heating and induction heating were varied in such a way to represent the free surface having moved upwards or downwards. We effectively related the change of the free surface position to the weight of the added cylinders, showing that a higher level of paste near the wall corresponded to a higher weight of cylinders on top. Our model produced encouraging results, predicting the presence of a recirculation zone which transports hot paste upwards, potentially giving rise to the observed pool of less viscous paste at the surface, and to segregation problems in the electrode.

In Chapter 5, we attempted to understand some more of the flow structures observed in the simulations from Chapter 4 by using asymptotic analysis in the limit where the casing is long and thin and the viscosity varies dramatically across its width. We simplified the calculations by considering a general two-dimensional geometry with the fluid occupying a rectangular domain to derive the model and reduce it asymptotically. We first analysed the flow problem for a known temperature profile. Exploiting the small aspect ratio of the geometry, we found a distinguished limit where the viscosity near the walls is much smaller than that in the bulk of the flow. The leading-order model consisted of an outer extensional (plug) flow with lubrication layers near the walls. We approximated the integrals of the temperature profile using Laplace's method and found that the flow problem can be reduced to a single ODE with coefficients which solely depend on the values of the temperature and temperature gradients at the wall and the centre-line. We found

that backflow may be present in the boundary layer, providing a mechanism for the hot paste at the wall to transport heat to the incoming paste cylinders. Then, we looked at the complementary problem for the temperature, assuming a known flow. We found that rapid reverse flow in the boundary layers near the walls leads to a novel thermal boundary condition that propagates information upstream, capturing both heat transfer with the casing wall and heat transport by the flow of softened paste in the boundary layer. We found that the interaction with the boundary layer at the casing wall is characterised by the parameter δ, which is the difference between the inlet velocity and the downstream velocity of the fluid. If $\delta < 0$, the boundary layer flow is in the same direction as the cylinder velocity, while if $\delta > 0$, then they are in opposite directions. The latter case is the relevant one for the industrial process, and we found that it was necessary to impose an unusual downstream condition on the wall temperature to obtain a well-posed problem. Finally, we coupled the two problems numerically which allowed us to show similar examples to the parameter exploration shown in Chapter 4. In particular, we found that larger recirculation zones occur for a smaller Pe, larger Bi, or larger u_{in}, consistent with our findings in Chapter 4. We confirmed that the electrodes operate under very sensitive conditions, as the upwards transport of hotter paste in the recirculating regions aids the softening process but also affects the location of the spreading. The hot air column was found to be essential for the softening and deformation of the paste cylinders, consistent with our conclusions in Chapters 2 and 3.

6.2 Future work

We have made a number of simplifying assumptions about the properties of the paste and the heating terms that lead to the paste softening. We could extend the work in this thesis by relaxing some of these assumptions and by including additional models for the other processes occurring inside the electrode column.

For instance, we could write a model for the hot air heating, and impose the material parameters as position or temperature dependent, such as the heat transfer coefficient and the thermal conductivity. The induction heating can also be modelled by solving an additional equation which would depend on the electric current supplied to the contact clamps and the proximity of the copper tubes to the electrode casing. This could then be coupled to the problem in Chapters 2 and 3 for a more realistic study of the effect of the heating terms in the model. We could also make our models more realistic by including the shear-thinning behaviour of the paste into the viscosity function, which would now depend on the shear rate.

Additionally, we could use a two-phase flow approach to capture the effects of segregation explicitly, similar to the work in Bergstrøm et al. (1989), where the length of the segregation region, where the coarse particles separate from the binder, depends on the applied load. We could incorporate this into the model in Chapter 2, writing down the governing equations for the interstitial fluid and the segregated paste. We would need to impose appropriate boundary conditions of continuous

stress at the interface, for example by requiring the (unsegregated) paste stress to have zero shear component, and the normal stress to balance the hydrostatic pressure in the segregated region. Then, our λ value would correspond to the length of the region of segregated paste. We could further extend this as a time-dependent problem following the same techniques as in Chapter 3. This would also be a way to combine the models in Chapters 2 and 3 with the one in Chapter 5, as we could interpret the viscous pool as either the segregated paste or the slightly hotter paste (without fines separation), depending on the viscosity we impose. Then, we would expect recirculation zones to appear for certain parameter regimes, as they do in Chapters 4 and 5, and we could analyse how these affect the segregation lengthscale. Depending on the viscosity of the viscous pool next to the added cylinders, we could incorporate buoyancy effects, as this is one of the dangers of having segregated paste preventing the cylinders from sinking properly (i.e. making them sink either too fast or too slow).

In addition to these general extensions, we have the following chapter-specific extensions that can be added to the relevant model:

- In Chapter 3, we could use our multiple scales approach from §3.5 for the coupled problem, using the isothermal solutions as a guide. Although they do not appear in the temperature and velocity solutions, it is likely that the position and amplitude of the oscillations in the area are affected by the other parameters in our problem. Additionally, we could also extend our asymptotic solutions for the fast applied load oscillations for a general, periodic, non-sinusoidal $P_{\text{in}}(t)$. This would allow us to impose a form that is closer to the industrial practice of adding cylinders, similar to the control strategies imposed in §3.3. Furthermore, we can incorporate the addition of briquettes in between cylinder addition events, which is closer to what is done in practice (Nelson and Prins, 2004) and investigate whether this changes the resulting softening profile. We could also perform a stability analysis for this problem and see whether we would encounter situations where cylinder addition leads to instabilities. Finally, in this chapter we could also modify the numerical method to reduce numerical dissipation, for instance similar to the one proposed in Kurganov and Lin (2007).
- We can make our model in Chapter 4 more realistic by incorporating the free boundary, rather than using a simplified geometry to flatten it. One way to do this is to implement the Arbitrary Lagrangian-Eulerian (ALE) method to deform the mesh according to the motion of the free surface. An example of an ALE implementation in FEniCS is given by Selim (2012) and in principle could be modified for our problem. This would also be a contact problem, which would require imposing additional boundary conditions where the paste touches the casing. Another extension of this work is to include the iterative procedure to allow for time dependence. We could start with the simplified problem presented in the chapter, but the goal is to eventually have a time dependent model of the free surface evolution. The time-dependent setup would allow us to include cylinder addition in a similar form as in Chapter 3, where add a specified number of cylinders at discrete times.

- In Chapter 5 we could formulate the problem for an axisymmetric geometry, which might be more mathematically involved as it will contain logarithmic and $1/r$ terms, but is closer to the real geometry of the electrode column.

Finally, some future directions we could take in the mathematical study of Søderberg electrodes are:

- A model for the baking, with the Ohmic heating from the (alternating) current supplied to the clamps, including skin effects, radiation effects from the furnace, and using temperature dependent material parameters. The output of this model would be the shape of the baking isotherm, similar to the work done in Van Gorder et al. (2021). We could eventually couple this to the softening model in this thesis.
- A model for the casing fins, perhaps similar to the one in Meyjes et al. (2010). We could start by formulating the problem for a horizontal cross-section, and perhaps even a slice of this section for one fin, where we model the heating effect of the fins on the baking of paste, under various simplifying assumptions. Then, we can use the intuition from this simple model to extend the baking model and incorporate the effects from the fins and then solve it together with the softening model, by modifying the boundary conditions accordingly.

6.3 Closing remarks

The study of Søderberg electrodes is a mathematically rich area, with significant potential for further study. The results summarised in §6.1 and the potential work discussed in §6.2 could lead to design changes in these types of electrodes, which would be improvements with a significant financial impact and lead to the prevention of segregation and electrode breakages. The asymptotic reductions used throughout this work are a good way to provide qualitative results and to gain an understanding of the physical effects behind them, which is sometimes difficult to obtain from numerical results. On the other hand, finite element models can tackle more realistic geometries and parameters, and can also guide the asymptotics work. In this thesis, we have used both an asymptotic and a numerical approach to analyse the softening profile of the electrode paste, a less studied problem than the baking process that makes the electrodes.

We have found that, when designing electrodes of a larger radius, it is important to modify the pertaining operating parameters that allow for the paste to soften in the required region, thus preventing a baked electrode with non-uniform material properties, which leads to breakages. This translates into increasing the weight or radius of added cylinders, decreasing the casing velocity, and increasing the heating from the wall, to balance the effects of the larger radius. We have also found that adding more cylinders is better than not enough, as the added weight aids the softening process, allowing the paste to spread more readily towards the casing. However, when incorporating the effects of the viscous pool of paste, we found the presence of recirculating regions which may

prevent the paste from reaching the electrode casing. In particular, a large recirculating zone of hot paste may lead to cylinders sinking rather than softening, which could lead to segregation problems and thus breakages. In this case, increasing the heating from the hot air, using electrode paste with a larger thermal conductivity, and decreasing the casing velocity are all linked to an increase of the recirculating region in our work, and therefore may lead to electrode problems. Conversely, a recirculating zone that is too small may prevent the cylinders from softening and spreading into the casing. In particular, in the absence of heating from the hot air, the paste softening process fails as its temperature is too low.

The models presented are far from a complete study on the softening of paste, but set a modelling foundation for the top area of the electrode. It is our hope to inspire further work that could eventually be coupled with the electrode baking process. This would allow Elkem ASA to optimise their silicon production process, reducing costs, and decreasing the risk of dangerous electrode breakages.

References

G. Andersen, B. Larsen, and R. Innvaer. Operation of Søderberg electrodes. Methods to avoid and solve electrode failures. In *International Ferroalloys Congress*, pages 494–500, Quebec, 2001.

U. Ayachit. *The ParaView Guide: A Parallel Visualization Application*. Kitware, 2015.

R. E. Banki and B. D. Welfert. A posteriori error estimates for the Stokes problem. *SIAM Journal of Numerical Analysis*, 28(3):591–623, 1991.

T. Bergstrøm, S. Cowley, A. C. Fowler, and P. E. Seward. Segregation of carbon paste in a smelting electrode. *IMA Journal of Applied Mathematics*, 43(1):83–99, 1989.

A. Bermúdez, J. Bullón, and F. Pena. A finite element method for the thermoelectrical modelling of electrodes. *Communications in numerical methods in engineering*, 14(6):581–593, 1998.

A. Costa and G. Macedonio. Viscous heating effects in fluids with temperature-dependent viscosity: Triggering of secondary flows. *Journal of Fluid Mechanics*, 540:21–38, 2005.

R. Courant, K. Friedrichs, and H. Lewy. On the partial difference equations of mathematical physics. *IBM Journal*, 11:215–234, 1959.

B. Y. W. R. Dean and P. E. Montagnon. On the steady motion of viscous fluid in a corner. *Mathematical Proceedings of the Cambridge Philosophical Society*, 45(3):389–394, 1949.

J. Dewynne, J. R. Ockendon, and P. Wilmott. On a mathematical model for fiber tapering. *SIAM Journal on Applied Mathematics*, 49(4):983–990, 1989.

J. N. Dewynne, J. R. Ockendon, and P. Wilmott. A systematic derivation of the leading-order equations for extensional flows in slender geometries. *Journal of Fluid Mechanics*, 24:323–338, 1992.

H. Elman, D. Silvester, and A. J. Wathen. The Stokes Equations. In *Finite Elements and Fast Iterative Solvers: With Applications in Incompressible Fluid Dynamics*, chapter 3, pages 119–188. Oxford University Press, Oxford, 2nd edition, 2014.

A. Fasano and M. Primicerio. *Free boundary problems: theory and applications*. Pitman Advanced Publishing Program, London, 1983.

N. Fehn, W. A. Wall, and M. Kronbichler. On the stability of projection methods for the incompressible Navier-Stokes equations based on high-order discontinuous Galerkin discretizations. *Journal of Computational Physics*, 351:392–421, 2017.

R. J. Fisher and M. M. Denn. Finite-amplitude stability and draw resonance in isothermal melt spinning. *Chemical Engineering Science*, 30(9):1129–1134, 1975.

A. D. Fitt. Two-phase flow methodology and modelling. In *Proceedings of the Fourth European Conference on Mathematics in Industry*, pages 277–281. Teubner Stuttgart and Kluwer Academic Publishers, 1991.

A. D. Fitt and J. M. Aitchison. Determining the effective viscosity of a carbon paste used for continuous electrode smelting. *Fluid Dynamics Research*, 11(1-2):37–59, 1993.

A. D. Fitt and P. D. Howell. The manufacture of continuous smelting electrodes from carbon-paste briquettes. *Journal of Engineering Mathematics*, 33(4):353–376, 1998.

S. K. Godunov. [A difference scheme for numerical solution of discontinuous solution of hydrodynamic equations]. *Matematicheskii Sbornik*, 47(3):271–306, 1959.

T. Hannesson. The Si process Drawings, 2016.

P. D. Howell. *Extensional thin layer flows*. PhD thesis, University of Oxford, 1994.

R. Innvaer. The Søderberg electrode system. Recent research and development. New challenges. In *International Ferro-Alloys Congress*, pages 216–226, New Orleans, 1989.

R. Innvaer and L. Olsen. Practical use of mathematical models for Soderberg electrodes. Technical report, Elkem-Spigerverket a/s, 1979.

R. Innvær, A. Vatland, and L. Olsen. Operational parameters for Soderberg electrodes from calculations, measurements, and plant experience. In *Mintek 50, Johannesburg 1984*, 1985.

R. Innvaer, K. Fidje, and K. Kalgraf. Expert system for Soderberg electrodes. In *Innovations in Ferro Alloy Industry*, pages 555–564, 1995.

M. T. Jonsson and H. T. Ingason. A three dimensional simulation model for a Soderberg electrode. In *The Proceedings of INFACON VIII*, pages 383–388, 1998.

D. D. Joseph. Variable viscosity effects on the flow and stability of flow in channels and pipes. *The Physics of Fluids*, 7(11):1761–1771, 1964.

S. Kase and T. Matsuo. Studies on melt spinning. I. Fundamental equations on the dynamics of melt spinning. *Journal of Polymer Science Part A: General Papers*, 3(7):2541–2554, jul 1965.

T. S. Khaleque, A. C. Fowler, P. D. Howell, and M. Vynnycky. Numerical studies of thermal convection with temperature-and pressure-dependent viscosity at extreme viscosity contrasts. *Physics of Fluids*, 27:76603, 2015.

J. Kierzenka and L. F. Shampine. A BVP solver based on residual control and the MATLAB PSE. *ACM Transactions on Mathematical Software*, 27(3):299–316, 2001.

A. Kurganov and C. T. Lin. On the reduction of numerical dissipation in central-upwind schemes. *Communications in Computational Physics*, 2(1):141–163, 2007.

A. Kurganov and E. Tadmor. New High-Resolution Central Schemes for Nonlinear Conservation Laws and Convection-Diffusion Equations. *Journal of Computational Physics*, 160:241–282, 2000.

A. A. Lacey. Thermal runaway in a non-local problem modelling Ohmic heating. Part II: General proof of blow-up and asymptotics of runaway. *European Journal of Applied Mathematics*, 6(3): 201–224, 1995.

W. E. Langlois and M. O. Deville. *Slow Viscous Flow*. Springer, 2 edition, 2014.

H. P. Langtangen and A. Logg. *Solving PDEs in Python-The FEniCS Tutorial Volume I*. 2017.

B. Larsen. Electrode models for Søderberg electrodes. Technical report, Kiev, 2012.

B. Larsen, J. P. M. Amaro, S. Z. Nascimento, K. Fidje, and H. Gran. Melting and densification of electrode paste briquettes in Søderberg electrodes. *Elkem*, pages 1–10, 1998.

B. Larsen, H. Feldborg, and S. A. Halvorsen. Minimizing thermal stress during shutdown of Soderberg electrodes. In *The thirteenth International Ferroalloys Congress Efficient technologies in ferroalloy industry*, pages 453–467, Almaty, Kazakhstan, 2013.

H. L. Larsen. Current distribution in the electrodes of industrial three-phase electric smelting furnaces. In *Proceedings of the 2006 Nordic COMSOL Conference*, 2006.

R. J. LeVeque. *Numerical Methods for Conservation Laws*. Zurich, second edition, 1992.

A. Logg, G. N. Wells, and J. Hake. DOLFIN: a C++/Python Finite Element Library. In A. Logg, K.-A. Mardal, and G. N. Wells, editors, *Automated Solution of Differential Equations by the Finite Element Method, Volume 84 of Lecture Notes in Computational Science and Engineering,*, chapter 10. Springer, 2012.

C. R. Mason. Correlations between pitch binder properties and properties of Soderberg electrodes. pages 165–174, 1970.

M. A. Matovich and J. R. A. Pearson. Spinning a molten threadline: steady-state isothermal viscous flows. *I&EC Fundamentals*, 8(3):512–520, 1969.

I. McDougall. Ferroalloys Processing Equipment. In M. Gasik, editor, *Handbook of Ferroalloys*, chapter 4, pages 83–138. Butterworth-Heinemann, 2013.

I. McDougall, C. F. R. Smith, B. Olmstead, and W. A. Gericke. A finite element model of a Soderberg electrode with an application in casing design. Technical report, 2004.

R. P. Meyjes, J. Venter, and U. Van Rooyen. Advanced modelling and baking of electrodes. In *The Twelfth International Ferroalloys Congress: Sustainable Future*, pages 779–788, Helsinki, 2010.

H. K. Moffatt. Viscous and resistive eddies near a sharp corner. *Journal of Fluid Mechanics*, 18(1): 1–18, 1964.

S. Morris. The effects of a strongly temperature-dependent viscosity on slow flow past a hot sphere. *Journal of Fluid Mechanics*, pages 1–26, 1982.

L. R. Nelson and F. X. Prins. Insights into the influences of paste additions and levels on Søderberg electrode management. In *Tenth International Ferroalloys Congress*, volume 1, pages 418–431, Cape Town, 2004.

H. Ockendon. Channel flow with temperature-dependent viscosity and internal viscous dissipation. *Journal of Fluid Mechanics*, 93(4):737–746, 1979.

H. Ockendon and J. R. Ockendon. Variable-viscosity flows in heated and cooled channels. *Journal of Fluid Mechanics*, 83(1):177–190, 1977.

H. Ockendon and J. R. Ockendon. *Viscous Flow*. Cambridge University Press, 1995.

D. O'Kiely, C. J. W. Breward, I. M. Griffiths, P. D. Howell, and U. Lange. Edge behaviour in the glass sheet redraw process. *Journal of Fluid Mechanics*, 785:248–269, 2015.

I. Olsen and O. Sandberg. Problems connected with segregation of Søderberg electrode paste. Technical report, Elektrokemisk, Kristiansand, 1967.

L. Olsen, A. G. Arnesen, I. Bencze, and R. Innvaer. Temperature distribution in Soderberg electrodes. *U.I.E.*, VII(405):1–5, 1972.

R. J. Ord, J. G. Schofield, and C. G. Tan. Improved Performance of Soderberg electrodes. *CIM Bulletin*, 88(991), 1995.

H. Palsson and M. R. Jonsson. Finite element analysis of proximity effects in Sderberg electrodes. Technical report, 2000.

J. R. A. Pearson. Variable-viscosity flows in channels with high heat generation. *Journal of Fluid Mechanics*, 83(1):191–206, 1977.

J. R. A. Pearson and Y. T. Shah. The use of tensors to describe and predict fiber orientation in short fiber composites. *Transactions of the Society of Rheology*, 16:19–533, 1972.

C. J. S. Petrie. Extensional flow - a mathematical perspective. *Rheologica Acta*, 34:12–26, 1995.

C. R. Ray, P. K. Sahoo, and S. S. Rao. Electrode management - investigation into soft breaks at 48 MVa FeCr closed furnace. In *Innovations in Ferro Alloy Industry*, pages 740–751, 2007.

P. L. Roe. Approximate Riemann Solvers, Parameter Vectors, and Difference Schemes. *Journal of Computational Physics*, 43:357–372, 1981.

F. Sawo and T. Bernard. Finite element model of a complex glass forming process as a tool for control optimization. In *COMSOL Conference 2009 Milan*, Milan, 2009.

B. Scheid, S. Quiligotti, R. Gy, and H. A. Stone. On the (de)stabilization of draw resonance due to cooling. *Journal of Fluid Mechanics*, 636:155–176, 2009.

W. E. Schiesser and G. W. Griffiths. *A compendium of partial differential equation models - method of lines analysis with Matlab*. Cambridge University Press, 2009.

K. Selim. An adaptive finite element solver for fluid-structure interaction problems. In A. Logg, editor, *Automated Solution of Differential Equations by the Finite Element Method - The FEniCS Book*, chapter 29, pages 553–569. Springer Berlin Heidelberg, 2012.

Y. T. Shah and J. R. A. Pearson. On the stability of nonisothermal fiber spinning. *Ind. Eng. Chem. Fundam*, 11(2):145–149, 1972.

L. Shoko, J. P. Beukes, and C. A. Strydom. Determining the baking isotherm temperature of Søderberg electrodes and associated structural changes. *Minerals Engineering*, 49:33–39, 2013.

A. Skjeldestad. *Electrode paste behaviour in Soderberg electrodes in ferroalloy production.* PhD thesis, Norwegian University of Science and Technology, 2019.

A. Skjeldestad, M. Tangstad, L. Lindstad, and B. Larsen. Temperature profiles in Søderberg electrodes. In *Production Technologies and Operation, Kiev, 2015. The Fourteenth International Ferroalloys Congress*, pages 327–338, Kiev, 2015. The Fourteenth International Ferroalloys Congress.

B. M. Sloman, C. P. Please, and R. A. Van Gorder. Melting and dripping of a heated material with temperature-dependent viscosity in a thin vertical tube. *Journal of Fluid Mechanics*, 905(A16), 2020.

C. W. Söderberg. Electrode for electric furnaces and process for manufacturing the same, 1923.

P. S. Stewart, J. Feng, L. S. Kimpton, I. M. Griffiths, and H. A. Stone. Stability of a bi-layer free film: simultaneous or individual rupture events? *Journal of Fluid Mechanics*, 777:27–49, 2015.

M. Taroni, C. J. W. Breward, L. J. Cummings, and I. M. Griffiths. Asymptotic solutions of glass temperature profiles during steady optical fibre drawing. *Journal of Engineering Mathematics*, 80:1–20, 2013.

A. R. Terrel, L. R. Scott, M. G. Knepley, R. C. Kirby, and G. N. Wells. Finite elements for incompressible fluids. In A. Logg, G. Wells, and K.-A. Mardal, editors, *Automated Solution of Differential Equations by the Finite Element Method - The FEniCS Book*, chapter 20, pages 385–397. Springer Berlin Heidelberg, 2016.

F. T. Trouton. On the coefficient of viscous traction and its relation to that of viscosity. *The Phylosophical Magazine*, 19:426–440, 1906.

R. A. Van Gorder, A. Kamilova, R. G. Birkeland, and A. L. Krause. Locating the baking isotherm in a Søderberg electrode: analysis of a moving thermistor model. *SIAM*, pages 1–21, 2021.

S. Wilkinson, P. A. Ganguly, J. L. Williams, and P. M. Jensen. Impact of electrode paste on Soderberg electrode performance. In *The Ninth International Ferroalloys Congress*, pages 510–520, Quebec, 2001.

J. J. Wylie and J. R. Lister. The effects of temperature-dependent viscosity on flow in a cooled channel with application to basaltic fissure eruptions. *Journal of Fluid Mechanics*, 305:239–261, 1995.

Appendix A

Finite volume scheme for time dependent problem in Chapter 3

Given the structure of our governing equations (3.1), (3.2), and (3.14), we use a finite volume scheme for computing A, θ, and Φ evaluated at the cells, and a finite difference scheme for computing u evaluated at the interfaces, as shown in the stencils in Figure A.1. This figure also defines the indexing we use below.

We first solve (3.8b) for u, using a central differences scheme, which gives

$$\frac{3\mu(\theta_{k+1})A_{k+1}\left(\frac{u_{k+\frac{3}{2}}-u_{k+\frac{1}{2}}}{\Delta X}\right)-3\mu(\theta_k)A_k\left(\frac{u_{k+\frac{1}{2}}-u_{k-\frac{1}{2}}}{\Delta X}\right)}{\Delta X}=-\lambda^2\mathrm{St}A_{k+\frac{1}{2}}, \tag{A.1}$$

for $-1 \leq k < K$, where we define

$$A_{k+\frac{1}{2}}=\frac{1}{2}\left(A_k+A_{k+1}\right). \tag{A.2}$$

Equation (A.1) simplifies as

$$3\mu(\theta_{k+1})A_{k+1}u_{k+\frac{3}{2}}-3\left[\mu(\theta_{k+1})A_{k+1}+\mu(\theta_k)A_k\right]u_{k+\frac{1}{2}}+3\mu(\theta_k)A_ku_{k-\frac{1}{2}}=-\lambda^2\Delta X^2\mathrm{St}A_{k+\frac{1}{2}}, \tag{A.3}$$

for $-1 \leq k < K$.

We define the advective numerical flux $\bar{\mathcal{F}}$ of a quantity $\mathcal{U}$ as

$$\bar{\mathcal{F}}^{\mathcal{U}}_{k+\frac{1}{2}}:=\bar{\mathcal{F}}\left(\mathcal{U}_k,\mathcal{U}_{k+1}\right)=\frac{1}{2}v_{k+\frac{1}{2}}\left(\mathcal{U}_k+\mathcal{U}_{k+1}\right)-\frac{1}{2}|v_{k+\frac{1}{2}}|\left(\mathcal{U}_{k+1}-\mathcal{U}_k\right), \tag{A.4}$$

where v is the velocity, namely $v=u-\dot{\lambda}X$ for $0<X<1$. This is a form of Roe flux, introduced in Roe (1981). Note that $\bar{\mathcal{F}}$ is defined at the interfaces. We use Godunov's method (Godunov, 1959)

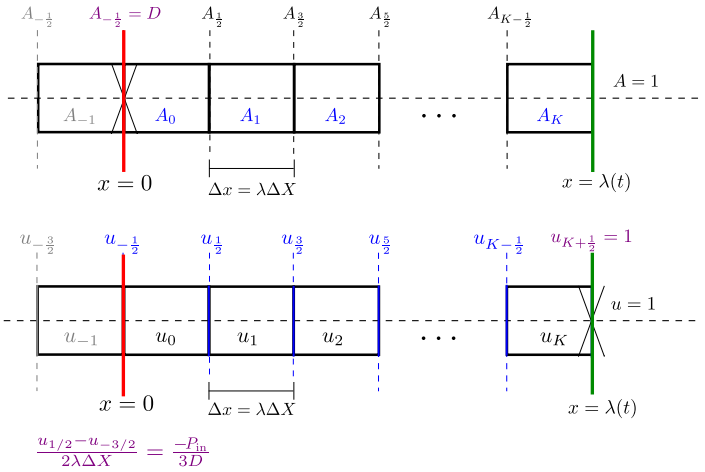

(a) Stencil for A and u.

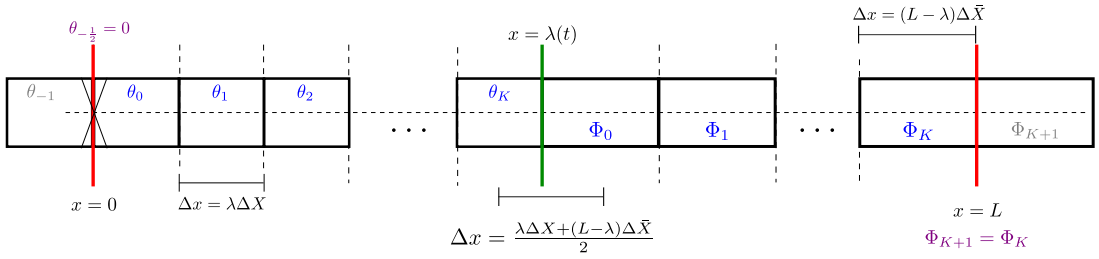

(b) Stencil for temperature.

Figure A.1 – Stencils for the spatial discretisation of (3.1), where grey indicates a ghost node/interface, purple corresponds to the boundary conditions, and blue represents the actual discrete values that are solved for. The free boundary λ is highlighted in the green interface, a red line marks $x = 0$ and $x = L$, and a crossed interface indicates that we do not solve for it (to impose Dirichlet boundary conditions). All x values are evaluated at the interfaces.

for discretising (3.8a), as described by LeVeque (1992). We write

$$\frac{\mathrm{d}}{\mathrm{d}t}\left(\lambda A_k\right) = \frac{\bar{\mathcal{F}}^A_{k-\frac{1}{2}} - \bar{\mathcal{F}}^A_{k+\frac{1}{2}}}{\Delta X}. \tag{A.5}$$

Since both A and u are equal to 1 for $0 < \bar{X} < 1$, we do not need to discretise them. The free boundary λ is defined at the interface, represented by the green line in Figure A.1, and evolves according to (3.9b). We discretise this condition using one sided derivatives of u and A, noting that $A = u = 1$ at $X = 1$, to get

$$\dot{\lambda} = 1 + \frac{1 - u_{K-\frac{1}{2}}}{2\left(1 - A_K\right)}. \tag{A.6}$$

The temperature problem must be solved in both the top and the bottom regions. For the top region, we define the diffusive flux $\hat{\mathcal{F}}$ as

$$\hat{\mathcal{F}}^E_{k+\frac{1}{2}} = \frac{-1}{\mathrm{Pe}\lambda \Delta X} A_{k+\frac{1}{2}}\left(\theta_{k+1} - \theta_k\right), \tag{A.7}$$

where $E = A\theta$ denotes the 'energy density', so that the total flux $\mathcal{F}^E$ is given by

$$\mathcal{F}^E_{k+\frac{1}{2}} = \bar{\mathcal{F}}^E_{k+\frac{1}{2}} + \hat{\mathcal{F}}^E_{k+\frac{1}{2}}, \tag{A.8}$$

where the advective flux $\bar{\mathcal{F}}_{k+1}$ is defined by (A.4). Then we write the discretisation for θ as

$$\dot{E}_k = \frac{\mathcal{F}^E_{k-\frac{1}{2}} - \mathcal{F}^E_{k+\frac{1}{2}}}{\lambda \Delta X} - \frac{\dot{\lambda} E_k}{\lambda} - \frac{2\ \mathrm{Bi}}{\mathrm{Pe}} \sqrt{A_k}\,(\theta_k - \theta_\mathrm{a}(\lambda X_k)) + Q(\lambda X_k) A_k. \tag{A.9}$$

Note that the X values are defined at the interfaces, so we use averaging to evaluate them at the cells.

For the temperature at the bottom region, we define the total flux for Φ as

$$\mathcal{F}^\Phi_{k+\frac{1}{2}} = \bar{\mathcal{F}}^\Phi_{k+\frac{1}{2}} + \hat{\mathcal{F}}^\Phi_{k+\frac{1}{2}}, \tag{A.10}$$

where the diffusive flux is given by

$$\hat{\mathcal{F}}^\Phi_{k+\frac{1}{2}} = \frac{-1}{\mathrm{Pe}\,(L-\lambda)\,\Delta \bar{X}}\,(\Phi_{k+1} - \Phi_k)\,, \tag{A.11}$$

and the advective flux is defined by (A.4) but now with velocity $v = \left(\bar{X} - 1\right)\dot{\lambda} + 1$. Then we write the discretisation for Φ as

$$\dot{\Phi}_k = \frac{\mathcal{F}^\Phi_{k-\frac{1}{2}} - \mathcal{F}^\Phi_{k+\frac{1}{2}}}{(L-\lambda)\,\Delta \bar{X}} + \frac{\dot{\lambda}\Phi_k}{L-\lambda} - \frac{2\ \mathrm{Bi}}{\mathrm{Pe}}\left[\Phi_k - \theta_\mathrm{a}(\lambda + \bar{X}_k\,(L-\lambda))\right] + Q(\lambda + \bar{X}_k\,(L-\lambda)). \tag{A.12}$$

The discretised boundary conditions are implemented with a ghost node approach, implicitly assuming the boundary conditions in the discretisation, which are shown in purple in Figure A.1.

Additionally, the different scalings on both sides of the λ interface need to be reflected in the diffusive flux that is used at that interface. Thus we define

$$\hat{\mathcal{F}}^E_{K+\frac{1}{2}} = \hat{\mathcal{F}}^\Phi_{-\frac{1}{2}} = \frac{-2\,(\Phi_0 - \theta_K)}{\mathrm{Pe}\left(\lambda \Delta X + (L-\lambda)\Delta \bar{X}\right)}, \tag{A.13}$$

which encapsulates the continuity of temperature and heat flux across the λ interface. We also enforce $\theta_{K+1} = \Phi_0$ in the advective flux (A.4) for this purpose.